DISSERTATION | DOCTORAL THESIS

Titel | Title

A Linear Vibronic Coupling/Molecular Mechanics Method and Analysis of Large-Scale Simulations of Nonadiabatic Solute–Solvent Dynamics

verfasst von | submitted by

Severin Carl Claudio Polonius B.Sc. MSc ETH

angestrebter akademischer Grad | in partial fulfilment of the requirements for the degree of

Doktor der Naturwissenschaften (Dr.rer.nat.)

Wien | Vienna, 2024

Studienkennzahl lt. Studienblatt | Degree programme code as it appears on the student record sheet:	UA 796 605 419
Dissertationsgebiet lt. Studienblatt | Field of study as it appears on the student record sheet:	Chemie
Betreut von | Supervisor:	Univ.-Prof. Dr. Dr. h.c. Leticia Gonzalez Herrero
Mitbetreut von | Co-Supervisor:	Dipl.-Chem. Dr. Sebastian Mai

Für meine Eltern, Claudia und Kay

ABSTRACT

The excited-state dynamics of solvated systems is governed by the interactions between the solute and solvent molecules. In order to understand this dynamics, we need to study not only the response of the solute's degrees of freedom to the excitation but also the accompanying changes in the solvent structure over possible many pico- or even nanoseconds. A popular approach for simulating the excited-state dynamics of solvated systems is the trajectory surface hopping method combined with mixed quantum mechanical / molecular mechanical (QM/MM) methods. In this approach, the computational cost of the chosen QM method determines how long and how many of trajectories may be propagated, which can be used to study and resolve the different degrees of freedom of a solvated system. This means that access to more efficient QM methods enables the simulation of excited-state dynamics on longer time scales and with more trajectories that resolve more details of the dynamical solvent structure.

This thesis describes a theoretical framework to combine linear vibronic coupling (LVC) models with a molecular mechanics description of the environment via electrostatic embedding, and its implementation into the SHARC package. The combination of LVC models with surface hopping already is a highly efficient approach for simulating nonadiabatic dynamics of rigid molecules in the gas phase. The thesis explains how vibronic coupling Hamiltonians can be extended to include electrostatic interaction with external point charges, analogous to the widely used QM/MM approach; the resulting method is called LVC/MM. The description of the electrostatic interaction in LVC models is realized through the use of diabatic distributed multipole expansions. The parameters for the distributed multipole expansions can be obtained by the restrained electrostatic potential fitting algorithm, which we extended to evaluate dipole and quadrupole terms. The thesis presents the working equations of all these components, as well as other computational aspects.

The new method is applied to resolve the dynamics of two small thiocarbonyls in water, demonstrating that the LVC/MM method is both efficient and able to accurately reproduce reference results in terms of solvation structure and electronic energies. Additionally, the thesis describes in detail how the simulation of large trajectory swarms allows the analysis of the three dimensional solvation structure from two different perspectives. These different perspectives reveal drastic differences in the relaxation dynamics of both thiocarbonyls. The thesis further describes the simulation of the photo-induced dynamics of $[\mathrm{Fe(CN)_4(bipy)}]^{2-}$ in water. In comparison to a previous study on this system, the application of LVC/MM facilitates surface hopping simulations on much longer time scales and with larger trajectory swarms so that not only the electronic dynamics of long-lived excited states but also the detailed behavior of the solvation shell in three dimensions could be analyzed for the first time.

ZUSAMMENFASSUNG

Die Dynamik angeregter Zustände von Systemen in Lösung wird durch die Wechselwirkungen zwischen den gelösten und den Lösungsmittelmolekülen bestimmt. Um diese Dynamik zu verstehen, müssen wir nicht nur die Reaktion der Freiheitsgrade des gelösten Molekels auf die Anregung, sondern auch die begleitenden Veränderungen in der Lösungsmittelstruktur über möglicherweise viele Piko- oder sogar Nanosekunden untersuchen. Ein beliebter Ansatz hierfür ist die *trajectory surface hopping*-Methode unter Verwendung von gemischten quantenmechanischen/-molekularmechanischen (QM/MM) Methoden. Bei diesem Ansatz bestimmen die Rechenkosten der gewählten QM-Methode die Simulationszeit und die Anzahl der Trajektorien, die zur Untersuchung und Auflösung der verschiedenen Freiheitsgrade eines solvatisierten Systems verwendet werden können. Dies bedeutet, dass der Zugang zu effizienteren QM-Methoden die Simulation der Dynamik angeregter Zustände auf längeren Zeitskalen und mit mehr Trajektorien, die mehr Details der dynamischen Lösungsmittelstruktur auflösen, ermöglicht.

Die Dissertation beschreibt den theoretischen Rahmen für die Kombination von *linear vibronic coupling* (LVC) Modellen mit einer MM-Beschreibung der Umgebung durch elektrostatische Kopplung und deren Implementierung in das SHARC-Paket. Die Kombination von LVC-Modellen mit *trajectory surface hopping* hat sich bereits als hocheffizienter Ansatz zur Simulation der nichtadiabatischen Dynamik starrer Moleküle in der Gasphase erwiesen. In dieser Arbeit wird erläutert, wie vibronische Kopplungs-Hamiltoniane erweitert werden können, sodass die elektrostatische Wechselwirkung mit externen Punktladungen beschrieben werden kann. Die resultierende Methode funktioniert analog zum weit verbreiteten QM/MM-Ansatz und wird daher LVC/MM genannt. Die Beschreibung der elektrostatischen Wechselwirkung in LVC-Modellen wird durch die Verwendung diabatischer verteilter, atomzentrierter Multipol-Entwicklungen realisiert. Die Parameter dafür können mit dem *restrained electrostatic potential*-Algorithmus ermittelt werden, den wir für die zusätzliche Ermittlung von Dipol- und Quadrupoltermen erweitert haben. In dieser Arbeit werden die Gleichungen all dieser Komponenten sowie weitere rechnerische Aspekte vorgestellt.

In der Anwendung auf die Dynamik von zwei kleinen Thiocarbonylen in Wasser wird gezeigt, dass die LVC/MM-Methode sowohl effizient als auch in der Lage ist, Referenzergebnisse in Bezug auf die Solvatationsstruktur und elektronische Energien genau zu reproduzieren. Zusätzlich wird in der Arbeit detailliert beschrieben, wie die Simulation großer Trajektorienschwärme die Analyse der dreidimensionalen Solvatationsstruktur aus zwei verschiedenen Perspektiven ermöglicht. Diese verschiedenen Perspektiven zeigen drastische Unterschiede in der Relaxationsdynamik der beiden Thiocarbonyle auf. Die Dissertation enthält auch Ergebnisse über die Simulation der photoinduzierten Dynamik eines Eisenkomplexes in Wasser, der zuvor in der Gruppe untersucht wurde. Die Anwendung von LVC/MM ermöglicht *surface-hopping*-Simulationen auf viel längeren Zeitskalen und mit größeren Trajektorienschwärmen, so dass nicht nur die elektronische Dynamik von langlebigen angeregten Zuständen, sondern auch das detaillierte Verhalten der Solvatationsschale analysiert werden kann.

CONTENTS

1 INTRODUCTION 1

2 THEORY 5
- 2.1 The Schrödinger Equation and the Born-Oppenheimer Approximation . . . 5
- 2.2 Nonadiabatic Dynamics . . . 8
- 2.3 Diabatic Representation and the Vibronic Coupling Hamiltonian . . 11
- 2.4 The Quantum Mechanical/Molecular Mechanical Method . . . 13
- 2.5 The Restrained Electrostatic Potential Fitting Method . . . 15
- 2.6 Distributed Multipole Expansions . . . 17

3 METHODOLOGICAL DEVELOPMENTS 19
- 3.1 Generalized SHARC-Interfaces . . . 20
- 3.2 Extension of VC Hamiltonians for Electrostatic Embedding . . . 24
- 3.3 Extension of the RESP Fitting Method . . . 28
- 3.4 Computational Efficiency of the LVC/MM method in SHARC . . . 30
- 3.5 Generation and Analysis of 3D-SDFs . . . 33

4 SIMULATIONS ON SMALL THIOCARBONYLS IN WATER 37
- 4.1 Validation and Performance of the LVC/MM Method . . . 37
- 4.2 Time-Dependent Three-Dimensional Solute–Solvent Dynamics . . . 41

5 APPLICATION TO AN IRON COMPLEX IN WATER 44
- 5.1 LVC/MM SHARC Dynamics and Solvent Reorganisation . . . 44
- 5.2 Comparison with TDDFT Results . . . 49

6 CONSIDERATIONS ON THE CONSTRUCTION OF LVC/MM MODELS 51
- 6.1 Prerequisites of the Molecular System and the Normal Modes . . . 51
- 6.2 The Diabatic Basis and ϵ . . . 52
- 6.3 Standard parametrization with κ and λ Parameters . . . 54
- 6.4 Second-order Parameters γ . . . 56
- 6.5 Preparing for Simulations in Solutions and Evaluating the DME . . 57
- 6.6 Validation of the Model . . . 58

7 CONCLUSIONS & OUTLOOK 60

BIBLIOGRAPHY 63

A APPENDIX 75
- A.1 Simulations on Small Thiocarbonyls in Water . . . 77
  - A.1.1 LVC/MM: A Hybrid Linear Vibronic Coupling/Molecular Mechanics Model with Distributed Multipole-Based Electrostatic Embedding for Highly Efficient Surface Hopping Dynamics in Solution, *J. Chem. Theory Comput.*, **19**, 7171–7186 (2023). 77
  - A.1.2 Resolving Photoinduced Femtosecond Three-Dimensional Solute–Solvent Dynamics through Surface Hopping Simulations, *J. Chem. Theory Comput.*, **20**, 4738-–4750 (2024). . . . 95
- A.2 Application to an Iron Complex in Water . . . 109

A.2.1 Three-Dimensional Nonadiabatic Solvent Reorganization Dynamics of an Iron Complex,*unpublished manuscript* 109

CURRICULUM VITAE 141

ACRONYMS

BOA	Born-Oppenheimer Approximation
DFT	Density Functional Theory
DME	Distributed Multipole Expansion
EE	Electrostatic Embedding
ESP	ElectroStatic Potential
FF	Force Field
ISC	InterSystem Crossing
KDE	Kernel Density Estimation
LVC	Linear Vibronic Coupling
LVC/MM	Linear Vibronic Coupling / Molecular Mechanics
MAD	Mean Absolute Deviation
MC	Metal-Centered
MLCT	Metal to Ligand Charge Transfer
MD	Molecular Dynamics
MM	Molecular Mechanics
NAC	NonAdiabatic Coupling
PES	Potential Energy Surface
QM	Quantum Mechanics
QM/MM	Quantum Mechanics / Molecular Mechanics
RESP	Restrained ElectroStatic Potential
RDF	Radial Distribution Function
RMSD	Root-Mean-Square Deviation
SH	Surface Hopping
SHARC	Surface Hopping including Arbitrary Couplings
SOC	Spin–Orbit Coupling
SVD	Singular Value Decomposition
TDDFT	Time-Dependent Density Functional Theory
TDSE	Time-Dependent Schrödinger Equation
TISE	Time-Independent Schrödinger Equation
TSH	Trajectory Surface Hopping
vdW	van-der-Waals
3D-SDF	Three-Dimensional Spatial Distribution Function

1

INTRODUCTION

A molecule seldom comes alone. More often, molecules are encountered in the condensed phase, as mixtures of different classes of compounds in interaction with each other. In the simplest case, one molecular species, the solute, is surrounded by an abundance of molecules of another species, the solvent. The solvent molecules interact with each other and the solute according to their charge distribution, resulting in Coulomb forces and Pauli repulsion, as well as their polarizability, leading to London forces. These general interactions can, in some cases, also be conceptualized into special mechanisms such as hydrophilicity/lipophilicity, hydrogen bonding or aromatic interactions. Additionally, the macroscopic properties of the solute's environment are determined by the solvent, which hinders the solute's movement through viscosity and structure of the solvent molecules. Through these various interaction modes, the solvent can considerably affect the physical and chemical properties of the solute, and influence reaction kinetics and thermodynamics,[1,2] as well as its photochemistry and spectroscopic properties;[3–7] phenomena such as electron and proton transfer[8], photo-isomerization[9], and charge-transfer in metal complexes[10] are also affected by the solvent.

The solute–solvent interaction is highly dynamic and responsive, with the solvent molecules being able to react to changes of the solute within the femto-second timescale, but can also stretch over long time scales into the pico- and nanosecond range.[11,12] These changes in the solute can be induced through the absorption or emission of photons which affect the electronic structure. Researchers have been long interested in understanding the mutual interaction between solute and solvent during the excited-state dynamics, and controlling such interactions can not only help in the interpretation of experimental data and but also the design of solvated-systems for technical applications. Therefore, one focus of this thesis is the investigation and analysis of the intricate interplay between the solute and solvent molecules in the context of photo-induced dynamical processes. For this investigation, we have developed a new method for theoretical simulations of the occurring dynamics and the obtained simulated results may ultimately be used for interpreting, aiding and/or guiding experimental research, (see Fig. 1.1).

Experimentally, the dynamics of photo-induced processes can be investigated via various sophisticated apparatus and techniques. The collection of methods, which can be used for this purpose and is referred to as ultrafast spectroscopy, has emerged into an active domain of research spanning many disciplines.[4,13,14] Especially interesting for the investigation of dynamical solute–solvent interactions are experimental techniques that resolve the nuclear degrees of freedom and their dynamical response after excitation. A widely used technique for this purpose is X-ray scattering.[15–21] For the solute, this spectroscopy can reveal vibrational relaxation channels.[6] Further, the response of the solvent in terms of libration, rotation, vibration and diffusion is also measured.[11,12] If one is additionally interested in the changes of the solute's electronic structure either transient absorption spectroscopy[19,22,23], X-ray fluorescence spectroscopy[20,24,25] or photoelectron spectroscopy.[26,27] may be used.

Despite X-ray scattering being a powerful and widely used technique,[15] there are limits on its the temporal and spatial resolution: (i) The temporal resolution

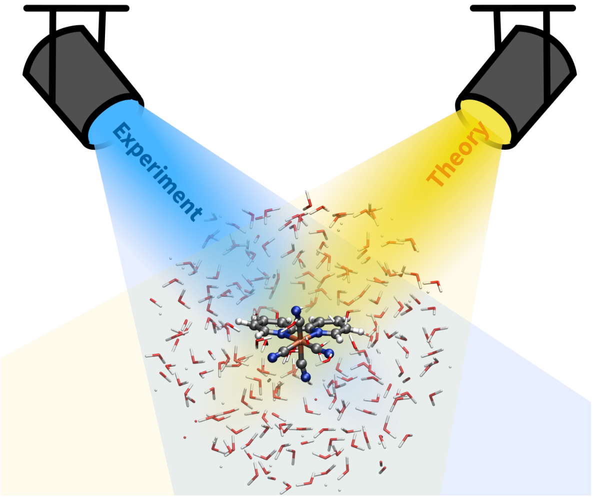

Figure 1.1: Illustration of how the combination experimental and theoretical investigations “illuminate” excited-state solute–solvent dynamics.

of X-ray scattering is limited by characteristic instrument response times which are typically 50 fs or longer.[28] (ii) The X-ray scattering technique only yields information on the inter-atomic distances in reciprocal space, and the full three-dimensional information on all atomic positions in the condensed-phase system cannot be obtained. (iii) The information on the structural changes of the solute (solute term), of the bulk solvent (solvent term), and solvation shell surrounding the solute (solute–solvent cross term) is entangled in the measured data.[15] For these reasons, complementary information from other experiments and theoretical simulations are very beneficial for the interpretation of the results and in the experimental design of X-ray scattering experiments (see Fig. 1.1).[15,29] For such complementary theoretical simulations, the methodological developments presented in this thesis are deemed especially useful, since they can aid in the distinction of the solute, solvent and solute–solvent cross terms by resolving the solvation shell in three dimensions over long time scales.

Theoretical simulations of solvated system can be approached in various ways and span a huge range of methodology.[30–34] Usually, the solvent term is evaluated theoretically through **M**olecular **D**ynamics (MD) simulations using **F**orce **F**ields (FFs).[15,35–38] In FF-MD simulations, the dynamics are computed by numerically integrating Newton’s equation of motion; the molecular system is described mainly in terms of two-body interactions between the atomic nuclei that carry an effective charge.[39–41] This makes the simulations very affordable, and even large systems in solution such as the full SARS-CoV-2 spike protein, which contains more than 4 million atoms, have been simulated.[42] FF-MD simulations give access to the equilibrium solvation structure of the chosen system in terms of **R**adial **D**istribution **F**unctions (RDFs) but also the distributions of solvent molecules in Cartesian space, referred to as **T**hree-**D**imensional **S**patial **D**istribution **F**unctions (3D-SDFs).[43,44] The RDFs obtained are in close relation to the data obtained by an X-ray scattering experiment; the 3D-SDFs can complement the experimental data by providing the corresponding three-dimensionally resolved data to the RDFs. In order to obtain all three fully dynamical terms (solute, solvent and cross term) contained in the response function of the X-ray scattering experiment through simulations, it is necessary to describe the photo-induced changes in the electronic structure of the solute over possibly long timescales. However, FF-MD simulations are not able to describe the photo-induced changes in the electronic structure of the solute. Typically, parameters for only one single electronic state are contained in the FF.[45] Despite this limitation, FF-MD simulations are used to obtain the solvent term of the equilibrium which can be used to disentangle the different contributions in the X-ray scattering data to some degree.[15]

Unfortunately, the dynamical solute–solvent interaction cannot be investigated through a fully quantum mechanical description of the whole system, including the solute and several thousand solvent molecules. The reason is that such a description would involve solving the temporal evolution of the electronic structure and nuclei for a system of many thousand particles for long timescales, which is either prohibitively expensive or outright impossible, even with modern algorithms and hardware. Therefore, the introduction of the **Q**uantum **M**echanics / **M**olecular **M**echanics (QM/MM) method presented a major breakthrough.[30,46–49] This method allows the accurate quantum-mechanical description of the solute, including different electronic states, in combination with describing the solvent molecules approximately through computationally affordable FF-MD. Here, the full electronic structure is only evaluated for a manageable subset of particles belonging to the solute, which makes the whole QM/MM simulation computationally feasible. However, even when using QM/MM, often only stationary electronic structure calculations are used to study the solvent effects on more complex solute molecules.[50–54] For a dynamical description, a combination of **T**rajectory **S**urface **H**opping (TSH)[34,55,56] with QM/MM may be used for the simulations which can still be computationally very demanding.[30,47,48] This high computational demand makes it extremely challenging to simulate a full representation of the dynamical response of not only the solute but all solvent molecules over long timescales. Therefore, theoreticians often limit themselves to only represent the solute's degrees of freedom in full and to shorter timescales (up to a few picoseconds); this is especially the case for large solutes with many important electronic states, such as transition-metal complexes.[57,58] For example, TSH in combination with QM/MM has been used to simulated the photo-induced dynamics of an iron complex and yield accurate time-dependent solute and solvent terms.[59] However, the study also illustrates the limits in the resolution the solute–solvent dynamics imposed by the computational cost. While the authors were able to produce time-dependent electronic populations and RDFs, they were limited to a simulation length of 700 fs and are not able to resolve the solute–solvent dynamics in three-dimensions. These theoretical investigations could have benefited from an increased the number and propagation time of the TSH trajectories to gain insight the solute–solvent dynamics over longer time scales and with more details on the changes in the solvent structure. In order to increase the number and propagation time of trajectories, it is necessary to reduce the computational cost of the QM/MM single-point calculations. Approaches for a reduction of the computational cost include include semi-empirical methods in wave function or **D**ensity **F**unctional **T**heory (DFT) formulations,[60–62] the application of machine learning to predict energies, gradients, and other properties,[63,64] the construction of the potential energy surface through interpolation,[65,66] and excited-state self-consistent field methods, called ΔSCF.[67,68]

An alternative method for cost-effectively representing the coupled excited-state potential energy surfaces of molecules can be found in vibronic coupling models, specifically **L**inear **V**ibronic **C**oupling (LVC) models.[69] The LVC method has been mainly utilized in multi-configurational time-dependent Hartree and other quantum dynamics studies,[69–71] but later was combined with the TSH approach within the **S**urface **H**opping including **Ar**bitrary **C**ouplings (SHARC) package.[56,72,73] Using LVC models for TSH enables the accurate modeling of nonadiabatic gas-phase dynamics for rigid molecules and transition-metal complexes encompassing numerous electronic states.[74] Although the applicability of LVC is limited to rigid systems, it presents several merits compared to other low-cost computational methods. Notably, the LVC method demonstrates high computational efficiency—exhibiting linear scaling with the number of degrees of freedom and an effectively quadratic scaling with the number of states— and does not use basis functions or a self-consistent field cycle. Furthermore, LVC models can be parametrized using any reference electronic structure calculations, giving access to a desired level of accuracy with minimal computational expense. The models are able to reproduce the correct shape of conical intersections which, depending on the reference method used, includes intersections with the ground state. In the context of TSH, LVC models give access to analytical nonadiabatic coupling vectors, regardless of the reference method used. For these reasons, we decided to aim at extending LVC models for the simulations of explicitly solvated systems.

The goal of this thesis is the facilitation of large-scale simulations of photoinduced solute–solvent dynamics. This thesis aims at enabling simulations that allow not only for the description of dynamics on increasingly long timescales but also the temporal resolution of three-dimensional solvation shells which go beyond RDFs. For this, we want to capitalize on the advantages of the LVC method for solvated systems by adapting the underlying LVC Hamiltonian to be used in the QM/MM approach. This new methodology is termed **L**inear **V**ibronic **C**oupling / **M**olecular **M**echanics (LVC/MM). This thesis will present the combination of several published techniques used in the construction of the LVC/MM Hamiltonian, its application to small thiocarbonyl test systems in aqueous solution, the generation and analysis of time-dependent **T**hree-**D**imensional **S**patial **D**istribution **F**unctions (3D-SDFs), and the application of LVC/MM to an iron complex investigated previously by members of this group.[59]

The contents of thesis are structured as follows. With the introduction being done in this chapter, the basic concepts of quantum dynamics, as well as the previously published techniques on which the LVC/MM is built, are presented in Chapter 2. Chapter 3 then describes the changes made in the SHARC package, all necessary equations and the formalism of the LVC/MM method published in Ref. 75, its validation and scaling, and explains details on the generation and analysis of time-dependent **T**hree-**D**imensional **S**patial **D**istribution **F**unctions (3D-SDFs) published in Ref. 76. Subsequently, applications of the LVC/MM method are presented: first on solvated thiocarbonyls as test systems in Chapter 4 published in Refs. 75 and 76, and second on an iron complex in aqueous solution in Chapter 5. Additionally, Chapter 6 presents a guide and considerations in the construction of LVC models in general, and uses results on the iron system as examples in the context of LVC/MM. The thesis draws conclusions and a resume of the achieved contribution to research in the field nonadiabatic dynamics of solvated systems in Chapter 7.

THEORY

2

This thesis presents the investigation of coupled nonadiabatic solute–solvent dynamics using a novel combination of LVC Hamiltonians with **M**olecular **M**echanics (MM) called LVC/MM. The newly developed method, published in Ref. 75 (see Section A.1.1), is based on extending and combining various already existing methodology. This chapter lays the theoretical foundation and present the preexisting methodology this work is built on. The first two sections focus on the quantum mechanical fundamentals: Section 2.1 will describe the basis of quantum mechanics for the description of molecular systems, and Section 2.2 introduces the elementary equations in nonadiabatic dynamics and **S**urface **H**opping (SH). The subsequent three sections highlight different aspects in the description of a molecular system in an environment: Section 2.3 introduces the diabatic basis and the LVC model, Section 2.4 summarizes QM/MM method and electrostatic embedding, Section 2.5 derives how one can obtain an approximation of an electronic density for the evaluation of electrostatic interactions, and finally Section 2.6 describes electrostatic interaction in terms of a **D**istributed **M**ultipole **E**xpansion (DME).

2.1 The Schrödinger Equation and the Born-Oppenheimer Approximation

The foundation of quantum mechanics is the general **T**ime-**D**ependent **S**chrödinger **E**quation (TDSE),[77] which states in its non-relativistic form that

$$\mathrm{i}\hbar\frac{\partial}{\partial t}\Psi(\mathbf{R},t)=\hat{H}(\mathbf{R},t)\Psi(\mathbf{R},t). \tag{2.1}$$

Here, $\hbar$ is Planck's reduced constant, $\Psi(\mathbf{R},t)$ is the wave function in the position basis, $\hat{H}(\mathbf{R},t)$ is the Hamiltonian operator. The latter two depend on the coordinates of all particles in the system $\mathbf{R}$ and the time t. The wave function contains the state of the whole system and all information on it; $|\Psi(\mathbf{R})|^2$ yields the probability distribution of the particles in the system. The wave function can be represented as a vector ($|\cdot\rangle$) inside a Hilbert space and its inner product is postulated to be normalized. The wave function is expressed in the position basis through a projection onto the basis vectors $\langle\mathbf{R}|$ as $\langle\mathbf{R}\,|\Psi\rangle=\Psi(\mathbf{R},t)$. Generally, the Hamiltonian operator holds the applied physical laws and interactions within the system. The TDSE is a partial differential equation that relates the temporal evolution of the wave function to the result of the Hamiltonian operator acting on it.

In quantum chemistry, the Hamiltonian operator, short Hamiltonian, describes molecular systems in terms of electrons and nuclei, and their Coulomb interaction as

$$\begin{aligned}\hat{H}(\mathbf{R},\mathbf{r}) = {} & \underbrace{\sum_{a}^{N_\mathrm{n}} -\frac{1}{2m_a}\boldsymbol{\nabla}_a^2}_{\hat{T}_\mathrm{n}} + \underbrace{\sum_{k}^{N_\mathrm{e}} -\frac{1}{2}\boldsymbol{\nabla}_k^2}_{\hat{T}_\mathrm{e}} \\ & + \underbrace{\sum_{a}^{N_\mathrm{n}}\sum_{b\neq a}^{N_\mathrm{n}} \frac{Z_a Z_b}{|\mathbf{R}_a - \mathbf{R}_a|}}_{\hat{V}_\mathrm{nn}} + \underbrace{\sum_{a}^{N_\mathrm{n}}\sum_{k}^{N_\mathrm{e}} -\frac{Z_a}{|\mathbf{R}_a - \mathbf{r}_k|}}_{\hat{V}_\mathrm{en}} + \underbrace{\sum_{k}^{N_\mathrm{e}}\sum_{l\neq k}^{N_\mathrm{e}} \frac{1}{|\mathbf{r}_k - \mathbf{r}_l|}}_{\hat{V}_\mathrm{ee}}\end{aligned} \tag{2.2}$$

in atomic units;[78] $\hat{T}$ are the kinetic energy operators, $\hat{V}$ are the potential operators, N_n and N_e are the numbers of nuclei n and electrons e, m_a is the mass of the nucleus a, $\boldsymbol{\nabla}^2$ is the inner product of the nabla operator $\boldsymbol{\nabla}$, Z_a is the nuclear charge of atom a, $\mathbf{R}_a$ is the vector of the Cartesian coordinates of atom a, and $\mathbf{r}_k$ is the vector of the Cartesian coordinates of electron k. The described Hamiltonian $\hat{H}(\mathbf{R},\mathbf{r})$ already includes some approximation to the physical description of the system: The interactions between the particles are instantaneous and there are no relativistic effects, the particles are point-charges, and space-time is perfectly flat and not influenced by the masses of the particles. This Hamiltonian does not contain any external fields and is time-independent.

Since the molecular Hamiltonian is time-independent, we can split the TDSE into an eigenvalue problem for the Hamiltonian, which is called the **T**ime-**I**ndependent **S**chrödinger **E**quation (TISE), and a differential equation for the time-dependent part of the wave function. The TISE can be written as

$$\hat{H}(\mathbf{R},\mathbf{r})\Psi_j(\mathbf{R},\mathbf{r}) = E_j\Theta_j(\mathbf{R},\mathbf{r}). \tag{2.3}$$

Here, $\Theta_j(\mathbf{R},\mathbf{r})$ is the j-th eigenstate of the molecular Hamiltonian which is called a stationary state, and E_j is the corresponding eigenvalue which represents the total energy of the molecular system in that state. Given a solution of the TISE in the form of a stationary state, we can formulate a particular solution to the TDSE as

$$\Psi_j(\mathbf{R},\mathbf{r},t) = \Theta_j(\mathbf{R},\mathbf{r})e^{-\mathrm{i}\left(E_j/\hbar\right)t}. \tag{2.4}$$

In this equation, the complex phase factor is a rotation on the unit circle in the complex plane with its phase depending on the total energy of the system E_j. The probability density of such a time-dependent wave function in a stationary state is time-independent. A general solution to the TDSE, $\Psi(\mathbf{R},\mathbf{r},t)$, can be constructed as a linear combination of all stationary states,

$$\Psi(\mathbf{R},\mathbf{r},t) = \sum_{j}^{\infty} c_j(t)\Theta_j(\mathbf{R},\mathbf{r})e^{-\mathrm{i}\left(E_j/\hbar\right)t}. \tag{2.5}$$

This general solution is then referred to as a wave packet and its probability distribution is time-dependent.[34,70] The wave packet may be propagated in time by propagating its time-dependent coefficients $c_j(t)$, which will be shown in the next section.

Even though we can formulate general solutions of the Schrödinger equation in either the time-dependent or time-independent form, an analytical solution only exists for two-particle systems, such as the hydrogen atom. For larger systems, only numerical solutions are possible. For these solutions, one usually includes approximations to the equation itself, the Hamiltonian operator, and/or the wave function.

Before we can tackle the solution of the TISE, we can consider a simpler version of this problem, which involves only the electronic part of the molecular Hamiltonian (Eq. (2.2)) with fixed nuclei at configuration $\mathbf{R}$, called the electronic Schrödinger equation:

$$\hat{H}_{\text{ele}}(\mathbf{r};\mathbf{R})\Xi(\mathbf{r};\mathbf{R}) = V_{\text{ele}}(\mathbf{R})\Xi(\mathbf{r};\mathbf{R}), \tag{2.6}$$

with

$$\hat{H}_{\text{ele}} = \hat{T}_{\text{e}} + \hat{V}_{\text{ee}} + \hat{V}_{\text{ne}} + \hat{V}_{\text{nn}}. \tag{2.7}$$

Here, $\hat{H}_{\text{ele}}$ is the electronic Hamiltonian and $\Xi(\mathbf{r};\mathbf{R})$ is the corresponding electronic wave function with parametric dependence on $\mathbf{R}$. $V_{\text{ele}}(\mathbf{R})$ is a function that maps a set of the nuclear coordinates to the electronic potential energy. We can use Eq. (2.6) to solve the full TISE by making the assumption that the full molecular wave function (adiabatic wave function) can be written as a product of a nuclear wave function and the mentioned electronic wave function $\Xi(\mathbf{r};\mathbf{R})$:

$$\Theta(\mathbf{R},\mathbf{r}) = \Phi(\mathbf{R})\Xi(\mathbf{r};\mathbf{R}). \tag{2.8}$$

This assumption is made with the following argument: The electron mass is much smaller than the masses of the nuclei and thus the electronic relaxation time is so fast that the nuclear dynamics are affected by the electrons in a mean-field sense. This argument is not generally valid and tends to break down drastically when the electronic relaxation is not fast enough to adapt to changes in nuclear positions. Upon substitution of Eq. (2.8) into the full TISE Eq. (2.3) with $\hat{H} = \hat{T}_n + \hat{H}_{\text{ele}}$, we obtain

$$\begin{aligned} \hat{H}(\mathbf{R},\mathbf{r})\left[\Phi(\mathbf{R})\Xi(\mathbf{r};\mathbf{R})\right] = {} & V_{\text{ele}}(\mathbf{R})\Phi(\mathbf{R})\Xi(\mathbf{r};\mathbf{R}) \\ & - \sum_{a}^{N_{\text{n}}} \frac{1}{2m_a}\Big[\boldsymbol{\nabla}_a^2\Phi(\mathbf{R})\Xi(\mathbf{r};\mathbf{R}) \\ & \qquad + 2\boldsymbol{\nabla}_a\Phi(\mathbf{R})\boldsymbol{\nabla}_a\Xi(\mathbf{r};\mathbf{R}) \\ & \qquad + \Phi(\mathbf{R})\boldsymbol{\nabla}_a^2\Xi(\mathbf{r};\mathbf{R})\Big] \\ = {} & E\Phi(\mathbf{R})\Xi(\mathbf{r};\mathbf{R}). \end{aligned} \tag{2.9}$$

In this, the last two terms, where $\boldsymbol{\nabla}_a$ acts on $|\Xi(\mathbf{r};\mathbf{R})\rangle$, are proportional to $1/m_a$ in atomic units and thus are several orders of magnitude smaller than the other terms.[79] These terms are neglected and we can approximate Eq. (2.9) as

$$\hat{H}(\mathbf{R})\,\Phi(\mathbf{R}) = \left[\hat{T}_{\text{n}} + V_{\text{ele}}(\mathbf{R})\right]\Phi(\mathbf{R}) = E\Phi(\mathbf{R}). \tag{2.10}$$

This is a TISE for nuclei under the influence of an effective electronic potential V_{ele}, which is known as a **P**otential **E**nergy **S**urface (PES). The above stated approximations to the full molecular TISE are known as the **B**orn-**O**ppenheimer **A**pproximation (BOA). Eq. (2.10) only describes the nuclei on a single PES; most often this corresponds to the lowest eigenstate of $\hat{H}_{\text{ele}}$ called the electronic ground state.

If we want to describe excited state dynamics, we cannot employ the BOA. Instead of using Eq (2.8), we can start with the formally exact[a] Born-Huang expansion,[80]

$$\Psi(\mathbf{R},\mathbf{r}) = \sum_{i}^{\infty} \Phi_i(\mathbf{R}) \Xi_i(\mathbf{r},\mathbf{R}), \tag{2.11}$$

where $\{\Xi_i(\mathbf{r},\mathbf{R})\}$ is the full set of electronic states which solve the electronic TISE Eq. (2.6). Inserting the Born-Huang expansion into the TISE (Eq. (2.3)), multiplying with $\langle \Xi_j |$, and integrating over the electronic coordinates yields the exact nuclear Schrödinger equation:[79]

$$\begin{aligned} \sum_i \langle \Xi_j | \hat{H} | \Xi_i \rangle \Phi_i(\mathbf{R}) &= \sum_i \left[\langle \Xi_j | \hat{T}_\mathrm{n} | \Xi_i \rangle + \langle \Xi_j | \Xi_i \rangle V_{i,\mathrm{ele}}(\mathbf{R}) \right] \Phi_i(\mathbf{R}) \\ &= \left[\hat{T}_\mathrm{n} + V_{j,\mathrm{ele}}(\mathbf{R}) \right] \Phi_j(\mathbf{R}) - \sum_i \hat{\boldsymbol{\Lambda}}_{ij} \Phi_i(\mathbf{R}) \\ &= E_j \Phi_j(\mathbf{R}). \end{aligned} \tag{2.12}$$

The equation above does not include any approximation yet and would result in exact dynamics. Here,

$$\begin{aligned} \hat{\boldsymbol{\Lambda}}_{ij} &= \delta_{ij} \hat{T}_\mathrm{n} - \langle \Xi_j | \hat{T}_\mathrm{n} | \Xi_i \rangle \\ &= \delta_{ij} \hat{T}_\mathrm{n} - \langle \Xi_j | \left[\sum_a^{N_\mathrm{n}} - \frac{1}{2m_a} \left(\boldsymbol{\nabla}_a^2 | \Xi_i \rangle + \boldsymbol{\nabla}_a | \Xi_i \rangle \boldsymbol{\nabla}_a + | \Xi_i \rangle \boldsymbol{\nabla}_a^2 \right) \right] \\ &= - \sum_a^{N_\mathrm{n}} - \frac{1}{2m_a} \left[\langle \Xi_j | \boldsymbol{\nabla}_a^2 | \Xi_i \rangle + \langle \Xi_j | \boldsymbol{\nabla}_a | \Xi_i \rangle \boldsymbol{\nabla}_a \right] \end{aligned} \tag{2.13}$$

are the **N**on**A**diabatic **C**ouplings (NACs). These terms represent couplings resulting from nuclear motion of the eigenstates of the electronic Hamiltonian in the TISE also called adiabatic electronic states, and are neglected in the BOA. Through the NACs, not only is the nuclear wave function influenced by one adiabatic electronic state, but all electronic states are also influenced by the motion of the nuclei and can in-turn affect the nuclei. The NACs are not negligible where multiple PES come energetically close and the electronic wave function changes drastically with respect to small changes in nuclear coordinates. Both of these cases occur in the study of electronic excited states. Nevertheless, the BOA remains useful and is intrinsic to chemical intuition, where reactants and products of a chemical reaction are different points on a single PES. For excited-state dynamics, in which many states are involved, the chemical landscape needs to be envisioned as not only one but multiple coupled PES, on which the nuclear wave function is evolving. The BOA and the mental picture of multiple coupled PES can be very instructive for interpreting nonadiabatic dynamics presented in the next section.

2.2 Nonadiabatic Dynamics

While the previous section presented solutions for the TISE, this section is dedicated to solving the TDSE. The starting point for this is the general solution in the form of the wave packet introduced in Eq. (2.5). As mention above, the wave packet can be propagated in time from step t to step $t+\Delta t$ by propagating the time-dependent coefficients, $c_j(t)$.[34,70] This is called wave packet dynamics or quantum dynamics. It is the most rigorous way to numerically integrate the nuclear wave function, as the accuracy only depends on the chosen basis set, as well as the electronic potentials and couplings used in Eq. (2.12).[81] Quantum effects such as zero-point energy, coherence phenomena, tunneling processes, or branching at conical intersections are fully accounted for.[34] However, the discretization on a grid scales exponentially with the degrees of freedom, which are $3N_\text{n}-6$ for the nuclei. Therefore, only very low dimensional systems can be described or the number of relevant degrees of freedom needs to be reduced drastically for ultrafast chemical processes; typically three to four degrees of freedom are feasible.[70] The multi-configurational time-dependend Hartree method uses time-dependent functions as a basis, but is still restricted to systems with about a dozen atoms.[70,71,82] Handling the dynamics of bigger systems requires further approximations.

---

[a] neglecting the continuum states

The most common approximation is intuitive: the nuclear wave function is collapsed to discrete $3N_\text{n}$ atomic positions. This means that the nuclei can be described with classical mechanics as points with an associated mass. The complexity of this approach scales linearly with the number of atoms. Instead of employing the Schrödinger equation, we can treat the dynamics of the nuclei with Newton's second law:

$$\frac{\partial^2}{\partial t^2}\mathbf{R}_a = -M_a^{-1}\boldsymbol{\nabla}_a V_{i,\text{ele}}(\mathbf{R}). \tag{2.14}$$

This equation states that the temporal evolution of the coordinates of nucleus a is proportional to the derivative of the electronic potential energy function or PES with respect to the same coordinates. The integration of this method yields a time-series $\mathbf{R}(t)$, which will be referred to as a trajectory. The propagation of the nuclei through Newton's equation of motion is generally called MD.[34,79] There are two popular algorithms for numerically integrating Eq. (2.14): the leap-frog[83] algorithm and the velocity-Verlet[84] algorithm. Regardless of the choice of algorithm, the numerical integration involves the evaluation of Eq. (2.14) for all $\mathbf{R}(t)$ sequentially. It is not necessary to compute the whole PES a priori; rather evaluation of the derivative at the current nuclear positions or nuclear gradients is sufficient. If the nuclear gradients are evaluated via solving the electronic TISE, the method is referred to as ab-initio molecular dynamics.[34] As will be shown below in Section 2.4, the PES can also be approximated by sets of classical equations, referred to as FF; using this to obtain the nuclear gradients leads to classical MD.

Simulated dynamics with Eq. (2.14) are limited to one PES ($V_{i,\text{ele}}(\mathbf{R})$). In order to treat excited state dynamics with MD, it is necessary to extend the approach. Similarly to the nuclear wave function, the electronic wave function may also be expanded in a basis of electronic states; the adiabatic basis in this case:

$$|\Xi(t)\rangle = \sum_i c_i(t)\,|\Xi_i(\mathbf{R}(t))\rangle\,. \tag{2.15}$$

This leads to a wave function that is a mixture of multiple electronic states, and results in an effective potential energy function. The corresponding effective gradient applied to the nuclei can then be evaluated from $\boldsymbol{\nabla}\langle\Xi(t)|\,H_\text{ele}\,|\Xi(t)\rangle$, which is the gradient of a mixture of multiple eigenstates of the electronic Hamiltonian. This approach is called Ehrenfest dynamics.[85] Central to quantum mechanics is the concept that the expectation value of an observable may be a mixture of different solutions to the Schrödinger equation; however upon wave function collapse, the expectation value of one solution will be measured. Unfortunately, the Ehrenfest approach does not split the wave packet into respective reaction channels but rather one unphysical average channel.[86]

The problem of the Ehrenfest approach arises because the wave packet is propagated on an effective PES, when it is supposed to follow different reaction channels on respective PES. The correct distribution of the wave packet among all PES may be recovered by a stochastic approach. In **S**urface **H**opping (SH),[34,55,87] the wave packet can be represented by a set of trajectories which are propagated using one PES corresponding to one electronic state, referred to as active state. Each trajectory can then stochastically change its active state by “hopping" to another state; the probability for the hop is derived from the NAC term (Eq. (2.13)) between the states. Overall, this results in a set of trajectories that follow physical reaction channels. The fraction of the ensemble that follows a given channel converges to the probability of the wave packet with increasing ensemble sizes,

$$\lim_{N_{\text{traj}}\to\infty} \frac{N_{\text{traj},i}}{N_{\text{traj}}} = \left|c_i^2(t)\right|. \tag{2.16}$$

This is only possible if the electronic wave function is propagated alongside the classical nuclei.

The time-dependent electronic wave function in the basis of the electronic eigenstates (Eq. (2.15)) can be inserted into the electronic TDSE and integrated over the electronic states with $\left\langle \Xi_{0,j} \right|$; this yields the equation of motion for the electronic coefficients $c_i(t)$ as

$$\frac{\partial}{\partial t} c_j(t) = -\sum_i \left[\mathrm{i} \left\langle \Xi_j \middle| \hat{H}_{\text{ele}} \middle| \Xi_i \right\rangle + \dot{\mathbf{R}} \cdot \hat{\mathbf{\Lambda}}_{ij} \right] c_i(t). \tag{2.17}$$

As before, the second term represents the coupling between the surfaces. This term depends on the chosen basis $\{\Xi_i\}$ used to expand the wave function, which is usually referred to as a representation.[34,88] Eq. (2.17) can also be written in a compact tensor form for all coefficients at once,

$$\frac{\partial}{\partial t} \mathbf{c}(t) = -\left[\mathrm{i}\mathbf{H} + \dot{\mathbf{R}} \cdot \mathbf{\Lambda} \right] \mathbf{c}(t), \tag{2.18}$$

where $\mathbf{\Lambda}$ is the NAC matrix (Eq. (2.13)). The evaluation of NAC terms is expensive and often not possible. This problem is solved by the local diabatization approach[60,89] which reformulates Eq. (2.18) to use the overlap of the current electronic wave function with the previous one $\langle \Xi(t+\Delta t) \, | \Xi(t) \rangle$. With this, the propagation in SH is achieved by cycling through three basic steps: (i) Evaluation of the electronic energies, nuclear gradients, and the overlap matrix using the TISE. (ii) Propagation of the electronic wave function and stochastic selection of an active state. (iii) Propagation of the nuclei with respect to the gradient of the active electronic states. These steps are not exhaustive, as one also needs to ensure energy conservation upon "hops" between electronic states and sufficient decoherence between the trajectories.[34,90,91]

The efficiency of the SH approach is determined by the efficiency of step (i). For big systems, the evaluation of (i) can prohibitively expensive which renders the SH less favorable. For these systems, one can apply further approximations in the solution of the TISE to decrease the computational cost. The approximations used in the frame of this thesis, which are the LVC Hamiltonian, the QM/MM approach and the DME, are presented in the following sections.

2.3 Diabatic Representation and the Vibronic Coupling Hamiltonian

A commonly chosen alternative to the above introduced adiabatic basis is the so called diabatic basis.[79] In this basis, the eigenfunctions of the electronic Hamiltonian have small or absent nuclear derivatives $\boldsymbol{\nabla}_a \Xi_i$ and $\boldsymbol{\nabla}_a^2 \Xi_i$. This means, the basis is set up to minimize $\hat{\boldsymbol{\Lambda}}_{ij}$; the change of $\Xi_i(\mathbf{r};\mathbf{R})$ is minimized with respect to $\hat{T}_\mathrm{n}$. The simplest version of achieving this is to choose electronic states as basis functions which are independent of $\mathbf{R}$: $\Xi_i(\mathbf{r};\mathbf{R}) \mapsto \Xi_i(\mathbf{r};\mathbf{R}_0)$. This is called the "crude adiabatic basis" and its basis functions are by construction solutions to the electronic TISE for a specific set of nuclear coordinates $\mathbf{R}_0$:[79]

$$\Psi(\mathbf{R},\mathbf{r}) = \sum_i \Phi_i(\mathbf{R})\Xi_i(\mathbf{r};\mathbf{R}_0), \tag{2.19}$$

$$\hat{H}_\mathrm{ele}(\mathbf{r};\mathbf{R}_0)\Xi_i(\mathbf{r};\mathbf{R}_0) = V_{i,\mathrm{ele}}(\mathbf{R}_0)\Xi_i(\mathbf{r};\mathbf{R}_0). \tag{2.20}$$

The electronic eigenstates of the diabatic basis, $\Xi_i(\mathbf{r};\mathbf{R}_0)$, will be abbreviated as $\Xi_{0,i}$. Inserting this into the full TISE and multiplying from the left with $\left\langle \Xi_{0,j} \right|$ yields:

$$\sum_i \left\langle \Xi_{0,j} \middle| \hat{H}(\mathbf{r},\mathbf{R}) \middle| \Xi_{0,i} \right\rangle \Phi_i(\mathbf{R}) = \sum_i \left\langle \Xi_{0,j} \middle| \left[\hat{T}_\mathrm{n} + \hat{H}_\mathrm{ele}(\mathbf{r};\mathbf{R})\right] \middle| \Xi_{0,i} \right\rangle \Phi_i(\mathbf{R}). \tag{2.21}$$

The integrated equation above can be also simplified[69] to

$$\sum_i \left\langle \Xi_{0,j} \middle| \hat{H}(\mathbf{r},\mathbf{R}) \middle| \Xi_{0,i} \right\rangle \Phi_i(\mathbf{R}) = \sum_i \left[\left\langle \Xi_{0,j} \middle| \hat{T}_\mathrm{n} \middle| \Xi_{0,i} \right\rangle + W_{ji}(\mathbf{R})\right] \Phi_i(\mathbf{R}). \tag{2.22}$$

Here, $W(\mathbf{R})$ summarizes the electronic Hamiltonian in the diabatic basis so that

$$\left\langle \Xi_{0,j} \middle| \hat{H}_\mathrm{ele}(\mathbf{r},\mathbf{R}) \middle| \Xi_{0,i} \right\rangle = W_{ji}(\mathbf{R}). \tag{2.23}$$

The equations introduced above and the form of the potential-energy and kinetic-energy expressions depends on the choice of the coordinate system in which $\mathbf{R}$ is expressed. The construction of the kinetic-energy and potential-energy operators simplify considerably under the assumption that there are no motions with large amplitude in the molecular system. This allows us to express the nuclear coordinates $\mathbf{R}$ as displacements from a suitable reference; the equilibrium geometry of the electronic ground state $\mathbf{R}_0$ is often used. With this, we can describe nuclear motion in terms of vibrations with moderate amplitude around the reference geometry. For the description of these vibration, we introduce a new set of coordinates $\mathbf{Q} = \left(Q_1, \ldots, Q_{N_\mathrm{vib}}\right)^T$, called normal coordinates;[92] N_vib is $3N_\mathrm{n} - 6$ or $3N_\mathrm{n} - 5$ for linear molecules. These normal coordinates are obtained in their dimensionless form as

$$Q_k = \sqrt{\omega_k} \sum_l^{3N_\mathrm{n}} \sqrt{M_l} L_{kl}^{-1} \Delta\mathbf{R}_l \left(\mathbf{R}_l - \mathbf{R}_{0,l}\right). \tag{2.24}$$

Here, ω_k is the vibrational frequency of the k-th normal mode, $\Delta\mathbf{R}_l$ is displacements of the nuclear Cartesian coordinate l, and L_{kl} is an element of the linear transformation matrix that diagonalizes the Hessian matrix of the electronic ground-state potential. Expanding the electronic ground-state potential energy up to second order in $\Delta\mathbf{R}$ and approximating the frequencies by their value at $\mathbf{R}_0$, which is the harmonic approximation, $\hat{T}_\text{n}$ and the potential energy function of the electronic ground-state, $V_{0,\text{ele}}$, take the form[69,92]

$$\hat{T}_\text{n} = -\frac{1}{2}\sum_k \omega_k \frac{\partial^2}{\partial Q_k^2}, \tag{2.25}$$

$$V_{0,\text{ele}}(\mathbf{Q}) = \frac{1}{2}\sum_k \omega_k Q_k^2. \tag{2.26}$$

The elements of vibronic-coupling potential energy matrix $W_{ij}(\mathbf{Q})$ also called vibronic coupling Hamiltonian can be expressed in the following expansion:[69]

$$W_{ii}(\mathbf{Q}) = V_{0,\text{ele}}(\mathbf{Q}) + \epsilon_i + \sum_k \kappa_k^{(i)} Q_k + \sum_{kl} \gamma_{kl}^{(ii)} Q_k Q_l + \cdots \tag{2.27}$$

$$W_{ij}(\mathbf{Q}) = \eta_{ij}(0) + \sum_k \lambda_k^{(ij)} Q_k + \sum_{kl} \gamma_{kl}^{(ij)} Q_k Q_l \cdots, \tag{2.28}$$

where

$$\kappa_k^{(i)} = \left(\frac{\partial W_{ii}}{\partial Q_k}\right)_{\mathbf{Q}=0} \tag{2.29}$$

$$\lambda_k^{(ij)} = \left(\frac{\partial W_{ij}}{\partial Q_k}\right)_{\mathbf{Q}=0} \tag{2.30}$$

$$\gamma_{kl}^{(ij)} = \left(\frac{\partial^2 W_{ij}}{\partial Q_k \partial Q_l} - \omega_k \delta_{kl}\right)_{\mathbf{Q}=0}. \tag{2.31}$$

Here, ϵ_i is the vertical excitation energy of the i-th electronic state, $\kappa_k^{(i)}$ are the first-order intra-state vibronic coupling constants, $\eta^{(ij)}$ are constant inter-state couplings, $\lambda_k^{(ij)}$ are the first-order inter-state vibronic coupling constants, and $\gamma_{kl}^{(ij)}$ are the second-order vibronic coupling constants. In the parametrization done with the SHARC code, the assumption is made that the adiabatic and diabatic bases coincide at $\mathbf{Q} = 0$, so that $\eta^{(ij)} = 0$. The $\gamma_{kk}^{(ii)}$ are state-specific shifts in frequency and $\gamma_{kl}^{(ii)}$ represent Duschinsky rotations[93] which transform the normal coordinates of the electronic ground state into the ones of the respective electronic excited state. The parameters ϵ_i and $\kappa_k^{(i)}$ can be obtained via the electronic energies and gradients at $\mathbf{R}_0$.[94] The $\lambda_k^{(ij)}$ parameters can be obtained from the NACs at $\mathbf{R}_0$ or via numerical differentiation.[72,94] The $\gamma_{kl}^{(ij)}$ can be obtained via numerical differentiation.

Additionally to these parameters, the **S**pin–**O**rbit **C**ouplings (SOCs) can be added as static parameters $\eta^{(ij)}$ to $W_{ij}(\mathbf{Q})$. SOCs describe the interaction of the electronic spin with the magnetic field induced by the moving electron in a spatial orbital. The SOCs are derived by solving the Dirac equation (the relativistic analogue to the Schrödinger equation) and are formulated as an component in the Breit–Pauli-Hamiltonian.[95] The SOCs tend to be larger in elements of later periods as they depend on nuclear charge. In excited-state dynamics, the SOCs introduce coupling between otherwise uncoupled states of different multiplicity and can lead to **I**nter**S**ystem **C**rossing (ISC).[34,96]

The LVC method used in this thesis corresponds to the vibronic coupling Hamiltonian truncated after the first-order terms. It presents a highly-efficient way of solving the TISE, even for larger systems with many electronic states.[72,74] In this work, we additionally used a subset of the γ parameters $\gamma_{kk}^{(ii)}$ for more accurate state-specific frequencies in our LVC model in Section 5.

2.4 The Quantum Mechanical/Molecular Mechanical Method

As stated above, solving the electronic TISE for systems in the condensed phase can be prohibitively expensive, especially in the context of dynamics simulations. This is because of the polynomial scaling in terms of electrons and basis functions of many electronic structure methods. However, if the molecular system investigated can be split into a molecular region of interest and its environment, one can treat the environment more approximately.[30,46] The approximations to the environment are approximations to the electronic potential energy function $V_{\text{ele}}(\mathbf{R})$ from Eq. (2.6) (also referred to as PES). The approximated potential energy function can then be used to propagate the nuclei using Newton's equation of motion (see Eq. 2.14). Commonly, the electrons are not treated explicitly and all nuclei have effective charges q. A general expression for an approximated V_{ele} can be written as:

$$V_{\text{ele}} \approx V_{\text{bonded}} + V_{\text{nonbonded}}. \tag{2.32}$$

Here, the first term generally describes the potential energy between pairs of nuclei that are considered to be connected by chemical bonds and the second term for all others. Most commonly, V_{bonded} is a truncated many-body expansion with $V_{\text{bonded}} = V_{\text{bond}} + V_{\text{angle}} + V_{\text{dihedral}}$ for two-body, three-body and four-body interactions. The nonbonded interaction only consists of two-body interactions: $V_{\text{nonbonded}} = V_{\text{Coulomb}} + V_{\text{Lennard-Jones}}$. The Coulomb potential contains electrostatic interactions between point-like nuclei with effective charges q. The Lennard-Jones term models both the repulsion from the Pauli exclusion principle and the attractive **v**an-**d**er-**W**aals (vdW) interaction. The Coulomb interaction term has a much longer range and dominates the computational cost for large systems. The effective scaling of evaluating V_{ele} in this approximation is $\mathcal{O}(N_{\text{n}}^2)$. All terms in the approximated electronic potential energy operator are formed from empirically determined parameters and their collection is usually referred to as a FF ($V_{\text{ele}} \approx V_{\text{FF}}$).[39–41]

Now that we have a way of treating the environment part of our molecular system approximately with a FF, we need to establish how the molecular system can interact with its environment and vice-versa. In the widely used **E**lectrostatic **E**mbedding (EE) formalism,[30] both parts interact, as the name implies, via electrostatic interactions. These are included into the electronic Hamiltonian of the molecule (Eq. (2.7)) as

$$\hat{H}_{\text{ele,EE}} = \hat{H}_{\text{ele}} + \sum_{b}^{N_{\text{env}}} \sum_{a}^{N_{\text{n}}} \frac{q_b Z_a}{|\mathbf{R}_a - \mathbf{R}_b|} - \sum_{b}^{N_{\text{env}}} \sum_{i}^{N_{\text{e}}} \frac{q_b}{|\mathbf{r}_i - \mathbf{R}_b|}. \tag{2.33}$$

Here, q_b is the effective charge of the FF of one of the atoms in the environment N_{env}; these charges are collected in $\mathbf{P}_{\mathrm{env}} = \{q_b\}$. Eq. (2.33) states that the environment electrostatically influences the result of the TISE and therefore the wave function. Since the molecular system (mol) part of the system is treated quantum mechanically and the environment part with classical mechanics, this approach is usually referred to as QM/MM.[30,46] The total energy of the system $E_{\mathrm{QM/MM}}$ can be obtained as

$$E_{\mathrm{QM/MM}} = E_{\mathrm{ele,EE}} - E_{\mathrm{FF,mol'}} + E_{\mathrm{FF,mol'+env}}, \tag{2.34}$$

where $E_{\mathrm{ele,EE}}$ is the solution to the TISE using $\hat{H}_{\mathrm{ele,EE}}$. $E_{\mathrm{FF,mol'}}$ is the FF energy of the molecular part with its charges set to zero (mol'). $E_{\mathrm{FF,mol'+env}}$ is the energy of the entire system at FF level; again the charges of the molecule are set to zero (mol'). Setting the charges of the molecule in the FF to zero (env') prevents double-counting of the Coulomb interactions between the atoms of the molecule and environment.

As stated above in Eq. (2.33), the Coulomb interaction between the molecule of interest and its environment can be described by

$$\hat{V}_{\mathrm{ele,env}} = \sum_b^{N_{\mathrm{env}}} \sum_a^{N_{\mathrm{n}}} \frac{q_b Z_a}{|\mathbf{R}_a - \mathbf{R}_b|} - \sum_b^{N_{\mathrm{env}}} \sum_i^{N_{\mathrm{e}}} \frac{q_b}{|\mathbf{r}_i - \mathbf{R}_b|}. \tag{2.35}$$

The Coulomb potential energy function $V^{(ij)}_{\mathrm{ele,env}}(\mathbf{R})$ for the coordinates of the whole system $\mathbf{R}$ and the pairs of electronic states ij can be calculated as[97]

$$\begin{aligned} V^{(ij)}_{\mathrm{ele,env}}(\mathbf{R}) &= V^{(ij)}_{\mathrm{n,env}}(\mathbf{R}) \\ &\quad - \sum_b^{N_{\mathrm{env}}} q_b \int d\mathbf{r}_1 \cdots d\mathbf{r}_n \Xi_i^*(\mathbf{r}_1,\ldots,\mathbf{r}_n) \cdot \left[\sum_k^{N_{\mathrm{e}}} \frac{1}{|\mathbf{r}_k - \mathbf{R}_b|} \right] \cdot \Xi_j(\mathbf{r}_1,\ldots,\mathbf{r}_n), \end{aligned} \tag{2.36}$$

with

$$V^{(ij)}_{\mathrm{n,env}}(\mathbf{R}) = \delta_{ij} \sum_b^{N_{\mathrm{env}}} \sum_a^{N_{\mathrm{n}}} \frac{q_b Z_a}{|\mathbf{R}_a - \mathbf{R}_b|}. \tag{2.37}$$

Here, the Coulomb potential of the molecule's electrons at the positions of the environment charges $\mathbf{R}_b$ (in brackets) is integrated over the electronic coordinates $\int d\mathbf{r}_1 \cdots d\mathbf{r}_n \Xi^*(\mathbf{r}_1,\ldots,\mathbf{r}_n)$ for the wave functions of two electronic states Ξ_i and Ξ_j. We can simplify this equation by using Pauli's principle, which states that electrons are indistinguishable, to obtain

$$\begin{aligned} V^{(ij)}_{\mathrm{ele,env}}(\mathbf{R}) &= V^{(ij)}_{\mathrm{n,env}}(\mathbf{R}) \\ &\quad - \sum_b^{N_{\mathrm{env}}} q_b \int d\mathbf{r}_1 \cdots d\mathbf{r}_n \Xi_i^*(\mathbf{r}_1,\ldots,\mathbf{r}_n) \cdot \left[N_{\mathrm{e}} \frac{1}{|\mathbf{r}_1 - \mathbf{R}_b|} \right] \cdot \Xi_j(\mathbf{r}_1,\ldots,\mathbf{r}_n). \end{aligned} \tag{2.38}$$

After this, we can introduce the one-particle density $\rho^{(ij)}$ for the pair of electronic states i,j as[98]

$$\rho^{(ij}(\mathbf{r}_1) = N_{\mathrm{e}} \int d\mathbf{r}_2 \cdots d\mathbf{r}_n \int d\bar{\mathbf{r}}_2 \cdots d\bar{\mathbf{r}}_n \, \Xi_i^*(\mathbf{r}_1,\ldots,\mathbf{r}_n) \Xi_j(\mathbf{r}_1,\ldots,\mathbf{r}_n). \tag{2.39}$$

Under orthogonality constraints of both wave functions, the integral over the one-particle density yields the number of electrons N_e or 0,

$$\int d\mathbf{r}_1 \rho^{(ij)}(\mathbf{r}_1) = N_\mathrm{e}\delta_{ij}. \tag{2.40}$$

Now, if we apply the substitution of Eq. (2.39) to Eq. (2.38), we obtain $V^{(ij)}_{\text{ele,env}}(\mathbf{R})$ as

$$V^{(ij)}_{\text{ele,env}}(\mathbf{R}) = V^{(ij)}_{\text{n,env}}(\mathbf{R}) - \sum_b^{N_\text{env}} q_b \int d\mathbf{r}_1 \frac{\rho^{(ij)}(\mathbf{r}_1)}{|\mathbf{r}_1 - \mathbf{R}_b|}, \tag{2.41}$$

where the second term describes the Coulomb interaction between all environment charges and the electronic density of the molecule.

In force fields, the Coulomb potential of the one-particle density $\rho^{(ij)}(\mathbf{r}_1)$ is approximated as

$$-\int d\mathbf{r}_1 \frac{\rho^{(ij)}(\mathbf{r}_1)}{|\mathbf{r}_1 - \mathbf{R}|} \approx \sum_a \frac{q_a'^{(ij)}}{|\mathbf{R}_a - \mathbf{R}|}. \tag{2.42}$$

Here, $q_a'^{(ij)}$ are monopolar charges at the positions $\mathbf{R}_a$. Most commonly, every nucleus of the molecule is assigned such a charge. Further, the charges may already include the nuclear charge of the corresponding nucleus $q_a^{(ij)} = q_a'^{(ij)} + \delta_{ij} Z_a$, so that we can simplify Eq. (2.41) to

$$\begin{aligned} V^{(ij)}_{\text{ele,env}}(\mathbf{R}) &= \sum_b^{N_\text{env}} \sum_a^{N_\text{n}} \frac{q_b Z_a}{|\mathbf{R}_a - \mathbf{R}_b|} + \sum_b^{N_\text{env}} q_b \sum_a^{N_\text{n}} \frac{q_a'^{(ij)}}{|\mathbf{R}_a - \mathbf{R}_b|} \\ &= \sum_b^{N_\text{env}} q_b \sum_a^{N_\text{n}} \frac{q_a^{(ij)}}{|\mathbf{R}_a - \mathbf{R}_b|}. \end{aligned} \tag{2.43}$$

One method to perform the approximation of Eq. (2.42) which evaluates the charges on the nuclear position based on the **E**lectro**S**tatic **P**otential (ESP) is presented in the next section.

2.5 The Restrained Electrostatic Potential Fitting Method

There are many different methods to obtain a representation, e.g., $q_a^{(ij)}$, of the one-particle density $\rho^{(ij)}$ according to Eq. (2.42).[50] One method, where $q_a^{(ij)}$ lead to physical observables, such as solvation shells, that are in good agreement with an ab initio reference,[50] is the **R**estrained **E**lectro**S**tatic **P**otential (RESP) method.[99] This method tries to find a $\{q_a^{(ij)}\}$ that minimizes the error of the approximation made in Eq. (2.42) in a least-squares fashion. The notation below is an adaption of the original work of Bayly and coworkers,[99] which is used in the reprinted publication A.1.1.[75] The criterion for the minimization is the difference between ESP of the reference and that of $q_a^{(ij)}$ at the grid points $\mathbf{R}_g$,

$$\delta_{ij} \sum_a^{N_\text{n}} \frac{Z_a}{|\mathbf{R}_a - \mathbf{R}_g|} - \int d\mathbf{r}_1 \frac{\rho^{(ij)}(\mathbf{r}_1)}{|\mathbf{r}_1 - \mathbf{R}_g|} \approx \sum_a^{N_\text{n}} \frac{q_a^{(ij)}}{|\mathbf{R}_a - \mathbf{R}_g|}, \tag{2.44}$$

$$V^{(ij)}_{\text{esp}}(\mathbf{R}_g) \approx \tilde{V}^{(ij)}_{\text{esp}}(\mathbf{R}_g). \tag{2.45}$$

Note that, the term $\int d\mathbf{r}_1 \frac{\rho^{(ij)}(\mathbf{r}_1)}{|\mathbf{r}_1 - \mathbf{R}_g|}$ can be evaluated as

$$\int d\mathbf{r}_1 \frac{\rho^{(ij)}(\mathbf{r}_1)}{\left|\mathbf{r}_1 - \mathbf{R}_g\right|} = \sum_\alpha \sum_\beta D^{(ij)}_{\alpha\beta} \langle \alpha\beta | \gamma_g \rangle. \tag{2.46}$$

Here, $\langle \alpha\beta | \gamma_g \rangle$ denotes a 3-center-2-electron integral over the atomic orbitals α and β; γ_g represents the grid point as a Dirac delta function at $\mathbf{R}_g$; $D^{(ij)}_{\alpha\beta}$ is an element of the (transition) density matrix for state pair ij.

Now, the difference between the reference potential $V^{(ij)}_{\text{esp}}(\mathbf{R}_g)$ and the approximated one $\tilde{V}^{(ij)}_{\text{esp}}(\mathbf{R}_g)$ is minimized via a least-squares procedure,

$$\frac{d}{dq^{(ij)}_{a'}} \sum_g \left[V^{(ij)}_{\text{esp}}(\mathbf{R}_g) - \tilde{V}^{(ij)}_{\text{esp}}(\mathbf{R}_g) \right]^2 = -2 \sum_g \frac{V^{(ij)}_{\text{esp}}(\mathbf{R}_g) - \tilde{V}^{(ij)}_{\text{esp}}(\mathbf{R}_g)}{\left|\mathbf{R}_{a'} - \mathbf{R}_g\right|} = 0. \tag{2.47}$$

This equation can be analytically solved and would yield $q^{(ij)}_a$ that reproduce the ESP at all $\mathbf{R}_g$. However, these charges can be unphysically large[50,99]; especially for atoms without any grid points in the vicinity. For this reason, the RESP adds a hyperbolic restraint function to Eq. (2.47),

$$\begin{aligned} &\frac{d}{dq^{(ij)}_{a'}} \sum_g \left[V^{(ij)}_{\text{esp}}(\mathbf{R}_g) - \tilde{V}^{(ij)}_{\text{esp}}(\mathbf{R}_g) \right]^2 + c_1 \sum_a \left[\sqrt{\left(q^{(ij)}_a - q^{(ij)}_{a,0} \right)^2 - c_2^2} - c_2 \right] = \\ &-2 \sum_g \frac{V^{(ij)}_{\text{esp}}(\mathbf{R}_g) - \tilde{V}^{(ij)}_{\text{esp}}(\mathbf{R}_g)}{\left|\mathbf{R}_{a'} - \mathbf{R}_g\right|} - \frac{c_1 q^{(ij)}_a}{\sqrt{\left(q^{(ij)}_{a'} - q^{(ij)}_{a,0} \right)^2 - c_2^2}} = 0. \end{aligned} \tag{2.48}$$

Here, c_1 is a scale factor defining the asymptotic limits of the restraint, c_2 is the curvature of the hyperbola, and $q^{(ij)}_{a,0}$ are target charges for the restraint. The latter are often set to charges derived from population analysis or to 0. The derivative of the restraint function will be abbreviated as

$$dF_{\text{restr.}}(q^{(ij)}_{a'}) = \frac{c_1}{\sqrt{\left(q^{(ij)}_{a'} - q^{(ij)}_{a,0} \right)^2 - c_2^2}}. \tag{2.49}$$

Now, Eq. (2.48) can be rearranged by substituting $dF_{\text{restr.}}(q^{(ij)}_{a'})$ and inserting $\tilde{V}^{(ij)}_{\text{esp}}(\mathbf{R}_g)$ explicitly,

$$-2 \sum_g \frac{V^{(ij)}_{\text{esp}}(\mathbf{R}_g)}{\left|\mathbf{R}_{a'} - \mathbf{R}_g\right|} + \sum_g \frac{2}{\left|\mathbf{R}_{a'} - \mathbf{R}_g\right|} \sum_a^{N_\text{n}} \frac{q^{(ij)}_a}{|\mathbf{R}_a - \mathbf{R}|} - q^{(ij)}_a dF_{\text{restr.}}(q^{(ij)}_{a'}) = 0. \tag{2.50}$$

We can then establish a system of linear equations, while swapping the sums over a and g as

$$\sum_a^{N_\text{n}} \left[-dF_{\text{restr.}}(q^{(ij)}_{a'}) \delta_{a'a} + \sum_g \frac{2}{\left|\mathbf{R}_{a'} - \mathbf{R}_g\right|} \frac{1}{|\mathbf{R}_a - \mathbf{R}|} \right] q^{(ij)}_a = 2 \sum_g \frac{V^{(ij)}_{\text{esp}}(\mathbf{R}_g)}{\left|\mathbf{R}_{a'} - \mathbf{R}_g\right|}. \tag{2.51}$$

By defining

$$Y^{(ij)}_{a'} = 2 \sum_g \frac{V^{(ij)}_{\text{esp}}(\mathbf{R}_g)}{\left|\mathbf{R}_{a'} - \mathbf{R}_g\right|} \tag{2.52}$$

and

$$L_{a'a} = \sum_g \frac{2}{\left|\mathbf{R}_{a'} - \mathbf{R}_g\right|} \frac{1}{\left|\mathbf{R}_a - \mathbf{R}\right|}, \tag{2.53}$$

we can write Eq. (2.51) in matrix notation as

$$\left[\mathbf{L} - \mathbf{1}\, d\mathbf{F}_{\text{restr.}}(\mathbf{P}'^{(ij)})\right] \mathbf{P}^{(ij)} = \mathbf{Y}^{(ij)}. \tag{2.54}$$

Here, $\mathbf{P}^{(ij)} = \{q_a^{(ij)}\}$, $\mathbf{1}$ is the identity matrix and $d\mathbf{F}_{\text{restr.}}(\mathbf{P}'^{(ij)})$ is a vector containing all elements $dF_{\text{restr.}}(q_{a'}^{(ij)})$. Since $d\mathbf{F}_{\text{restr.}}(\mathbf{P}'^{(ij)})$ depends on the fitted charges, Eq. (2.54) has to be solved iteratively. The initial $\mathbf{P}^{(ij)}$ is obtained using Eq. (2.54) without restraints. Afterwards, $\mathbf{P}^{(ij)}$ is used to compute the constraint, which is then added to the diagonal of $\mathbf{L}$, and the linear equation system is solved to obtain new $\mathbf{P}^{(ij)}$. This procedure is iterated until self-consistency.

In order to perform the RESP fit, the set of grid points $\mathbf{R}_g$ around the molecule needs to be constructed[100] at which the ESP of the one electron density $V_{\text{esp}}^{(ij)}(\mathbf{R}_g)$ can be calculated. The authors of Ref 99 use the Merz–Singh–Kollman scheme[100–102] which works as follows: First, a set of spherical shells s is generated around each atom a; the radii r_{sa} of these shells are multiples of the atom's vdW radius $r_{\text{vdW},a}$. The set of shells of the Merz–Singh–Kollmann scheme (1.4, 1.6, 1.8, and 2.0 times $r_{\text{vdW},a}$)[100–102] can be reproduced with the algorithm:[103]

$$r_{sa} = \left[1.4 + \frac{0.4}{\sqrt{N_{\text{shells}}}}(i-1)\right] r_{\text{vdW},a}, \tag{2.55}$$

where $N_{\text{shells}} = 4$. Second, a set of points on a shell are generated by a spherical surface quadrature. For this, the Lebedev quadrature[104] is most suitable; its high symmetry (point group O_h) ensures that the fitted point charges align with the symmetry of the molecule for most point groups. This results in a set of point charges in shells around each atom $\{\mathbf{R}_g^{(sa)}\}$. Lastly, all points $\mathbf{R}_g^{(sa)}$ in a shell s that are closer to another atom a' than its scaled radius $r_{sa'}$ are removed. The residual points serve as $\mathbf{R}_g$ in the fitting scheme described above.

We chose the RESP method over other population analysis methods to obtain representations of the one-electron densities in the LVC/MM method as charges obtained by the RESP fit accurately reproduces the ESP of an electronic state and lead to RDFs which are close to an ab-initio reference.[50] The next section shows an extension of the presented representation in terms of charges at the nuclear positions that also includes higher-order terms of the multipolar expansion on the nuclear coordinates.

2.6 Distributed Multipole Expansions

The charges $q_a^{(ij)}$ in the representation of the one-particle densities shown so far are fully isotropic and hence cannot reproduce the anisotropies of $\rho^{(ij)}$ at short distances. Stone proposed a solution to this by employing a the Tailor expansion of the Coulomb potential around the nuclear coordinates as centers called DME.[105–107] Higher-order terms of the Tailor expansion, such as the dipole and quadrupole terms, capture aforementioned anisotropies in the short-range. This allows representing, e.g., out-of-plane transition densities in planar molecules or lone pair electron clouds. For this reason, DMEs can be included into FFs for a more accurate description of electrostatic interactions.[39]

The ESP at coordinate $\mathbf{R}_g$ arising from $\rho^{(ij)}$ (see Eq. (2.41) and Eq. (2.48)) can be approximated as a Taylor expansion[107]

$$V_{\text{esp}}^{(ij)}(\mathbf{R}_g) \approx \sum_{a}^{N_\text{n}} \left[\frac{P_a^{(ij)}}{\left|\mathbf{R}_{ag}\right|} + \sum_{x}^{3} \frac{P_{ax}^{(ij)} R_{agx}}{\left|\mathbf{R}_{ag}\right|^3} + \sum_{xx'}^{3} \frac{P_{axx'}^{(ij)} R_{agx} R_{agx'}}{2\left|\mathbf{R}_{ag}\right|^5} + O(\mathbf{R}_{ag}^7) \right]. \quad (2.56)$$

Here, R_{agx} is the element of the distance vector between atom a and point g in Cartesian direction x. Additionally to the monopolar terms $P_a^{(ij)} = q_a^{(ij)}$, there are the corresponding dipolar term $\mathbf{P}_{\text{dip},a}^{(ij)} = \left(P_{a\text{x}}^{(ij)}, P_{a\text{y}}^{(ij)}, P_{a\text{z}}^{(ij)}\right)^T$ and the corresponding quadrupole terms $\mathbf{P}_{\text{quad},a}^{(ij)} = \left(P_{a\text{xx}}^{(ij)}, \ldots, P_{a\text{yz}}^{(ij)}\right)^T$. This expansion can be cast into a sum of scalar products between a tensor $\mathbf{P}^{(ij)}$, which contains all multipole terms, and a geometric tensor $\mathbf{T}$ containing all corresponding prefactors. Note that we use the index p to refer to the different elements in the multipole expansion on an atom a (in the order: monopole, x, y, z, xx, yy, zz, xy, xz, yz); the mixed quadrupole terms xy, xz, yz are here multiplied by 2. Eq. (2.56) can then be written as

$$V_{\text{esp}}^{(ij)}(\mathbf{R}_g) = \sum_{a}^{N_\text{n}} \sum_{p}^{10} \left(P_{ap}^{(ij)} \cdot T_{agp}\right), \quad (2.57)$$

which equates a contraction over the indices a and p.

With the end of this section, the theoretical foundations and the preexisting methodology are introduced, on which the work of this thesis is based: The nonadiabatic dynamics of system in solution described by the TDSE are numerically integrated using SH, for which we solve the TISE using LVC models in a QM/MM approach called LVC/MM. The details on how a DME can be evaluated by extending the RESP method and how the LVC Hamiltonian is adapted for the QM/MM approach are shown in the next chapter.

3

METHODOLOGICAL DEVELOPMENTS

The goal of this thesis is the simulation and analysis of time-dependent three-dimensional nonadiabatic dynamics of solvated photoactive compounds over long time scales. The methodological developments for efficient simulation of nonadiabatic SH dynamics in solution in terms of the novel LVC/MM method and the analysis in terms of time-dependent three-dimensional solvation shells are described in this chapter.

This chapter will start by introducing the building blocks of the LVC/MM implementation in the SHARC package[108] shown in Fig. 3.1 from top to bottom in addition to all necessary details.

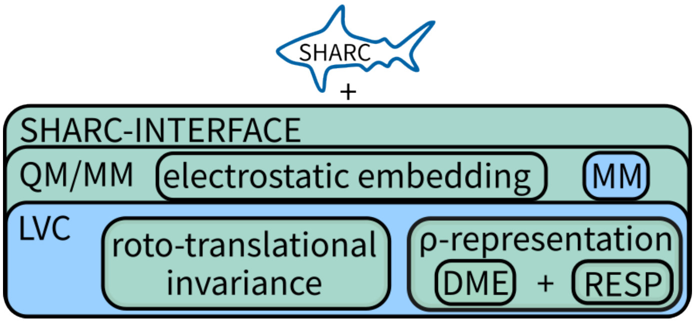

Figure 3.1: Schematic overview of the most important methodological developments achieved for the realization the LVC/MM method. All boxes with blue outlines are pre-existing blocks while green outlines mark novel additions.

Section 3.1 outlines the basic workflow in the SHARC package[108] and the development of the pySHARC framework,[109] and introduces new generalized Python-interface classes to be used with pySHARC (Fig. 3.1: SHARC-INTERFACE). The latter allow for standardized interfaces with the same base functionality for the LVC model and OpenMM program[110] (Fig. 3.1: LVC and MM), and a hierarchical QM/MM interface (Fig. 3.1: QM/MM) which is in principle ignorant and independent of the **Q**uantum **M**echanics (QM) and MM interfaces used. Because of the standardized base functionality of each interface, a modified version of pySHARC is able to utilize all of them. Section 3.2 derives and elucidates the electrostatically-coupled and roto-translationally invariant LVC Hamiltonian including all necessary equations for energies, gradients and NACs. For this, we decouple the evaluation of the LVC Hamiltonian from its reference nuclear coordinates via a superimposition algorithm. Then, we include a DME (Section 2.6) into the LVC model as a representation of the electronic densities, $\rho^{(ij)}$, to evaluate electrostatic interaction with point charges. In order to fit the parameters of the DME used in the LVC model, we formulate an extension of the RESP method (Section 2.5) in Section 3.3 so that it also yields higher order terms of the multipole expansion.

Section 3.4 describes additional details on the implementation of the LVC/MM method to increase its efficiency and shows an analysis of the method's scaling behavior with different system parameters. Lastly, Section 3.5 explains the generation and analysis of time-dependent three-dimensional solvent structures via so-called 3D-SDFs.

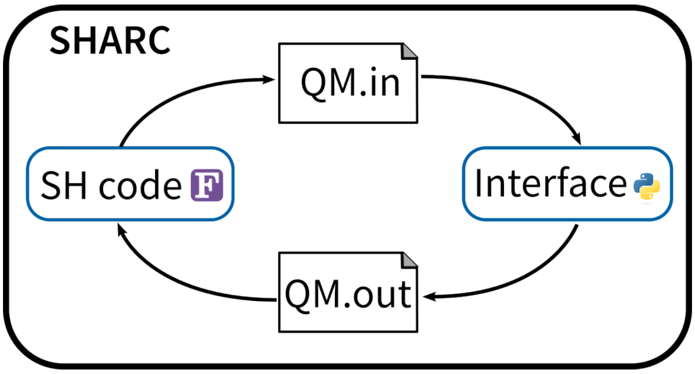

Figure 3.2: Illustration of information exchange in the SHARC program adapted from Refs. 56 and 109.

3.1 Generalized SHARC-Interfaces

The general working mechanism of the SHARC program[56] is illustrated in Fig. 3.2. The whole program is split in two parts: (i) the SH algorithm written in Fortran and (ii) the code interacting with the electronic structure codes which is called “interface” written in Python. During an MD simulation, the SHARC program cycles between its two parts. The propagation of the electronic wave function (see Eq. (2.17)) and the hops are evaluated in the SH code. Then, the nuclear coordinates and specifications on required properties of the electronic wave function, such as energies, gradients, NACs, SOCs, and the wave-function overlap to the prior time step, are written to the `QM.in` file. This file is read by the interface code and processed to perform an electronic structure calculation either through an external program or directly, in the case of LVC. The requested results are then written to the `QM.out` file and parsed by the SH code. The cycle is repeated from here. The description of this cycle demonstrates two important aspects of the code: (i) it is necessary to read and write files at two instances every cycle and (ii) the interface code to every electronic structure program or other Hamiltonian behaves the same in each cycle. Menger showed in his thesis that the first aspect poses a hurdle to simulations using the LVC Hamiltonian and other highly efficient methods.[109] He showed that writing and reading the files every cycle, generally referred to as “file input/output” or “file I/O”, is responsible for over 50% of the computation time. In order to leverage the full efficiency of the LVC Hamiltonian, Menger modified the SH and LVC interface code to directly communicate the information contained in the `QM.in` and `QM.out` files between both parts of the SHARC code.[72,109] This drastically reduced the computation time of each cycle and was also applied for SHARC simulations using machine learning models.[64] The codebase connecting the SH code in Fortran and the Python interface via Python bindings in C is called pySHARC, and is illustrated in Fig. 3.3.

Fig. 3.3 does not only illustrate pySHARC, but also introduces further developments based on it. The second aspect of the SHARC program (vide infra), that every interface should behave in the same way, can also be seen in the illustration: The interface puzzle piece is connected to the Fortran code via pySHARC but it is split in two parts: the base part (blue) and the specific part (green). The base part is defined as all points of interaction that are necessary to perform a single point calculation with either pySHARC or the file I/O. The specific part is then all programmatic logic to operate an external program or other model. Menger’s

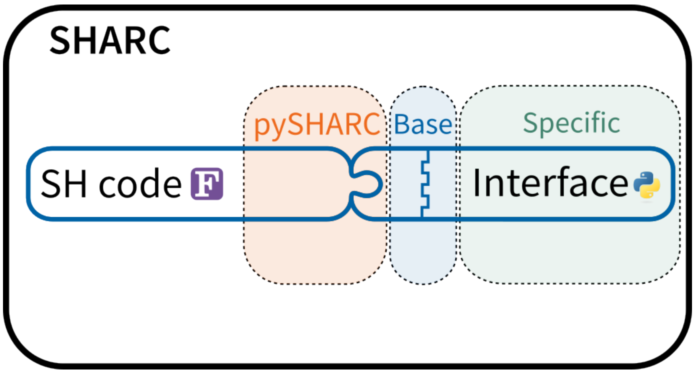

Figure 3.3: Illustration of the pySHARC scheme[64,72,109] including a general interface scheme. The Fortran part of SHARC is connected to the Python interfaces via pySHARC (orange shaded area). pySHARC interacts with the interfaces via a layer of base functionality (blue shaded area) which then call specific implementations (green shaded area) to perform electronic structure calculations.

work concluded with the application of pySHARC to the LVC and machine learning models specifically, but this structure can be generally applied to all interfaces in the SHARC code.[108]

The first step in achieving the overall goal of this thesis lies in continuing where Menger left off and defining a generalized form of a SHARC interface. In preparation for this step, the whole Python code base was ported from Python2.7 to Python3.[108] In version 3.0 of the SHARC program every interface is essentially a script, with a collection of functions, that adheres to the general working principle depicted in Fig. 3.2. The generalization of the interfaces to the general structure shown in Fig. 3.3 can be accomplished with object-oriented programming. In this, every interface is an object with the same base functionality. This functionality can be realized by a shared implementation or a specific one, which is referred to as polymorphism. All programmatic logic that is specific to an external program or model is then placed “behind” the base functionality, which is called abstraction. The implementation of a specific interface can be fully or in parts obtained from the implementation of the base interface object, which is called inheritance. In this way, the interface object class can be implemented in a tree-like fashion. The base functionality is implemented in the base class which can then be inherited in the so-called derived classes.

The general concept of the base class and its functionality is illustrated in Fig. 3.4 for both a single point calculation using file I/O (from the right) and the calculation of a trajectory using pySHARC (from the left). In reference to Fig. 3.3, all functions that have the same logic for all interfaces and can be implemented in the base class have a blue border, and all functions with a green border will have specific logic for every interface. The first step in a single-point calculation is obtaining information about the molecular system that will be handled in the computation; the `setup_mol` routine is receiving this information from either the `QM.in` file or directly from pySHARC. Next, the information from the `.resources` and `.template` files is processed in the corresponding functions `read_resources` and `read_template`. The `.resources` file contains all information that does not influence the result of a single-point calculation, such as the number of CPUs and memory available. Therefore, this file looks similar for different interfaces and the `read_resources` function is implemented in the base class; this function can

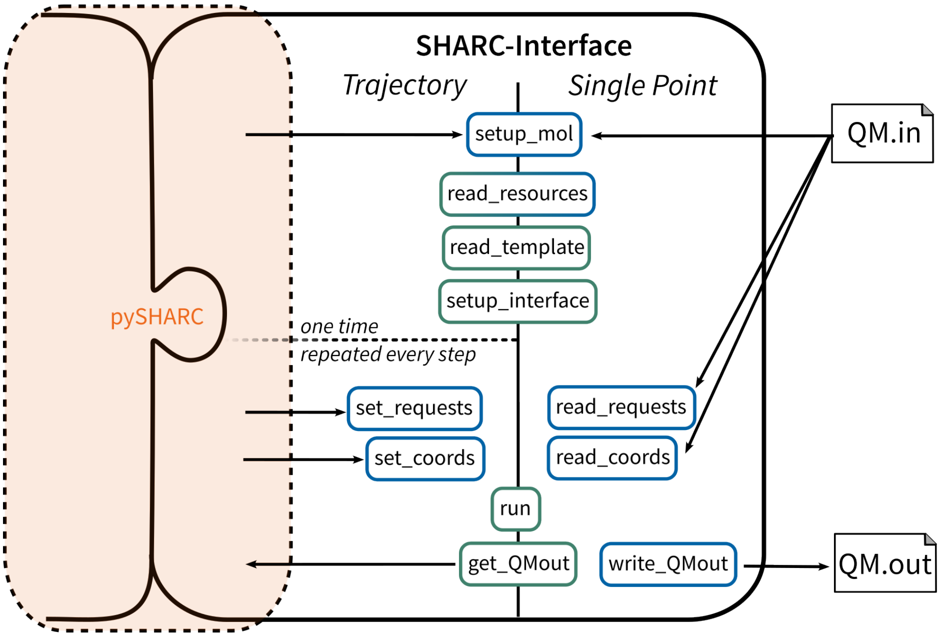

Figure 3.4: Illustration of the generalized SHARC-interface class in the context of a single-point calculation with the old SHARC scheme (from the right) and a trajectory with the pySHARC scheme (from the left). The routines are called from top to bottom and have borders indicating whether the implemented logic can be in the base class (blue) or have to be implemented for every derived interface separately (green). The arrows indicate communication of information from and to the interface.

then be altered or extended in the derived class if necessary. The `.template` file contains all method specific information, e.g., as the basis set and functional in the case of **T**ime-**D**ependent **D**ensity **F**unctional **T**heory (TDDFT) calculations. Hence, the `.template` file and the `read_template` routine are specific for every interface. The `setup_interface` routine generally combines and processes the information received in the three prior routines (`setup_mol`, `read_resources`, `read_template`). A this point there is a break on the trajectory side in Fig. 3.4. All routines prior to this point are handling information that does not change during a trajectory. Therefore these are only called once. The next routines, however, have to be called every cycle or time step in the SHARC simulation. The properties of the electronic wave function that need to be computed can either be parsed from the `QM.in` file (`read_requests`) as before or be set by pySHARC in separate routines (`set_requests`). The same goes for the nuclear coordinates of the current time step (`read_coords` or `set_coords`). Now that all necessary information is gathered and processed, the `run` function is called, which is an abstraction of setup and computation for the external programs or models. The `run` function also calls post-processing programs like `wfoverlap` and the TheoDORE[111] program. The `get_QMout` routine then handles parsing and prepares the results of the single-point calculation. In pySHARC, this information can be directly communicated in memory to the SH code. In the old, file I/O based approach `write_QMout` generates the `QM.out` file. Additionally, all interface specific functionality that is used to setup single-point calculations or trajectories was moved from the respective scripts of SHARC3.0[108] into the interface themselves.

Based on the definition of the base functionality of any interface (Fig. 3.4), the specialized pySHARC code for the LVC and machine learning models was generalized so that it can replace `sharc.x` as the driver of the SHARC simulations in nearly all cases.

The new interface scheme not only can be applied to rewrite existing interfaces to be usable with pySHARC but also to generate interfaces in a new way. In QM/MM calculations, one has to perform single-point calculations with a chosen electronic structure method or model and a FF (see Eq. (2.34)). With the new interface base class, writing an interface that generally uses SHARC interfaces for an QM/MM approach is straight forward. This is illustrated in Fig. 3.5. Here, the QM/MM interface itself forwards requested properties and nuclear coordinates to the chosen MM and QM interfaces. For electrostatic embedding, the point charges are communicated from the MM interface to the QM interface. The QM/MM interface then combines the properties (energies and gradients in Fig. 3.5) accordingly and returns them.

The underlying concept of SHARC interfaces and its base class is currently being generalized and extended by the SHARC development team, so that interfaces can be grouped into (i) interfaces that use other interfaces (hybrid interfaces), such as the QM/MM interface, (ii) interfaces that call external programs, and (iii) interfaces with all algorithms directly implemented in SHARC, such as the LVC interface.

For the evaluation of a single point on a PES with FFs (see Eq. (2.32)), a new interface for the OpenMM[110] code was written. The OpenMM[110] package comes with two advantageous features: (i) its Python-based API, which allows in memory communication and direct access to force and energy components, and (ii) its inter-compatibility with topology and trajectory files of other popular FF programs like Amber[41] and GROMACS.[112]

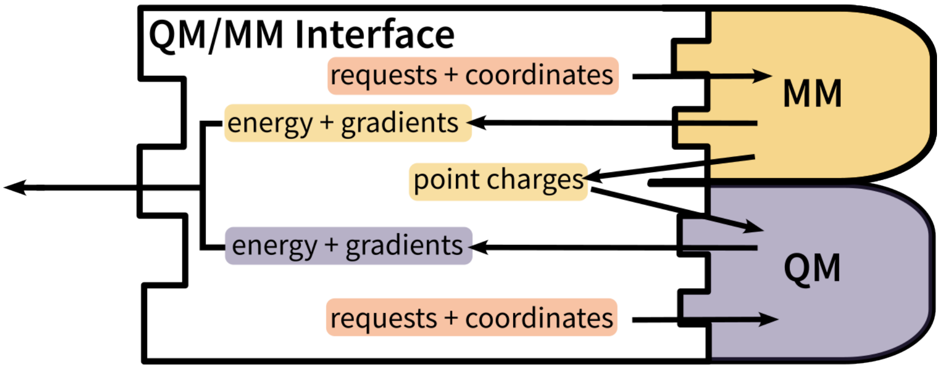

Figure 3.5: Schematic of the working principle inside the hierarchical QM/MM interface. Upon receiving externally requested properties and coordinates (orange) from pySHARC, it utilizes two generalized SHARC interfaces for QM (purple) and MM (yellow) calculations, and combines their results.

For the nonadiabatic simulations using LVC/MM, we use the above described QM/MM interface structure and chose the LVC method and its corresponding interface for the QM part. Hence, the LVC method needs to be extended to include the interaction with point charges into the Hamiltonian. Once this is achieved, the above described QM/MM interface can be used together with the OpenMM interface to facilitate LVC/MM calculations. The extension of the LVC Hamiltonian and further modifications of the algorithm, published in Ref. 75 (see Section A.1.1), are described in the following section.

3.2 Extension of VC Hamiltonians for Electrostatic Embedding

Before we can modify the LVC Hamiltonian to include electrostatic interactions, we need to solve an arising issue: The LVC Hamiltonian is defined in terms of mass–frequency-weighted normal-mode coordinates $\mathbf{Q}$ (see Eq. (2.24)), i.e. as displacements from a reference or equilibrium geometry $\mathbf{R}_0$. $\mathbf{Q}$ explicitly excludes all rotational and translational degrees of freedom. This is not a problem in gas-phase calculations, where the molecule is in total isolation and these degrees of freedom do not influence the potential energy of the system. However, if we include an external force into the LVC Hamiltonian, energy will be transferred into the roto-translational degrees of freedom which leads to corresponding motion the whole LVC system. In the context of an environment, this is referred to as diffusion of the molecule. The motion of the molecule in these roto-translational degrees of freedom moves the center of mass away from $\mathbf{R}_0$, which translates into artificially larges displacements in $\mathbf{Q}$ and leads to unphysical forces. However, the potential energy function is not dependent on roto-translational degrees of freedom. Through a coordinate transformation, we can remove the contributions to the roto-translational degrees of freedom from the nuclear coordinates in our surface hopping simulation $\mathbf{R}_\mathrm{S}$. In other words, we can transform $\mathbf{R}_\mathrm{S}$ into the basis of our reference geometry $\mathbf{R}_0$ as

$$\mathbf{R}_{\mathrm{S}(0)} = F_{S\mapsto 0}(\mathbf{R}_\mathrm{S}). \tag{3.1}$$

Here, $\mathbf{R}_{\mathrm{S}(0)}$ are the coordinates of the simulation in the basis of the reference coordinates and $F_{S\mapsto 0}$ is the function transforming between the two coordinate systems. The transformation function may be constructed in multiple ways; here, it is done by superimposing $\mathbf{R}_\mathrm{S}$ onto $\mathbf{R}_0$ via the Kabsch algorithm.[113] In this algorithm, the first step is calculating the centers of mass $\mathbf{c}_\mathrm{S}$ and $\mathbf{c}_0$ of $\mathbf{R}_\mathrm{S}$ and $\mathbf{R}_0$ as

$$\mathbf{c} = \frac{1}{m_\mathrm{tot}} \sum_a^{N_\mathrm{n}} m_a \mathbf{R}_a. \tag{3.2}$$

Here, m_a is the mass of atom a and m_tot is the total mass of the molecule. Next, the coordinates of all atoms in both $\mathbf{R}_\mathrm{S}$ and $\mathbf{R}_0$ are shifted towards a common origin as $\mathbf{R}_{\mathrm{S},a} - \mathbf{c}_\mathrm{S} = \tilde{\mathbf{R}}_{\mathrm{S},a}$ and $\mathbf{R}_{0,a} - \mathbf{c}_0 = \tilde{\mathbf{R}}_{0,a}$. Now, an optimal rotation matrix $\mathbf{T}^\mathrm{rot}$, that minimizes the mass-weighted root-mean-square distances to the reference coordinates, can be determined. For this, we construct the mass-weighted 3×3 cross-covariance matrix $\mathbf{K}_{\mathrm{S}0}$ and perform a **S**ingular **V**alue **D**ecomposition (SVD) of it:

$$\mathbf{K}_{\mathrm{S}0} = \left(\tilde{\mathbf{R}}_\mathrm{S}\,\mathbf{m}\right)^T \cdot \tilde{\mathbf{R}}_0 = \mathbf{U}\boldsymbol{\Sigma}\mathbf{V}^T. \tag{3.3}$$

Here, $\tilde{\mathbf{R}}_\mathrm{S}$ and $\tilde{\mathbf{R}}_0$ are $N_\mathrm{n} \times 3$ matrices and $\mathbf{m}$ is a vector containing all masses m_a. Afterwards, the optimal rotation matrix $\mathbf{T}^\mathrm{rot}_{\mathrm{S}0}$ between the coordinate systems of the simulation "S" and the one of the reference "0" is defined as

$$\mathbf{T}^\mathrm{rot}_{\mathrm{S}0} = \mathbf{U} \begin{pmatrix} 1 & 0 & 0 \\ 0 & 1 & 0 \\ 0 & 0 & d \end{pmatrix} \mathbf{V}^T. \tag{3.4}$$

In this equation, d is the determinant of $\mathbf{U}\cdot\mathbf{V}^T$. With this, we can rewrite Eq. (3.1) as

$$\mathbf{R}_{\mathrm{S}(0)} = (\mathbf{R}_\mathrm{S} - \mathbf{1}\mathbf{c}_\mathrm{s}) \cdot \mathbf{T}^\mathrm{rot}_{\mathrm{S}0} + \mathbf{1}\mathbf{c}_0, \tag{3.5}$$

where $\mathbf{1c}$ is a short-hand notation for an $N_\mathrm{n} \times 3$ matrix with all rows being equal to $\mathbf{c}$.

After establishing the coordinate transformation between the simulation and reference, the basic LVC Hamiltonian may be evaluated from transformed coordinates, $\mathbf{R}_{\mathrm{S}(0)}$, as before (Eq. (2.24)). All invariant properties, which do not change under this transformation, may be used directly; these quantities are the energies and wave function overlap in the context of SH. All other quantities like dipole moments, gradients, and NACs may be trivially transformed back to the coordinate system of the simulation by applying the inverse rotation matrix $\mathbf{T}_{\mathrm{S0}}^{\mathrm{rot},T}$ similar to Eq. (3.5). However, the derivative of the vibronic coupling potential energy matrix $\mathbf{W}(\mathbf{Q})$ (Eqs. (2.23) and (2.25-2.28)) now also depend on the derivative of the coordinates with respect to the transformation:

$$\frac{\partial \mathbf{W}(\mathbf{Q})}{\partial R_{\mathrm{S},ax}} = \sum_k \frac{\partial \mathbf{W}(\mathbf{Q})}{\partial Q_k} \sum_{a'}^{N_\mathrm{n}} \sum_{x'}^{3} \frac{\partial Q_k}{\partial R_{\mathrm{S}(0),a'x'}} \frac{\partial R_{\mathrm{S}(0),a'x'}}{\partial R_{\mathrm{S},ax}}. \tag{3.6}$$

$\frac{\partial R_{\mathrm{S}(0),a'x'}}{\partial R_{\mathrm{S},ax}}$ can be obtained by differentiating Eq. (3.5) by applying the chain rule:

$$\frac{\partial R_{\mathrm{S}(0),a'x'}}{\partial R_{\mathrm{S},ax}} = \sum_y^3 \left(\delta_{aa'} \delta_{xy} - \frac{m_{a'}}{m_\mathrm{tot}} \right) \mathbf{T}^{\mathrm{rot}}_{\mathrm{S0},x'y} + \sum_y^3 \left(R_{\mathrm{S},a'y} - c_{\mathrm{S},y} \right) \frac{\partial \mathbf{T}^{\mathrm{rot}}_{\mathrm{S0},x'y}}{\partial R_{\mathrm{S},ax}}. \tag{3.7}$$

In this equation, the derivatives of the coordinates and the corresponding center of mass are trivial to obtain. However, the derivative of the rotation matrix with respect to the coordinates in the simulation $\frac{\partial \mathbf{T}^{\mathrm{rot}}_{\mathrm{S0},x'y}}{\partial R_{\mathrm{S},ax}}$ has to be obtained by differentiating Eq. (3.4), which includes the differentiation of all matrices in the SVD.[114] Note that this derivative was evaluated numerically in the first two publications[75,76] (see Sections A.1.1 and A.1.2). The following analytical evaluation will be included in the next publication. The analytical derivative of the rotation matrix can be calculated as

$$\frac{\partial \mathbf{T}^{\mathrm{rot}}_{\mathrm{S},0}}{\partial R_{\mathrm{S},ax}} = \frac{\partial \mathbf{U}}{\partial R_{\mathrm{S},ax}} \begin{pmatrix} 1 & 0 & 0 \\ 0 & 1 & 0 \\ 0 & 0 & d \end{pmatrix} \mathbf{V}^T + \mathbf{U} \begin{pmatrix} 1 & 0 & 0 \\ 0 & 1 & 0 \\ 0 & 0 & d \end{pmatrix} \frac{\partial \mathbf{V}^T}{\partial R_{\mathrm{S},ax}}. \tag{3.8}$$

As shown in Ref. 114, the derivatives of the matrices $\mathbf{U}$ and $\mathbf{V}^T$ can be expressed in terms of the derivatives of the covariance matrix $\mathbf{K}_{\mathrm{S0}}$:

$$\frac{\partial K_{\mathrm{S0},x'y}}{\partial R_{\mathrm{S},ax}} = \sum_{a'} \delta_{aa'} \delta_{xx'} m_a R_{0,a'y}. \tag{3.9}$$

With $d\mathbf{K}_{\mathrm{S0}}$ being a differential of $\mathbf{K}_{\mathrm{S0}}$, the differentials of the matrices $\mathbf{U}$ and $\mathbf{V}$ can be obtained as

$$d\mathbf{U} = \mathbf{U}\left[\mathbf{F} \circ \left(\mathbf{U}^T d\mathbf{K}_{SO} \mathbf{V}\boldsymbol{\Sigma} + \boldsymbol{\Sigma}\mathbf{V}^T d\mathbf{K}_{SO} \mathbf{U}\right)\right] + \left(\mathbf{1} - \mathbf{U}\mathbf{U}^T\right) d\mathbf{K}_{SO} \mathbf{V}\boldsymbol{\Sigma}^{-1}, \tag{3.10}$$

$$d\mathbf{V} = \mathbf{V}\left[\mathbf{F} \circ \left(\boldsymbol{\Sigma}\mathbf{U}^T d\mathbf{K}_{SO} \mathbf{V} + \mathbf{V}^T d\mathbf{K}_{SO}^T \mathbf{U}\boldsymbol{\Sigma}\right)\right] + \left(\mathbf{1} - \mathbf{V}\mathbf{V}^T\right) d\mathbf{K}_{SO}^T \mathbf{U}\boldsymbol{\Sigma}^{-1} \tag{3.11}$$

with

$$F_{kl} = \begin{cases} \frac{1}{\Sigma_{ll}^2 - \Sigma_{kk}^2} & k \neq l \\ 0 & k = l \end{cases}. \tag{3.12}$$

In this, $\circ$ denotes the Hadamard product. The full derivation of the SVD derivative can be found in Ref. 114.

With the formalism above, we have the ability to evaluate all properties needed for SH using an LVC Hamiltonian, even if the molecule investigated is able to move roto-translationally. Now, we can move on to add an external force into the Hamiltonian in the shape of an electrostatic potential generated by a set of point charges.

The addition of the electrostatic interaction into the vibronic coupling potential energy matrix $\mathbf{W}(\mathbf{Q})$ (Eqs. (2.23) and (2.25-2.28)) can be trivially written in matrix form as

$$\mathbf{W}_{\text{ee}}(\mathbf{R}_{\text{mol}}, \mathbf{R}_{\text{env}}, \mathbf{P}_{\text{env}}) = \mathbf{W}(\mathbf{Q}(\mathbf{R}_{\text{mol}})) + \mathbf{X}(\mathbf{R}_{\text{mol}}, \mathbf{R}_{\text{env}}, \mathbf{P}_{\text{env}}). \tag{3.13}$$

Here, the vibronic coupling potential energy matrix including electrostatic embedding $\mathbf{W}_{\text{ee}}(\mathbf{R}_{\text{mol}}, \mathbf{R}_{\text{env}}, \mathbf{P}_{\text{env}})$ directly depends on the coordinates of the whole system $\mathbf{R} = \mathbf{R}_{\text{mol}} + \mathbf{R}_{\text{env}}$ and the point charges of the environment $\mathbf{P}_{\text{env}}$. Note that for a simpler notation, $\mathbf{W}(\mathbf{Q}(\mathbf{R}_{\text{mol}}))$, implies a transformation with the above described procedure to superimpose $\mathbf{R}_{\text{mol}}$ onto the reference coordinates. An element for the pair of electronic states ij in the electrostatic coupling matrix X_{ij} is directly related to the Coulomb potential energy function between the molecule and a set of point charges $V^{(ij)}_{\text{esp}}$ (see Eqs. (2.41) and (2.44)):

$$\begin{aligned} X_{ij}(\mathbf{R}_{\text{mol}}, \mathbf{R}_{\text{env}}, \mathbf{P}_{\text{env}}) &= \sum_{b}^{N_{\text{env}}} q_b V^{(ij)}_{\text{esp}}(\mathbf{R}_b) \\ &= \sum_{b}^{N_{\text{env}}} q_b \left[\delta_{ij} \sum_{a}^{N_{\text{mol}}} \frac{Z_a}{|\mathbf{R}_a - \mathbf{R}_b|} - \int d\mathbf{r}_1 \frac{\rho^{(ij)}(\mathbf{r}_1)}{|\mathbf{r}_1 - \mathbf{R}_b|} \right]. \end{aligned} \tag{3.14}$$

This definition of the electrostatic coupling matrix cannot be used for an LVC model, since the model does not include electronic densities $\rho^{(ij)}(\mathbf{r}_1)$ for the model states. For this reason, we chose to approximate $V^{(ij)}_{\text{esp}}(\mathbf{R}_b)$ via a DME[105,106] (see Eqs. (2.56-2.57)), which is derived in Section 2.6. The LVC model based on Eq. (3.13) is defined in the diabatic electronic basis, which means that the DME parameters $P^{(ij)}_{ap}$ also represent the electronic (transition) densities of the diabatic states. For this reason, the electrostatic LVC/MM model is related to the diabatic charge matrix approach of Park and Rhee,[115] who demonstrated that diabatic charges retain validity for the same diabatic pair of states at different geometries. We assume that the approximation made in employing a diabatic DME remains valid in the same phase space as the LVC model itself.

By inserting Eq. (2.57) into the expression for $X_{ij}(\mathbf{R}_{\text{mol}}, \mathbf{R}_{\text{env}}, \mathbf{P}_{\text{env}})$, we can write the element ij in the interaction matrix as

$$X_{ij}(\mathbf{R}_{\text{mol}}, \mathbf{R}_{\text{env}}, \mathbf{P}_{\text{env}}) = \sum_{b}^{N_{\text{env}}} q_b \sum_{a}^{N_{\text{mol}}} \sum_{p}^{10} \left[F^{\text{rot}} \left(\mathbf{P}^{(ij)}_a, \mathbf{T}^{\text{rot}}_{\text{S0}} \right)_p \cdot T_{abp} \right]. \tag{3.15}$$

Note that the DME, especially the higher order terms, are defined for a set coordinate system, which makes it analogous to other parameters in the LVC model; the coordinate system in which the LVC model and the DME are constructed to coincide. In Eq. (3.15), the DME parameters $\mathbf{P}^{(ij)}_a$ have to be rotated to the coordinate system of the simulation by the function F^{rot} using the rotation matrix $\mathbf{T}_{\text{S0}}^{\text{rot},T}$ from above (Eq (3.4)); the entries in the geometric tensor T_{abp} are already constructed from coordinates $\mathbf{R}_{\text{mol}}$ and $\mathbf{R}_{\text{env}}$ in the coordinate system of the simulation. The function F^{rot} can be written as

$$F^{\text{rot}}\left(\mathbf{P}_a^{(ij)},\mathbf{T}_{\text{S0}}^{\text{rot}}\right)=\left\{q_a^{(ij)},\mathbf{P}_{\text{dip},a}^{(ij)}\cdot\mathbf{T}_{\text{0S}}^{\text{rot}},\mathbf{T}_{\text{S0}}^{\text{rot}}\cdot\mathbf{P}_{\text{quad},a}^{(ij)}\cdot\mathbf{T}_{\text{0S}}^{\text{rot}}\right\}, \tag{3.16}$$

so that it rotates all orders of the DME accordingly. Note that the change in indices from S0 to 0S for the rotation matrix indicates the transpose of it. By rotating the DME to the coordinate system of the simulation, we can evaluate the total potential energy according to Eq. (3.13).

Additionally, we require the derivatives of X_{ij}. The derivative with respect to one Cartesian coordinate of an environment atom in the coordinate system of the simulation $R_{\text{S},b'x'}$ is

$$\frac{\partial X_{ij}}{\partial R_{\text{S},b'x'}}=q_b\sum_a^{N_{\text{mol}}}\sum_p^{10}\left[F^{\text{rot}}\left(\mathbf{P}_a^{(ij)},\mathbf{T}_{\text{S0}}^{\text{rot},T}\right)_p\cdot\frac{\partial T_{apb}}{\partial R_{\text{S},b'x'}}\right], \tag{3.17}$$

with $\frac{\partial T_{apb}}{\partial R_{\text{S},b'x'}}$ being the pth element in the vector (with the subscript S dropped)

$$\begin{aligned}\frac{d\mathbf{T}_{ab}}{dR_{bx'}}=\delta_{bb'}\Bigg(&-\frac{R_{abx'}}{|\mathbf{R}_{ab}|^3},\frac{\mathbf{R}_{ab}\cdot\mathbf{R}_{ab}-2r_{abx'}^2}{|\mathbf{R}_{ab}|^5},-\frac{R_{abx'}R_{abx''}}{|\mathbf{R}_{ab}|^5},\\&-\frac{R_{abx'}R_{abx'''}}{|\mathbf{R}_{ab}|^5},-\frac{R_{abx'}\left(5r_{abx'}^2-2\mathbf{R}_{ab}\cdot\mathbf{R}_{ab}\right)}{2|\mathbf{R}_{ab}|^7},-\frac{5R_{abx'}r_{abx''}^2}{2|\mathbf{R}_{ab}|^7},\\&-\frac{5R_{abx'}r_{abx''}^2}{2|\mathbf{R}_{ab}|^7},-\frac{R_{abx''}\left(5r_{abx'}^2-2\mathbf{R}_{ab}\cdot\mathbf{R}_{ab}\right)}{2|\mathbf{R}_{ab}|^7},\\&-\frac{R_{abx'''}\left(5r_{abx'}^2-2\mathbf{R}_{ab}\cdot\mathbf{R}_{ab}\right)}{2|\mathbf{R}_{ab}|^7},-\frac{5R_{abx'}R_{a'x''}R_{abx'''}}{2|\mathbf{R}_{ab}|^7}\Bigg).\end{aligned} \tag{3.18}$$

The term R_{abx} is the element in Cartesian direction x in the distance vector $\mathbf{R}_{ab}$ between atom a and b, which has the length $|\mathbf{R}_{ab}|$.

The derivatives with respect to a Cartesian coordinate of an LVC atom $R_{\text{S},ax}$ is more complex because the rotation matrix depends on these coordinates:

$$\begin{aligned}\frac{\partial X_{ij}}{\partial R_{\text{S},a'x'}}=\sum_b^{N_{\text{env}}}q_b\sum_p^{10}\Bigg[&F^{\text{rot}}\left(\mathbf{P}_a^{(ij)},\mathbf{T}_{\text{S0}}^{\text{rot}}\right)_p\cdot\frac{\partial T_{apb}}{\partial R_{\text{S},a'x'}}\\&+\frac{\partial F^{\text{rot}}\left(\mathbf{P}_a^{(ij)},\mathbf{T}_{\text{S0}}^{\text{rot}}\right)_p}{\partial R_{\text{S},a'x'}}\cdot T_{apb}\Bigg],\end{aligned} \tag{3.19}$$

with $\frac{\partial T_{apb}}{\partial R_{\mathrm{S},a'x'}}$ being the pth element in the vector (subscript S dropped)

$$\begin{aligned}\frac{d\mathbf{T}_{ab}}{dR_{a'x'}} = \delta_{aa'}\Bigg(& \frac{R_{abx'}}{|\mathbf{R}_{ab}|^3}, \frac{\mathbf{R}_{ab}\cdot\mathbf{R}_{ab} - 2r_{abx'}^2}{|\mathbf{R}_{ab}|^5}, \frac{R_{abx'}R_{abx''}}{|\mathbf{R}_{ab}|^5}, \\ & \frac{R_{abx'}R_{abx'''}}{|\mathbf{R}_{ab}|^5}, \frac{R_{abx'}\left(5r_{abx'}^2 - 2\mathbf{R}_{ab}\cdot\mathbf{R}_{ab}\right)}{2\,|\mathbf{R}_{ab}|^7}, -\frac{5R_{abx'}r_{abx''}^2}{2\,|\mathbf{R}_{ab}|^7}, \\ & -\frac{5R_{abx'}r_{abx''}^2}{2\,|\mathbf{R}_{ab}|^7}, \frac{R_{abx''}\left(5r_{abx'}^2 - 2\mathbf{R}_{ab}\cdot\mathbf{R}_{ab}\right)}{2\,|\mathbf{R}_{ab}|^7}, \\ & \frac{R_{abx'''}\left(5r_{abx'}^2 - 2\mathbf{R}_{ab}\cdot\mathbf{R}_{ab}\right)}{2\,|\mathbf{R}_{ab}|^7}, \frac{5R_{abx'}R_{ax''}R_{abx'''}}{2\,|\mathbf{R}_{ab}|^7}\Bigg),\end{aligned} \tag{3.20}$$

and with the derivative of the rotation function $F^{\mathrm{rot}}\left(P_{ap}^{(ij)}, \mathbf{T}_{\mathrm{S0}}^{\mathrm{rot},T}\right)$ evaluated as

$$\begin{aligned}\frac{\partial F^{\mathrm{rot}}\left(P_{ap}^{(ij)}, \mathbf{T}_{\mathrm{S0}}^{\mathrm{rot},T}\right)}{\partial R_{\mathrm{S},a'x'}} = \Bigg\{ & 0, \mathbf{P}_{\mathrm{dip},a}^{(ij)} \cdot \frac{\partial \mathbf{T}_{0\mathrm{S}}^{\mathrm{rot}}}{\partial R_{\mathrm{S},a'x'}}, \qquad (3.21) \\ & \frac{\partial \mathbf{T}_{\mathrm{S0}}^{\mathrm{rot}}}{\partial R_{\mathrm{S},a'x'}} \cdot \mathbf{P}_{\mathrm{quad},a}^{(ij)} \cdot \mathbf{T}_{0\mathrm{S}}^{\mathrm{rot}} + \mathbf{T}_{\mathrm{S0}}^{\mathrm{rot}} \cdot \mathbf{P}_{\mathrm{quad},a}^{(ij)} \cdot \frac{\partial \mathbf{T}_{0\mathrm{S}}^{\mathrm{rot}}}{\partial R_{\mathrm{S},a'x'}} \Bigg\}.\end{aligned}$$

The expression for the derivative of the rotation matrix is given above in Eq. (3.8). Concluding this section, we have successfully included electrostatic interactions with environment point charges into the LVC Hamiltonian.

3.3 Extension of the RESP Fitting Method

For the calculation of the electrostatic interaction in the LVC/MM model shown above, we need to be able to compute the terms in the DME $P_{ap}^{(ij)}$ from an electron density ρ^{ij}. We accomplish that by extending the RESP method[99] introduced in Section 2.5 to yield atomic multipoles.[75] We chose RESP because it is derived to reproduce the molecular ESP, which is precisely the term we are interested in for electrostatic embedding (see Eq. (3.14)). It has been shown that RESP produces more accurate electrostatics compared to other population analysis methods, especially if buried atoms are involved.[50]

In our implementation, we use the PySCF package[116,117] to evaluate $V_{\mathrm{esp}}^{(ij)}$ at all $\mathbf{R}_g$ using Eq. (2.46). The required density matrices $\mathbf{D}^{(ij)}$ are extracted from the same electronic structure calculation at the equilibrium geometry that is used in the LVC parametrization. However, for linear-response methods, only the ground-state density matrix $\mathbf{D}^{(00)}$ and the ground-to-excited-state transition-density matrices $\mathbf{D}^{(0i)}$ ($i > 0$) are readily available. The relaxed excited-state densities $\mathbf{D}^{(ii)}$ ($i > 0$) are obtained from, e.g., the Z-vector approach and require additional computational effort.[118] The excited-to-excited-state transition density matrices $\mathbf{D}^{(ij)}$ ($i, j > 0$) can be approximated[119] as

$$\mathbf{D}^{(ij)} = (\mathbf{D}^{(0i)})^T \cdot \mathbf{D}^{(0j)} - \mathbf{D}^{(0j)} \cdot (\mathbf{D}^{(0i)})^T. \tag{3.22}$$

The above extraction of density matrices necessitates that we transform the basis set information given by the individual program into the standard used in PySCF; this includes the normalization of primitive and contracted Gaussian basis functions, the order of basis functions, and the normalization of the density matrices.

The RESP method[99] can be extended to also obtain higher order multipoles[106] with the following extension. For this, we redefine the matrices used in the system of linear equations from Eq. (2.53) and Eq. (2.52) in terms of the geometric tensor with elements T_{apg} based on the atom and grid positions. First, we define

$$L_{a'p',ap} = \sum_{g}^{G} 2T_{a'p'g}T_{apg}, \tag{3.23}$$

which are the elements of the matrix $\mathbf{L}$ with composite index ap. Second, for each state pair ij, we compute the vector $\mathbf{Y}$ with elements

$$Y_{a'p'}^{(ij)} = 2\sum_{g}^{G} V_{\text{esp}}^{(ij)}(\mathbf{R}_g)T_{a'p'g}. \tag{3.24}$$

Then, we can obtain all DME parameters $\mathbf{P}^{(ij)}$ (i.e., all elements $P_{ap}^{(ij)}$) analogous to Eq. (2.54)

$$\left[\mathbf{L} - \mathbf{1}d\mathbf{F}_{\text{restr.}}(\mathbf{P}^{(ij)})\right]\mathbf{P}^{(ij)} = \mathbf{Y}^{(ij)}, \tag{3.25}$$

where $d\mathbf{F}_{\text{restr.}}(\mathbf{P}^{(ij)})$ is the vector collecting the restraint elements as in Eq. (2.49)

$$dF_{\text{restr.}}(P_{a'}^{(ij)}) = \frac{c_1}{\sqrt{\left(P_{a'}^{(ij)}\right)^2 - {c_2}^2}}. \tag{3.26}$$

The system of linear equations in Eq. (3.25) can be used to fit all orders of the DME at once. In order to recover standard RESP charges, we fit the parameters order by order, i.e. monopoles first, then dipoles, then quadrupoles. In this, each subsequent order is fitted onto the residual ESP of the preceding order. This procedure also allows the restraint parameters c_1 and c_2 to differ for different multipole orders, typically with stronger restraints for higher orders (see discussion in the next paragraph). In addition to the “soft” restraints described above, we utilize “hard” constraints to the DME parameters in our fit procedure. These “hard” constraints ensure that all monopoles sum up to the total molecular charge and that the quadrupoles on each atom are traceless. Traceless quadrupoles are important, as the potential of the trace of a quadrupole is equivalent to a monopolar term. The constraints are added as additional equations to the system of linear equation represented by Eq. (3.25).[120]

Fig. 3.6 demonstrates the effect of different c_1 parameters on the sulfur–water oxygen RDF of thioformaldehyde. It can be seen that the strength of the c_1 parameter 0.0005[99] does not lead to an accurate reproduction of the RDF if applied to all multipole orders. It appears that the restraint parameter has to be increased to prevent overfitting the multipole orders with a larger number of degrees of freedom. For this reason, we set the default c_1 strength to 0.0015 for dipoles and to 0.003 for the quadrupole terms, which lead to the most accurate RDF according to Fig. 3.6 (gray curve). The chosen values align with the base restraint strength scaled by the number of degrees of freedom of each DME order where monopoles have one, dipoles three, and quadrupoles six degrees of freedom.

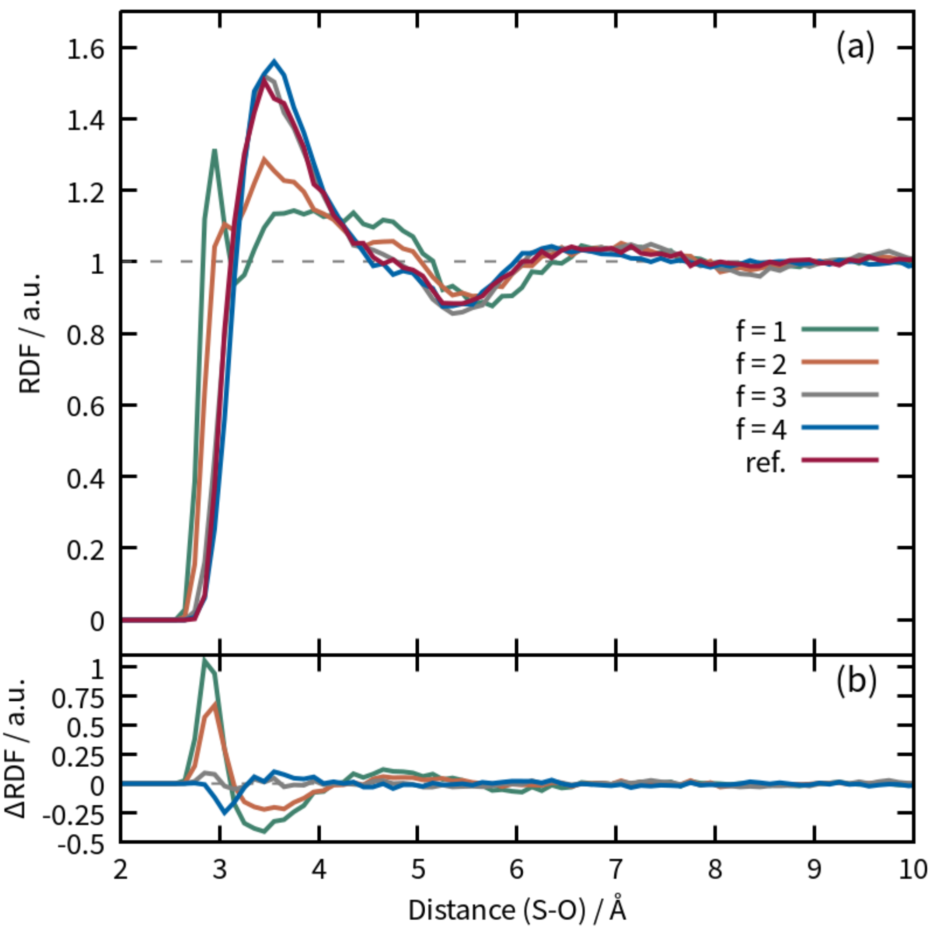

Figure 3.6: **R**adial **D**istribution **F**unctions (RDFs) of waters oxygen (O) atoms around the sulfur (S) atom of thioformaldehyde for different RESP fits (panel a) and their deviations from the reference (panel b). The RDFs stem from a 1 ns QM/MM simulation using SHARC-MD in the S0 state. The different RDFs are evaluated for LVC models with different DME RESP fits and their BP86/def2-SVP reference (red). The base restraint parameter $c_1 = 0.0005$ in the RESP fit is scaled for the dipole term as fc_1 and for the quadrupole terms as $2fc_1$ for the factors $f = 1$ (green), $f = 2$ (orange), $f = 3$ (gray) and $f = 4$ (blue).

3.4 Computational Efficiency of the LVC/MM method in SHARC

In order to analyze solvent dynamics in detail, it is necessary to perform SH dynamics on long time scales with possibly many electronic states and environment atoms on a large set of trajectories (see Section 3.5). For such simulations, both execution time and the amount of data produced impose constraints onto the systems that can be investigated. The performance of the LVC/MM method plays a central role in the realization and feasibility of this enterprise. This section briefly summarizes the additional measures taken to optimize the runtime of LVC/MM single-point calculations, as well as one measure to reduce the amount of data stored. Not included are the already mentioned steps taken to alleviate the file-based communication inside of SHARC and the QM/MM interface (see Section 3.1).

In the process of rewriting the LVC interface into an interface class described above, the internal algorithm to evaluate energies, gradients, and NACs was implemented based on NumPy[121] arrays. This allowed us to move from using Python-based loops in SHARC3.0[108] to highly-optimized and pre-compiled libraries for linear algebra, like BLAS, LAPACK or MKL. The usage of NumPy is known to drastically increase the performance of any code base performing linear algebra operations. This already reduced the execution time by a factor of about six for gas phase calculations.

The next important measure added to the LVC interface is the possibility of calculating an adiabatic subspace of states in the interface, i.e. only the lowest n adiabatic states from $N > n$ diabatic states in the model. In this, the full diabatic Hamiltonian is diagonalized but gradients and NACs are only evaluated for the specified lowest n adiabatic states. Technically, one could also avoid diagonalizing the full Hamiltonian by using a Krylov subspace algorithm such as the Davidson–Liu algorithm[122] to obtain the lowest n states directly; the diagonalization, however does not represent a bottleneck for the number of diabatic states used so far. The subspace evaluation of gradients and NACs is achieved by storing the rectangular transformation matrices between the full diabatic state space and the truncated adiabatic space, and rotating all necessary components in the evaluation of the derivatives beforehand. Without introducing any approximation, this saves additional computational effort in the most demanding parts of the algorithm and also lessens the amount of data that has to be stored on the electronic wave function in the SH algorithm.

For the later discussed system, $[\mathrm{Fe(CN)_4(bipy)}]^{2-}$ in a droplet of 5412 water molecules (Section 5), scans along the different system parameters to gauge the effective scaling of the LVC/MM implementation are performed. For this, the evaluation time of the LVC/MM single points along a short trajectory (25 fs, 50 time steps) are averaged. The reference system included 29 "LVC" atoms, 16236 "MM" atoms and 21 singlet states. Different sets of trajectories are then computed, where (a) the LVC model is altered to include between 22 and all 29 atoms (disregarding physical meaning), (b) the number of water molecules is changed between 500 and 5000 (between 1500 and 15000 atoms), (c) diabatic states from the LVC model are scanned between 1 and all 21 singlet states,[a] and (d) the number of requested adiabatic states is scaled from 1 to 21 states, while using all 21 diabatic states in the LVC model. The results for these scans are shown in Fig. 3.7 in the respective panels. The data sets and linear fits in all panels point to linear scaling, which can be reasoned by analyzing the algorithm behind the LVC method. The panels c and d have two separate linear fits for states values below and above 10, as there are two scaling regimes visible. The most expensive part of the calculation of a single point within the LVC method are obtaining the gradients (Eqs. (3.18)–(3.21)). The evaluation of the gradients includes components with different scaling: (i) the derivative of the geometric tensor T_{abp} with scaling $\mathcal{O}(N_{\text{LVC atoms}} N_{\text{MM atoms}} N_{\text{DME}})$ (Eq. (3.18) and Eq. (3.20)), (ii) the differentiation of the DME terms with scaling $\mathcal{O}(N_{\text{LVC atoms}} N^2_{\text{diabatic states}} N_{\text{DME}})$, (iii) the multiplication and summing of all components of the gradient with scaling $\mathcal{O}(N_{\text{LVC atoms}} N_{\text{MM atoms}} N_{\text{diabatic states}})$, and (iv) the computation of the differentiated vibronic coupling matrix scaling with $\mathcal{O}(N_{\text{LVC atoms}} N^2_{\text{diabatic states}})$. Since Fig. 3.7 indicates linear scaling with respect to the scanned parameters, we conclude that the calculation is dominated by either contribution (i) or (iii). This is the case as (ii) and (iv) scale quadratically with the number of diabatic states

---

[a] the number of adiabatic states in the SH simulation is altered accordingly.

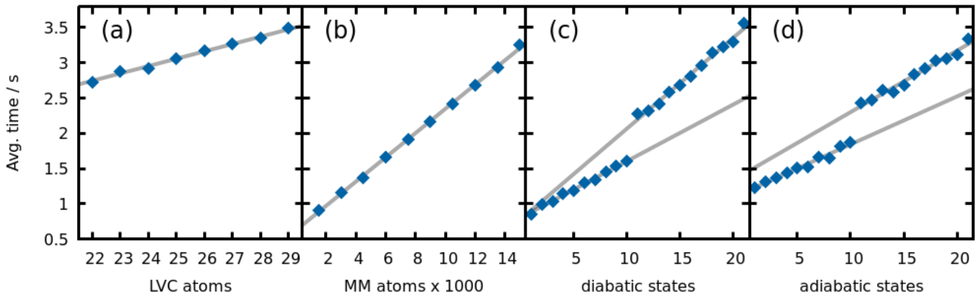

Figure 3.7: Scaling of the LVC/MM implementation in SHARC with respect to different system parameters for $[\mathrm{Fe(CN)_4(bipy)}]^{2-}$ (29 atoms) in water (16236 atoms) and 21 singlet states. Shown are the average execution time (blue squares) of 50 single points calculations (energies, gradients and overlap) with different numbers of LVC atoms (panel a), MM atoms (panel b), diabatic states (panel c), and adiabatic states (panel d); the calculations are performed on a single Intel Xeon E5-2650 v3 CPU. The gray lines indicate linear fits of the measured execution times (blue squares); there are two separate fits for panel c and d or states values below and above 10.

but not the MM atoms, so that $21^2 = 441$ does not exceed 16236. The kink in the execution times at 10 included states for both electronic state scaling plots (panels c and d) can be attributed to a change of regime from being dominated by (i) to (iii) as the number of adiabatic states surpasses the number of terms in the DME ($N_{\mathrm{DME}} = 10$). The execution times in panel c and d are very close to each other after including 10 states, respectively, but differ at a lower number. This can originate from the difference in the number of diabatic states and therefore the execution time of (ii) and (iv).

For the chosen system, the scaling along all parameters is dominated by the algorithms inside the LVC model; the computation with the FF and the embedding logic inside the QM/MM interface are neglected. In the limit of having few LVC atoms and few diabatic states, the execution time will be limited by the computation of the Coulomb forces with the FF; this may be remedied by resorting to the use of graphics processing units in such cases.

Overall, the execution time for the whole system (29 LVC atoms, 16236 MM atoms, and 21 singlet states) of about 3.5 s demonstrates the high efficiency of the implemented LVC/MM method. This efficiency allowed the high number of trajectories and time steps simulated in this thesis. The linear scaling with respect to system size can be maintained for all systems,where $N_{\text{MM atoms}} > N^2_{\text{adiabatic states}}$, which should be the case for most systems.

Another issue arose from the calculation of large solvated systems over long time scales with SHARC:[108] The amount of stored electronic and nuclear data. The nuclear data includes the coordinates and velocities of all atoms in the system. The electronic data includes the Hamiltonian, wave-function overlap, and unitary transformation matrices, as well as the coefficients in different bases. For the discussed $[\mathrm{Fe(CN)_4(bipy)}]^{2-}$ system (Section 5), a single trajectory produces 900 MB per 1000 time steps. This can be partially alleviated by reducing the number of steps recorded. However, as nuclear and electronic properties evolve on different time scales, it can be difficult to find a acceptable compromise between resolution and storage (especially for the electronic data). For large solvated systems the majority of the storage is used for the nuclear data. The electronic data does not scale with system size, and is often needed at a higher temporal resolution than the nuclear data. For this reason, the existing code base of the SHARC driver was altered to allow the generation of two separate binary files containing the electronic and nuclear data at different temporal resolutions.

All the above measures were necessary to be able to perform the large-scale simulations on the $[\mathrm{Fe(CN)_4(bipy)}]^{2-}$ system described in Section 5 and Section A.2.1 in a timely manner and with manageable amounts of data produced

3.5 Generation and Analysis of 3D-SDFs

A partial goal of this thesis lies in the analysis of the structure and dynamics of the solvent around the investigated molecule. This analysis is independent of the method used for the MD simulation and is applicable for systems inside and outside of equilibrium. Commonly, the ensemble of nuclear coordinates resulting from a MD simulation are evaluated with respect to solvation shells in terms of RDFs. RDFs are one-dimensional functions and show the occurrence of a set of atoms of the solvent at different distances from another set of atoms on the solute. Hence, RDFs cannot provide a complete representation of the solvent dynamics occurring during the simulation. A more complete representation may be obtained from a three-dimensional spatial distribution function which shows the frequency of an atom type in a region in space. We will call these functions 3D-SDFs. This section will focus on the generation and analysis of 3D-SDFs, which we published in Ref. 76.

In the simplest case, 3D-SDFs can be obtained as three-dimensional histograms around the solute with voxels as bins. Unlike RDFs, 3D-SDFs are not invariant to the roto-translational motion of the solute and depend on the solutes position and orientation. Assuming a random distribution of samples of nuclear coordinates from the MD simulation, the coordinates have to be aggregated by aligning them. The aggregation of nuclear coordinates from trajectories may be done in (at least) two different ways: The coordinates of the full system can be aligned (i) with respect to the solute at every time step or (ii) at $t = 0$, so that they diverge over time. We refer to the resulting sets of coordinates as the "molecule's perspective" and "solvent's perspective". The molecule's perspective aligns with RDFs and allows analysis of solute–solvent interactions. The solvent's perspective is akin to a fixed and initial frame of reference, from which the absolute motions of solute and solvent can be observed. This perspective gives access to the intrinsic solvent fluctuations in three-dimensional space and the solvent relaxation times.

3D-SDFs are fundamentally a statistical device for the analysis of solvent structures. Their ability to depict the solvent structure strongly depends on the number of data points sampled. If we want to temporally resolve the solvent dynamics, it is necessary to sample every time step sufficiently. Consequently, the question arises how many data points (here, the number of trajectories) are needed to obtain interpretable 3D-SDFs. The estimation of the number of trajectories needed in order to resolve solvent dynamics with a specific spatial resolution via 3D-SDFs will be analyzed here. Inside the volume of a three-dimensional cell V_{cell}, the expectation value of the number of, in this case, water molecules as the number of oxygen (O) atoms can be computed as

$$\langle N_{\mathrm{O\,per\,cell}} \rangle = N_{\mathrm{traj}} \frac{\rho_{\mathrm{water}} N_A V_{\mathrm{cell}}}{M_{\mathrm{water}}}, \tag{3.27}$$

where ρ_{water} is the density of water, N_A is Avogadro's constant, and M_{water} is the molar mass of water. The equation includes the number of trajectories N_{traj}, as the nuclear coordinates of all aligned trajectories can be added. For $V_{\text{cell}} = 0.125\,\text{Å}^3$, at room temperature and for a single trajectory, the expectation value is about 0.0042; the grid cells are much smaller than a water molecule. The standard deviation of this expectation value $\langle N_{\text{O per cell}} \rangle$ arising from density fluctuations[123,124] can be computed as

$$\sigma_{\text{O per cell}} = \sqrt{\frac{k_B T \chi}{V_{\text{cell}} N_{\text{traj}}}} \langle N_{\text{O per cell}} \rangle = \sqrt{k_B T \chi V_{\text{cell}} N_{\text{traj}}} \frac{\rho_{\text{water}} N_A}{M_{\text{water}}}. \tag{3.28}$$

Here, k_B is Boltzmann's constant, T is temperature, and χ is the isothermal compressibility (about $0.45\,\text{GPa}^{-1}$ for water at standard conditions[125]). Fig. 3.8 shows that the macroscopic value of χ is not accurate for the small grid cells used for the histograms; using TIP3P[126] water at standard conditions and $V_{\text{cell}} = 0.125\,\text{Å}$ leads to $\chi = 7.32\,\text{GPa}^{-1}$.

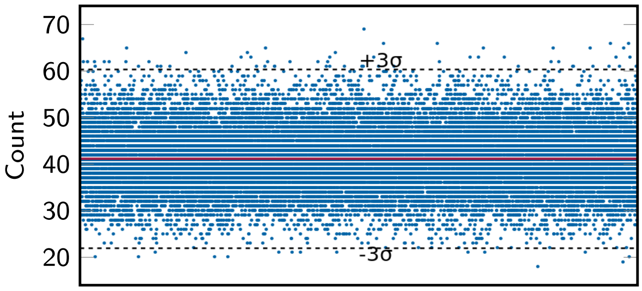

Figure 3.8: 3D histograms counts of a TIP3P water box with grid size 0.5 Å of 10,000 snapshots. The simulations were carried out with AMBER[41] at 300 K and 1 bar with periodic boundary conditions. The mean and standard deviation are $\langle N_{\text{O per cell}} \rangle = 41.10$ and $\sigma_{\text{O per cell}} = 6.40$, respectively (lines indicate μ (red) and $\langle N_{\text{O per cell}} \rangle \pm 3\sigma_{\text{O per cell}}$ (black)). Using Eq. (3.27), the effective isothermal compressibility of TIP3P for the used grid cells is $7.32\,\text{GPa}^{-1}$.

The accuracy of the 3D-SDFs may be estimated from the relative standard deviation:

$$\frac{\sigma_{\text{O per cell}}}{\langle N_{\text{O per cell}} \rangle} = \sqrt{\frac{k_B T \chi}{V_{\text{cell}} N_{\text{traj}}}}. \tag{3.29}$$

This equation shows that the error with respect to the number of particles in a grid cell decreases with the size of the grid cell and the number of trajectories in a simulation. This relation is depicted in Fig. 3.9. It can be recognized that many thousand trajectories are needed if one aims for low relative standard deviation at small grid spacings. Generally, we want to use three-dimensional grid cells with an edge length of 0.5 Å ($V_{\text{cell}} = 0.125\,\text{Å}^3$). This value roughly corresponds to the highest resolutions in contemporary experimental X-ray crystallography.[127,128] Since we do not want to miss out on this spatial resolution, we need to increase the number of trajectories to obtain high quality 3D-SDFs. Now, the question arises which relative standard deviation we should aim for. This question can be answered with Fig. 3.10.

The figure illustrates, at the example of thioformaldehyde, how the chosen isovalue and different numbers of trajectories affect the resolution of features in the

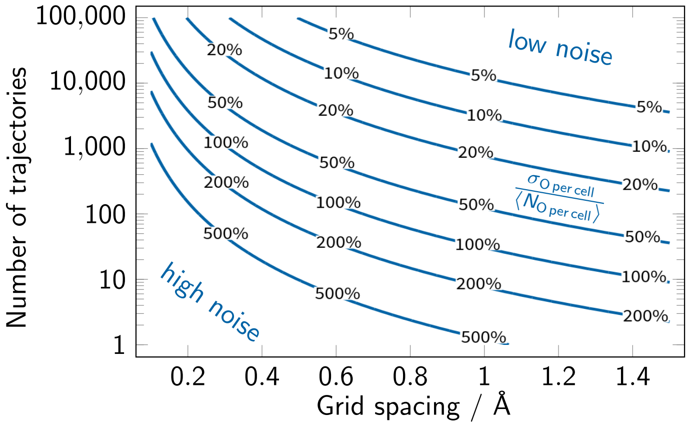

Figure 3.9: Contour plot of $\frac{\sigma_{\mathrm{O\,per\,cell}}}{\langle N_{\mathrm{O\,per\,cell}} \rangle}$ as a function of V_{cell} and N_{traj} for TIP3P at standard conditions and with $\chi = 7.32\,\mathrm{GPa}^{-1}$ (Eq. (3.29)).

solvation shell. Strong features, such as the in-plane hydrogen bonding at the sulfur atom in equilibrium (Fig. 3.10a-d) stay visible, even at low numbers of trajectories. However, weaker features such as the second solvation shell or the out-of-plane hydrogen bonds of thioformaldehyde out of equilibrium in Fig. 3.10e-h are only visible at larger numbers of trajectories or lower isovalues. It is important to recognize at which isovalues (in multiples of the average number of particles) the features appear that one wants to resolve. In principle, this requires one to know the strength of the solvent distribution around the solute and how this strength

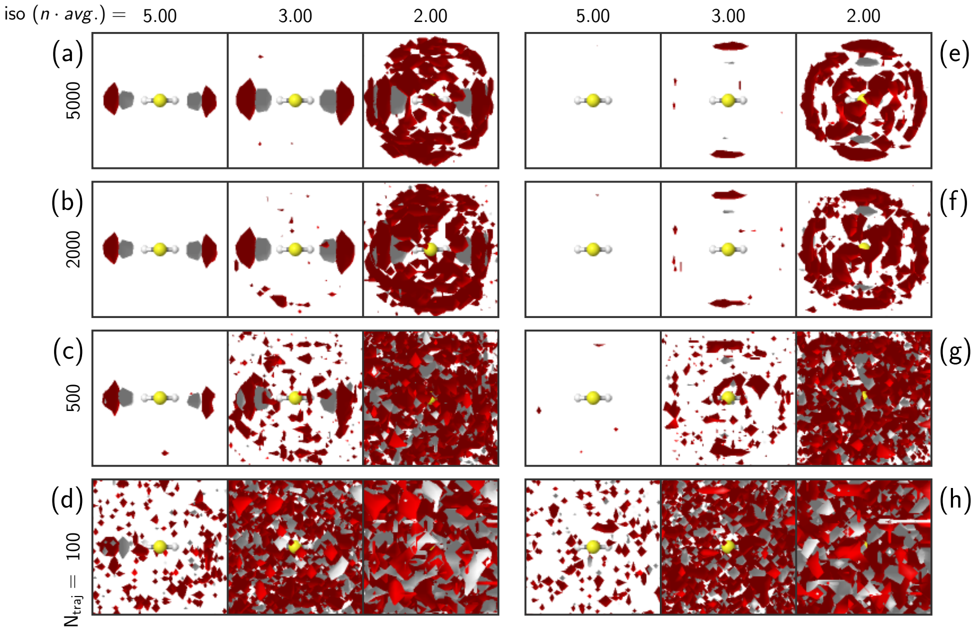

Figure 3.10: Comparison of time-dependent 3D-SDFs around CH_2S the ground state equilibrium (panels a to d) and excited state non-equilibrium (panels e to h) from the molecule's perspective for different isovalues for different numbers of trajectories. The different isovalues are given in multiples of the average number of water oxygen and hydrogen atoms, and the number of trajectories are given on the left of each panel. The distributions of oxygen atoms are shown in red and the hydrogen atoms in gray.

changes during the dynamics. However, as a general rule of thumb, the number of trajectories should be chosen so that

$$C_{\mathrm{iso}} > 3\frac{\sigma_{\mathrm{O\,per\,cell}}}{\langle N_{\mathrm{O\,per\,cell}}\rangle} + 1. \tag{3.30}$$

This means that the chosen isovalue should exceed the average number of solvent atoms by three standard deviations plus one. This ensures that the features visible at the chosen isovalue are significant. This can also be seen in Fig. 3.10: The relative standard deviation for 500 trajectories is about 0.7, so we expect to see noise at relative isovalues that are below $3 \cdot 0.7 = 2.1$ times above the average, i.e. isovalues below 3.1. Indeed, we can see noise appear in the respective panels.

3D-SDFs may not only be constructed from three-dimensional histograms. Alternatively, a 3D-SDF may also be constructed from a **K**ernel **D**ensity **E**stimation (KDE) procedure.[129,130] While being computationally more demanding in its construction than a histogram, a KDE requires less data points to achieve smooth distribution functions. In the analysis done on the $[\mathrm{Fe(CN)_4(bipy)}]^{2-}$ system (see Chapter 5 and Section A.2.1), we used a Gaussian distribution function as kernel for the KDE, which was computed as

$$\mathrm{KDE}(\mathbf{R}_g) = \sum_i^{N_{\mathrm{traj}}}\sum_a^{N_a}\frac{1}{\sqrt{2\pi\sigma^2}}\exp\left(\frac{|\mathbf{R}_g - \mathbf{R}_{ia}|^2}{2\sigma^2}\right). \tag{3.31}$$

Here, the KDE at the Cartesian grid point $\mathbf{R}_g$ is the sum of three-dimensional Gaussian distribution function for all trajectories N_{traj} and all atoms of chosen type in the system N_a with coordinates $\mathbf{R}_{ia}$.

Overall, 3D-SDFs are an important gauge for investigating and visualizing the dynamics of solvents in general. They extend the information obtained from RDFs and can give access to intrinsic properties of solvation shells during dynamics; as they may be constructed from the "molecule's perspective" and the "solvent's perspective". The construction of noise-free 3D-SDFs requires an adequate sampling size, which is the number of trajectories that can be estimated from first principles. However, it can generally be recommended to calculate the isothermal compressibility for the chosen solvent model and grid spacing so that the relative standard deviation can be accurately computed. Unfortunately, this section also shows that many thousand trajectories are generally necessary to obtain noise-free time-dependent 3D-SDFs. Therefore, the efficiency of the method chosen to evaluate the energies and gradients during the simulations is decisive.

4

SIMULATIONS ON SMALL THIOCARBONYLS IN WATER

After establishing the theoretical and methodological framework of LVC/MM in the last two chapters, we will now assess its accuracy and demonstrate its capabilities. Using small thiocarbonyls a test systems, the following sections will show that LVC/MM is both able to reproduce the results of a DFT/MM reference and go beyond the capabilities of standard QM/MM methods in the extent of SH simulations facilitating time-dependent 3D-SDFs. The thiocarbonyls CH_2S and CMe_2S are highly reactive compounds that oligomerize quickly in the gas phase and are short-lived in solution.[131] Despite this, they are suitable test systems, and are used here to validate the LVC/MM method and demonstrate its capabilities. This has three reasons: (i) As the smallest thiocarbonyl, thioformaldehyde (CH_2S) has been already used as a test bed for electronic structure methods and decoherence schemes in SH simulations.[132,133] (ii) The nonadiabatic dynamics of simple thiocarbonyls are governed by their $^1n\pi^*$–$^3\pi\pi^*$ (S_1–T_2) energy gap, which mainly involve orbitals along the C-S bond. This energy gap is too large in the gas phase to allow fast ISC, but can be dynamically modulated by hydrogen bonds (shown in the next section).[75] (iii) Insights from studies on simple thiocarbonyls can help in the analysis of solute-solvent dynamics of larger molecules containing thiocarbonyl groups, such as thionated nucleobase analogues.[134–138]

The following two sections recapitulate investigations on CH_2S and CMe_2S from the publications in Refs. 75 and 76 (see Section A.1). The first section demonstrates that an LVC model for CH_2S is accurate with respect to its TDDFT (BP86/def2-SVP) reference in terms of their generated ESP, energies in gas phase and solution, and most importantly their solvation shells in terms of their sulfur-water oxygen RDF and water 3D-SDFs. The second section highlights how the efficiency of the LVC/MM method can be leveraged to access not only time-dependent RDFs and but also 3D-SDFs (see Section 3.5). The latter give insights into the solvent dynamics that are unobtainable without low-scaling methods such as LVC/MM and reveal drastic differences in the temporal evolution of the solvation shell of both thiocarbonyls. In contrast to the section before, the corresponding LVC models are constructed from complete active-space second-order perturbation theory reference data for which long QM/MM simulations would be computionally immensely demanding.

4.1 Validation and Performance of the LVC/MM Method

CH_2S has four electronic states at low energies (< 3.5 eV) that are relevant for the following results.[132] These are the closed-shell ground state (S_0), the singlet $^1n\pi^*$ state (S_1), the triplet $^3n\pi^*$ state (T_1), and the triplet $^3\pi\pi^*$ state (T_2). The corresponding vertical excitation energies at the gas phase minimum structure are 2.22 eV, 1.96 eV, and 3.44 eV computed with BP86/def2-SVP. These four electronic states arise from different electronic occupations of the n, π, and π^* orbitals located at the sulfur and carbon atoms. The arising ESP from this density is depicted in two planes in Fig. 4.1. The most important details about the ESPs of the dif-

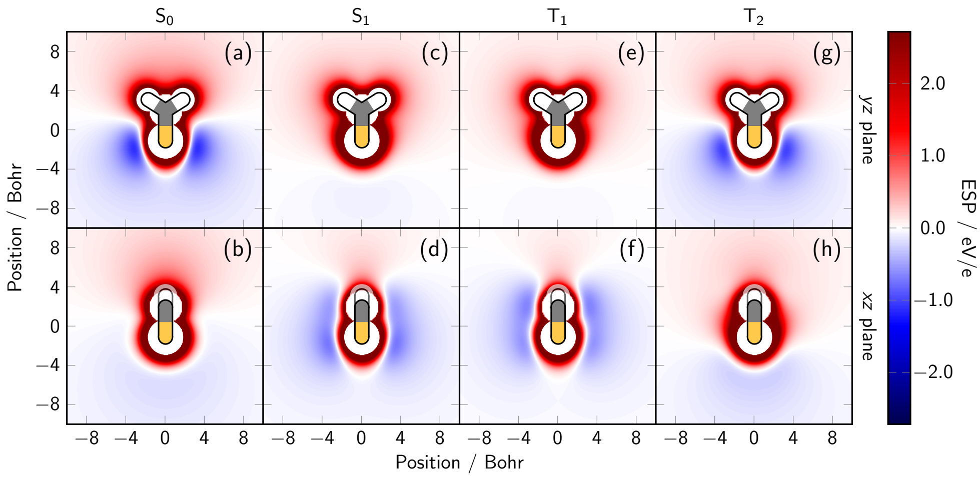

Figure 4.1: Electrostatic potential in the yz and xz planes of the first four excited states of thioformaldehyde for a unit positive charge computed with BP86/def2-SVP.

ferent states are the overall dipole moment along the C-S axis, the minima (blue areas) in the molecular plane for the S_0 and T_2 states, and the minimal out of the molecular plane for the other two states. Generally, it can be recognized that the ESP of the S_0 and T_2 states as well as the S_1 and T_1 states appear almost equal to each other. In order to obtain the correct solvation structure, it is imperative that these features of the ESP can be reproduced with the fitted DME. The overall dipole moment of the molecular can be reproduced by monopoles already (BP86/def2-SVP: 1.57 Debye, monopoles: 1.62 Debye). However, only the inclusion quadrupolar terms can produce anisotropic minima in the molecular plane for the S_0 state.

The ESP generated by an electronic state (computed from Eq. (2.41)) is always positive in the vicinity of the nuclei and can be negative at further away as can be seen from Fig. 4.1. This behavior cannot be reproduced by a DME: The ESP produced by the the point-multipoles on an atom, cannot radially change sign, i.e. on a straight line pointing away from the atom. Fortunately, atoms cannot come close enough to penetrate deeply into the electron density due to Pauli repulsion. This means that the ESP in the vicinity of the nuclei is less important for accurate results in MD simulations. The Pauli repulsion is represented in FF simulations by the Lennard-Jones potential; this induces a repulsive potential that is dominant around the nuclei. Tab. 4.1 shows the **M**ean **A**bsolute **D**eviation (MAD) and **R**oot-**M**ean-**S**quare **D**eviation (RMSD) of for a grid with 6482 grid points between 1.0 and 2.5 times the vdW radii which is different from the grid used for the fit. The label “LJ weighted” indicates that the deviation from the reference at each point are Boltzmann weighted (at 300 K) corresponding to the Lennard-Jones interaction energy of a hydrogen atom at the grid point position. Compared to the unweighted analysis, with MADs of about 80 meV and RMSDs of about 150–180 meV, the Boltzmann-weighted analysis shows significantly better results, with MADs of about 10 meV and RMSDs of about 15 meV. All four electronic states can be reproduced at approximately the same accuracy. This attests to the ability of the DME representation to accurately reproduce the reference ESP around the molecule.

Next, we compare the results of 1 ns MD trajectories in the S_0 state computed with DFT/MM and LVC/MM with DME. The computations used TIP3P water[126]

Table 4.1: **M**ean **A**bsolute **D**eviation (MAD) and **R**oot-**M**ean-**S**quare **D**eviation (RMSD) of the fitted DME of CH_2S with respect to the BP86/def2-SVP reference of the distributions 6482 grid points between 1.0 and 2.5 time the vdW radii in eV.

	unweighted		LJ weighted	
	MAD	RMSD	MAD	RMSD
S_0	0.075	0.148	0.008	0.014
S_1	0.082	0.180	0.008	0.013
T_1	0.080	0.179	0.007	0.013
T_2	0.080	0.151	0.009	0.016

and GAFF2[139] parameters for CH_2S. During the simulations, the water sphere that extends about 15 Å in every direction from the solute is stabilized with a droplet potential[140] and the solute is kept in the center with a harmonic restraint. After an equilibration time of 50 ps, 9502 snapshots are taken from the remaining 950 ps of each trajectory. From these ensembles, we computed S-O RDFs and 3D-SDF of water which can be seen in Fig. 4.2. Starting with the DFT/MM reference in panel (a), we can see that around CH_2S there are two regions with increased hydrogen and oxygen atom counts. These regions are located in the yz molecular plane around the sulfur atom. This finding indicates the formation of hydrogen bonds in the molecular plane. The positions of the hydrogen bonds coincide with the minima in the ESP of the S_0 state from Fig. 4.1. We follow from this that the lone pair at the sulfur atom is responsible for these hydrogen bonds, which are well-known for carbonyls.[141,142] This finding shows how anisotropic the solvation shell around CH_2S is.

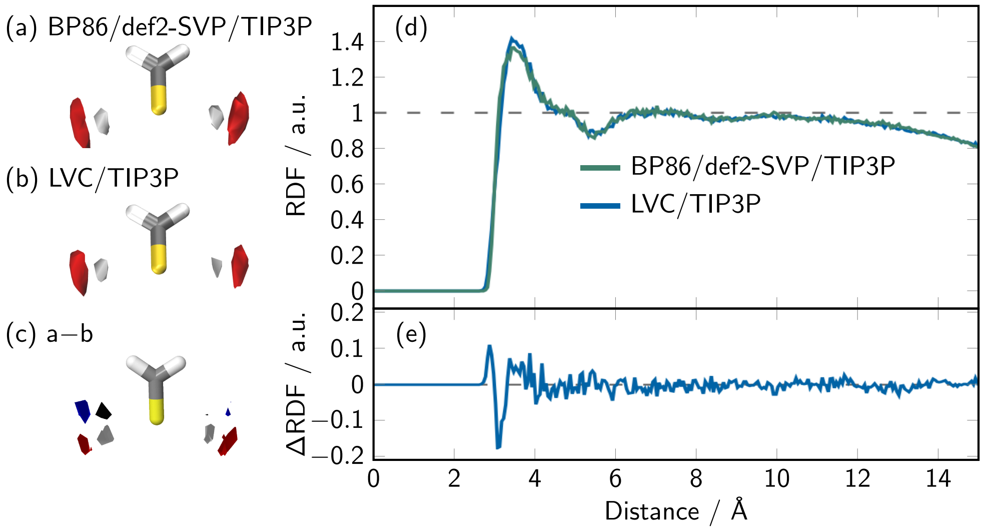

Figure 4.2: Solvent distribution of water around thioformaldehyde. Panels (a) and (b) show **T**hree-**D**imensional **S**patial **D**istribution **F**unctions (3D-SDFs) (grid spacing 0.5 Å) of water H (gray) and O atoms (red); the isovalue is three times the average density in the box, for the DFT reference and LVC; panel (c) shows the difference between the 3D-SDFs between (a) and (b) at 1.5 times the average density (negative deviations are blue for O atoms and black for H atoms). Panel (d) shows the **R**adial **D**istribution **F**unction (RDF) of water O atoms around the S atom with BP86/def2-SVP/TIP3P(green) and LVC/TIP3P (blue); panel (e) shows their difference.

Fig. 4.2b shows a distribution of hydrogen and oxygen atoms compared to the reference in panel a. The inclusion of quadrupole terms in the DME reproduce the anisotropic minima in the ESP (Fig. 4.1) which result in the in-plane hydrogen bonds. Even though there the 3D-SDFs are in good agreement visually, there are still a few differences. The hydrogen bonds in panel a are slightly stronger (with higher maximum occurrence) and are at an angle of 110° with the S-C bond, whereas in panel d the hydrogen bonds are closer to an 90° angle (Fig. 4.2c). Fig. 4.2d-e compare the RDFs of water oxygen atoms around the sulfur atom. Here, the DFT/MM reference (blue) and LVC/MM (green) are in close agreement. Both RDFs start to decrease after 12 Å due to the finite droplet used. We can conclude from the results above that the accuracy of the ESP exerted by the DME, also leads to an accurate reproduction of the solvation shell, especially in this strongly anisotropic case.

Lastly, we compare the energies of the four electronic states computed with TDDFT/MM and LVC/MM at each of the 9502 snapshots of the DFT/MM trajectory. The results are collected in Fig. 4.3. Panel a establishes the reference results and shows the difference between the results for the molecule surrounded by point charges and in the gas phase at the same geometry. Hence, this plot depicts the energy shifts induced by the electrostatic interaction with the environment, which we will refer to as solvent shift. It can be recognized that both the S_0 and T_2 states are shifted towards lower energies by a similar margin (−0.30 eV and −0.26 eV), while the S_1 and T_1 states are much less affected. Reason for this are the similar ESPs of the S_0 and T_2 states (see Fig. 4.1) The corresponding results of the LVC/MM model are depicted in panel b and paint a very similar picture. The general trends of the solvation shifts are reproduced, with strong shifts for the S_0 and T_2 states and little effect on the S_1 and T_1 states. There are however slight differences, especially that the energy shifts of the S_0 and T_2 states are systematically smaller than the reference. This aligns with the observations above that the DME result in slightly weaker hydrogen bonds. Panels c and d give more quantitative information on this difference, where we compare the two methods directly. Panel c shows the difference in the gas phase energies, where the agreement is excellent with errors below 0.02 eV (0.5 kcal/mol). However, panel d displays the difference between the calculations that included point charges and we can see the exact error of LVC/MM that appear by comparing panel a and b. The energies of all electronic states are underestimated by about 0.05±0.04 eV (1−2 kcal/mol). Fortunately, systematic shifts in the energy of all states should not influence the results of the dynamics. Hence, the dynamics should be influenced by the residual error of about 1 kcal/mol. This is typically a desirable accuracy in the computation of electronic energies.

In total, this section showed that the LVC/MM model can reproduce the results of an ab-initio reference to a satisfactory degree. The inclusion of quadrupolar terms recovers anisotropic minima in the ESP which are needed do describe the hydrogen bonding in thiocarbonyl bonds. Both the RDF and 3D-SDF of the ground state are recovered and the corresponding shifts in the electronic state energies are in close agreement. Due to the computational efficiency of the LVC/MM model (see Section 3.4), the nanosecond-long ground-state trajectory was computed more than ten times faster than the DFT/MM reference.[75]

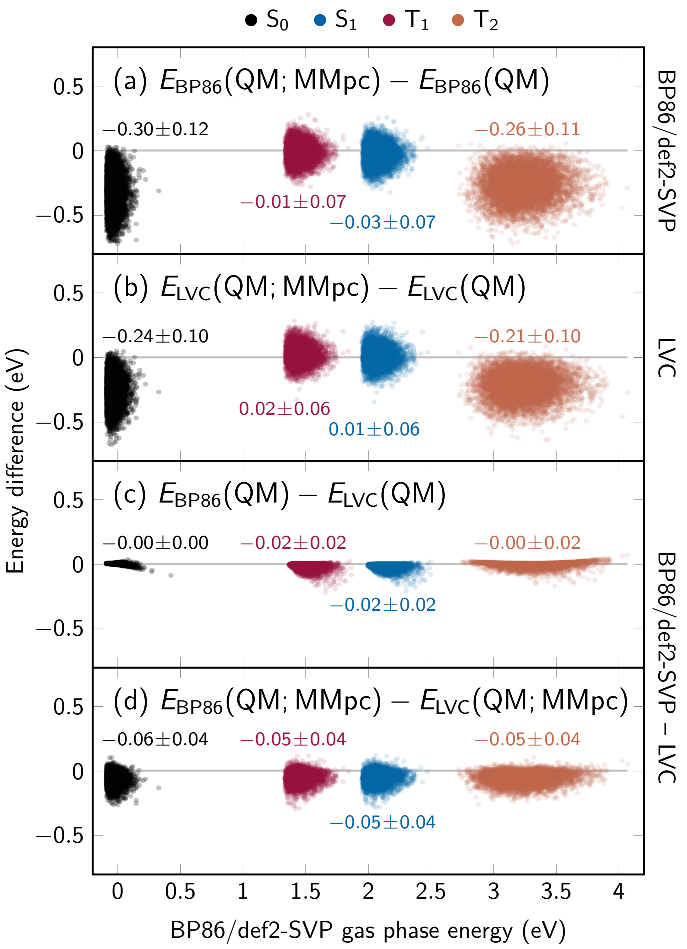

Figure 4.3: Scatter plots of energy differences computed at 9502 geometries. (a) Energy difference between BP86 calculation including point charges E_{BP86}(QM;MMpc) and BP86 without MM charges E_{BP86}(QM), i.e., electronic solvent stabilization energy. (b) Analogous energy difference using LVC-DME2/MM. (c) Energy difference between BP86 and LVC without MM charges, i.e., gas-phase agreement between the methods. (d) Energy difference between BP86/MM and LVC-DME2/MM, i.e., solution-phase agreement. The states are color-coded as S_0 (black), S_1 (blue), T_1 (red), and T_2 (orange). The mean values with standard deviations are included for each distribution (all in eV).

4.2 Time-Dependent Three-Dimensional Solute–Solvent Dynamics

The LVC/MM model was validated against its reference in the section before. Now, we can demonstrate the full capabilities of the method. We used the procedure from above to generate 9500 initial conditions, so that we can launch that many trajectories and use them to resolve the time-dependent solvation shells via 3D-SDFs. To the best of our knowledge, this has never been done before in nonadiabatic dynamics. For this following section, we used a complete active-space second-order perturbation theory reference for the parametrization of LVC models for CH_2S and CMe_2S. The latter molecule can be seen as a heavier analog with roughly equivalent electronic structure with the first four excited states majorly involving the orbitals at the S-C bond. However, CMe_2S has a much higher steric extent due to its methyl groups. As we will show in this section, this has drastic effects on the behavior of the solvation shell especially in the 3D-SDFs.

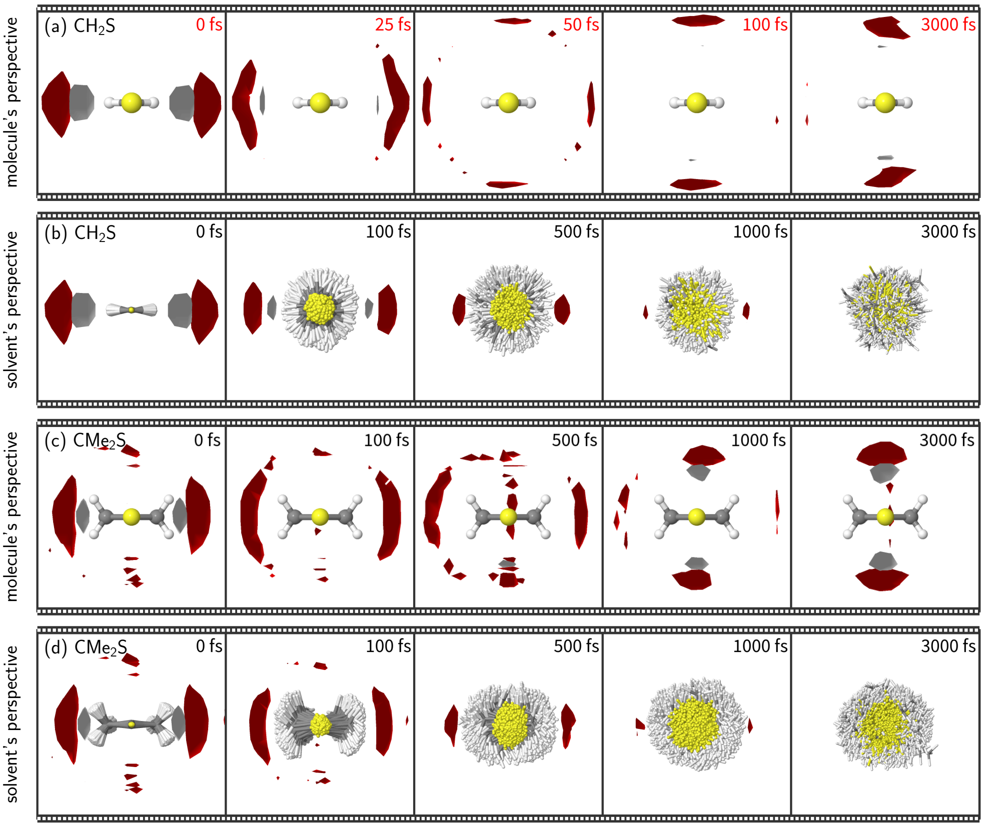
molecule's perspective
(a) CH₂S
0 fs
25 fs
50 fs
100 fs
3000 fs
solvent's perspective
(b) CH₂S
0 fs
100 fs
500 fs
1000 fs
3000 fs
molecule's perspective
(c) CMe₂S
0 fs
100 fs
500 fs
1000 fs
3000 fs
solvent's perspective
(d) CMe₂S
0 fs
100 fs
500 fs
1000 fs
3000 fs

Figure 4.4: Time-resolved **T**hree-**D**imensional **S**patial **D**istribution **F**unctions (3D-SDFs) of water H and O atom occurrences around (a,b) CH_2S and (c,d) CMe_2S. The solvent dynamics is displayed in two different ways, from the (a,c) molecule's perspective and (b,d) from the solvent's perspective (see Section 3.5). In (a,c) all snapshots are aligned to the ground state equilibrium of the respective solute molecule which is depicted. The gray and red regions indicate H and O occurrences with an isovalue of $3N_\text{traj}\langle N_\text{O per cell}\rangle$. Note that in (a) different points in time are shown than in the other panels, because the solvent dynamics around CH_2S in the molecule's perspective has a much shorter timescale than the ones in the other panels, as discussed in the text.

In order to investigate the time-dependent reaction of the solvation shell due to a change in electronic state, we excited all 9500 trajectories from the S_0 state to the S_1. For both thiocarbonyls, the trajectories are propagated for 3000 fs. The resulting coordinates are aggregated as described in Section 3.5 to obtain not only time-dependent RDFs but also 3D-SDFs in both the molecule's and solvent's perspective. The constructed time-dependent 3D-SDFs are shown in Fig. 4.4. We start by looking the panel a and b for time 0 fs. Here, we see the 3D-SDFs indicating hydrogen bonding in the molecular plane mentioned before. Note that the distributions are exactly the same in both perspectives by construction. We can now compare this to the results of CMe_2S in panels c and d. Here, we also find the in-plane hydrogen bonds. However, they appear weaker and the calculated RDF also shows that they are further away from the sulfur atoms due to the methyl groups. There is also a weaker distribution of oxygen atoms behind the methyl groups orthogonal to the molecular plane.

Now that we have quickly described the solvation shell of the ground state equilibrium present at 0 fs, we can analyse the time-dependent reaction of this solvation shell to the change in electronic state. As a reminder, the S_1 state is characterized by a n-π^* excitation and two minima in the ESP at the sulfur atom orthogonal to the molecular plane. From the molecule's perspective in panel a, we can see that the solvation shell adapts to this new state within roughly 100 fs, establishing out-of-plane hydrogen bonds. These do not change drastically between 100 fs and 3000 fs, and appear to be weaker compared to the ground state. The reason for this exceptionally fast solvent relaxation can be found in panel b displaying the solutes perspective. We see that the solute coordinates quickly diverge from each other within 100 fs; this especially is the case for the hydrogen atoms. In contrast to panel a, the solvent distribution stays in place and weakens with time. An analysis of the angular distribution of the molecular plane revealed that CH_2S is able to relax its solvation shell by rotating around the S-C axis. After the rotation, the solvent distribution established in the ground state is able to stabilize the excited state. For CMe_2S, we see a very similar picture in panel d. The solvent distribution gets weaker over time, but the solute coordinates do not diverge as quickly and a rotation of the solute is not observed. This is due to the steric hindrance introduced by the methyl groups. From the molecule's perspective in panel c, we see the effect of this. The relaxation of the solvation shell takes much longer, the out-of-plane hydrogen bonds to establish later and remnants of the in-plane oxygen distributions can still be seen after 1000 fs. Analysis of the time scales using SVD of the water oxygen distributions quantify the above described findings: The solvation shells evolve on similar time scales for both molecules in the solvent's perspective; a bi-exponential fit of the first SVD component shows 38 fs and 866 fs for CH_2S, and 50 fs and 947 fs for CMe_2S. These time scales also agree well with experimentally measured libration and relaxation of water.[11,16,21,143] However, the time scales obtained for the same analysis in the molecule's perspective differ drastically; 22 fs for CH_2S, and 5 fs and 360 fs for CMe_2S.

The above analysis for the comparably simple thiocarbonyls shows that temporally resolved 3D-SDFs hold valuable information of the excited-state dynamics of the solute and solvent, which cannot be obtained through RDFs. The analysis from both the molecule's and solvent's perspective revealed an unexpected relaxation mechanism for the smaller CH_2S. This kind of detailed picture can only be obtained from the generation of many data points facilitated by the efficiency of LVC/MM. For the system discussed in the next chapter, this efficiency is even more essential.

5

APPLICATION TO AN IRON COMPLEX IN WATER

In this chapter, we apply LVC/MM to an iron(II) complex in water in order to resolve the dynamical response of the solvation shell to photo-excitation in three dimensions and over long time scales. Transition metal clusters—prominently of 4d and 5d metals and recently also 3d metals—find applications in medicine, catalysis and energy conversion.[74,144–148] Complexes with 4d/5d metals have long lived **M**etal to **L**igand **C**harge **T**ransfer (MLCT) states, extending to nano- to microsecond lifetimes in ruthenium(II)-poly-pyridyl complexes.[149,150] By contrast, in similar iron(II) complexes, the MLCT population is quenched typically via **M**etal-**C**entered (MC) states within femtoseconds.[21,151,152] This is caused by smaller d-orbital splitting in 3d metals compared to 4d/5d metals which leads to low-lying MC states that quickly drain the MLCT population.[144,153] The complex investigated here, $[\mathrm{Fe(CN)_4(bipy)}]^{2-}$, has a particularly strong ligand field introduced by the cyano and bipyridyl ligands, and high charge, which destabilizes the MC states against the MLCT states.[153] The complex is an interesting system (i) to investigate the influence of combining σ-donating and π-accepting ligands to increase the lifetime of MLCT states,[154–156] (ii) to observe a potentially meta-stable MC state in experiments,[153] and (iii) to additionally gauge the influence of the solvent on the lifetimes of both MC and MLCT states.[24,59,153] The solvent has a considerable effect on the dynamics of $[\mathrm{Fe(CN)_4(bipy)}]^{2-}$ as the MLCT populations is quenched in less than 200 fs in water[24,153] but has lifetimes of multiple picoseconds in dimethyl sulfoxide.[157,158]

A previous collaboration of members in our group simulated the excited-state dynamics of $[\mathrm{Fe(CN)_4(bipy)}]^{2-}$ in water for 700 fs using QM/MM together with SHARC.[56,108] These simulations helped disentangling the dynamics observed by experiments in terms of electronic populations, as well as nuclear solute and solvent degrees of freedom, and provided corresponding time constants.[59] By using a fit onto a kinetic model, the authors found that the initial singlet MLCT population bifurcates within 210 ± 20 fs into the MLCT and MC triplet states via ISC. The lifetimes of the both triplet manifolds were found to be 2.2 ± 1.5 and 6.9^{+13}_{-5} ps. The high uncertainty of these two lifetimes results from the small number of trajectories that underwent these pathways and the simulation time that is much smaller than the determined lifetimes. The authors also investigated the coupled solute–solvent response via time-dependent RDFs. Their results indicate that SHARC simulations on longer time scales and with more trajectories can be beneficial to resolve the long term dynamics and the different contributions of the coupled solute–solvent response. The following two sections will first present our investigation and most important findings (for the full manuscript see Section A.2.1), and then compare these findings with the results from Ref. 59.

5.1 LVC/MM SHARC Dynamics and Solvent Reorganisation

We investigate the excited state dynamics of $[\mathrm{Fe(CN)_4(bipy)}]^{2-}$ in water by simulating a swarm of 4473 SHARC trajectories using an LVC/MM model for 5000 fs.

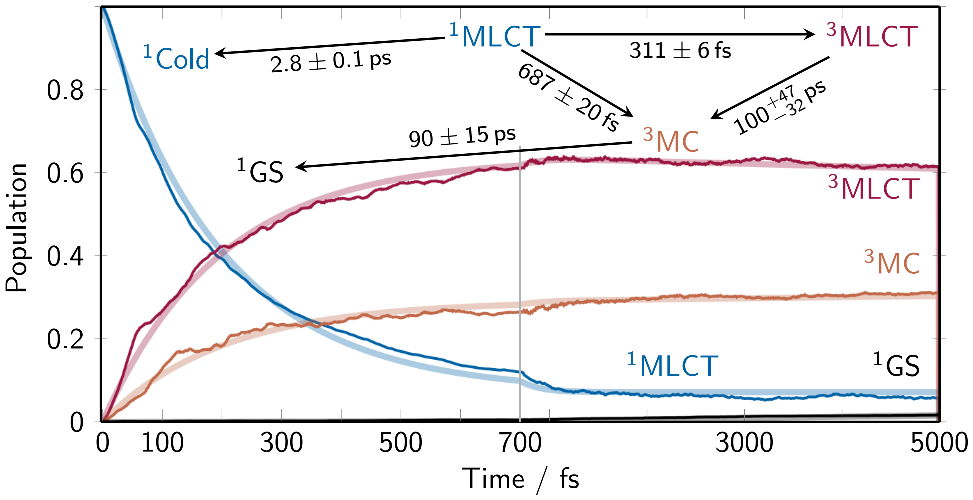

Figure 5.1: Dynamics of the electronic populations during the simulation. Time-dependent diabatic populations (thin lines) for the ground state (GS) in black, the ^{1}MLCT states that was excited into in blue, the ^{3}MC states in orange, and the ^{3}MLCT states comprising all other triplet states (majorly MLCT character) in red. The thick lines indicate the global fitting results from the shown kinetic model; the given time constants and uncertainties are obtained from a bootstrapping procedure.[159]

In addition to electronic populations, time-dependent RDFs and bond length distributions, we extend the analysis with 3D-SDFs and time-dependent hydrogen bond counts. We find similar electronic populations, time-dependent solute bond lengths and RDFs as the previous work[59] at a fraction of the computational cost. This section only briefly presents the most important results on the simulated excited-state dynamics of $[Fe(CN)_4(bipy)]^{2-}$ in water using LVC/MM. The full description of our preliminary findings, all computational details and additional analyses can be found in the manuscript draft in Section A.2.1 and corresponding supporting information.

Before discussing the most important results, it should be noted that the parametrization of the LVC/MM model for $[Fe(CN)_4(bipy)]^{2-}$ includes two novelties: (i) the inclusion of state-specific frequency shifts in the form of $\gamma_{kk}^{(ii)}$ parameters (Section 2.3) for all MC states and normal modes that affect the equatorial Fe–ligand distances (discussed in Section 6.4 and in Section A.2.1), and (ii) the inclusion of the polarizability of water solvent molecules due to their electron densities through implicit solvation (dielectric constant set to $\varepsilon_r = 1.7689$) to alleviate problems with low-lying excited states and avoid doubly counting solvent effects (discussed in Section 6.2, Section 6.5 and Section A.2.1). The inclusion of the $\gamma_{kk}^{(ii)}$ parameters significantly improved the accuracy of the MC states in the gas phase compared to the reference. Further details can be found in the sections mentioned above and will not be discussed here for brevity.

After preparing 30,000 initial conditions in a procedure similar to Ref. 59, we were able to excite 4473 initial conditions in a window between 487 nm to 497 nm (around 2.52 eV) centered on the peak of the first absorption band; from them 4366 initial conditions (97.6%) are excited into the adiabatic S_3 state, which has MLCT character. We proceeded to propagate all 4473 initial conditions for 5000 fs with LVC/MM SHARC.

The dynamics of the diabatic populations can be seen in Fig. 5.1. The total singlet population depletes quickly with a time constant $\tau = 210 \pm 4$ fs from the ^{1}MLCT states (see Section. A.2.1); no ^{1}MC population is observed during the dynamics. The terminal singlet population of about 6% is found to mostly stem from the adiabatic S_1 state; a "cold" singlet state is added to the kinetic model to account for that. Via ISC, the electronic population bifurcates into ^{3}MC states and the other triplet states with dominantly MLCT character. The ^{3}MC population reaches a final value of about 32% with a trend to increase; the other triplet states reach a final population of 62% with a decreasing trend; yet we determined that the major dynamics have concluded and did not extend the propagation. The ground-state singlet is slowly populated over time. The proposed kinetic model in Fig. 5.1 is used to evaluate time constants for the population dynamics. The bifurcation into the MLCT and MC triplet manifolds occurs with time constants of 311 ± 6 fs and 687 ± 20 fs, respectively, and the states are populated with a ratio of about 2.2/1. The aforementioned "cold" singlet population, labelled as ^{1}Cold, is populated slowly with a constant of about 2.8 ps. The fitted time constant of the internal conversion from the ^{3}MLCT to the ^{3}MC with about 100 ps far exceeds the simulated time which leads to large uncertainty values. Similarly, the radiationless relaxation into the ground state from the ^{3}MC is on the same time scale. The final populations at $t = 5$ ps are 62% ^{3}MLCT, 31% ^{3}MC, 6% ^{1}MLCT, and 2% ground state.

The dynamics of the electronic states and the solvation structure mutually affect each other. As the exerted electrostatic potential of an electronic state interacts with the solvent molecules, they are attracted or repelled to or from different sites at the molecule and in turn stabilize or destabilize different electronic states. This interplay of the population dynamics of Fig. 5.1 can be recognized in the time-dependent three-dimensional solvation shells displayed in Fig. 5.2.

At $t = 0$, a strong solvation shell surrounding the cyanide ligands is visible which forms rings around the nitrogen atoms; the features around the axial cyanide ligands are more extensive and reach towards the nitrogen atoms on the bipyridyl ligand. As expected from an aromatic system, the 3D-SDFs do not indicate a strong hydrogen bonds or other features in the solvation shell at the bipyridyl carbon atoms as expected from an aromatic system, which can also be seen in the corresponding RDF in Fig. 4a in Section A.2.1.

After 100 fs, the solvation shell is diminished around all nitrogen atoms, particularly in the vicinity of the bipyridyl ligand; at the equatorial cyanide ligands, this decrease is only observable on the outward-facing side. Additionally, the oxygen atom occurrence is visibly increased above the center of the bipyridyl ligand (see respective image in Fig. 5.2c). This inertial response/libration motion is triggered by the initial repulsion of the hydrogen atoms due to the change in partial charge at the cyanide nitrogen atoms. Consistent with time scales from experiments for such responses,[11,12] a mono-exponential fit on the first SVD component of the Δ3D-SDFs results in a time constant of 75 fs. Analysis on corresponding time-dependent difference RDFs lead to a similar time constant, which confirms this result.

After 500 and 1000 fs, the solvation shell surrounding the equatorial cyanide ligands is further reduced. The initial increase in oxygen atom occurrence at the bipyridyl nitrogen sites diminishes after 500 fs. In the same time frame, the stable ^{3}MLCT population leads to a subsequent increase in oxygen occurrence observed above and below the para-carbon atoms of the bipyridyl ligand. Towards the end

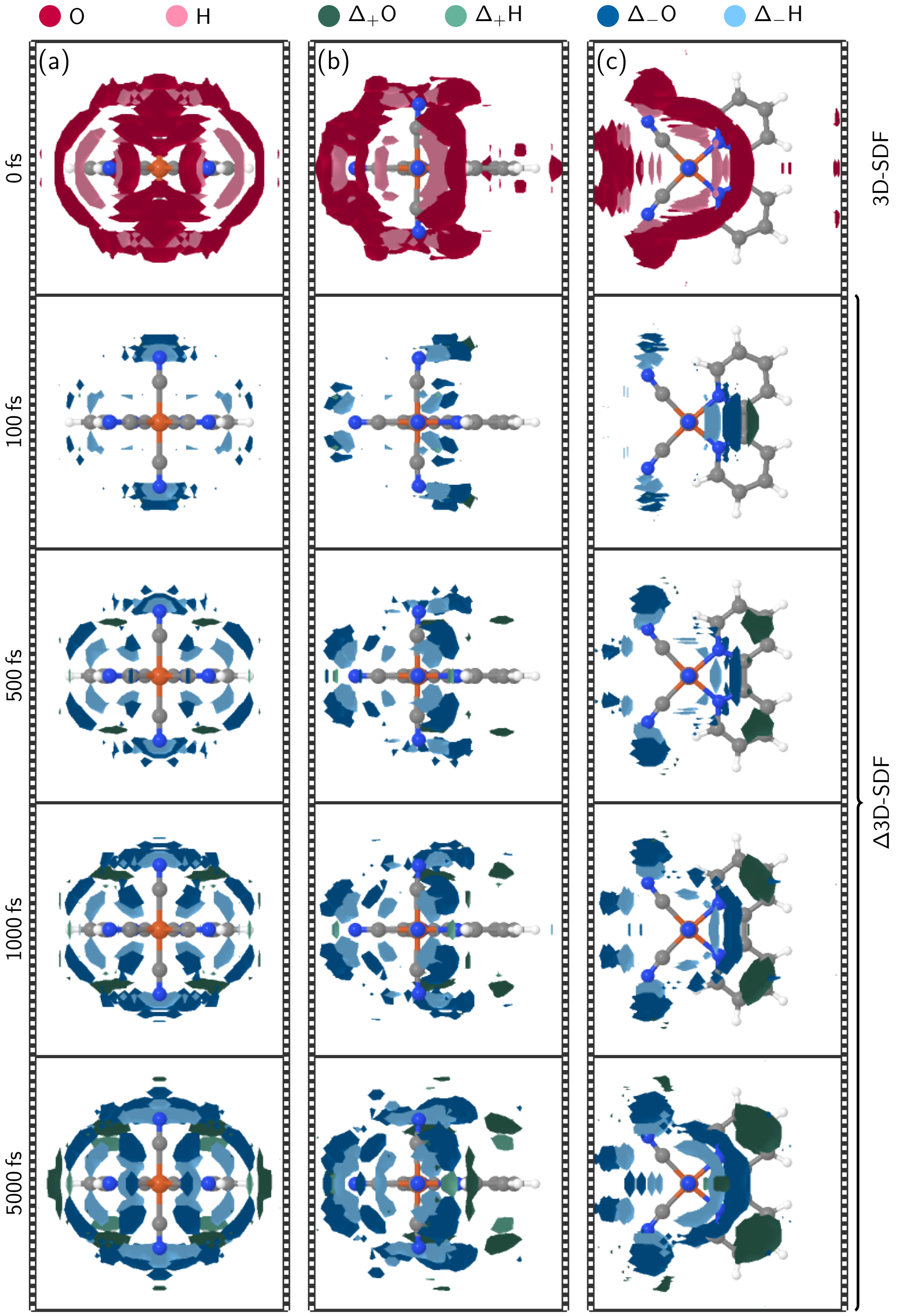
O
H
Δ_+O
Δ_+H
Δ_-O
Δ_-H
(a)
(b)
(c)
0 fs
100 fs
500 fs
1000 fs
5000 fs
3D-SDF
Δ3D-SDF

Figure 5.2: Symmetry adapted three-dimensional solvent distribution functions (3D-SDFs) of water oxygen and hydrogen atoms at $t = 0$ fs and difference 3D-SDFs thereafter. In all panels at $t = 0$ fs, spatial regions with an occurrence higher than 2.5 times the average are colored red for oxygen atoms and pink for hydrogen atoms. For the Δ3D-SDFs ($t > 0$ fs), the iso value is set to 0.5 times the average; positive deviations are colored with green colors and negative deviations with blue colors with oxygens in the darker and hydrogens in the lighter shade. Panels (a-c) show different different orientations of the system.

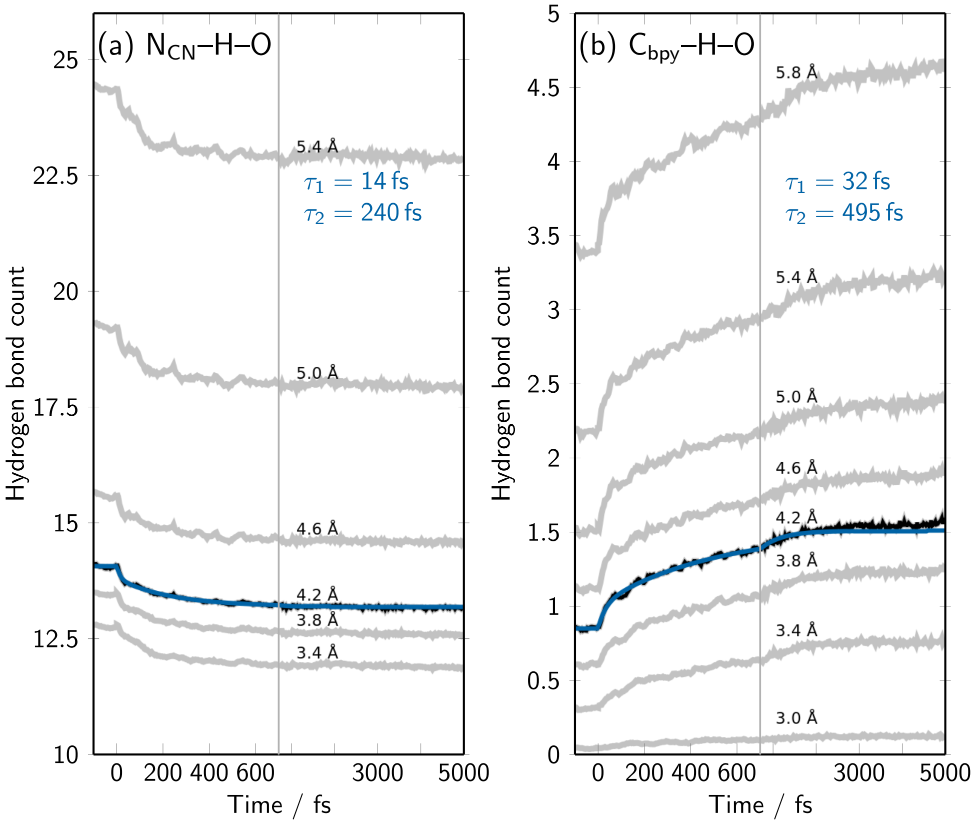

Figure 5.3: Time-dependent hydrogen bond counts averaged over all 4473 trajectories determined from geometric criteria scanned over the distance cutoff; the angular cutoff is kept at 135°. Panel (a) shows the hydrogen bond counts for the cyanide nitrogen atoms and panel (b) the counts for the bipyridyl carbon atoms. A bi-exponential fit (blue line) for the first curve showing a libration response, which is indicated by a drastic change at $t = 0$ fs, (black curve) results in the two time constants given in the plot.

of the simulation, these trends continue at a slower pace so that the established solvation structure is intensified.

Investigation on the time-dependent difference RDF of the bipyridyl carbon and water hydrogen pair shows an oscillation with 378 cm^{-1} after the initial increase. This frequency matches the frequency of the bipyridyl ring-ring stretch mode that stretches both rings outward parallel to their connecting bond and has been simulated in Ref. 59. We expect that this oscillation solely stems from the solute vibration and not from an oscillation in the solvation shell, as this feature is not visible in the 3D-SDFs. This expectation is additionally confirmed by analyzing the time-dependent behavior of slices originating from the bipyridyl feature in the 3D-SDFs (see supporting information in Section A.2.1), in which no such oscillation is recognizable.

Fig. 5.3 shows time-dependent hydrogen bond counts for N$_{CN}$ and C$_{bpy}$. The overall hydrogen bond counts at both sites are drastically different with N$_{CN}$ having a count that is about ten times higher than C$_{bpy}$. The results confirm the visible changes in the 3D-SDFs and show a fast initial response leading to a decrease in N$_{CN}$–H–O counts and an increase C$_{bpy}$–H–O counts; the latter increase is continued further at a slower pace. Bi-exponential fits of the curves with a cutoff of 4.2 Å result in respective time constants of $\tau_1(\mathrm{N_{CN}}) = 14$ fs and $\tau_1(\mathrm{C_{bpy}}) = 240$ fs

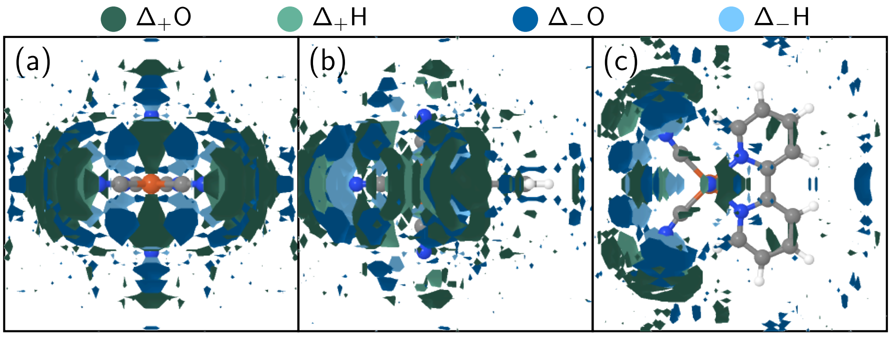

Figure 5.4: Deviations of in the three-dimensional spatial distribution function for a subset of trajectories with dominant ^{3}MC at $t = 5000$ fs in comparison with the ground-state equilibrium from three different perspectives. The used subset of trajectories had a stable population in the ^{3}MC states of at least 76% for the last 1000 fs. In all panels spatial regions with an occurrence deviating more than 0.5 times the average are colored shown for oxygen atoms and pink for hydrogen atoms; positive deviations are colored with green colors and negative deviations with blue colors with oxygens in the darker and hydrogens in the lighter shade.

for the initial response and $\tau_2(\mathrm{N_{CN}}) = 132$ fs and $\tau_2(\mathrm{C_{bpy}}) = 495$ fs for the secondary response; this cutoff value was chosen because the curves show a drastic change at $t = 0$ fs showing the libration motion of the water molecules. The established hydrogen bonds at the $\mathrm{C_{bpy}}$ atoms represent a stark increase with respect to the ground state and are expected to stabilize the long-lived the MLCT states further. This reasoning is additionally strengthened by constructing the 3D-SDF at $t = 5000$ fs from a subset of the trajectories that are dominantly in the ^{3}MC states. This subset of trajectories is confirmed to have at least 90% MC character for 84% of the final 1000 fs; this means that the chosen trajectories had a ^{3}MC population of at least 76% in that time frame. The constructed 3D-SDF shown in Fig. 5.4 is therefore assumed to be characteristic for the MC states. Since the 3D-SDF shown is constructed from a smaller number of trajectories, it is subject to some noise which is mostly visible around the edges. In contrast to the solvation shell of the full set of trajectories at 5000 fs (see Fig. 5.2), the MC-solvation shell does not indicate changes in hydrogen bonds above and below the bipyridyl ligand. The figure rather shows that the first solvation shell recedes around at the cyanide ligands, which correlates with the bond length changes of the ^{3}MC states (Fig. 3 in the manuscript in Section A.2.1). This suggests that the strength in hydrogen bonds at the cyanide and bipyridyl ligands affects the MLCT and MC states differently which can lead to different stabilization and lifetimes of the two states; stronger hydrogen bonding at the bipyridyl ligand can be expected to stabilize the MLCT states but do not affect the MC states.

5.2 Comparison with TDDFT Results

After showing the most important results obtained with LVC/MM SHARC, the results should be briefly compared to the results of the on-the-fly TDDFT/MM simulations in Ref. 59, which will be referred to as "reference" here.

We obtain qualitatively equal results in terms of overall ISC rate, time-dependent RDFs, and average time-dependent bond lengths. However, the time scales of the bifurcation into ^{3}MLCT and ^{3}MC states are not perfectly reproduced as the transfer into the ^{3}MC states here takes about 30% longer (see Fig. 5.1). Even more drastic are the difference in the time scales for the transfer from ^{3}MLCT to ^{3}MC states and relaxation from ^{3}MC into the ground state. The respective time constants reported here are both a magnitude larger than the ones reported in the reference (2.2 and 6.9 ps) and their ratio does also not match. These drastic differences can neither be explained by the additional "^{1}Cold" state in our kinetic model, which accounts for persistent singlet population, nor the difference in simulated time (5000 fs against 700 fs in the reference). The time constant for the relaxation into the ground state of 6.9^{+13}_{-5} ps reported in the reference aligns with the experimentally determined ones of about 13 ps.[153] Hence, we conclude that the inaccuracy must be caused by the used LVC/MM model. Kjær and coworkers describe that the ^{3}MLCT–^{3}MC conversion is directly influenced by the stabilization of the respective ^{3}MC states.[153] Both the t_{2g} and e_g orbitals of the metal center are influenced by the environment and in turn influence the stabilization of the MC triplet states. The stabilization of the MC states can also be expected to affect the relaxation into the ground state. Hence, it can be reasoned that the ^{3}MC states are not stabilized enough in the LVC/MM model compared to the other triplet states, by either restrictions in the harmonic oscillators or the solvent interaction. An analysis of the average diabatic excitation energies over time confirms that the lowest ^{3}MC states are close in energy to the lowest ^{3}MLCT states; the analysis is shown in Fig. S4 of Section A.2.1 and shows the time-dependent excitation energies of all MLCT and MC states. Comparing the time-dependent bond length distributions with the reference (Fig. 3 in Ref. 59 and Fig. 3 in the manuscript in Section A.2.1), we find that, even though the average bond lengths are reproduced, the shape and width of the distributions differ. The reference distributions of the Fe–N_{bpy} and Fe–CN_{eq} in the ^{3}MC states are broad and appear to be skewed towards longer bond lengths. This indicates both state-specific normal modes as well as strong anharmonicity in corresponding modes. The respective distributions in the LVC model are both symmetric and less broad. Both state-specific normal modes as well as strong anharmonicity cannot be represented in an LVC model. We, thus, conclude that for a better description of the system additional second-order terms and terms that account for anharmonicity have to be included into the model, so that the PES of the MC states can be accurately modeled. This finding shows that anharmonicity is very important for the excited-state dynamics of $[\mathrm{Fe(CN)_4(bipy)}]^{2-}$.

Besides the described shortcoming of the LVC/MM model, it needs to be reiterated that the results for solvent structure, solute dynamics and ISC rate are remarkably close to the reference. With each trajectory being computed in about 13 h on a single Intel Xeon E5-2650 v3 CPU, the whole SHARC simulation amounted to about 60,000 CPUh. This represents a fraction of the much smaller simulation done in Ref. 59, which has cost about 550,000 CPUh for 99 trajectories propagated over 700 fs. The additionally information obtained in terms of 3D-SDFs, the resolved oscillation in the time-dependent RDF and the possibility of analyzing specific, yet large enough, subsets of trajectories show the merit of utilizing LVC/MM SHARC simulations to supplement experimental findings.

6

CONSIDERATIONS ON THE CONSTRUCTION OF LVC/MM MODELS

LVC models are by no means a "black box" approach for any type of rigid molecular system. Throughout the work presented thesis, there were many pitfalls regarding the construction and use of the LVC models, and by extension the LVC/MM model, specially during the work on the $[\mathrm{Fe(CN)_4(bipy)}]^{2-}$ system. The purpose of this chapter is to offer a guide in the construction of LVC/MM models including practices that help avoiding some of the pitfalls encountered here. For this purpose, this chapter is accompanied by an exemplary analysis on the $[\mathrm{Fe(CN)_4(bipy)}]^{2-}$ system.

A good starting point for the construction and evaluation of LVC models can be found in Refs. 72,74,94, which present the parameterization of the model and an overview over its capabilities. The chapter is divided into construction steps and refer to the different parts of the LVC model (see Section 2.3): (i) prerequisites of the molecular system and $\mathbf{Q}$ (Section 6.1), (ii) the included diabatic states and ϵ_i (Section 6.2), (iii) standard parametrization with $\kappa_k^{(i)}$ and $\lambda_k^{(ij)}$ (Section 6.3), (iv) inclusion of second order parameters, $\gamma_{kk}^{(ii)}$, (Section 6.4), (v) preparing simulations in solution and DME (Section 6.5), and a concluding section on final validations of the model (Section 6.6).

One aspect not mentioned here is the choice of the level of theory to describe the selected system. The choice of the level of theory is specific to each system and situation, and goes beyond the scope of this chapter.

6.1 Prerequisites of the Molecular System and the Normal Modes

The most important prerequisite is that the molecule of choice must be suitable to be described by an LVC model. The key consideration for this are the constraints on the nuclear degrees of freedom in the system. All nuclear motion in the phase space one wants to observe must be mappable to normal coordinates in the harmonic approximation. Consequently, every non-linear motion or rearrangements of atoms cannot be described; this includes, e.g., torsions, dihedral rotations, dissociations, and proton transfers. However, if these degrees of freedom are not expected to greatly influence the dynamics, e.g., as in the case of the rotation of methyl groups, one can exclude them or simply apply the harmonic approximation to them. For the ground state, the constraints in the nuclear degrees of freedom can usually be gauged through chemical intuition. If one cannot be sure whether the geometry and hence the normal coordinates of the ground state are a good basis for describing nuclear motion in the excited states, one should perform a conformational analysis of the target states.[160]

In the LVC model, the normal modes of one electronic state build the basis for the description of nuclear motion in all electronic states. However, normal modes that can describe the nuclear motion well in one state are not necessarily suitable for all other electronic states. An example of this is 2-thiouracil. Here, the normal coordinates of the ground state are not a good basis to describe nuclear motion in the excited states. 2-Thiouracil is planar in the ground state, but pyramidalizes in the first excited states by moving its sulfur atom out of plane.[161] This changes the center of mass and also the normal modes for the corresponding states. As a consequence, these excited states cannot be well described with an LVC model.

If the molecule is deemed suitable, we can obtain the normal modes from a frequency calculation. Usually, this is done with an optimized geometry for the ground state. In order to obtain the normal coordinates in high quality it is recommended to set very tight convergence parameters and use large integration grids. If the molecule is symmetric, one should optimize using symmetry, as symmetry imposes selection rules on the later derived coupling parameters; this leads to fewer non-zero parameters that can be validated by applicable selection rules.

6.2 The Diabatic Basis and ϵ

Choosing an appropriately sized diabatic basis for the LVC model is essential for the accuracy of the computed adiabatic states along the trajectories. In principle, one could include infinitely many states in the diabatic basis and, from it, be able to perfectly evaluate the adiabatic states. In practice, this is not possible. Even with the gradient evaluation adapted to an adiabatic subspace in the LVC interface (see Section 3.2), including too many diabatic states will considerably increase computational cost. Therefore, we should include only as many diabatic states as necessary to represent the desired adiabatic states during the dynamics. The choice of the included states depends very much on the system and dynamics that need to be described, as they are the basis of electronic states with which the wave function is propagated. If one or more important states are missing, the model will not be accurate for the system.

Generally, one can choose the diabatic states on the basis of their character, molecular orbitals in the state transitions, and/or energetic gap with other states. For gas phase simulations, obtaining an absorption spectrum on geometries sampled from a Wigner distribution can be a good starting point to choose a diabatic basis.

In the case of $[\mathrm{Fe(CN)_4(bipy)}]^{2-}$ in water (see Chapter 5), we needed to include all low-lying triplet states with metal centered character (^{3}MC).[59] As a first check, we calculated the first 30 singlet and 30 triplet states including water as implicit solvent (dielectric constant $\varepsilon_r = 80.2$); the excitation energies for these states are shown in Fig. 6.1a in the right column with the MC character highlighted. As can be seen, all MC states occur below 3.5 eV. We could include all electronic states below 3.5 eV into our diabatic states if we performed the whole parametrization with implicit solvation and $\varepsilon_r = 80.2$. However, as we will show in Section 6.5 this leads to accounting for the solvent effects twice. This poses a problem to solve: We want to include the MC states that occur in the aqueous solution but cannot simply parametrize the model with implicit solvation parameters for water. Therefore, we need to recover these states within a parametrization that does not include the water implicitly. Parametrizing the model in the gas phase ($\varepsilon_r = 1.0$) would be the logical conclusion; Fig. 6.1a shows in the left column that the MC states have similar excitation energies as with $\varepsilon_r = 80.2$. However, the low excitation energy of the first excited state (0.5 eV) can lead to convergence problems in the TDDFT calculations that are necessary for the numerical differentiation procedure in the parametrization.[94] For this reason, we explored another possibility than a parameterization in the gas phase. The center column in Fig. 6.1a shows the excitation energies with $\varepsilon_r = 1.7689$. This value is the limit of dielectric con-

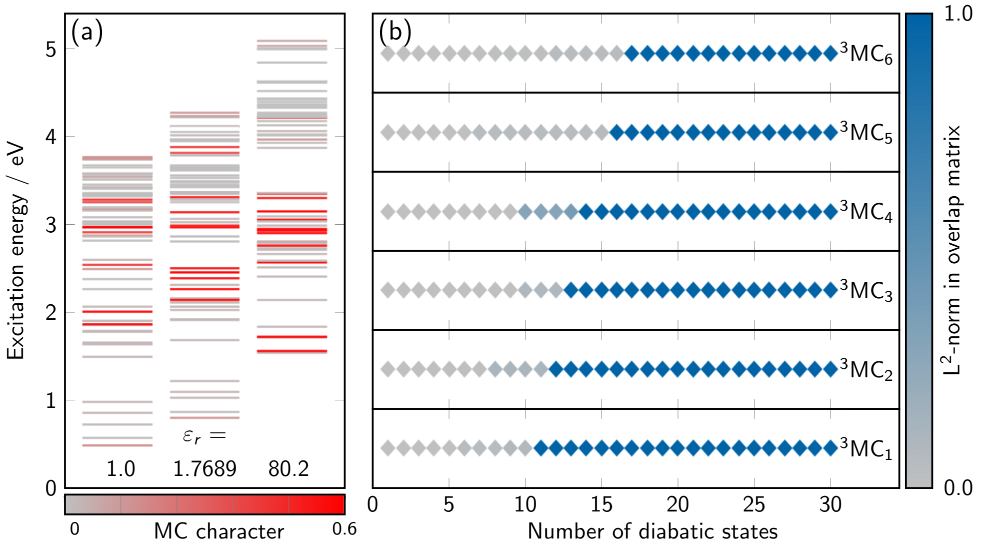

Figure 6.1: Excitation energies of the first 30 singlet and 30 triplet states of $[Fe(CN)_4(bipy)]^{2-}$ with implicit solvation at different dielectric constants, ε_r, (panel a) and L^2 norms of the rows in the overlap matrix corresponding the first six ^{3}MC states as function of the included diabatic states; the overlap is determined between the first 30 excited states calculated with dielectric constants set to 80.2 and 1.7689 (panel b). The color in panel a indicates the calculated MC character of the states.

stant for water at high frequencies and only accounts for the polarizability of the electronic density of the solvent water molecules. The polarizability of the electronic density is not included by the FF, which uses static point charges, in the LVC/MM calculations and thus do not lead to double counting. More importantly, we can see the increase in excitation energies in Fig. 6.1a (center column), which promise a better convergence behavior compared to the gas phase. Hence, the parametrization of the LVC model is performed with the inclusion of implicit solvation at this setting. Now, we need to pick the diabatic basis from the calculations with our new setting such that we recover the desired ^{3}MC states that occur in water ($\varepsilon_r = 80.2$).

Picking the diabatic basis only by considering the excitation energies can be unreliable. We need to ensure that the desired ^{3}MC states in the calculation with $\varepsilon_r = 80.2$ can be represented in the diabatic basis that includes states computed with $\varepsilon_r = 1.7689$. Therefore, we also performed an overlap calculation between the respective single-point calculations with $\varepsilon_r = 80.2$ and $\varepsilon_r = 1.7689$. Fig. 6.1b shows the L^2 norms in the overlap matrix for the desired six ^{3}MC states as a function of the included triplet states. The L^2 norm of a row in the overlap matrix shows to what extend the corresponding state in the calculation with $\varepsilon_r = 80.2$ is represented by the basis of states in the calculation with $\varepsilon_r = 1.7689$. It can be seen that the lowest ^{3}MC state reaches a norm close to 1 after including ten states and the highest ^{3}MC at 16. This means, that including the first 16 triplet states is sufficient to recover the desired six ^{3}MC states. By also considering the singlet states and gaps in the excitation energies of all excited states, we decided to include the first 21 singlet and 20 triplet states into our diabatic basis; their excitation energies are included in the LVC model as the ϵ_i parameters.

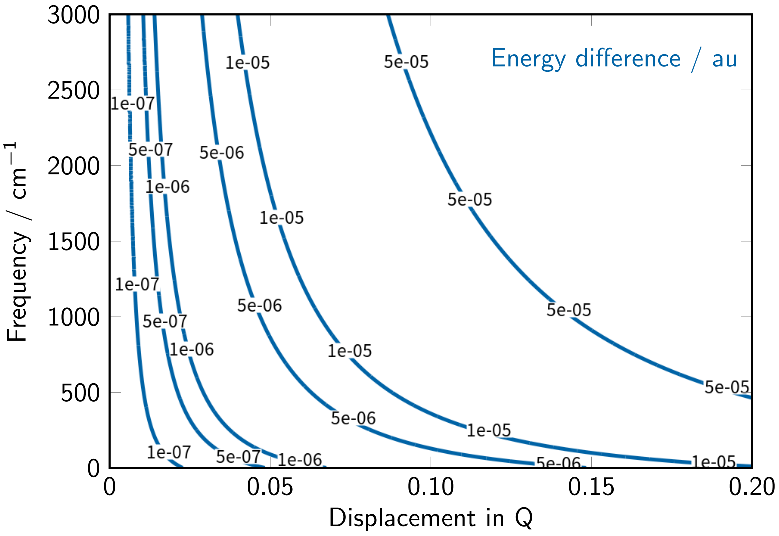

Figure 6.2: Contour plot of the differences in energy in an harmonic oscillator as a function of the displacement along a normal mode and the frequency of that mode.

6.3 Standard parametrization with κ and λ Parameters

An LVC model can be parameterized in the SHARC program from either a singular single-point calculation, which includes gradients and NACs,[72] or from a set of single-point calculations for numerical differentiation.[94] Regardless of the approach, tight convergence parameters for energies and derivatives are essential to obtain a stable LVC model.

All parameters are then evaluated using the assumption that the diabatic and adiabatic bases coincide at the reference geometry ($\mathbf{Q} = 0$); this also means that $\eta^{(ij)}(\mathbf{Q} = 0) = 0$. The ϵ parameters are the excitation energies of all states at the reference geometry. In the normal mode basis, the κ parameters are defined as the gradients at the reference geometry and the λ are closely related to the NACs at the reference geometry (see Eqs. (2.29) and (2.30)). Although the gradients at the reference geometry might be computationally expensive to evaluate, the NACs are not readily available in every software or level of theory. For this reason, we can approximate these quantities through numerical differentiation.[94] We calculate the excitation energies at geometries that are displaced along the normal mode coordinates and transform them into the diabatic basis using the wave function overlap between the displaced and reference geometries. We can then use the full diabatized energy matrices at the displaced geometries to calculate κ and/or λ parameters using a finite-difference procedure. The accuracy of the parameters depends on the numerical accuracy of the finite-difference procedure and the overlap calculated. Usually, both are more accurate the smaller the displacements along $\mathbf{Q}$. However, displacements that are too small lead to numerical instabilities as Fig. 6.2 shows. The figure displays the energy difference as a function of displacement and frequency of a normal mode that can be expected by using the harmonic approximation $\Delta E = \frac{1}{2}\omega Q^2$. We can see that at very low displacements and low frequencies the expected energy difference is at or below $1 \cdot 10^{-7}$ au, which can be below the convergence thresholds of the excitation energies calculated. As a rule of thump, a difference in energy of at least $5 \cdot 10^{-6}$ au should be aimed for, which is above the convergence threshold for “tight” energy

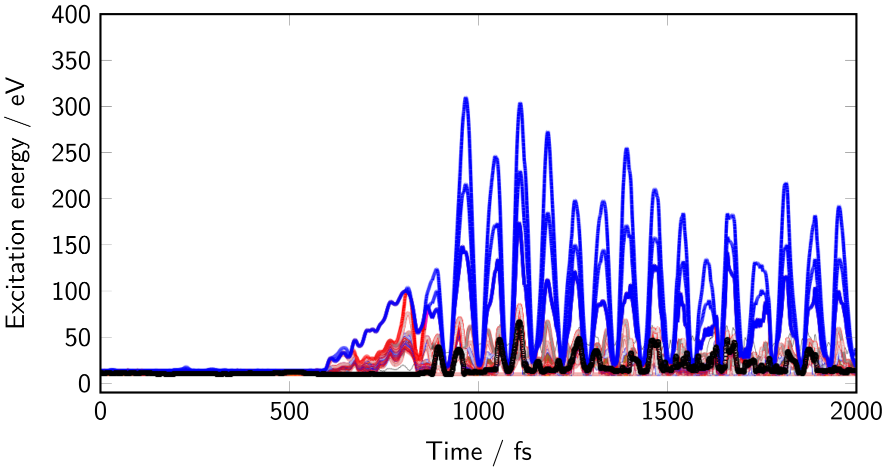

Figure 6.3: Excitation energies of singlet and triplet states in a gas phase trajectory of $[\mathrm{Fe(CN)_4(bipy)}]^{2-}$ with an LVC model over time; the model is parametrized using a finite differences procedure with displacements in $\mathbf{Q}$ of 0.05. The excitation energies of singlet states are shaded in blue and triplet states are shaded in red; the active electronic state at every time step is indicated by a black circle. The excitation energies show unphysically large oscillations (up to 300 eV) indicating an unstable LVC model.

convergence in the GAUSSIAN program.[103] As can be recognized from Fig. 6.2, especially for normal modes with lower frequencies it is advisable to calculate a proper displacement value and specify it in the setup accordingly. Following the recommendation to reach $\Delta E \geq 5 \cdot 10^{-6}$ au, normal modes with frequencies lower than 100 cm^{-1} need displacements of about 0.10 to 0.15, frequencies between 100 cm^{-1} and 700 cm^{-1} need displacements between 0.05 and 0.10. Otherwise, the recommended displacement value of 0.05 in SHARC is sufficient.

Especially the coupling parameters, λ, are heavily influenced by the displacement value chosen. Numerical instabilities in the model can lead to detrimental behavior of the model; this is illustrated by Fig. 6.3 showing the time-resolved excitation energies of all singlet and triplet states in a gas-phase trajectory. With the efficiency of the LVC method, simulating a small set of gas phase trajectories can be done with less effort and presents a solid check of the stability of the model. In first 600 fs, the excitation energies of the states stay within a band that is less than 10 eV broad. However, after 600 fs there are unphysically large oscillations of up to 300 eV in the singlet states; these oscillations likely stem from unphysical geometries, i.e. large displacements in $\mathbf{Q}$. Such behavior can often be attributed to the λ parameters. Generally, $|\lambda| \leq 1 \cdot 10^{-3}$ which can be checked in the `LVC.template` file. $|\lambda|$ values that are much large than $1 \cdot 10^{-3}$ are rare and often encountered due to problems in the numerical differentiation. In the case of the model for $[\mathrm{Fe(CN)_4(bipy)}]^{2-}$, the problems shown in Fig. 6.3 could be alleviated by increasing the convergence threshold of the excitation energies in all single point calculations to $1e-7$ au. Otherwise, instabilities can be often be alleviated by choosing larger displacements (> 0.05) for an affected normal mode; if this does not help, one can resort to removing/altering the suspicious λ parameters, or removing problematic normal modes altogether. A procedure to find important normal modes for the dynamics and assess the validity of the parameters can also be found in Ref. 162.

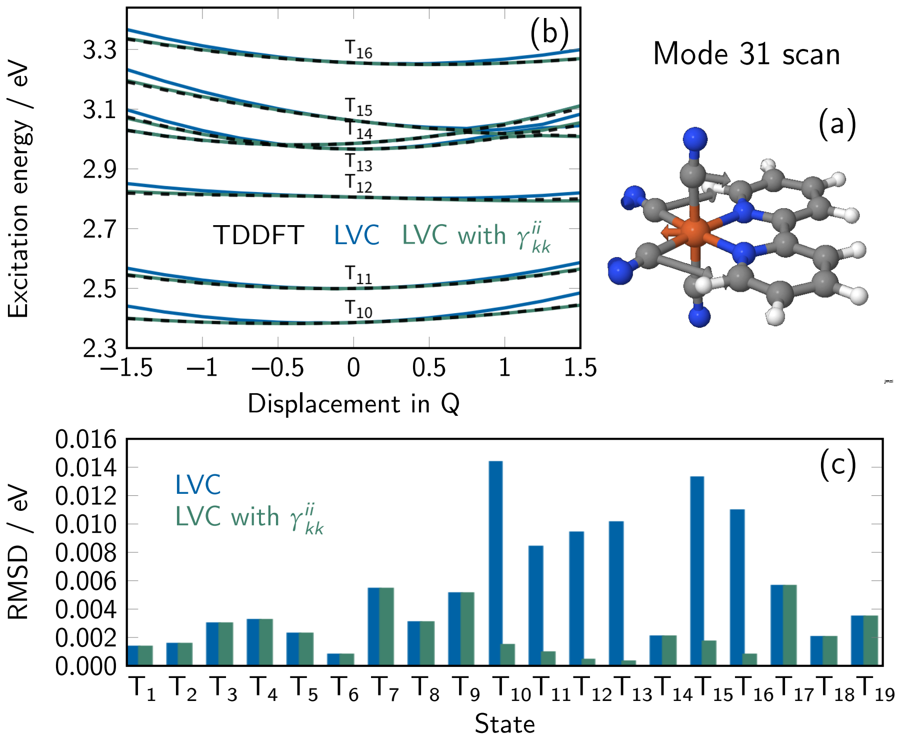

Figure 6.4: Influence of the inclusion of $\gamma_{kk}^{(ii)}$ parameters (see Section 2.3) on the accuracy of the LVC model in the gas phase for normal mode 31 and all ^{3}MC states (states 10,11, 12, 13, 15 16). Panel a shows the motion of the nuclei in the normal mode 31 which is a symmetric stretching mode of the axial CN ligands. The results of a scan along this normal mode (panel b) with the TDDFT reference (black) against an LVC model with $\gamma_{kk}^{(ii)}$ parameters (green) and without them (blue). The state-wise RMSD for the latter two against the reference is shown in panel c.

6.4 Second-order Parameters γ

Second-order parameters, γ, can alter the basis of normal coordinates to some extent and might be added to the LVC model for this purpose. Eq. (2.31) is for arbitrary γ parameters, but we generally divide these parameters into three classes (see Section 2.3): $\gamma_{kk}^{(ii)}$ for state-specific frequency shifts, $\gamma_{kl}^{(ii)}$ for Duschinsky rotations[93], and $\gamma_{kk}^{(ij)}/\gamma_{kl}^{(ij)}$ for second-order inter-state couplings. We have included only the parametrization of the $\gamma_{kk}^{(ii)}$ parameters in SHARC so far, even though the LVC interface is able to handle all $\gamma_{kl}^{(ij)}$ parameters. The evaluation of all γ_{kl} parameters would necessitate the calculation of full Hessian matrices for the excited states, either analytically or numerically, which makes the parameterization much more expensive.[70]

For the $[\mathrm{Fe(CN)_4(bipy)}]^{2-}$ system, the ^{3}MC states change the strength of the axial Fe-ligand bonds leading to different frequencies in the corresponding normal modes. For this reason, we performed scans with the reference method, TDDFT in our case, along different normal modes which change the distances between the iron center and the axial ligands. As an example, the results for such a scan in normal mode 31 are compiled in Fig. 6.4 It can be seen that the states T_{10}, T_{11}, T_{12}, T_{13}, T_{15} and T_{16} have a significantly higher RMSDs along the scan (panel b).

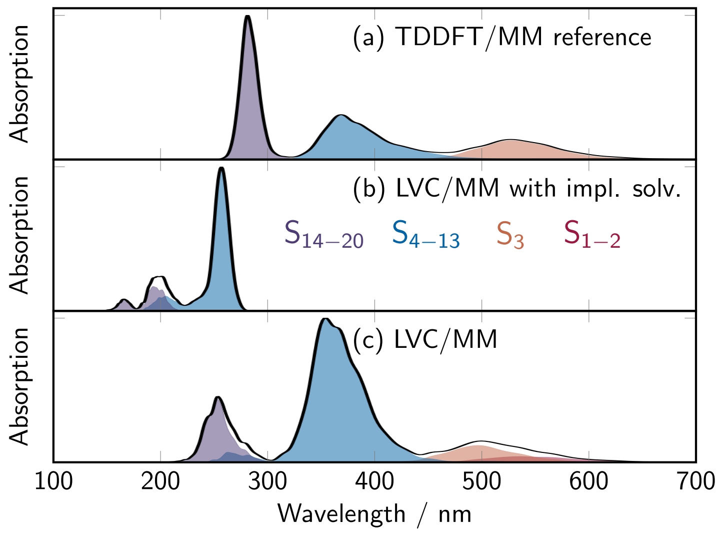

Figure 6.5: Comparison of spectra in explicit solvation using TDDFT/MM (panel a) and LVC/MM with models parameterized with implicit solvation using $\varepsilon_r = 80.2$ (panel b) and $\varepsilon_r = 1.7689$ (panel c). The singlet states are collected into absorption bands as in Ref 59.

The inclusion of $\gamma_{kk}^{(ii)}$ mitigated these errors in the RMSDs and lead to a better alignment of the energy curves in panel a. In this case, the $\gamma_{kk}^{(ii)}$ are evaluated as

$$\gamma_{kk}^{(ii)} = \frac{1}{N_{\text{disp.}}} \sum_{n}^{N_{\text{disp.}}} 2 \frac{W_{ii}(Q_k + h_n) - W_{ii}(0)}{h_n^2} \tag{6.1}$$

where $N_{\text{disp.}}$ is the number of displacements and $W_{ii}(Q_k + h_n)$ is the diabatized energy matrix at the n-th displacement h_n in the normal mode coordinate Q_k. The displacements chosen are ±0.2 and ±0.4. $\gamma_{kk}^{(ii)}$ parameters were calculated for all ^{3}MC states for normal modes that alter the axial Fe–ligand bonds and lead to similar results as shown for mode 31.

6.5 Preparing for Simulations in Solutions and Evaluating the DME

In order to do calculations with the LVC/MM method, we need to add representations of the electronic densities to our model. This is done by fitting a DME at the reference geometry using the our extended RESP method (Sections 2.6 and 3.3). The goal is to use the LVC model to describe a solute in some environment, so that the question arises of whether to include solvent effects in the parameterization. An argument for including these effects is that the basis of diabatic states will be closer to the actual electronic states in solution. Fig. 6.5 compares the spectra in explicit solvation of the TDDFT/MM reference (panel a) with LVC/MM for a model that was parametrized with implicit solvation (panel b) and without it (panel c). It can be seen that the spectrum for the model with $\varepsilon_r = 80.2$ (panel a) is shifted towards higher energies and does not reproduce the band structure. The band for the S_3 state is completely absent. The LVC model that was parametrized with $\varepsilon_r = 1.7689$ is only shifted by a small margin and has a similar band structure. The absorption bands of the higher singlet states are not expected to be as accurate, as the completeness of the diabatic bases decreases for these higher states. It should be noted that the LVC model in panel c also includes γ parameters, and no

DMEs for the transition densities. However, the strong shift in energy can only be attributed to the double counting of solvent interaction: once within the model through the parametrization with implicit solvation $\varepsilon_r = 80.2$ and a second time through explicit solvation. As said in the discussion in the section above, it is possible to set ε_r to the value in the high frequency limit so that only the polarizability of the electronic densities of the solvent molecules is accounted for. Preferably, the LVC model for the LVC/MM method and the DME should always be obtained without accounting for the solvent via implicit solvation.

Although the RESP fit is stable with respect to the produced ESP at the fitting points, there are some parameters that can be modified to improve the results. A good starting point and common reference for this thesis is the work of Abedi and coworkers[50] that investigated the quality of RDFs of transition metal complexes using different population analysis methods. For RESP, they recommend using higher restraints of 0.01 and at least 1000 fitting points per atom. For the generation of the fitting grid, the Merz–Singh–Kollman scheme is the standard algorithm.[100] However, the used vdW radii for the atoms can influence the results and might be adapted for different systems and atom types.[163] The monopole terms of the obtained fits can be checked for physical meaning, as they should roughly reflect the electronic character of the states and should reproduce in tandem with the dipole terms the overall dipole moment of the electronic state.[75,105] Another aspect lies within the target charges specified for the restraint in the RESP fit. These target charges are usually set either to 0 or the Mulliken charges.[164] These charges should not significantly influence the quality of the RESP fit,[50] but can help enforce a certain physically-sensible charge distribution.

6.6 Validation of the Model

After constructing an LVC or LVC/MM model, one should first try to validate the model before starting many trajectories with it. As mentioned above, a few gas phase trajectories can help to assert the stability of the parameters, as well as having a closer look at the spectrum. If there are already initial conditions available for solvated systems, one can perform a scan by scaling the point-charge strength. Doing so will generate a plot comparable to Fig. S20 in the supporting information of Ref. 59, which shows how the individual states are increasingly influenced by electrostatic interactions with the environment. Of course, it is also possible to repeat this scan with the reference method and compare the results. In difficult cases, scans along selected normal modes calculated in the gas phase with the reference method can provide a lot of information (see Section 6.4 and Fig. 6.4b). Compared to the results generated by the LVC model, problems with κ, λ, and the necessity for γ parameters may be identified from the plotted scans. The LVC method also allows the computation of minimum energy geometries for all diabatic states and the efficient optimization of the adiabatic minima in the PES, which can be compared to the reference results.

Regardless of the simplicity of the system and the respective LVC model, performing computations, e.g., scans along normal modes, short trajectories, absorption spectra, or scans with scaled environment point charges (see Ref. 59 Fig. S20), to validate the model (possibly against the reference method) and gauge its behavior in different situations is always advised. These computations can not only help to avoid pitfalls and subsequent erroneous simulations, but also aid in the understanding of the molecular system investigated. After all, a LVC Hamiltonian is an analytical model of the electronic and nuclear degrees of freedom of the molecule.

7

CONCLUSIONS & OUTLOOK

This thesis presents a newly developed combination of LVC models with MM FF via EE, called LVC/MM, for the simulation of excited-state dynamics in solvated systems within the SHARC program.[108] Such simulations are important for the interpretation of time-resolved experimental results and the underlying physical phenomena, and can help in guiding new research or in the design of new solvated systems for different applications. While there are a number of methods to perform such simulations, the excited-state dynamics of solvated systems often require the description of many atoms and electronic states over long time scales. Therein, the presented LVC/MM method is shown to be powerful enough for this task and enables new ways of analyzing the produced structural data. Therefore, this thesis does not only present the methodological developments of the LVC/MM method and its application to solvated systems, but also describes how the simulated data can be analyzed in new ways with focus on the time-resolved solute–solvent dynamics.

The central achievement of this thesis, the LVC/MM method, is based on the vibronic coupling Hamiltonian[69], which is available within SHARC for large scale simulations in the gas phase.[74,94] The thesis describes how the LVC Hamiltonian can be extended to both allow for roto-translational motion, which is necessary for diffusion processes, and the interaction with external point charges via a set of diabatic DMEs. The diabatic DMEs are evaluated via an adjusted RESP fit during the parametrization of the LVC model.

Another achievement of the thesis lies in several further development done within the SHARC program.[108] The work of this thesis provides a generalization of the SHARC interfaces and leverages in-memory communication between different parts of the code. This builds the foundation for interfaces with hierarchical structure such as the QM/MM interface that is used for the LVC/MM method. Additional developments contribute to drastically improving the overall efficiency of the LVC interface and allowing for more control over stored data in SHARC.

The efficiency of the LVC/MM method enables the simulation of large trajectory swarms that open new possibilities in the analysis of nonadiabatic solute–solvent dynamics. The possibility of constructing and analyzing the time-dependent solvation structure in three dimensions via 3D-SDFs represents another achievement. The thesis includes an in-depth analysis of the key considerations for the construction of 3D-SDFs, which are the strength of solvation features, the density fluctuations and the number of necessary trajectories. Additionally, the thesis describes how these 3D-SDFs can be built as either histograms or from a convolution, and how the preparation of the nuclear data leads to two different perspectives that each highlight different aspects of the solute–solvent dynamics.

At the example of two small thiocarbonyls in water, the thesis validates the LVC/MM model and shows that the solvation shell in terms of RDF and three-dimensional distribution of a TDDFT/MM reference can be reproduced. The shifts in the energies of the electronic states due to the interaction with the solvent molecules is sufficiently well described with an error between 1–2 kcal/mol. The analysis of the time-resolved 3D-SDFs from two perspectives, facilitated by large trajectory swarms in the excited-state simulations, revealed how the self-rotation of CH_2S can relax its solvation shell within less than 100 fs.

This thesis further investigates the excited-state dynamics of $[Fe(CN)_4(bipy)]^{2-}$ in water. While this system was previously studied by members of the group, it became apparent that SH simulations with vastly more trajectories and longer time scales can be beneficial to the comprehension and interpretation of the excited-state dynamics of $[Fe(CN)_4(bipy)]^{2-}$ in water.[59] Therein, LVC/MM is not only efficient enough to enable simulation with 45 times more trajectories over 5000 fs instead of 700 fs, but also reproduces the overall ISC rate, the bifurcating population transfer rates of the initial singlet population and time-dependent RDFs. While the inaccuracy in the life times of the MLCT and MC states appear as a problem, the analysis of the time-dependent bond length analysis shows the importance of anharmonicity for the stabilization of the MC states. Additionally, the time-dependent 3D-SDFs give detailed insight into the dynamical response of the solvation structure in space. The analysis of a subset of trajectories with dominant MC character reveals drastic differences in the solvation structure in comparison to the MLCT dominated full set with considerable implications on the stabilization and life times of both triplet manifolds.

The thesis also includes a chapter on considerations for the construction of LVC/MM models, which aims to navigate several hurdles and pitfalls that may be encountered. The corresponding chapter gives general advice on the construction of LVC models, suggests different criteria for the choice of diabatic basis, the calculation of first-order coupling parameters and describes the possibility of including second-order parameters to describe state-specific frequencies. Additionally, the chapter describes how to prepare the model for simulations in solution, how to compute the diabatic DMEs, and concludes with different ways of validating the final model.

In conclusion, the LVC/MM model proved to be a immensely efficient method to simulate excited-state dynamics in solution that is multiple orders of magnitude less costly than typical TDDFT/MM simulations. This method facilitates simulations in which the temporal response of the coupled solute–solvent dynamics can not only be analyzed in terms of electronic degrees of freedom and nuclear dynamics via solute vibrations and RDFs over longer time scales than before, but the solvent structure can also be resolved in three dimensions which leads to new insights.

Since LVC models are well-researched,[69,74,94,165] their possibilities and limits in the applicability to various systems are well-known. This knowledge is almost directly transferable to the application of LVC/MM models. Computational research on many different systems that have used LVC models in the gas phase, or that have been limited to the use of implicit solvation and short time scales in explicit solvation using other methods can likely benefit substantially from simulations performed with LVC/MM models. There is much that is still unknown about excited-state dynamics of solvated systems and this thesis demonstrates how the LVC/MM method can be applied to illuminate some of the fundamental processes.

BIBLIOGRAPHY

[1] C. Reichardt, T. Welton: *Solvents and Solvent Effects in Organic Chemistry*, John Wiley & Sons (2011).

[2] J. T. Hynes: Chemical Reaction Dynamics in Solution, *Annual Review of Physical Chemistry*, **36**, 573 (1985).

[3] T. Kumpulainen, B. Lang, A. Rosspeintner, E. Vauthey: Ultrafast Elementary Photochemical Processes of Organic Molecules in Liquid Solution, *Chem. Rev.*, **117**, 10826 (2017).

[4] A. Rosspeintner, B. Lang, E. Vauthey: Ultrafast Photochemistry in Liquids, *Annu. Rev. Phys. Chem.*, **64**, 247 (2013).

[5] R. K. Venkatraman, A. J. Orr-Ewing: Solvent Effects on Ultrafast Photochemical Pathways, *Acc. Chem. Res.*, **54**, 4383 (2021).

[6] A. Pigliucci, G. Duvanel, L. M. L. Daku, E. Vauthey: Investigation of the Influence of Solute-Solvent Interactions on the Vibrational Energy Relaxation Dynamics of Large Molecules in Liquids, *J. Phys. Chem. A*, **111**, 6135 (2007).

[7] J. Burgess: Solvent Effects on Visible Absorption Spectra of Bis-(2,2'-Bipyridyl) Biscyanoiron(II), Bis-(1,10-Phenanthroline)Biscyanoiron(II), and Related Compounds, *Spectrochim. Acta A: Mol. Spectrosc.*, **26**, 1369 (1970).

[8] P. F. Barbara, G. C. Walker, T. P. Smith: Vibrational Modes and the Dynamic Solvent Effect in Electron and Proton Transfer, *Science*, **256**, 975 (1992).

[9] D. Polli, P. Altoè, O. Weingart, K. M. Spillane, C. Manzoni, D. Brida, G. Tomasello, G. Orlandi, P. Kukura, R. A. Mathies, M. Garavelli, G. Cerullo: Conical Intersection Dynamics of the Primary Photoisomerization Event in Vision, *Nature*, **467**, 440 (2010).

[10] P. Chen, T. J. Meyer: Medium Effects on Charge Transfer in Metal Complexes, *Chem. Rev.*, **98**, 1439 (1998).

[11] R. Jimenez, G. R. Fleming, P. V. Kumar, M. Maroncelli: Femtosecond Solvation Dynamics of Water, *Nature*, **369**, 471 (1994).

[12] W. Linert, V. Gutmann: Structural and Electronic Responses of Coordination Compounds to Changes in the Molecule and Molecular Environment, *Coord. Chem. Rev.*, **117**, 159 (1992).

[13] P. J. Rossky, J. D. Simon: Dynamics of Chemical Processes in Polar Solvents, *Nature*, **370**, 263 (1994).

[14] P. J. Sadkowski, G. R. Fleming: The Influence of Solvent—Solute Interaction on Radiationless Processes: Excited State Dynamics of 1,8-Anilinonaphthalene Sulphonate and Related Molecules, *Chem. Phys.*, **54**, 79 (1980).

[15] K. S. Kjær, T. B. van Driel, J. Kehres, K. Haldrup, D. Khakhulin, K. Bechgaard, M. Cammarata, M. Wulff, T. J. Sørensen, M. M. Nielsen: Introducing a Standard Method for Experimental Determination of the Solvent Response in Laser Pump, X-ray Probe Time-Resolved Wide-Angle X-ray Scattering Experiments on Systems in Solution, *Phys. Chem. Chem. Phys.*, **15**, 15003 (2013).

[16] A. Nimmrich, M. R. Panman, O. Berntsson, E. Biasin, S. Niebling, J. Petersson, M. Hoernke, A. Björling, E. Gustavsson, T. B. van Driel, A. O. Dohn, M. Laursen, D. B. Zederkof, K. Tono, T. Katayama, S. Owada, M. M. Nielsen, J. Davidsson, J. Uhlig, J. S. Hub, K. Haldrup, S. Westenhoff: Solvent-Dependent Structural Dynamics in the Ultrafast Photodissociation Reaction of Triiodide Observed with Time-Resolved X-ray Solution Scattering, *J. Am. Chem. Soc.*, **145**, 15754 (2023).

[17] K. H. Kim, J. G. Kim, K. Y. Oang, T. W. Kim, H. Ki, J. Jo, J. Kim, T. Sato, S. Nozawa, S.-i. Adachi, H. Ihee: Femtosecond X-ray Solution Scattering Reveals That Bond Formation Mechanism of a Gold Trimer Complex Is Independent of Excitation Wavelength, *Struct. Dyn.*, **3**, 043209 (2016).

[18] T. Katayama, T.-K. Choi, D. Khakhulin, A. O. Dohn, C. J. Milne, G. Vankó, Z. Németh, F. A. Lima, J. Szlachetko, T. Sato, S. Nozawa, S.-i. Adachi, M. Yabashi, T. J. Penfold, W. Gawelda, G. Levi: Atomic-Scale Observation of Solvent Reorganization Influencing Photoinduced Structural Dynamics in a Copper Complex Photosensitizer, *Chem. Sci.*, **14**, 2572 (2023).

[19] L. X. Chen, M. L. Shelby, P. J. Lestrange, N. E. Jackson, K. Haldrup, M. W. Mara, A. B. Stickrath, D. Zhu, H. Lemke, M. Chollet, B. M. Hoffman, X. Li: Imaging Ultrafast Excited State Pathways in Transition Metal Complexes by X-ray Transient Absorption and Scattering Using X-ray Free Electron Laser Source, *Faraday Discuss.*, **194**, 639 (2016).

[20] K. J. Gaffney: Capturing Photochemical and Photophysical Transformations in Iron Complexes with Ultrafast X-ray Spectroscopy and Scattering, *Chem. Sci.*, **12**, 8010 (2021).

[21] K. Haldrup, W. Gawelda, R. Abela, R. Alonso-Mori, U. Bergmann, A. Bordage, M. Cammarata, S. E. Canton, A. O. Dohn, T. B. van Driel, D. M. Fritz, A. Galler, P. Glatzel, T. Harlang, K. S. Kjær, H. T. Lemke, K. B. Møller, Z. Németh, M. Pápai, N. Sas, J. Uhlig, D. Zhu, G. Vankó, V. Sundström, M. M. Nielsen, C. Bressler: Observing Solvation Dynamics with Simultaneous Femtosecond X-ray Emission Spectroscopy and X-ray Scattering, *J. Phys. Chem. B*, **120**, 1158 (2016).

[22] A. L. Dobryakov, S. A. Kovalenko, A. Weigel, J. L. Pérez-Lustres, J. Lange, A. Müller, N. P. Ernsting: Femtosecond Pump/Supercontinuum-Probe Spectroscopy: Optimized Setup and Signal Analysis for Single-Shot Spectral Referencing, *Rev. Sci. Instrum*, **81**, 113106 (2010).

[23] S. A. Kovalenko, R. Schanz, H. Hennig, N. P. Ernsting: Cooling Dynamics of an Optically Excited Molecular Probe in Solution from Femtosecond Broadband Transient Absorption Spectroscopy, *J. Chem. Phys.*, **115**, 3256 (2001).

[24] K. Kunnus, M. Vacher, T. C. B. Harlang, K. S. Kjær, K. Haldrup, E. Biasin, T. B. van Driel, M. Pápai, P. Chabera, Y. Liu, H. Tatsuno, C. Timm, E. Källman, M. Delcey, R. W. Hartsock, M. E. Reinhard, S. Koroidov, M. G. Laursen, F. B. Hansen, P. Vester, M. Christensen, L. Sandberg, Z. Németh, D. S. Szemes, É. Bajnóczi, R. Alonso-Mori, J. M. Glownia, S. Nelson, M. Sikorski, D. Sokaras, H. T. Lemke, S. E. Canton, K. B. Møller, M. M. Nielsen, G. Vankó, K. Wärnmark, V. Sundström, P. Persson, M. Lundberg, J. Uhlig, K. J. Gaffney: Vibrational Wavepacket Dynamics in Fe Carbene Photosensitizer Determined with Femtosecond X-ray Emission and Scattering, *Nat. Commun.*, **11**, 634 (2020).

[25] P. Vester, K. Kubicek, R. Alonso-Mori, T. Assefa, E. Biasin, M. Christensen, A. O. Dohn, T. B. van Driel, A. Galler, W. Gawelda, T. C. B. Harlang, N. E. Henriksen, K. S. Kjær, T. S. Kuhlman, Z. Németh, Z. Nurekeyev, M. Pápai, J. Rittman, G. Vankó, H. Yavas, D. B. Zederkof, U. Bergmann, M. M. Nielsen, K. B. Møller, K. Haldrup, C. Bressler: Tracking Structural Solvent Reorganization and Recombination Dynamics Following E- Photoabstraction from Aqueous I-

with Femtosecond X-Ray Spectroscopy and Scattering, *J. Chem. Phys.*, **157**, 224201 (2022).

[26] C. Wang, M. D. J. Waters, P. Zhang, J. Suchan, V. Svoboda, T. T. Luu, C. Perry, Z. Yin, P. Slavíček, H. J. Wörner: Different Timescales during Ultrafast Stilbene Isomerization in the Gas and Liquid Phases Revealed Using Time-Resolved Photoelectron Spectroscopy, *Nat. Chem.*, **14**, 1126 (2022).

[27] J. W. Riley, B. Wang, J. L. Woodhouse, M. Assmann, G. A. Worth, H. H. Fielding: Unravelling the Role of an Aqueous Environment on the Electronic Structure and Ionization of Phenol Using Photoelectron Spectroscopy, *J. Phys. Chem. Lett.*, **9**, 678 (2018).

[28] J. D. Simon (editor): *Ultrafast Dynamics of Chemical Systems*, Springer Netherlands, Dordrecht (1994).

[29] I. Tavernelli: Nonadiabatic Molecular Dynamics Simulations: Synergies between Theory and Experiments, *Acc. Chem. Res.*, **48**, 792 (2015).

[30] H. M. Senn, W. Thiel: QM/MM Methods for Biomolecular Systems, *Angew. Chem. Int. Ed.*, **48**, 1198 (2009).

[31] J. J. Nogueira, M. Oppel, L. González: Enhancing Intersystem Crossing in Phenotiazinium Dyes by Intercalation into DNA, *Angew. Chem. Int. Ed.*, **54**, 4375 (2015).

[32] F. Santoro, J. A. Green, L. Martinez-Fernandez, J. Cerezo, R. Improta: Quantum and Semiclassical Dynamical Studies of Nonadiabatic Processes in Solution: Achievements and Perspectives, *Phys. Chem. Chem. Phys.*, **23**, 8181 (2021).

[33] R. Crespo-Otero, M. Barbatti: Recent Advances and Perspectives on Nonadiabatic Mixed Quantum–Classical Dynamics, *Chem. Rev.*, **118**, 7026 (2018).

[34] L. González, R. Lindh: *Quantum Chemistry and Dynamics of Excited States: Methods and Applications*, John Wiley & Sons Canada, Limited (2020).

[35] M. Christensen, K. Haldrup, K. Bechgaard, R. Feidenhans'l, Q. Kong, M. Cammarata, M. L. Russo, M. Wulff, N. Harrit, M. M. Nielsen: Time-Resolved X-ray Scattering of an Electronically Excited State in Solution. Structure of the 3A2u State of Tetrakis-μ-pyrophosphitodiplatinate(II), *J. Am. Chem. Soc.*, **131**, 502 (2009).

[36] K. Haldrup, M. Christensen, M. Cammarata, Q. Kong, M. Wulff, S. O. Mariager, K. Bechgaard, R. Feidenhans'l, N. Harrit, M. M. Nielsen: Structural Tracking of a Bimolecular Reaction in Solution by Time-Resolved X-Ray Scattering, *Angewandte Chemie International Edition*, **48**, 4180 (2009).

[37] K. Haldrup, M. Christensen, M. Meedom Nielsen: Analysis of Time-Resolved X-ray Scattering Data from Solution-State Systems, *Acta Cryst A*, **66**, 261 (2010).

[38] K. Haldrup, T. Harlang, M. Christensen, A. Dohn, T. B. van Driel, K. S. Kjær, N. Harrit, J. Vibenholt, L. Guerin, M. Wulff, M. M. Nielsen: Bond Shortening (1.4 Å) in the Singlet and Triplet Excited States of [Ir2(Dimen)4]2+ in Solution Determined by Time-Resolved X-ray Scattering, *Inorg. Chem.*, **50**, 9329 (2011).

[39] J. W. Ponder, C. Wu, P. Ren, V. S. Pande, J. D. Chodera, M. J. Schnieders, I. Haque, D. L. Mobley, D. S. Lambrecht, R. A. J. DiStasio, M. Head-Gordon, G. N. I. Clark, M. E. Johnson, T. Head-Gordon: Current Status of the AMOEBA Polarizable Force Field, *J. Phys. Chem. B*, **114**, 2549 (2010).

[40] P. Jørgensen, J. Simons: *Second Quantization-Based Methods in Quantum Chemistry*, Academic Press, New York, 1 edition (1981).

[41] D. Case, H. Aktulga, K. Belfon, I. Ben-Shalom, J. Berryman, S. Brozell, D. Cerutti, T. Cheatham III, G. Cisneros, V. Cruzeiro, T. Darden, N. Forouzesh, G. Giambaşu, T. Giese, M. Gilson, H. Gohlke, A. Goetz, J. Harris, S. Izadi, S. Izmailov, K. Kasavajhala, M. Kaymak, E. King, A. Kovalenko, T. Kurtzman, T. Lee, P. Li, C. Lin, J. Liu, T. Luchko, R. Luo, M. Machado, V. Man, M. Manathunga, K. Merz, Y. Miao, O. Mikhailovskii, G. Monard, H. Nguyen, K. O'Hearn, A. Onufriev, F. Pan, S. Pantano, R. Qi, A. Rahnamoun, D. Roe, A. Roitberg, C. Sagui, S. Schott-Verdugo, A. Shajan, J. Shen, C. Simmerling, N. Skrynnikov, J. Smith, J. Swails, R. Walker, J. Wang, J. Wang, H. Wei, X. Wu, Y. Wu, Y. Xiong, Y. Xue, D. York, S. Zhao, Q. Zhu, P. Kollman: Amber 2023 (2023).

[42] B. Turoňová, M. Sikora, C. Schürmann, W. J. H. Hagen, S. Welsch, F. E. C. Blanc, S. von Bülow, M. Gecht, K. Bagola, C. Hörner, G. van Zandbergen, J. Landry, N. T. D. de Azevedo, S. Mosalaganti, A. Schwarz, R. Covino, M. D. Mühlebach, G. Hummer, J. K. Locker, M. Beck: In Situ Structural Analysis of SARS-CoV-2 Spike Reveals Flexibility Mediated by Three Hinges, *Science* (2020).

[43] S. Woutersen, B. Ensing, M. Hilbers, Z. Zhao, C. A. Angell: A Liquid-Liquid Transition in Supercooled Aqueous Solution Related to the HDA-LDA Transition, *Science*, **359**, 1127 (2018).

[44] G. N. Clark, C. D. Cappa, J. D. Smith, R. J. Saykally, T. Head-Gordon: The Structure of Ambient Water, *Molecular Physics*, **108**, 1415 (2010).

[45] E. Heid, S. Schmode, P. Chatterjee, A. D. MacKerell, C. Schröder: Solvation Dynamics: Improved Reproduction of the Time-Dependent Stokes Shift with Polarizable Empirical Force Field Chromophore Models, *Phys. Chem. Chem. Phys.*, **21**, 17703 (2019).

[46] A. Warshel, M. Levitt: Theoretical Studies of Enzymic Reactions: Dielectric, Electrostatic and Steric Stabilization of the Carbonium Ion in the Reaction of Lysozyme, *J. Mol. Biol.*, **103**, 227 (1976).

[47] E. Brunk, U. Rothlisberger: Mixed Quantum Mechanical/Molecular Mechanical Molecular Dynamics Simulations of Biological Systems in Ground and Electronically Excited States, *Chem. Rev.*, **115**, 6217 (2015).

[48] T. R. Nelson, A. J. White, J. A. Bjorgaard, A. E. Sifain, Y. Zhang, B. Nebgen, S. Fernandez-Alberti, D. Mozyrsky, A. E. Roitberg, S. Tretiak: Non-Adiabatic Excited-State Molecular Dynamics: Theory and Applications for Modeling Photophysics in Extended Molecular Materials, *Chem. Rev.*, **120**, 2215 (2020).

[49] M. Bondanza, M. Nottoli, L. Cupellini, F. Lipparini, B. Mennucci: Polarizable Embedding QM/MM: The Future Gold Standard for Complex (Bio)Systems?, *Phys. Chem. Chem. Phys.*, **22**, 14433 (2020).

[50] M. Abedi, G. Levi, D. B. Zederkof, N. E. Henriksen, M. Pápai, K. B. Møller: Excited-State Solvation Structure of Transition Metal Complexes from Molecular Dynamics Simulations and Assessment of Partial Atomic Charge Methods, *Phys. Chem. Chem. Phys.*, **21**, 4082 (2019).

[51] M. Pápai, M. Abedi, G. Levi, E. Biasin, M. M. Nielsen, K. B. Møller: Theoretical Evidence of Solvent-Mediated Excited-State Dynamics in a Functionalized Iron Sensitizer, *J. Phys. Chem. C*, **123**, 2056 (2019).

[52] A. Francés-Monerris, P. C. Gros, X. Assfeld, A. Monari, M. Pastore: Toward Luminescent Iron Complexes: Unravelling the Photophysics by Computing Potential Energy Surfaces, *ChemPhotoChem*, **3**, 666 (2019).

[53] G.-J. Zhao, K.-L. Han: Hydrogen Bonding in the Electronic Excited State, *Acc. Chem. Res.*, **45**, 404 (2012).

[54] A. PETRONE, J. CEREZO, F. J. A. FERRER, G. DONATI, R. IMPROTA, N. REGA, F. SANTORO: Absorption and Emission Spectral Shapes of a Prototype Dye in Water by Combining Classical/Dynamical and Quantum/Static Approaches, *J. Phys. Chem. A*, **119**, 5426 (2015).

[55] J. C. TULLY: Molecular Dynamics with Electronic Transitions, *J. Chem. Phys.*, **93**, 1061 (1990).

[56] S. MAI, P. MARQUETAND, L. GONZÁLEZ: Nonadiabatic Dynamics: The SHARC Approach, *WIREs Comput. Mol. Sci.*, **8**, e1370 (2018).

[57] J. P. ZOBEL, L. GONZÁLEZ: The Quest to Simulate Excited-State Dynamics of Transition Metal Complexes, *JACS Au*, **1**, 1116 (2021).

[58] I. TAVERNELLI, B. F. E. CURCHOD, U. ROTHLISBERGER: Nonadiabatic Molecular Dynamics with Solvent Effects: A LR-TDDFT QM/MM Study of Ruthenium (II) Tris (Bipyridine) in Water, *J. Chem. Phys.*, **391**, 101 (2011).

[59] D. B. ZEDERKOF, K. B. MØLLER, M. M. NIELSEN, K. HALDRUP, L. GONZÁLEZ, S. MAI: Resolving Femtosecond Solvent Reorganization Dynamics in an Iron Complex by Nonadiabatic Dynamics Simulations, *J. Am. Chem. Soc.*, **144**, 12861 (2022).

[60] G. GRANUCCI, M. PERSICO, A. TONIOLO: Direct Semiclassical Simulation of Photochemical Processes with Semiempirical Wave Functions, *J. Chem. Phys.*, **114**, 10608 (2001).

[61] E. FABIANO, T. W. KEAL, W. THIEL: Implementation of Surface Hopping Molecular Dynamics Using Semiempirical Methods, *Chem. Phys.*, **349**, 334 (2008).

[62] A. HUMENIUK, R. MITRIĆ: DFTBaby: A Software Package for Non-Adiabatic Molecular Dynamics Simulations Based on Long-Range Corrected Tight-Binding TD-DFT(B), *Comput. Phys. Commun.*, **221**, 174 (2017).

[63] P. O. DRAL, M. BARBATTI: Molecular Excited States through a Machine Learning Lens, *Nat. Rev. Chem.*, **5**, 388 (2021).

[64] J. WESTERMAYR, M. GASTEGGER, M. F. S. J. MENGER, S. MAI, L. GONZÁLEZ, P. MARQUETAND: Machine Learning Enables Long Time Scale Molecular Photodynamics Simulations, *Chem. Sci.*, **10**, 8100 (2019).

[65] T. J. FRANKCOMBE, M. A. COLLINS, G. A. WORTH: Converged Quantum Dynamics with Modified Shepard Interpolation and Gaussian Wave Packets, *Chemical Physics Letters*, **489**, 242 (2010).

[66] J. W. PARK, Y. M. RHEE: Towards the Realization of Ab Initio Dynamics at the Speed of Molecular Mechanics: Simulations with Interpolated Diabatic Hamiltonian, *ChemPhysChem*, **15**, 3183 (2014).

[67] M. NOTTOLI, P. MAZZEO, F. LIPPARINI, L. CUPELLINI, B. MENNUCCI: A ΔSCF Model for Excited States within a Polarisable Embedding, *Mol. Phys.*, **121**, e2089605 (2023).

[68] M. MALIŠ, S. LUBER: Trajectory Surface Hopping Nonadiabatic Molecular Dynamics with Kohn–Sham ΔSCF for Condensed-Phase Systems, *J. Chem. Theory Comput.*, **16**, 4071 (2020).

[69] H. KÖPPEL, W. DOMCKE, L. S. CEDERBAUM: Theory of Vibronic Coupling in Linear Molecules, *J. Chem. Phys.*, **74**, 2945 (1981).

[70] H.-D. MEYER, F. GATTI, G. A. WORTH: *Multidimensional Quantum Dynamics: MCTDH Theory and Applications*, John Wiley & Sons (2009).

[71] H.-D. Meyer: Studying Molecular Quantum Dynamics with the Multiconfiguration Time-Dependent Hartree Method, *WIREs Computational Molecular Science*, **2**, 351 (2012).

[72] F. Plasser, S. Gómez, M. F. S. J. Menger, S. Mai, L. González: Highly Efficient Surface Hopping Dynamics Using a Linear Vibronic Coupling Model, *Phys. Chem. Chem. Phys.*, **21**, 57 (2019).

[73] S. Mai, M. Richter, M. Heindl, M. F. S. J. Menger, A. Atkins, M. Ruckenbauer, F. Plasser, L. M. Ibele, S. Kropf, M. Oppel, P. Marquetand, L. González: SHARC2.1: Surface Hopping Including Arbitrary Couplings — Program Package for Non-Adiabatic Dynamics (2019).

[74] J. P. Zobel, M. Heindl, F. Plasser, S. Mai, L. González: Surface Hopping Dynamics on Vibronic Coupling Models, *Acc. Chem. Res.*, **54**, 3760 (2021).

[75] S. Polonius, O. Zhuravel, B. Bachmair, S. Mai: LVC/MM: A Hybrid Linear Vibronic Coupling/Molecular Mechanics Model with Distributed Multipole-Based Electrostatic Embedding for Highly Efficient Surface Hopping Dynamics in Solution, *J. Chem. Theory Comput.*, **19**, 7171 (2023).

[76] S. Polonius, D. Lehrner, L. González, S. Mai: Resolving Photoinduced Femtosecond Three-Dimensional Solute–Solvent Dynamics through Surface Hopping Simulations, *J. Chem. Theory Comput.*, **20**, 4738 (2024).

[77] J. S. Briggs, J. M. Rost: On the Derivation of the Time-Dependent Equation of Schrödinger, *Foundations of Physics*, **31**, 693 (2001).

[78] A. Szabo, N. L. Ostlund: *Modern Quantum Chemistry: Introduction to Advanced Electronic Structure Theory*, Dover Publications, New York, 1 edition (1996).

[79] D. J. Tannor: *Introduction to Quantum Mechanics : A Time-Dependent Perspective*, University Science Books, Sausalito, CA (2007).

[80] L. Piela: *Ideas of Quantum Chemistry*, Elsevier (2006).

[81] R. S. Mulliken, C. C. J. Roothaan: Broken Bottlenecks and the Future of Molecular Quantum Mechanics*, *Proc. Natl. Acad. Sci.*, **45**, 394 (1959).

[82] Q. Meng, H.-D. Meyer: A Multilayer MCTDH Study on the Full Dimensional Vibronic Dynamics of Naphthalene and Anthracene Cations, *J. Chem. Phys.*, **138**, 014313 (2013).

[83] W. F. Van Gunsteren, H. J. C. Berendsen: A Leap-frog Algorithm for Stochastic Dynamics, *Molecular Simulation*, **1**, 173 (1988).

[84] L. Verlet: Computer "Experiments" on Classical Fluids. I. Thermodynamical Properties of Lennard-Jones Molecules, *Phys. Rev.*, **159**, 98 (1967).

[85] X. Li, J. C. Tully, H. B. Schlegel, M. J. Frisch: Ab Initio Ehrenfest Dynamics, *J. Chem. Phys.*, **123**, 084106 (2005).

[86] F. Agostini, B. F. E. Curchod: Different Flavors of Nonadiabatic Molecular Dynamics, *WIREs Comput. Mol. Sci.*, **9**, e1417 (2019).

[87] J. C. Tully: Perspective: Nonadiabatic Dynamics Theory, *J. Chem. Phys.*, **137**, 22A301 (2012).

[88] M. F. Herman: Choosing a Good Representation of the Quantum State Wave Functions for Semiclassical Surface Hopping Calculations, *J. Chem. Phys.*, **111**, 10427 (1999).

[89] F. Plasser, G. Granucci, J. Pittner, M. Barbatti, M. Persico, H. Lischka: Surface Hopping Dynamics Using a Locally Diabatic Formalism: Charge Transfer in the Ethylene Dimer Cation and Excited State Dynamics in the 2-Pyridone Dimer, *J. Chem. Phys.*, **137**, 22A514 (2012).

[90] G. Granucci, M. Persico, A. Zoccante: Including Quantum Decoherence in Surface Hopping, *J. Chem. Phys.*, **133**, 134111 (2010).

[91] J. E. Subotnik, A. Jain, B. Landry, A. Petit, W. Ouyang, N. Bellonzi: Understanding the Surface Hopping View of Electronic Transitions and Decoherence, *Annu. Rev. Phys. Chem.*, **67**, 387 (2016).

[92] E. B. Wilson, J. C. Decius, P. C. Cross: *Molecular Vibrations: The Theory of Infrared and Raman Vibrational Spectra*, McGraw-Hill, New York (1955).

[93] Y. J. Yan, S. Mukamel: Eigenstate-free, Green Function, Calculation of Molecular Absorption and Fluorescence Line Shapes, *J. Chem. Phys.*, **85**, 5908 (1986).

[94] M. Fumanal, F. Plasser, S. Mai, C. Daniel, E. Gindensperger: Interstate Vibronic Coupling Constants between Electronic Excited States for Complex Molecules, *J. Chem. Phys.*, **148**, 124119 (2018).

[95] M. Reiher, A. Wolf: *Relativistic Quantum Chemistry: The Fundamental Theory of Molecular Science*, John Wiley & Sons (2015).

[96] T. J. Penfold, E. Gindensperger, C. Daniel, C. M. Marian: Spin-Vibronic Mechanism for Intersystem Crossing, *Chem. Rev.*, **118**, 6975 (2018).

[97] M. E. Madjet, A. Abdurahman, T. Renger: Intermolecular Coulomb Couplings from Ab Initio Electrostatic Potentials:\hspace0.167em Application to Optical Transitions of Strongly Coupled Pigments in Photosynthetic Antennae and Reaction Centers, *J. Phys. Chem. B*, **110**, 17268 (2006).

[98] G. D. Scholes: Long-Range Resonance Energy Transfer in Molecular Systems, *Annu. Rev. Phys. Chem.*, **54**, 57 (2003).

[99] C. I. Bayly, P. Cieplak, W. Cornell, P. A. Kollman: A Well-Behaved Electrostatic Potential Based Method Using Charge Restraints for Deriving Atomic Charges: The RESP Model, *J. Phys. Chem.*, **97**, 10269 (1993).

[100] U. C. Singh, P. A. Kollman: An Approach to Computing Electrostatic Charges for Molecules, *J. Comput. Chem.*, **5**, 129 (1984).

[101] S. R. Cox, D. E. Williams: Representation of the molecular electrostatic potential by a net atomic charge model, *J. Comput. Chem.*, **2**, 304 (1981).

[102] B. H. Besler, K. M. Merz Jr., P. A. Kollman: Atomic Charges Derived from Semiempirical Methods, *J. Comput. Chem.*, **11**, 431 (1990).

[103] M. J. Frisch, G. W. Trucks, H. B. Schlegel, G. E. Scuseria, M. A. Robb, J. R. Cheeseman, G. Scalmani, V. Barone, G. A. Petersson, H. Nakatsuji, X. Li, M. Caricato, A. V. Marenich, J. Bloino, B. G. Janesko, R. Gomperts, B. Mennucci, H. P. Hratchian, J. V. Ortiz, A. F. Izmaylov, J. L. Sonnenberg, D. Williams-Young, F. Ding, F. Lipparini, F. Egidi, J. Goings, B. Peng, A. Petrone, T. Henderson, D. Ranasinghe, V. G. Zakrzewski, J. Gao, N. Rega, G. Zheng, W. Liang, M. Hada, M. Ehara, K. Toyota, R. Fukuda, J. Hasegawa, M. Ishida, T. Nakajima, Y. Honda, O. Kitao, H. Nakai, T. Vreven, K. Throssell, J. A. Montgomery, Jr., J. E. Peralta, F. Ogliaro, M. J. Bearpark, J. J. Heyd, E. N. Brothers, K. N. Kudin, V. N. Staroverov, T. A. Keith, R. Kobayashi, J. Normand, K. Raghavachari, A. P. Rendell, J. C. Burant, S. S. Iyengar, J. Tomasi, M. Cossi, J. M. Millam, M. Klene, C. Adamo, R. Cammi, J. W. Ochterski, R. L. Martin, K. Morokuma, O. Farkas, J. B. Foresman, D. J. Fox: Gaussian 16 Revision C.01 (2016).

[104] V. I. LEBEDEV: Quadratures on a Sphere, *USSR Comput. Math. Math. Phys.*, **16**, 10 (1976).

[105] A. J. STONE: Distributed Multipole Analysis, or How to Describe a Molecular Charge Distribution, *Chem. Phys. Lett.*, **83**, 233 (1981).

[106] A. STONE: *The Theory of Intermolecular Forces*, OUP Oxford (2013).

[107] W. KUTZELNIGG: Zwischenmolekulare Kräfte, in *Einführung in die Theoretische Chemie*, chapter 15, 469–490, John Wiley & Sons, Ltd (2001).

[108] S. MAI, D. AVAGLIANO, M. HEINDL, P. MARQUETAND, M. F. S. J. MENGER, M. OPPEL, F. PLASSER, S. POLONIUS, M. RUCKENBAUER, Y. SHU, D. G. TRUHLAR, L. ZHANG, P. ZOBEL, L. GONZÁLEZ: SHARC3.0: Surface Hopping Including Arbitrary Couplings — Program Package for Non-Adiabatic Dynamics (2023).

[109] M. F. S. J. MENGER: *Development of Multiscale Models for the Static and Dynamic Description of Photoinduced Processes in Embedded Systems*, Ph.D. thesis, University of Vienna (2019).

[110] P. EASTMAN, J. SWAILS, J. D. CHODERA, R. T. MCGIBBON, Y. ZHAO, K. A. BEAUCHAMP, L.-P. WANG, A. C. SIMMONETT, M. P. HARRIGAN, C. D. STERN, R. P. WIEWIORA, B. R. BROOKS, V. S. PANDE: OpenMM 7: Rapid Development of High Performance Algorithms for Molecular Dynamics, *PLOS Comput. Biol.*, **13**, e1005659 (2017).

[111] F. PLASSER: TheoDORE: A Toolbox for a Detailed and Automated Analysis of Electronic Excited State Computations, *J. Chem. Phys.*, **152**, 084108 (2020).

[112] M. ABRAHAM, A. ALEKSEENKO, V. BASOV, C. BERGH, E. BRIAND, A. BROWN, M. DOIJADE, G. FIORIN, S. FLEISCHMANN, S. GORELOV, G. GOUAILLARDET, A. GREY, M. E. IRRGANG, F. JALALYPOUR, J. JORDAN, C. KUTZNER, J. A. LEMKUL, M. LUNDBORG, P. MERZ, V. MILETIC, D. MOROZOV, J. NABET, S. PALL, A. PASQUADIBISCEGLIE, M. PELLEGRINO, H. SANTUZ, R. SCHULZ, T. SHUGAEVA, A. SHVETSOV, A. VILLA, S. WINGBERMUEHLE, B. HESS, E. LINDAHL: GROMACS 2024.2 Manual (2024).

[113] W. KABSCH: A Solution for the Best Rotation to Relate Two Sets of Vectors, *Acta Crystallogr. A*, **32**, 922 (1976).

[114] J. TOWNSEND: Differentiating the Singular Value Decomposition, Technical report, Technical Report 2016 (2016).

[115] J. W. PARK, Y. M. RHEE: Diabatic Population Matrix Formalism for Performing Molecular Mechanics Style Simulations with Multiple Electronic States, *J. Chem. Theory Comput.*, **10**, 5238 (2014).

[116] Q. SUN, T. C. BERKELBACH, N. S. BLUNT, G. H. BOOTH, S. GUO, Z. LI, J. LIU, J. D. MCCLAIN, E. R. SAYFUTYAROVA, S. SHARMA, S. WOUTERS, G. K.-L. CHAN: PySCF: The Python-based Simulations of Chemistry Framework, *WIREs Comput. Mol. Sci.*, **8**, e1340 (2018).

[117] Q. SUN, X. ZHANG, S. BANERJEE, P. BAO, M. BARBRY, N. S. BLUNT, N. A. BOGDANOV, G. H. BOOTH, J. CHEN, Z.-H. CUI, J. J. ERIKSEN, Y. GAO, S. GUO, J. HERMANN, M. R. HERMES, K. KOH, P. KOVAL, S. LEHTOLA, Z. LI, J. LIU, N. MARDIROSSIAN, J. D. MCCLAIN, M. MOTTA, B. MUSSARD, H. Q. PHAM, A. PULKIN, W. PURWANTO, P. J. ROBINSON, E. RONCA, E. R. SAYFUTYAROVA, M. SCHEURER, H. F. SCHURKUS, J. E. T. SMITH, C. SUN, S.-N. SUN, S. UPADHYAY, L. K. WAGNER, X. WANG, A. WHITE, J. D. WHITFIELD, M. J. WILLIAMSON, S. WOUTERS, J. YANG, J. M. YU, T. ZHU, T. C. BERKELBACH, S. SHARMA, A. Y. SOKOLOV, G. K.-L. CHAN: Recent Developments in the PySCF Program Package, *J. Chem. Phys.*, **153**, 024109 (2020).

[118] F. FURCHE, R. AHLRICHS: Adiabatic Time-Dependent Density Functional Methods for Excited State Properties, *J. Chem. Phys.*, **117**, 7433 (2002).

[119] M. E. CASIDA: Time-Dependent Density Functional Response Theory for Molecules, in *Recent Adv. Density Funct. Methods*, 155–192, World Scientific, Singapore (1995).

[120] A. ALENAIZAN, L. A. BURNS, C. D. SHERRILL: Python Implementation of the Restrained Electrostatic Potential Charge Model, *Int. J. Quantum Chem.*, **120**, e26035 (2020).

[121] C. R. HARRIS, K. J. MILLMAN, S. J. VAN DER WALT, R. GOMMERS, P. VIRTANEN, D. COURNAPEAU, E. WIESER, J. TAYLOR, S. BERG, N. J. SMITH, R. KERN, M. PICUS, S. HOYER, M. H. VAN KERKWIJK, M. BRETT, A. HALDANE, J. F. DEL RÍO, M. WIEBE, P. PETERSON, P. GÉRARD-MARCHANT, K. SHEPPARD, T. REDDY, W. WECKESSER, H. ABBASI, C. GOHLKE, T. E. OLIPHANT: Array Programming with NumPy, *Nature*, **585**, 357 (2020).

[122] B. LIU: The Simultaneous Expansion Method for the Iterative Solution of Several of the Lowest-Lying Eigenvalues and Corresponding Eigenvectors of Large Real-Symmetric Matrices, *Numer. Algorithms Chem.: Algebr. Methods*, 49–53 (1978).

[123] N. J. ENGLISH, J. S. TSE: Density Fluctuations in Liquid Water, *Phys. Rev. Lett.*, **106**, 037801 (2011).

[124] B. A. STRØM, J.-M. SIMON, S. K. SCHNELL, S. KJELSTRUP, J. HE, D. BEDEAUX: Size and Shape Effects on the Thermodynamic Properties of Nanoscale Volumes of Water, *Phys. Chem. Chem. Phys.*, **19**, 9016 (2017).

[125] R. A. FINE, F. J. MILLERO: Compressibility of Water as a Function of Temperature and Pressure, *J. Chem. Phys.*, **59**, 5529 (2003).

[126] W. L. JORGENSEN, J. CHANDRASEKHAR, J. D. MADURA, R. W. IMPEY, M. L. KLEIN: Comparison of Simple Potential Functions for Simulating Liquid Water, *J. Chem. Phys.*, **79**, 926 (1983).

[127] M. P. BLAKELEY, S. S. HASNAIN, S. V. ANTONYUK: Sub-Atomic Resolution X-ray Crystallography and Neutron Crystallography: Promise, Challenges and Potential, *Int. Union Crystallogr.*, **2**, 464 (2015).

[128] V. R. A. DUBACH, A. GUSKOV: The Resolution in X-ray Crystallography and Single-Particle Cryogenic Electron Microscopy, *Crystals*, **10**, 580 (2020).

[129] D. W. SCOTT: *Multivariate Density Estimation: Theory, Practice, and Visualization*, John Wiley & Sons (2015).

[130] I. NARSKY, F. C. PORTER: *Statistical Analysis Techniques in Particle Physics: Fits, Density Estimation and Supervised Learning*, John Wiley & Sons (2013).

[131] R. D. LIPSCOMB, W. H. SHARKEY: Characterization and Polymerization of Thioacetone, *J. Polym. Sci. A-1: Polym. Chem.*, **8**, 2187 (1970).

[132] S. MAI, A. J. ATKINS, F. PLASSER, L. GONZÁLEZ: The Influence of the Electronic Structure Method on Intersystem Crossing Dynamics. The Case of Thioformaldehyde, *J. Chem. Theory Comput.*, **15**, 3470 (2019).

[133] L. ZHANG, Y. SHU, S. SUN, D. G. TRUHLAR: Direct Coherent Switching with Decay of Mixing for Intersystem Crossing Dynamics of Thioformaldehyde: The Effect of Decoherence, *J. Chem. Phys.*, **154**, 094310 (2021).

[134] R. BORREGO-VARILLAS, D. C. TELES-FERREIRA, A. NENOV, I. CONTI, L. GANZER, C. MANZONI, M. GARAVELLI, A. MARIA DE PAULA, G. CERULLO: Observation of the Sub-100 Femtosecond Population of a Dark State in a Thiobase Mediating Intersystem Crossing, *J. Am. Chem. Soc.*, **140**, 16087 (2018).

[135] J. A. Sánchez-Rodríguez, A. Mohamadzade, S. Mai, B. Ashwood, M. Pollum, P. Marquetand, L. González, C. E. Crespo-Hernández, S. Ullrich: 2-Thiouracil Intersystem Crossing Photodynamics Studied by Wavelength-Dependent Photoelectron and Transient Absorption Spectroscopies, *Phys. Chem. Chem. Phys.*, **19**, 19756 (2017).

[136] S. Mai, M. Pollum, L. Martínez-Fernández, N. Dunn, P. Marquetand, I. Corral, C. E. Crespo-Hernández, L. González: The Origin of Efficient Triplet State Population in Sulfur-Substituted Nucleobases, *Nat. Commun.*, **7**, 13077 (2016).

[137] M. Pollum, L. Martínez-Fernández, C. E. Crespo-Hernández: Photochemistry of Nucleic Acid Bases and Their Thio- and Aza-Analogues in Solution, in M. Barbatti, A. C. Borin, S. Ullrich (editors), *Photoinduced Phenomena in Nucleic Acids I: Nucleobases in the Gas Phase and in Solvents*, Topics in Current Chemistry, 245–327, Springer International Publishing, Cham (2015).

[138] M. Pollum, S. Jockusch, C. E. Crespo-Hernández: 2,4-Dithiothymine as a Potent UVA Chemotherapeutic Agent, *J. Am. Chem. Soc.*, **136**, 17930 (2014).

[139] X. He, V. H. Man, W. Yang, T.-S. Lee, J. Wang: A Fast and High-Quality Charge Model for the next Generation General AMBER Force Field, *J. Chem. Phys.*, **153**, 114502 (2020).

[140] R. Sankararamakrishnan, K. Konvicka, E. L. Mehler, H. Weinstein: Solvation in Simulated Annealing and High-Temperature Molecular Dynamics of Proteins: A Restrained Water Droplet Model, *Int. J. Quantum Chem.*, **77**, 174 (2000).

[141] A. C. Legon, D. J. Millen: Angular Geometries and Other Properties of Hydrogen-Bonded Dimers: A Simple Electrostatic Interpretation of the Success of the Electron-Pair Model, *Chem. Soc. Rev.*, **16**, 467 (1987).

[142] J. E. Del Bene: Molecular Orbital Theory of the Hydrogen Bond. IV. The Dimers ROH···OCH2, *J. Chem. Phys.*, **58**, 3139 (1973).

[143] E. Biasin, Z. W. Fox, A. Andersen, K. Ledbetter, K. S. Kjær, R. Alonso-Mori, J. M. Carlstad, M. Chollet, J. D. Gaynor, J. M. Glownia, K. Hong, T. Kroll, J. H. Lee, C. Liekhus-Schmaltz, M. Reinhard, D. Sokaras, Y. Zhang, G. Doumy, A. M. March, S. H. Southworth, S. Mukamel, K. J. Gaffney, R. W. Schoenlein, N. Govind, A. A. Cordones, M. Khalil: Direct Observation of Coherent Femtosecond Solvent Reorganization Coupled to Intramolecular Electron Transfer, *Nat. Chem.*, **13**, 343 (2021).

[144] O. S. Wenger: Is Iron the New Ruthenium?, *Chem. – Eur. J.*, **25**, 6043 (2019).

[145] S. De Kreijger, O. Schott, L. Troian-Gautier, E. Cauët, G. S. Hanan, B. Elias: Red Absorbing Cyclometalated Ir(III) Diimine Photosensitizers Competent for Hydrogen Photocatalysis, *Inorg. Chem.*, **61**, 5245 (2022).

[146] M. Pastore, S. Caramori, P. C. Gros: Iron-Sensitized Solar Cells (FeSSCs), *Acc. Chem. Res.*, **57**, 439 (2024).

[147] S. Bonnet: Ruthenium-Based Photoactivated Chemotherapy, *J. Am. Chem. Soc.*, **145**, 23397 (2023).

[148] M. Chergui: Ultrafast Photophysics of Transition Metal Complexes, *Acc. Chem. Res.*, **48**, 801 (2015).

[149] N. H. Damrauer, G. Cerullo, A. Yeh, T. R. Boussie, C. V. Shank, J. K. McCusker: Femtosecond Dynamics of Excited-State Evolution in [Ru(Bpy)3]2+, *Science*, **275**, 54 (1997).

[150] D. G. Brown, N. Sanguantrakun, B. Schulze, U. S. Schubert, C. P. Berlinguette: Bis(Tridentate) Ruthenium–Terpyridine Complexes Featuring Microsecond Excited-State Lifetimes, *J. Am. Chem. Soc.*, **134**, 12354 (2012).

[151] J. E. Monat, J. K. McCusker: Femtosecond Excited-State Dynamics of an Iron(II) Polypyridyl Solar Cell Sensitizer Model, *J. Am. Chem. Soc.*, **122**, 4092 (2000).

[152] S. Nozawa, T. Sato, M. Chollet, K. Ichiyanagi, A. Tomita, H. Fujii, S.-i. Adachi, S.-y. Koshihara: Direct Probing of Spin State Dynamics Coupled with Electronic and Structural Modifications by Picosecond Time-Resolved XAFS, *J. Am. Chem. Soc.*, **132**, 61 (2010).

[153] K. S. Kjær, K. Kunnus, T. C. B. Harlang, T. B. V. Driel, K. Ledbetter, R. W. Hartsock, M. E. Reinhard, S. Koroidov, L. Li, M. G. Laursen, E. Biasin, F. B. Hansen, P. Vester, M. Christensen, K. Haldrup, M. M. Nielsen, P. Chabera, Y. Liu, H. Tatsuno, C. Timm, J. Uhlig, V. Sundstöm, Z. Németh, D. S. Szemes, É. Bajnóczi, G. Vankó, R. Alonso-Mori, J. M. Glownia, S. Nelson, M. Sikorski, D. Sokaras, H. T. Lemke, S. E. Canton, K. Wärnmark, P. Persson, A. A. Cordones, K. J. Gaffney: Solvent Control of Charge Transfer Excited State Relaxation Pathways in [Fe(2,2′-Bipyridine)(CN)4]2-, *Phys. Chem. Chem. Phys.*, **20**, 4238 (2018).

[154] Y. Liu, T. Harlang, S. E. Canton, P. Chábera, K. Suárez-Alcántara, A. Fleckhaus, D. A. Vithanage, E. Göransson, A. Corani, R. Lomoth, V. Sundström, K. Wärnmark: Towards Longer-Lived Metal-to-Ligand Charge Transfer States of Iron(II) Complexes: An N-heterocyclic Carbene Approach, *Chem. Commun.*, **49**, 6412 (2013).

[155] T. C. B. Harlang, Y. Liu, O. Gordivska, L. A. Fredin, C. S. Ponseca, P. Huang, P. Chábera, K. S. Kjaer, H. Mateos, J. Uhlig, R. Lomoth, R. Wallenberg, S. Styring, P. Persson, V. Sundström, K. Wärnmark: Iron Sensitizer Converts Light to Electrons with 92% Yield, *Nature Chem*, **7**, 883 (2015).

[156] T. Duchanois, T. Etienne, C. Cebrián, L. Liu, A. Monari, M. Beley, X. Assfeld, S. Haacke, P. C. Gros: An Iron-Based Photosensitizer with Extended Excited-State Lifetime: Photophysical and Photovoltaic Properties, *European Journal of Inorganic Chemistry*, **2015**, 2469 (2015).

[157] W. Zhang, K. S. Kjær, R. Alonso-Mori, U. Bergmann, M. Chollet, L. A. Fredin, R. G. Hadt, R. W. Hartsock, T. Harlang, T. Kroll, K. Kubiček, H. T. Lemke, H. W. Liang, Y. Liu, M. M. Nielsen, P. Persson, J. S. Robinson, E. I. Solomon, Z. Sun, D. Sokaras, T. B. van Driel, T.-C. Weng, D. Zhu, K. Wärnmark, V. Sundström, K. J. Gaffney: Manipulating Charge Transfer Excited State Relaxation and Spin Crossover in Iron Coordination Complexes with Ligand Substitution, *Chemical Science*, **8**, 515 (2017).

[158] K. Kunnus, L. Li, C. J. Titus, S. Jun Lee, M. E. Reinhard, S. Koroidov, K. S. Kjær, K. Hong, K. Ledbetter, W. B. Doriese, G. C. O'Neil, D. S. Swetz, J. N. Ullom, D. Li, K. Irwin, D. Nordlund, A. A. Cordones, K. J. Gaffney: Chemical Control of Competing Electron Transfer Pathways in Iron Tetracyano-Polypyridyl Photosensitizers, *Chemical Science*, **11**, 4360 (2020).

[159] S. Nangia, A. W. Jasper, T. F. Miller, III, D. G. Truhlar: Army Ants Algorithm for Rare Event Sampling of Delocalized Nonadiabatic Transitions by Trajectory Surface Hopping and the Estimation of Sampling Errors by the Bootstrap Method, *J. Chem. Phys.*, **120**, 3586 (2004).

[160] P. Pracht, F. Bohle, S. Grimme: Automated Exploration of the Low-Energy Chemical Space with Fast Quantum Chemical Methods, *Phys. Chem. Chem. Phys.*, **22**, 7169 (2020).

[161] S. Mai, P. Marquetand, L. González: A Static Picture of the Relaxation and Intersystem Crossing Mechanisms of Photoexcited 2-Thiouracil, *J. Phys. Chem. A*, **119**, 9524 (2015).

[162] S. Gómez, M. Heindl, A. Szabadi, L. González: From Surface Hopping to Quantum Dynamics and Back. Finding Essential Electronic and Nuclear Degrees of Freedom and Optimal Surface Hopping Parameters, *J. Phys. Chem. A*, **123**, 8321 (2019).

[163] M. Janeček, P. Kührová, V. Mlýnský, M. Otyepka, J. Šponer, P. Banáš: W-RESP: Well-Restrained Electrostatic Potential-Derived Charges. Revisiting the Charge Derivation Model, *J. Chem. Theory Comput.* (2021).

[164] R. S. Mulliken: Electronic Population Analysis on LCAO–MO Molecular Wave Functions. I, *J. Chem. Phys.*, **23**, 1833 (1955).

[165] F. Aleotti, D. Aranda, M. Yaghoubi Jouybari, M. Garavelli, A. Nenov, F. Santoro: Parameterization of a Linear Vibronic Coupling Model with Multiconfigurational Electronic Structure Methods to Study the Quantum Dynamics of Photoexcited Pyrene, *J. Chem. Phys.*, **154**, 104106 (2021).

[166] T. Piteša, S. Polonius, L. González, S. Mai: Excitonic Configuration Interaction: Going Beyond the Frenkel Exciton Model, *J. Chem. Theory Comput.*, **20**, 5609 (2024).

APPENDIX

A

This appendix contains the reprints of the two publications and the manuscript draft which are parts of this thesis, and were discussed in the previous chapters. Section A.1 contains the two reprinted publications that contain the method development and validation of the LVC/MM method (Section A.1.1), and the excited-state dynamics of two small thiocarbonyls in water as well as the theory behind the construction of 3D-SDFs (Section A.1.2). Section A.2 contains the manuscript draft on the excited-state dynamics of $[\mathrm{Fe(CN)_4(bipy)}]^{2-}$ in water and the corresponding supporting information.

During the course of my PhD studies, the following additional publication, which is not part of this thesis, has been produced:

T. PITEŠA, S. POLONIUS, L. GONZÁLEZ, S. MAI: Excitonic Configuration Interaction: Going Beyond the Frenkel Exciton Model, *J. Chem. Theory Comput.*, **20**, 5609 (2024).
Contribution: Suggestion of Guanine quadruplex as test system, algorithms for extraction and processing of density matrices and basis set information.

APPENDIX A.1.1

LVC/MM: A Hybrid Linear Vibronic Coupling/Molecular Mechanics Model with Distributed Multipole-Based Electrostatic Embedding for Highly Efficient Surface Hopping Dynamics in Solution

Severin Polonius, Oleksandra Zhuravel, Brigitta Bachmair, Sebastian Mai

J. Chem. Theory Comput., **19**, 7171–7186 (2023).
https://doi.org/10.1021/acs.jctc.3c00805

Contributions:

Severin Polonius ...devised the necessary algorithms, made all necessary developments in SHARC, performed the analyses, wrote the first draft and finalized the manuscript.

Oleksandra Zhuravel ...contributed supplementary computations.

Brigitta Bachmair ...implemented the droplet and tether force algorithms, and contributed to the final manuscript.

Sebastian Mai ...planned the manuscript with the authors, supervised all developments, analyses and writing of the initial draft, and contributed to the final manuscript.

Article reprinted under the terms of the Creative Commons CC BY license.

JCTC Journal of Chemical Theory and Computation

Open Access

This article is licensed under CC-BY 4.0

pubs.acs.org/JCTC

Article

LVC/MM: A Hybrid Linear Vibronic Coupling/Molecular Mechanics Model with Distributed Multipole-Based Electrostatic Embedding for Highly Efficient Surface Hopping Dynamics in Solution

Severin Polonius, Oleksandra Zhuravel, Brigitta Bachmair, and Sebastian Mai*

Cite This: J. Chem. Theory Comput. 2023, 19, 7171−7186

Read Online

ACCESS | Metrics & More | Article Recommendations | Supporting Information

Downloaded via UNIV OF VIENNA on March 4, 2024 at 07:57:13 (UTC).
See https://pubs.acs.org/sharingguidelines for options on how to legitimately share published articles.

ABSTRACT: We present a theoretical framework for a hybrid linear vibronic coupling model electrostatically embedded into a molecular mechanics environment, termed the linear vibronic coupling/molecular mechanics (LVC/MM) method, for the surface hopping including arbitrary coupling (SHARC) molecular dynamics package. Electrostatic embedding is realized through the computation of interactions between environment point charges and distributed multipole expansions (DMEs, up to quadrupoles) that represent each electronic state and transition densities in the diabatic basis. The DME parameters are obtained through a restrained electrostatic potential (RESP) fit, which we extended to yield higher-order multipoles. We also implemented in SHARC a scheme for achieving roto-translational invariance of LVC models as well as a general quantum mechanics/molecular mechanics (QM/MM) interface, an OpenMM interface, and restraining potentials for simulating liquid droplets. Using thioformaldehyde in water as a test case, we demonstrate that LVC/MM can accurately reproduce the solvation structure and energetics of rigid solutes, with errors on the order of 1−2 kcal/mol compared to a BP86/MM reference. The implementation in SHARC is shown to be very efficient, enabling the simulation of trajectories on the nanosecond time scale in a matter of days.

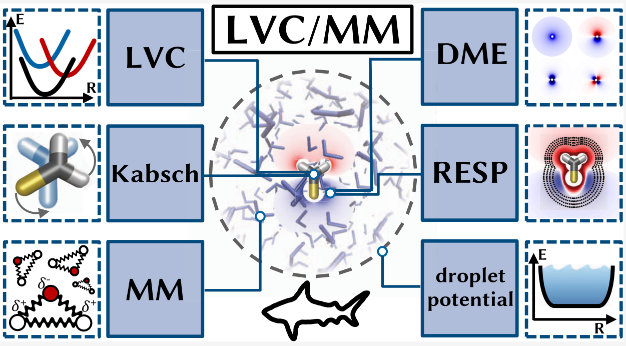

1. INTRODUCTION

In computational studies on photoinduced processes in chemistry, biology, and materials sciences, nonadiabatic molecular dynamics (MD) simulations—MD simulations where more than one electronic state is considered—are nowadays an essential technique.[1−5] The trajectory surface hopping (TSH) method[6−8] is one of the widely adopted approaches for performing MD simulations of photoinduced processes. Using TSH, it is possible to simulate fundamental processes such as internal conversion (IC)[9] or intersystem crossing (ISC).[10−12] Therefore, TSH enables investigations into natural phenomena such as photoisomerization, photodissociation, and photocatalysis.[7] These phenomena not only occur in isolated molecules in the gas phase but are also important in solution or even aggregated molecular systems—which could be subsumed as "complex systems".[13]

Although TSH simulations (and other nonadiabatic dynamics techniques) can in principle elucidate essential details of the photoinduced process of molecular systems, they come at a sizable computational cost, especially for large systems. This cost arises because at every time step in TSH simulations, one needs to carry out excited-state electronic structure calculations, which yield the electronic potential energies, gradients, and nonadiabatic couplings. For typical small organic molecules, each such electronic structure calculation can take minutes to hours on modern computer hardware, scaling steeply with the system size. A simulation of a few picoseconds with adequate statistics requires thousands of electronic structure calculations multiplied by hundreds of trajectories, which leads to TSH projects that consume hundreds of thousands to millions of CPU hours.[3,14] For this reason, simulations of complex molecular systems interacting with their environment quickly reach the limits of feasibility, especially when such systems exhibit interesting dynamical processes on longer time scales.

If all relevant electronic excitations of a large system are localized only in a small region, one typically employs hybrid quantum mechanics/molecular mechanics (QM/MM) techniques.[15−17] In this way, the computational effort (dominated by the QM calculation) is focused on the relevant region, whereas the surroundings are treated at a lower cost. Despite the use of

Received: July 25, 2023
Published: October 3, 2023

ACS Publications

© 2023 The Authors. Published by American Chemical Society

https://doi.org/10.1021/acs.jctc.3c00805
J. Chem. Theory Comput. 2023, 19, 7171−7186

QM/MM, TSH projects can be computationally expensive—depending on the chosen method and QM region—and cheaper solutions are sought after. The latter include semiempirical methods in wave function or density functional theory (DFT) formulations,[18−20] the construction of the potential energy surface through interpolation,[21,22] the application of machine learning to predict energies, gradients, and other properties,[23,24] and excited-state self-consistent field methods (Δ*S*CF).[25,26]

Another possibility of representing the coupled excited-state potential energy surfaces of molecules in an inexpensive fashion is given by vibronic coupling models, in particular, linear vibronic coupling (LVC) models. Historically, LVC was predominantly employed in multiconfigurational time-dependent Hartree and other quantum dynamics simulations.[27] However, recently,[28] LVC was combined with TSH in the framework of the SHARC (surface hopping including arbitrary couplings) package.[29,30] The combination of TSH and LVC facilitates the description of the nonadiabatic gas-phase dynamics of rigid medium-sized molecules and transition-metal complexes with many states.[14] While the use of LVC is restricted to rigid systems, it offers some advantages over the other low-scaling methods mentioned above. For example, the LVC model is highly efficient: it scales linearly with the number of degrees of freedom and quadratically with the number of states, and it does not employ any basis functions or an SCF cycle. It can be fitted to any reference electronic structure calculation, thus potentially providing good accuracy at a minimal cost. The model can properly describe conical intersections with the ground state, which is not possible with single reference methods. In the context of TSH, it can also provide analytical nonadiabatic coupling vectors, even if the reference method/software does not.

In order to capitalize on the advantages of LVC models in the context of complex systems, the main goal of the present contribution is to extend the LVC Hamiltonian to make it compatible with electrostatic embedding and hence suitable for the QM/MM method. This novel approach, termed LVC/MM, can be used for highly efficient nonadiabatic dynamics simulations of stiff molecules embedded in an environment. In order to do so, we combine several previously published techniques.

We use a QM−MM interaction Hamiltonian that is based on an electrostatic embedding[15] scheme, where the MM charge distribution is represented by fixed point charges and directly affects the QM electronic states. As there are no explicit electronic wave functions in the LVC models, we represent all relevant electron and transition densities with static parameters. In order to represent these densities accurately—especially anisotropic densities like lone pairs, π-systems, or out-of-plane transition densities—we use an atomic multipole expansion[31,32] analogous to the one used in the AMOEBA force field.[33] These atomic multipoles are defined in a diabatic basis (the same basis is used to set up the LVC Hamiltonian), which has previously been suggested to enable a good charge representation even when the nuclear coordinates change.[34]

In order to obtain multipole parameters for all electronic states and transitions during the parameter generation of the LVC model, we employ the restrained electrostatic potential (RESP) method.[35] In RESP, atomic point charges are fitted to reproduce the ESP around the molecule, which ensures an accurate representation of electrostatic interactions with the surrounding solvent.[36] Alternative methods to obtain (multipolar) atomic charges are the distributed multipole analysis of Stone et al.[32,37] (as used in AMOEBA[33]) or various population analysis methods,[38−41] although the latter seem less suitable for reproducing the ESP.[35,42] In the present work, we extend the RESP method to fit not only point charges but also the higher multipole terms for both electron and transition densities.

In the following, we first describe the theory behind the essential ingredients of LVC/MM: the basic equations of the LVC model, achieving translational and rotational invariance for the LVC model, electrostatic embedding QM/MM, the QM−MM Coulomb interaction term, and finally the extended RESP procedure. Subsequently, we present the application of LVC/MM to the case of thioformaldehyde (CH_2S) in water. This molecule was used before as a testbed to compare electronic structure methods and decoherence schemes in TSH.[43,44] Note that thioformaldehyde is unstable under normal conditions (owing to fast oligomerization), but it is a useful model as the smallest molecule with a thiocarbonyl bond. Its nonadiabatic dynamics is governed by its $^1n\pi^* - {}^3\pi\pi^*$ (S_1−T_2) gap, which in the gas phase is too large to allow ISC.[43] Here, we investigate how the energies of the electronic states are influenced by the aqueous environment and especially how the $^1n\pi^* - {}^3\pi\pi^*$ (S_1−T_2) gap is affected. Focusing on these aspects, we scrutinize the performance of LVC/MM versus the reference QM/MM simulation at the BP86/def2-SVP level of theory in several aspects.

2. THEORY

In this section, we provide all of the working equations for the LVC/MM approach.

2.1. Linear Vibronic Coupling. In a general vibronic coupling model,[14,27,45] the diabatic electronic Hamiltonian matrix **V** (called LVC Hamiltonian here) is constructed from matrix elements V_{ij}, for all pairs of diabatic states *ij*, as

$$V_{ij} = \delta_{ij} V_0 + W_{ij} \tag{1}$$

where δ_{ij} is the Kronecker delta, V_0 is the reference potential, and W_{ij} is an element of the vibronic coupling matrix. V_0 is usually approximated as a harmonic potential[45] and is written in terms of the dimensionless mass−frequency-scaled normal coordinate vector **Q** as

$$V_0 = \frac{1}{2} \sum_n \omega_n Q_n^2 \tag{2}$$

where ω_n are the normal-mode frequencies. The components Q_n of **Q** for every normal mode *n* can be written as

$$Q_n = \sqrt{\omega_n} \sum_a^A \sqrt{M_a} K_{na} \bar{r}_a \tag{3}$$

Here, matrix **K** contains the orthogonal and mass-weighted normal-mode vectors for *A* atoms and $\bar{\mathbf{r}} = \mathbf{r} - \mathbf{r}_0$ is the Cartesian displacement vector from the reference geometry. In total, the reference potential V_0 can be calculated using eqs 2 and 3 from the current Cartesian coordinates **r**, the reference geometry $\mathbf{r}_0$, the transformation matrix **K**, the atomic masses **M**, and the normal-mode frequencies $\boldsymbol{\omega}$.

In an LVC model, the elements of **W** are expanded in a Taylor series around **Q** = 0 up to the linear terms

https://doi.org/10.1021/acs.jctc.3c00805
J. Chem. Theory Comput. 2023, 19, 7171−7186

$$W_{ij} = \begin{cases} \epsilon_i + \sum_n \kappa_n^{(i)} Q_n, & \text{if } i = j \\ \sum_n \lambda_n^{(ij)} Q_n, & \text{otherwise} \end{cases} \tag{4}$$

with the vertical excitation energies ϵ_i, and the intrastate and interstate vibronic coupling constants $\kappa_n^{(i)}$ and $\lambda_n^{(ij)}$.

The coupling constants $\kappa_n^{(i)}$ and $\lambda_n^{(ij)}$ are the first derivatives of the elements of the coupling matrix **W**, which is generally constructed in a diabatic basis. Thus, the values of the coupling constants cannot be extracted directly from the electronic structure calculations performed in the adiabatic basis. Therefore, in the construction of LVC models,[45] it is typically assumed that at the reference geometry ($\mathbf{Q} = \mathbf{0}$), the adiabatic and diabatic states coincide. This allows evaluating the $\kappa_n^{(i)}$ and $\lambda_n^{(ij)}$ as

$$\kappa_n^{(i)} = \left.\frac{\partial W_{ii}}{\partial Q_n}\right|_{\mathbf{Q}=\mathbf{0}}, \lambda_n^{(ij)} = \left.\frac{\partial W_{ij}}{\partial Q_n}\right|_{\mathbf{Q}=\mathbf{0}} \tag{5}$$

Hence, the $\kappa_n^{(i)}$ are accessible from the Cartesian gradient of the adiabatic state i at $\mathbf{Q} = 0$ after transformation into normal-mode coordinates. Likewise, $\lambda_n^{(ij)}$ can be obtained from nonadiabatic coupling (NAC) vectors.[28] As NAC vectors are only implemented for a few electronic structure methods, according to Fumanal et al.,[45] $\lambda_n^{(ij)}$ can alternatively be computed via finite differences of the excited-state energies after diabatization using wave function overlaps.

TSH simulations in SHARC typically employ electronic structure data (energies, gradients, couplings) in the eigenbasis of the molecular Coulomb Hamiltonian (MCH)[28,29] (often called the adiabatic basis). Therefore, we transform the diabatic LVC Hamiltonian **V** into the MCH eigenbasis and then calculate the energies and gradients. In detail, we obtain **Q** from the coordinates via eq 3 and calculate V_0 via eq 2. Subsequently, we calculate **W** (eq 4) and with it construct **V** via eq 1. The transformation to the MCH basis is done via the eigendecomposition

$$\mathbf{V} = \mathbf{U}^\dagger \mathbf{H} \mathbf{U} \tag{6}$$

where **H** is the Hamiltonian in the adiabatic basis, and **U** is a unitary transformation matrix. Analogous to many electronic structure methods, SOCs are only evaluated after diagonalization (here, by transforming diabatic SOCs η into the MCH basis) and added to the Hamiltonian as

$$\mathbf{H}' = \mathbf{H} + \mathbf{U}\eta\mathbf{U}^\dagger \tag{7}$$

Likewise, gradients $\frac{\partial \mathbf{V}}{\partial \mathbf{r}}$ are transformed as

$$\frac{\partial \mathbf{H}}{\partial \mathbf{r}} = \mathbf{U}\frac{\partial \mathbf{V}}{\partial \mathbf{r}}\mathbf{U}^\dagger \tag{8}$$

where $\frac{\partial \mathbf{V}}{\partial \mathbf{r}}$ is obtained from a coordinate transformation (following eq 3) of $\frac{\partial \mathbf{V}}{\partial \mathbf{Q}}$. Note that eq 8 also produces nonadiabatic coupling vectors.[28]

2.2. Rotationally and Translationally Invariant LVC.

The parametrization of the LVC Hamiltonian is done in terms of the normal-mode vector **Q**, which is obtained from Cartesian displacement vector $\overline{\mathbf{r}}$ and reference geometry $\mathbf{r}_0$ (eq 3). Here, the computation of the correct displacement vector requires that the current geometry **r** is aligned properly with the reference geometry $\mathbf{r}_0$. For TSH simulations in the gas phase, alignment is typically not a problem in the absence of roto-translational motion. However, in a system consisting of the LVC subsystem and environment, the position and orientation of the LVC subsystem can change due to diffusion processes.

For this reason, LVC/MM requires that the normal-mode vector **Q** be computed in a rotationally and translationally invariant fashion. This is achieved by superimposing (i.e., aligning) the current geometry $\mathbf{r}_\mathrm{S}$ onto $\mathbf{r}_0$ before computing **Q** with eq 3. In other words, we will switch the frame of reference and the coordinate system from the one in solution "S" to the one of the reference geometry "0". First, we calculate the centers of coordinates $\mathbf{c}_\mathrm{S}$ and $\mathbf{c}_0$ of $\mathbf{r}_\mathrm{S}$ and $\mathbf{r}_0$ as

$$\mathbf{c} = \frac{1}{A}\sum_a^A \mathbf{r}_a \tag{9}$$

Next, we shift the coordinates of all atoms a to the origin by subtracting to obtain $\mathbf{r}_{0,a} - \mathbf{c}_0 = \tilde{\mathbf{r}}_{0,a}$ and $\mathbf{r}_{\mathrm{S},a} - \mathbf{c}_\mathrm{S} = \tilde{\mathbf{r}}_{\mathrm{S},a}$. Using the Kabsch algorithm,[46] we determine the optimal rotation matrix $\mathbf{T}^\mathrm{rot}$, which transforms the current coordinates such that the root-mean-square distances with respect to the reference coordinates are minimized. The first step in this algorithm is the construction of a 3 × 3 cross-covariance matrix $\mathbf{K}_{\mathrm{S}0}$ and the computation of its singular value decomposition

$$\mathbf{K}_{\mathrm{S}0} = \tilde{\mathbf{r}}_\mathrm{S}^T \cdot \tilde{\mathbf{r}}_0 = \mathbf{U}\Sigma\mathbf{V}^T \tag{10}$$

where $\tilde{\mathbf{r}}_\mathrm{S}$ and $\tilde{\mathbf{r}}_0$ are $n_\mathrm{atom} \times 3$ matrices. We compute the optimal rotation matrix $\mathbf{T}_{\mathrm{S}0}^\mathrm{rot}$, which transforms from the solution frame "S" to the reference frame "0", as

$$\mathbf{T}_{\mathrm{S}0}^\mathrm{rot} = \mathbf{U}\begin{pmatrix} 1 & 0 & 0 \\ 0 & 1 & 0 \\ 0 & 0 & d \end{pmatrix}\mathbf{V}^T \tag{11}$$

where d is the determinant of $\mathbf{U}\mathbf{V}^T$. Finally, we transform $\mathbf{r}_\mathrm{S}$ into the reference frame $\mathbf{r}_{\mathrm{S}(0)}$ as

$$\mathbf{r}_{\mathrm{S}(0),\mathrm{a}} = (\mathbf{r}_{\mathrm{S},\mathrm{a}} - \mathbf{c}_\mathrm{S})\mathbf{T}_{\mathrm{S}0}^\mathrm{rot} + \mathbf{c}_0 \tag{12}$$

and subsequently calculate **Q** from eq 3 using $\mathbf{r}_{\mathrm{S}(0)}$ (i.e., in the reference frame).

This procedure enables the computation of the LVC Hamiltonian and thus energies of the LVC model in a rotationally and translationally invariant fashion. However, equivariant properties—like gradients or dipole moments, also need to be transformed back into the simulation frame. Dipole moments are simply rotated using the transpose of $\mathbf{T}_{0\mathrm{S}}^\mathrm{rot}$. The gradients of the diabatic LVC Hamiltonian matrix elements can be expanded as

$$\frac{\partial V_{ij}}{\partial r_{\mathrm{S},\mathrm{ax}}} = \sum_n \frac{\partial V_{ij}}{\partial Q_n} \sum_{a'}^{A} \sum_{x'}^{3} \frac{\partial Q_n}{\partial r_{\mathrm{S}(0),\mathrm{a}'\mathrm{x}'}} \frac{\partial r_{\mathrm{S}(0),\mathrm{a}'\mathrm{x}'}}{\partial r_{\mathrm{S},\mathrm{ax}}} \tag{13}$$

Here, the partial derivatives $\frac{\partial V_\mathrm{ij}}{\partial Q_n}$ on the right-hand side are given by differentiation of eqs 2 and 4, and the partial derivatives $\frac{\partial Q_n}{\partial r_{\mathrm{S}(0),\mathrm{ax}}}$ with respect to each atom a and direction x are given by differentiation of eq 3. The third term $\frac{\partial r_{\mathrm{S}(0),\mathrm{ax}}}{\partial r_{\mathrm{S},\mathrm{a}'\mathrm{x}'}}$ could in principle be obtained by differentiation of the Kabsch algorithm, although this is rather complicated (involving the differentiation of a singular value decomposition). Instead, we evaluate this term numerically, which is still efficient as it depends on only the number of atoms in the QM region (i.e., atoms considered in the LVC model).

2.3. Electrostatic Embedding. In a QM/MM calculation, the total molecular system is split into two parts; one that is described quantum-mechanically and the other by molecular mechanics.[15,47] In the widely used electrostatic embedding formalism,[15] the total energy of the system $E_{\mathrm{QM/MM}}$ can be constructed from the energies of three different calculations as

$$E_{\mathrm{QM/MM}} = E_{\mathrm{QM}}(\mathrm{QM};\ \mathrm{MMpc}) - E_{\mathrm{MM}}(\mathrm{QM}') + E_{\mathrm{MM}}(\mathrm{QM}' + \mathrm{MM}) \tag{14}$$

Here, $E_{\mathrm{QM}}(\mathrm{QM};\ \mathrm{MMpc})$ is the energy of the QM region at the QM level including the interaction of the point charges of the MM region with the QM region. $E_{\mathrm{MM}}(\mathrm{QM}' + \mathrm{MM})$ is the energy of the entire system at the MM level but with the point charges of the QM region set to zero. $E_{\mathrm{MM}}(\mathrm{QM}')$ is the energy of the QM region at the MM level also with the point charges of the QM region set to zero. Setting the point charges of the QM region to zero at the MM level avoids double-counting of the Coulomb interaction between QM and MM atoms, which is already considered in the QM calculation.

In LVC/MM, the Coulomb interaction between QM and MM atoms (a component of $E_{\mathrm{QM}}(\mathrm{QM};\ \mathrm{MMpc})$) is considered by extending the LVC Hamiltonian in eq 1 by interaction matrix $\mathbf{X}$

$$V_{ij} = \delta_{ij}V_0 + W_{ij} + X_{ij} \tag{15}$$

The interaction matrix elements X_{ij} formally consist of the electrostatic interaction between the point charges of the MM atoms b and the QM region's electronic densities $\rho^{(ij)}$ and nuclei a

$$X_{ij} = \sum_{b}^{B} q_b\left(-\int \mathrm{d}\mathbf{r}\frac{\rho^{(ij)}(\mathbf{r})}{|\mathbf{r} - \mathbf{r}_b|} + \delta_{ij}\sum_{a}^{A}\frac{Z_a}{|\mathbf{r}_a - \mathbf{r}_b|}\right) \tag{16}$$

Here, q_b are the point charges of the MM atoms, ρ^{ij} is the electronic density of state i of the QM region (transition density between i and j for $i \neq j$), and Z_a is the nuclear charge of atom a. Here, the diagonal elements X_{ii} produce solvent-induced energy shifts of the diabatic states, whereas the off-diagonal elements X_{ij} generate solvent-induced state mixing.

In an LVC calculation, we consider it unfavorable to work with the actual electron densities ρ^{ij}, as their representation (in terms of basis functions and density matrices) and evaluation (of the electrostatic interaction integrals) would present serious bottlenecks in the computation. Hence, the electrostatic potential (ESP) at a point $\mathbf{r}_b$ exerted by $\rho^{(ij)}$

$$V_{\mathrm{esp}}^{(ij)}(\mathbf{r}_b) = -\int \mathrm{d}\mathbf{r}\frac{\rho^{(ij)}(\mathbf{r})}{|\mathbf{r} - \mathbf{r}_b|} + \delta_{ij}\sum_{a}^{A}\frac{Z_a}{|\mathbf{r}_a - \mathbf{r}_b|} \tag{17}$$

needs to be approximated, as detailed in the next section.

2.4. Distributed Multipole Expansion. The distributed multipole expansion (DME) is a Tailor expansion of the Coulomb potential around the nuclear coordinates as centers.[37] Higher-order terms of the Tailor expansion capture anisotropies in the short-range electrostatics of the electronic density; we include terms up to the second order, i.e., up to quadrupoles on each atom. This allows representing, e.g., out-of-plane transition densities in planar molecules or lone pair electron clouds.

The ESP at a point in space $\mathbf{r}_g$ arising from all QM atoms a for a pair of states ij (see eq 17) can be approximated as a Taylor expansion

$$V_{\mathrm{esp}}^{(ij)}(\mathbf{r}_g) \approx \sum_{a}^{A}\left(\frac{P_a^{(ij)}}{|\mathbf{r}_{ag}|} + \sum_{x}^{3}\frac{P_{ax}^{(ij)}r_{agx}}{|\mathbf{r}_{ag}|^3} + \sum_{xx'}^{3}\frac{P_{axx'}^{(ij)}r_{agx}r_{agx'}}{2\,|\mathbf{r}_{ag}|^5} + O(\mathbf{r}_{ag}^7)\right) \tag{18}$$

Here, $P_a^{(ij)}$ is an atomic monopole parameter representing density ρ^{ij} and nuclear charge Z_a on atom a, equivalent to the partial charges typically used in most MM force fields.[33,48,49] Analogously, $P_{ax}^{(ij)}$ is a corresponding dipole term with the three Cartesian axes indexed by x, and $P_{axx'}^{(ij)}$ is a corresponding quadrupole term in the direction xx'. r_{agx} is a component of vector $\mathbf{r}_{ag}$, the difference vector between the coordinates of atom a and the point in space $\mathbf{r}_g$. This formula can be rewritten in terms of a sum over scalar products between a tensor $\mathbf{P}^{(ij)}$ containing multipole terms and a geometric tensor $\mathbf{T}$ containing all of the corresponding prefactors. For clarity, we use the index p to enumerate the different multipole elements on an atom a (in the order monopole, x, y, z, xx, yy, zz, xy, xz, yz). Then, the ESP is

$$V_{\mathrm{esp}}^{(ij)}(\mathbf{r}_g) = \sum_{a}^{A}\sum_{p}^{10}(P_{ap}^{(ij)}\cdot T_{apg}) \tag{19}$$

and the interaction elements of the LVC Hamiltonian become

$$X_{ij} = \sum_{b}^{B} q_b\sum_{a}^{A}\sum_{p}^{10}(P_{ap}^{(ij)}\cdot T_{apb}) \tag{20}$$

In order to compute the total LVC/MM gradients and nonadiabatic coupling vectors, we require the gradients of the interaction elements. The derivative with respect to the position of an MM atom b is

$$\frac{\partial X_{ij}}{\partial r_{\mathrm{S,bx}}} = q_b\sum_{a}^{A}\sum_{p}^{10}\left(P_{ap}^{(ij)}\cdot\frac{\partial T_{apb}}{\partial r_{\mathrm{S,bx}}}\right) \tag{21}$$

The gradients of the LVC atoms a are slightly more involved

$$\frac{\partial X_{ij}}{\partial r_{\mathrm{S,ax}}} = \sum_{b}^{B} q_b\sum_{p}^{10}\left(P_{ap}^{(ij)}\cdot\frac{\partial T_{apb}}{\partial r_{\mathrm{S,ax}}} + \frac{\partial P_{ap}^{(ij)}}{\partial r_{\mathrm{S,ax}}}\cdot T_{apb}\right) \tag{22}$$

For both equations, the multipole parameters $P_{ap}^{(ij)}$ are first rotated from the reference frame (in which they are defined) to the system frame. The derivative $\frac{\partial P_{ap}^{(ij)}}{\partial r_{S,ax}}$ arises because the rotation of the parameters depends on the position of the LVC atoms that enter the Kabsch algorithm (see the discussion of eq 13). This derivative can be computed numerically.

Because the LVC model based on eq 15 is defined on the diabatic electronic basis, the DME parameters $P_{ap}^{(ij)}$ also represent the electronic (transition) densities of the diabatic states. In this regard, the electrostatic LVC/MM model is related to the diabatic charge matrix approach of Park and Rhee,[34] who showed that diabatic charges retain validity for the same diabatic pair of states at different geometries.

https://doi.org/10.1021/acs.jctc.3c00805
J. Chem. Theory Comput. 2023, 19, 7171−7186

Although the use of constant diabatic charges in the LVC/MM model constitutes an approximation, we assume that this approximation is valid for the range of geometries for which the LVC model itself is valid. Thus, LVC/MM using constant diabatic charges $P_{ap}^{(ij)}$ should only be applied for relatively rigid systems that stay close to the reference geometry.

2.5. Restrained Electrostatic Potential Fit. The last key ingredient for the LVC/MM model is an algorithm to obtain the set of all DME parameters $P_{ap}^{(ij)}$ from an electron density ρ^{ij}. To this end, we extend the restrained electrostatic potential (RESP) method[35] to atomic multipoles. We chose RESP because it is derived to reproduce the molecular ESP, which is precisely the term we are interested in for electrostatic embedding (eq 16). It has been shown that RESP produces more accurate electrostatics compared to other population analysis methods, especially if buried atoms are involved.[36]

The underlying idea of the RESP method[35] is to define a grid of points g around the molecule,[50] compute the ESP arising from the electron density ρ^{ij} (and nuclei) at each grid point, and then optimize the atomic charges to best reproduce the ESP at all grid points.

In order to generate the fitting grid, we employ the Merz–Singh–Kollman scheme.[50−52] First, for each atom, a set of spherical shells is generated, with radii R_i that are multiples of the atom's van-der-Waals (vdW) radius R_{vdW}. The shells are equidistant with radii

$$R_i = \left[1.4 + \frac{0.4}{\sqrt{N_{\mathrm{shells}}}}(i-1)\right] R_{\mathrm{vdW}} \tag{23}$$

where the closest shell is at $1.4R_{\mathrm{vdW}}$ and $i = 1, \cdots, N_{\mathrm{shells}}$ enumerates the shells. This scheme is taken from Gaussian[53] and reproduces the original Merz–Singh–Kollman scheme with shells of 1.4, 1.6, 1.8, and 2.0 times R_{vdW} for $N_{\mathrm{shells}} = 4$. Second, each shell is discretized into a set of points by using a spherical surface quadrature. We use the Lebedev quadrature[54] because it is highly symmetric (point group O_h) and thus ensures that the fitted multipoles adhere to the symmetry of the molecule for most point groups. A user-defined point density is used to determine the order of the Lebedev quadrature for each shell. Third, as in the Merz–Singh–Kollman scheme,[50−52] all grid points are removed whose R_{vdW}-scaled distance to another atom is smaller than to the atom they are centered on. This produces the final set of grid points used for fitting.

Once the grid is set up, the ESP $V_{\mathrm{esp}}^{(ij)}$ at all grid points $\mathbf{r}_g$ is calculated using eq 16. In our present implementation, we use the PySCF package[55,56] to evaluate the integrals over $\rho^{(ij)}$ as

$$\int \mathrm{d}\mathbf{r} \frac{\rho^{(ij)}(\mathbf{r})}{|\mathbf{r} - \mathbf{r}_g|} = \sum_{\alpha} \sum_{\beta} D_{\alpha\beta}^{(ij)} \langle \alpha\beta | \gamma_g \rangle \tag{24}$$

Here, $\langle \alpha\beta | \gamma_g \rangle$ is a three-center-two-electron integral over the atomic orbitals α and β and a very tight (exponent 10^{16}) s function γ_g centered at $\mathbf{r}_g$. $D_{\alpha\beta}^{(ij)}$ is an element of the density matrix for state pair ij.

The required density matrices $\mathbf{D}^{(ij)}$ are obtained from the same electronic structure calculation that was used to derive the LVC parameters (ε's, κ's, λ's). For wave function-based methods (e.g., CASSCF), the matrices for all state pairs ij can typically be obtained directly from an electronic structure software. For linear-response methods, only the ground-state density matrix $\mathbf{D}^{00}$ and the ground-to-excited-state transition density matrices $\mathbf{D}^{0i}$ ($i > 0$) are automatically available. The relaxed excited-state densities $\mathbf{D}^{(ii)}$ ($i > 0$) require additional computational effort,[57] and the excited-to-excited-state transition density matrices $\mathbf{D}^{(ij)}$ ($i, j > 0$) can be approximated[58] as

$$\mathbf{D}^{(ij)} = (\mathbf{D}^{(0i)})^T \cdot \mathbf{D}^{(0j)} - \mathbf{D}^{(0j)} \cdot (\mathbf{D}^{(0i)})^T \tag{25}$$

In the last step, we perform the actual RESP fit. We first compute the geometric tensor with elements T_{apg} based on the atom and grid positions and then

$$L_{a'p',ap} = \sum_g^G 2T_{a'p'g}T_{apg} \tag{26}$$

which are the elements of the matrix $\mathbf{L}$ with composite index ap. Second, for each state pair ij, we compute the vector $\mathbf{Y}$ with elements

$$Y_{a'p'}^{(ij)} = 2\sum_g^G V_{\mathrm{esp}}^{(ij)}(\mathbf{r}_g) T_{a'p'g} \tag{27}$$

Then, we can obtain the desired DME parameter set $\mathbf{P}^{(ij)}$ (i.e., all elements $P_{ap}^{(ij)}$) from the equation

$$[\mathbf{L} - \mathbf{1}\mathbf{C}(\mathbf{P}^{(ij)})]\mathbf{P}^{(ij)} = \mathbf{Y}^{(ij)} \tag{28}$$

where $\mathbf{1}$ is a unit matrix and $\mathbf{C}(\mathbf{P}^{ij})$ is the vector collecting the restraint elements

$$C(P_{a'}^{(ij)}) = \frac{c_1}{\sqrt{(P_{a'}^{(ij)})^2 - c_2^2}} \tag{29}$$

Here, c_1 and c_2 are constants that define the hyperbolic restrictions of the RESP method. The full derivation is given in the Appendix.

Since $\mathbf{C}(\mathbf{P}^{(ij)})$ depends on the fitted charges, eq 28 has to be solved iteratively. The initial guess for $\mathbf{P}^{(ij)}$ is obtained using eq 28 without restraints. Subsequently, the constraint is evaluated and added to the diagonal of $\mathbf{L}$, the linear equation system is solved, and new $\mathbf{P}^{(ij)}$ are computed repeatedly until self-consistency.

The equations given above are general in the sense that one can fit all of the multipole orders at once. However, in practice, we fit the parameters order by order; i.e., we first fit the monopoles (recovering standard RESP charges). We subtract the ESP of the monopoles from the reference ESP and fit the dipoles to this residual. Finally, we repeat the procedure again for the quadrupoles. Here, we can employ different restraint parameters c_1 and c_2 for different multipole orders, typically with stronger restraints for higher orders. In addition to the "soft" restraints described above, we utilize "hard" constraints in our fit procedure. In this way, we ensure conservation of the total molecular charge (via a constraint acting on the monopoles) and ensure that the quadrupoles on each atom are traceless. The constraints are implemented by adding additional equations to the linear equation system represented by eq 28.[59]

3. COMPUTATIONAL DETAILS

In order to demonstrate that LVC/MM can reproduce QM/MM results and to verify that our implementation is correct, we validated several aspects of the model and simulation results against a reference. Although the method is intended to be used in TSH, in the present form, we carry out validation of the simulation results mostly for a single state, to focus on the solute−solvent interactions and the accuracy of the method. The investigation of the coupled solvent−solute excited-state dynamics of CH_2S via a TSH simulation will be presented in a separate work.

First, we constructed a set of LVC model parameters, including multipole charges for thioformaldehyde. Second, we constructed the full molecular system, thioformaldehyde in water, and performed preliminary equilibration using AMBER.[49] Subsequently, we ran both DFT/MM and LVC/MM simulations with SHARC,[29,60] from which we extracted snapshots to compute solvent distributions. Additionally, we performed single-point calculations on the snapshots with DFT and LVC in the gas phase and solution to scrutinize the agreement of LVC with its reference.

3.1. LVC Model.

The LVC model for thioformaldehyde was constructed at the BP86/def2-SVP[61−63] level of theory. We employed a combination of calculations using Gaussian 16[53]—which provides convenient access to all (relaxed) density matrices needed to fit the DME—and ORCA 5,[64] which provides spin−orbit couplings and is better supported in SHARC for efficient QM/MM trajectories. To ensure consistent results, we set the inputs for both programs to use the same definition of the BP86 functional with the VWN5[65] local correlation. Excited states were computed within the Tamm−Damcoff approximation.

The reference harmonic oscillator V_0 (eq 2) was parametrized from a ground-state optimization and frequency calculation in ORCA. The vibronic coupling parameters (eq 4) were obtained via finite differences[45] using excited-state calculations in Gaussian. We computed four states (S_0, S_1, T_1, and T_2) where we set a very tight convergence threshold ("conver = 9") and used the "superfine" grid. The various LVC parameters were computed as previously described.[28,45]

At the reference geometry (S_0 minimum), all relaxed-state densities and transition densities were extracted from the Gaussian output to fit the DME for each state pair. We used the original Merz−Singh−Kollman scheme[50−52] with four shells, the corresponding vdW radii,[50] and Lebedev quadratures[54] with a density of 10 points/Å^2, for a total of 6340 grid points. To prevent overfitting, the c_2 restraint parameter in eq 33 is increased for higher-order multipoles, using values of 0.0005, 0.0015, and 0.003 (in units of elementary charge) for monopoles, dipoles, and quadrupoles, respectively.

All LVC model parameters are reproduced in Sections S1 and S2 and Tables S1−S4.

3.2. System Preparation.

The system was prepared using tools from the Amber program package.[49] Thioformaldehyde was solvated in a 15 Å truncated octahedron box of 1091 TIP3P[66] water molecules. Using periodic boundary conditions, a 2 fs time step, and GAFF2 parameters[67] for thioformaldehyde, the system was then optimized for 1000 steps, heated for 50 ps to 300 K (NVT ensemble), and equilibrated for 50 ns at 300 K and 1 bar (NpT ensemble). The final coordinates and velocities were reimaged into the original box and converted to the SHARC initial condition format.[68]

3.3. SHARC Simulations.

Starting from this set of initial conditions, we performed four 1 ns trajectories in S_0 using a local development version of SHARC 3.0.[29,60] One trajectory was run with BP86/def2-SVP/MM using ORCA 5,[64] while the other three used LVC/MM, using the level of theory/parameters described above, respectively. Out of the three LVC/MM trajectories, one was restricted to only monopole charges (labeled as LVC-DME0/MM henceforth), the second was using monopoles and dipoles (LVC-DME1/MM), and the last one was using terms up to quadrupoles (LVC-DME2/MM). All trajectories used a 2 fs time step (500,000 steps). The TIP3P water molecules and the two C−H bonds of thioformaldehyde were constrained to their equilibrium values using the RATTLE algorithm implemented in SHARC 3.0.[69,70] The temperature was set to 293 K via the Langevin thermostat[71] implemented in SHARC.[72]

SHARC[29,60] is not able to perform simulations with periodic boundary conditions. Therefore, we utilized the droplet potential of Sankararamakrishnan et al.[73] to keep the water droplet spherical, with a radius of about 19.8 Å. An additional tethering potential was applied to thioformaldehyde to keep it centered within the droplet. Both potentials use the same flat-bottom harmonic potential

$$E_{\mathrm{drop}} = \sum_i \begin{cases} \frac{k}{2}(R_i - R_{\mathrm{cut}})^2, & \text{if } R_i \geq R_{\mathrm{cut}} \\ 0, & \text{otherwise} \end{cases} \tag{30}$$

where R_i is the distance of a given atom from the origin, k is the force constant, and R_{cut} is a threshold radius. For the droplet potential, the sum included all atoms, and R_{cut} was 15.86 Å. For the tethering potential, the sum included only the thioformaldehyde atoms, and R_{cut} was 2 Å. The force constant was 0.81 μE_{h}/Bohr in both cases.

As shown in eq 14, at each time step, we performed three calculations: one with ORCA or LVC, and two at the MM level. MM calculations were performed with a newly developed SHARC interface to the OpenMM package.[74] As input, this interface used the parameter/topology files from Amber, where the thioformaldehyde charges were set to zero. The three calculations were then combined in a newly developed general QM/MM interface in SHARC.

From each of the four 1 ns trajectories, the first 50 ps was discarded to allow for reequilibration. From the remaining 950 ps, snapshots were taken every 100 fs, giving four sets of 9502 snapshots for further analysis. The solvation structure obtained was investigated by using radial distribution functions (RDF) with a bin width of 0.05 Å. Furthermore, we computed the solvent distribution around thioformaldehyde using three-dimensional (3D) histograms of the O and H atoms of water, with a grid spacing of 0.5 Å. RDFs and 3D distributions were calculated from the entire data sets (9502 snapshots each) using ˚ %%( ) from AmberTools.[49]

In order to further compare LVC/MM to its reference method, we performed single-point energy calculations on all snapshots of the DFT/MM trajectory (either with water or after removing all waters). These single-point calculations were performed only at the LVC-DME2 level, not at the more approximate LVC-DME0 or LVC-DME1 levels.

4. RESULTS AND DISCUSSION

In this section, we first summarize the electronic structure of the relevant states of thioformaldehyde. Subsequently, we discuss the quality of the RESP fits in reproducing the ESP of the molecule's states in its vicinity. Finally, we discuss the results of the DFT/MM and LVC/MM trajectories and the computed solvation structure.

4.1. Electronic Structure of Thioformaldehyde.

As discussed in a previous work,[43] thioformaldehyde has four electronic states that are relevant at low energies (<3.5 eV). These are the closed-shell ground state (S_0), the singlet $^1n\pi^*$

state (S_1), the triplet $^3n\pi^*$ state (T_1), and the triplet $^3\pi\pi^*$ state (T_2). High-level multireference calculations[43] place their vertical excitation energies at 2.22, 1.96, and 3.44 eV, respectively, while our present BP86/def2-SVP calculations give values of 2.16, 1.54, and 3.34 eV. Higher states only appear above 5.5 eV with BP86. Note that these energies are given only for completeness; here, we are only interested in reproducing the BP86 results with LVC, without extensive concern for the accuracy of BP86.

The four electronic states have different electron distributions, owing to their different occupations of n, π, and π^* orbitals. These different electron densities give rise to different ESP energies (proportional to the ESP) around the molecule, as shown in Figure 1. The S_0 state (panels a and b) shows a clear dipole moment in the z direction (negative near the S atom, positive near the H atoms). The most interesting feature of the S_0 ESP are the two deep minima close to the S atom, which are located in the molecular plane; there are no such minima above/below the molecule. These two minima arise from the high electron density of the S atom's lone pair orbital *n*.

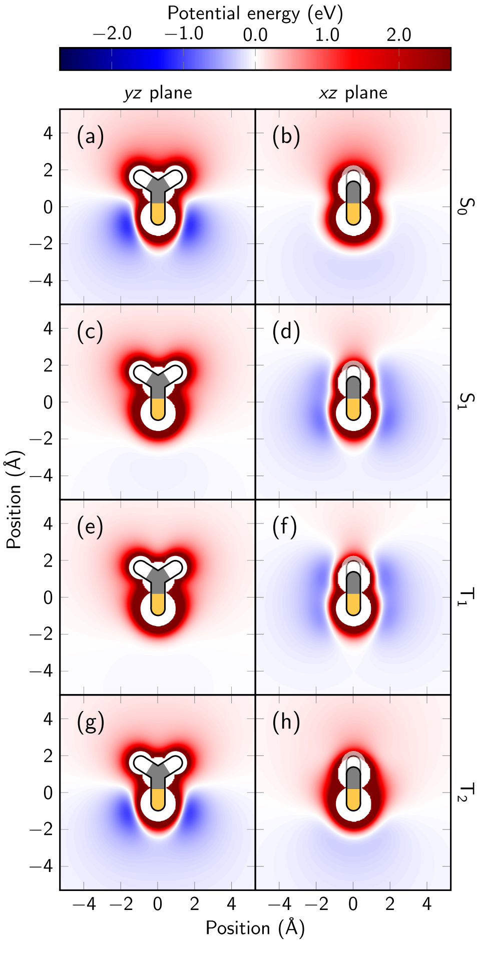

Figure 1. Electrostatic potential energy in the *yz* and *xz* planes of the first four excited states of thioformaldehyde for a unit positive charge computed with BP86/def2-SVP.

The S_1 (panels c and d) and T_1 (e and f) states show very similar ESPs, which are distinctively different from the S_0 ESP. Both S_1 and T_1 are $n\pi^*$ states, where one electron is removed from the in-plane lone pair and added to the out-of-plane π^* orbital. Consequently, the in-plane minima in the ESP vanish, and two shallow, somewhat delocalized minima above and below the C−S bond appear (i.e., in the *xz* plane). The shift of electron density from the S to the C atom also reduces the dipole moment considerably. Finally, the T_2 state (panels g and h) has a $\pi\pi^*$ configuration, and its electron density does not differ significantly from that of the S_0 state. Therefore, its ESP is very similar to that of S_0, including the two in-plane minima arising from the doubly occupied lone pair orbital.

We note that all states are strongly repulsive near the nuclei, where the positive probe charge penetrates the electron density. It would be desirable that the fitted DME for each state can reproduce all of the relevant features of the ESP from the BP86 calculations: the dipole far field, the attractive minima, and also the repulsive features.

4.2. Quality of the Fitted DME. In Figure 2, we present the ESP energies for the S_0 obtained from the reference BP86 (top row) and from three DMEs of orders 0, 1, and 2 (second−fourth rows, labeled DME0, DME1, and DME2 from here). The color scale and orientation of the molecule are identical to those in Figure 1. Additionally, we show the fitting grid points (black dots) that are located in the plot planes.

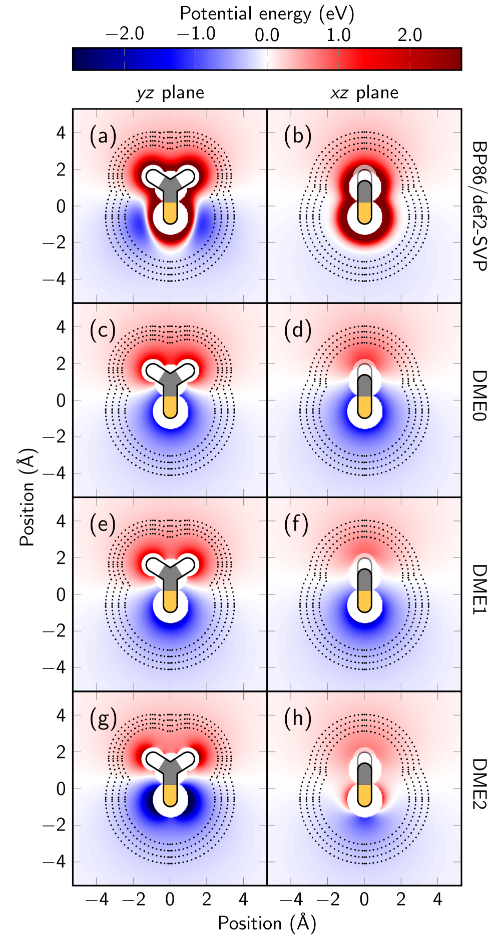

Figure 2. Electrostatic potential energy in the *yz* and *xz* planes of the S_0 for BP86/def2-SVP compared to DMEs of order 0, 1, and 2, labeled DME0, DME1, and DME2, respectively. The black dots indicate the position of the fitting grid points used in the RESP procedure.

The ESP shown in panels (a and b) is the same as that in Figure 1. One can nicely see the distribution of the fit grid points, which avoid the highly repulsive area where the electron density is penetrated and densely surrounds the molecule. In panels (c and d), we show the ESP plots obtained by using only the monopole charges fitted with RESP to the electron density of S_0 at the BP86/def2-SVP level of theory. As shown in Table 1, these are nearly identical to the RESP charges obtained with Gaussian and , . (/ ˚ 0 , 1 2 from /) AmberTools, using identical parameters for shell generation and point density. The minimal remaining differences arise because Gaussian generates the grid points by using a different quadrature.

Table 1. Fitted Monopole Charges of S_0 at BP86/def2-SVP Level of Theory Using Gaussian and Amber versus Our Implementation

atom	Gaussian + antechamber	present work
C	−0.06743	−0.06637
S	−0.13338	−0.13392
H	+0.10040	+0.10015
H	+0.10040	+0.10015
RMSD		+0.00062

While our fitted monopoles reproduce RESP charges, they are only partially able to reproduce the details of the electrostatics of the molecule. The dipole moment is relatively well-reproduced (BP86/def2-SVP: 1.573 D; DME0:1.619 D). However, it is not possible to represent the anisotropy of the ESP around the molecule—the attractive interaction is too weak at the fit points in the molecular (yz) plane and too strong in the xz plane. The introduction of dipole terms in panels (e and f) does not fundamentally change this behavior. The dipole moment increases slightly to 1.647 D, but we consider this to be still in good agreement with the reference because our fitting grid is not intended to probe the far-field ESP of the molecule. Only when adding the quadrupole terms (panels g and h) do we obtain increased attraction and two minima in the molecular plane as well as a much reduced attraction above/below the molecule.

Figure 2 also clearly shows that our DME approach cannot describe in any way the repulsive region very close to the nuclei where the probe charge penetrates the electron density. This is because the DME approach is based on numerically efficient pointlike multipoles, whereas the electron density is a distribution. Fortunately, in typical MD simulations, atoms cannot come close enough to penetrate deeply into another molecule's electron density due to Pauli repulsion. In MD simulations, Pauli repulsion is commonly represented by a part of the Lennard−Jones interaction.

In Figure 3, we show the sum of electrostatic and Lennard-Jones energies, where the latter will be very repulsive close to the nuclei, covering the region where the DME gives inaccurate results. Note that the Lennard−Jones interaction is shown for a probe H atom with GAFF2 parameters,[75] which has a very small vdW radius. For larger atoms, an even larger region around the nuclei would be blocked. It can be nicely seen in Figure 3 that the Merz−Singh−Kollman scheme[50] produces a sensible grid, where the innermost shell straddles the repulsive Lennard−Jones potential and the outer shells sample positions where it is very likely to encounter other atoms.

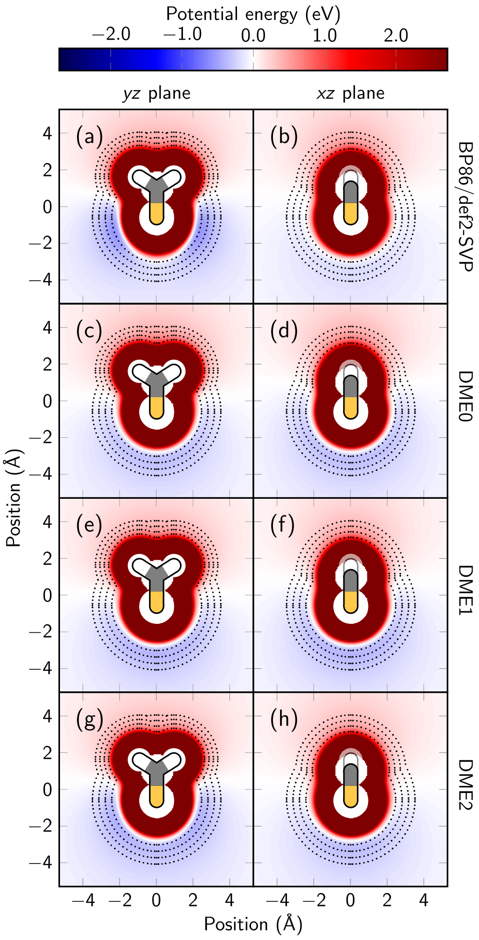

Figure 3. Electrostatic plus Lennard−Jones potential energy in the yz and xz planes of the S_0 for BP86/def2-SVP compared to DMEs of orders 0, 1, and 2 labeled DME0, DME1, and DME2, respectively. Lennard−Jones energies are computed using GAFF2 parameters. The black dots indicate the position of the fitting grid points used in the RESP procedure.

In order to show in more detail the quality of the multipolar RESP fit, in Figure 4, we show on a grid-point level the correlation of the ESP from the reference BP86 calculation with the one approximated by DME2. For this figure, we generated a test grid different from the fitting grid, with 6482 points (shell radii between 1.0 and 2.5 times the vdW radii). In addition to the correlation of the ESPs, the plots also show the distances of the grid points from the nearest atom.

In the left column, all points are shown with an equal point size. It can be seen that most of the test grid points are close to the diagonal, indicating that the DME can reproduce the ESP of the electron density adequately. However, there are a significant number of grid points where the BP86 ESP is more positive than the ESP of the DME. These are mostly points close to the nuclei where the BP86 ESP is rather positive because of electron density penetration.

The right column of Figure 4 shows the same data except that the point size is scaled according to the Boltzmann weight (at 300 K) corresponding to the Lennard-Jones interaction energy of a hydrogen atom at the grid-point position. This suppresses all of the points that are close to the molecule (most points with dark color) and therefore less relevant for MD simulations. With very few exceptions, these relevant

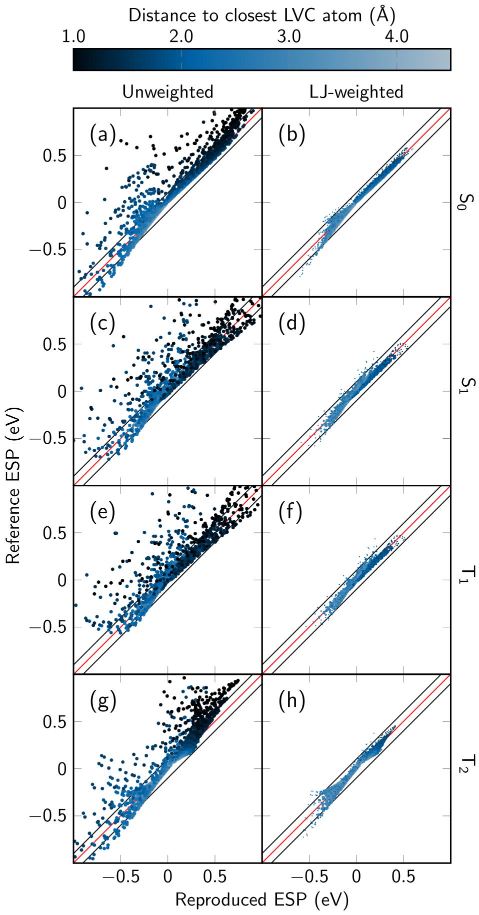

Figure 4. Correlation plots comparing the reference ESP energy (BP86/def2-SVP, vertical axes) with the ESP energy produced by the DME up to 2 order (horizontal axes). The plots use a test grid that is different from the fitting grid, with 6482 points in shells with radii 1.0−2.5 times the vdW radii. The color of the points indicates the distance to the closest atom. The red and two black lines indicate deviations of 0 and ±0.1 eV, respectively. On the left, all points are shown with equal point size, whereas on the right, the point size is scaled by the Boltzmann weight of the Lennard-Jones interaction energy (assuming 293.15 K), so that points at high energies are smaller.

points show deviations of the ESP of less than ±0.1 eV (region between the black lines). This is true for all four electronic states, where no significant differences can be seen.

The deviations shown in Figure 4 can be summarized by computing the mean absolute deviations (MAD) and root-mean-square deviations (RMSD) across all points. The results are shown in Table 2. The values for the unweighted analysis are rather high, with MADs of about 80 meV and RMSDs of about 150−180 meV. However, the Boltzmann-weighted analysis shows significantly better results, with MADs of about 10 meV and RMSDs of about 15 meV. All electronic states can be reproduced at approximately the same accuracy. This is similarly true for the representation of the $S_0 \rightarrow S_1$ and $T_1 \rightarrow T_2$ transition densities, where we obtain Boltzmann-weighted MADs of 4 meV and RMSDs of 8 meV (see Figure S1 and Table S5). Hence, the DME representation of the electron densities seems to allow for a faithful description of the electrostatics around the molecule.

Table 2. Mean Absolute Deviations (MAD) and Root-Mean-Square Deviations (RMSD) of the Fitted DME with Respect to the BP86/def2-SVP Reference of the Distributions of Points in Figure 4 in eV

	unweighted		LJ weighted	
	MAD	RMSD	MAD	RMSD
S_0	0.075	0.148	0.008	0.014
S_1	0.082	0.180	0.008	0.013
T_1	0.080	0.179	0.007	0.013
T_2	0.080	0.151	0.009	0.016

4.3. Solvation Structure.

Next, we compare the results for our electrostatic model of thioformaldehyde based on actual MD simulations with the reference electronic structure method and with LVC. Note that we only investigate the dynamics in S_0 here, as a detailed discussion of the solvent-driven nonadiabatic dynamics of thioformaldehyde in water is beyond the scope of this work. For the S_0 state, we computed four 1 ns trajectories (see above for details) and obtained 9502 snapshots from the DFT/MM trajectory and the same number from each of the three LVC/MM trajectories.

The electrostatics around a molecule fundamentally influence the surrounding solvent molecules, leading to a particular solvation structure. The solvation structure of thioformaldehyde in the S_0 state in water is presented in Figure 5. We first discuss the solvent distribution obtained from the 1 ns DFT/MM trajectory (panel a). As can be seen,

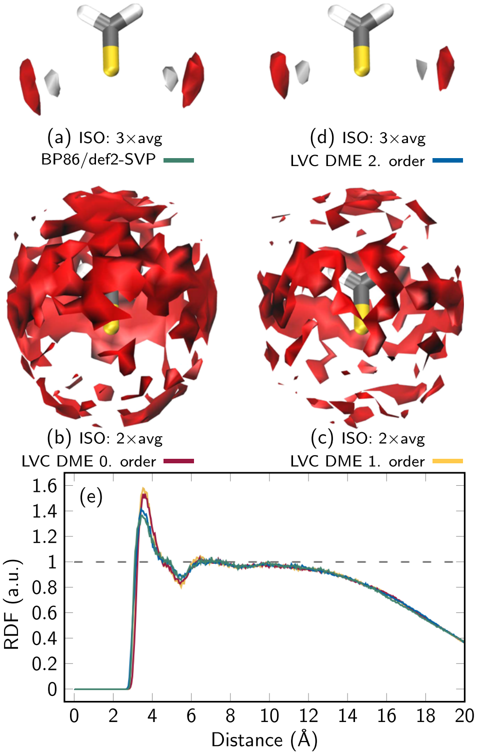

Figure 5. Solvent distribution of water around thioformaldehyde. (a−d) Isosurface plots (grid spacing 0.5 Å) of the most probable positions of water H atoms (white) and O atoms (red), with the isovalue specified as multiples of the average density in the box, for different levels of computation. Note the lower isovalues for panels (b and c). (e) Radial distribution functions (RDF) of water O atoms around the S atom with BP86/def2-SVP/TIP3P(green), LVC-DME0/TIP3P (red), LVC-DME1/TIP3P (orange), and LVC-DME2/TIP3P (blue).

thioformaldehyde forms two regions where it is very probable to find water H atoms (white) and likewise two larger regions of high-probability for O atoms (red). These regions are located in the *yz* molecular plane, orthogonal to the C—S bond (i.e., in *y* direction) around the S atom—clearly oriented toward the lone pair of the S atom. Therefore, it seems clear that the S atom lone pair forms distinct in-plane hydrogen bonds to water, which is well-known to occur for carbonyls.[76,77] This shows very clearly that the solvation shell around the molecule is strongly anisotropic.

Figure 5b shows the 3D solvent distribution for the LVC-DME0/MM trajectory that only employs monopole charges. This calculation is thus equivalent to typical classical MM—MD calculations. As can be seen, this calculation produces a solvation structure very different from that of the DFT/MM calculation. Even at a lower isovalue, preferred H atom positions cannot be identified. The distribution of the O atoms is approximately isotropic around the molecule. Clearly, no directional hydrogen bonds are formed at this level of computation. Similar results are also obtained for the LVC-DME1/MM computation (panel c), which additionally employs dipole charges.

However, as shown in panel (d), the inclusion of quadrupole charges in the LVC-DME2/MM level of computation leads to an accurate reproduction of the anisotropic solvation pattern in thioformaldehyde, in good agreement with DFT/MM. This is a direct result of the minima of the ESP in the *xy* plane (Figure 2) obtained through quadrupole terms on the S atom. We note that there are still smaller differences between panels (a) and (d). For example, the hydrogen bonds in panel (a) are slightly stronger (with higher maximum occurrence) and form an angle of about 110° with the S—C bond, whereas in panel (d), the hydrogen bonds are slightly weaker and the angle is closer to 90°. This can be seen more easily in the difference plot in Figure S2.

Panel (e) of Figure 5 presents the obtained RDFs of the water O atoms around the S atom. The RDF obtained with DFT/MM shows a first maximum at about 3.5 Å, corresponding to the hydrogen bonds formed between S and water O and the remaining first solvation shell. At 5—6 Å, there is a slight minimum, indicating the region between the first and second solvation shells. At 7 Å, there is another very weak maximum, but generally, at this distance, there is little solvent structure. After 12 Å, the RDF starts to decrease due to the finite droplet that we are using.

The RDFs obtained with LVC-DME0/MM and LVC-DME1/MM produce a too strong first solvation shell peak but less hydrogen bonding at 2.8—3.4 Å, compared to DFT/MM. On the contrary, the LVC-DME2/MM calculation generally agrees very well with the reference in terms of the shape and locations of the maxima and minima. The first maximum at the LVC-DME2/MM level is only slightly stronger (by about 4%) than the reference RDF. We assume that this discrepancy is mostly due to the approximations inherent to the DME, i.e., using point multipoles instead of delocalized electron densities and using constant diabatic multipoles that neglect the geometry dependence and polarizability of the electron density. Apart from the maximum, the RDFs are fully consistent with each other at the obtained noise level.

At distances above 10 Å, where the RDFs begin to decrease, slight deviations can be observed between the different simulations. These deviations arise because the thioformaldehyde molecule does not stay sufficiently close to the origin and instead diffuses through the droplet in a different way in each of the trajectory. This indicates that the tether potential might have been chosen to be too weak to keep the molecule close to the origin. For the present investigations, we are confident that this is not a problem because the molecule never reached the surface of the droplet and was always surrounded by water. However, for future studies where the long-range behavior is important (e.g., X-ray scattering simulations), we would certainly recommend significantly stronger tether potentials. Furthermore, it might be good practice to crop cube or truncated octahedron droplets to spherical droplets for SHARC simulations like the one presented above because equilibration to a spherical droplet would take very long otherwise.

To also investigate dynamical properties, we computed hydrogen bond lifetimes from the DFT/MM and LVC-DME2/MM trajectory using a residence time approach.[78] For this analysis, a hydrogen bond was defined by an O—S distance of <4.5 Å (see the main peak in the RDF in Figure 5e). The results are given in Figure S3, showing that both methods predict a biexponential hydrogen bond lifetime, although the ones from LVC-DME2/MM are larger by a factor of 2. We assume that the difference stems mostly from the missing polarizability of the employed single-state LVC-DME2 model. In models with multiple diabatic states, the interaction of the solvent with the respective transition densities is expected to recover the polarizability of the ground state to some degree, presumably increasing accuracy.

Furthermore, we analyzed the vibrational frequencies in the two simulations. We computed two new trajectories with identical settings, except saving coordinates every 0.5 fs between 5 and 10 ps and not constraining the C—H bond lengths. The normal-mode coordinates **Q** were subsequently Fourier-transformed. The results are shown in Figure S4 and Table S6. The vibrational spectra of the six normal modes agree reasonably well with each other. We assume that the differences (around 20 cm^{-1}) are due to vibrational coupling to the water modes.

4.4. Potential and Solvation Energies. For completeness, we also investigated how well our LVC/MM approach can reproduce the total potential energies from the reference method. For this, we performed DFT/MM and LVC-DM2/MM single-point calculations for all 9502 snapshots described above. Additional DFT and LVC single-point calculations were performed for all 9502 snapshots after removal of the MM part. Therefore, our energy analysis is based on four sets of 9502 single-point calculations, each considering four states (S_0, S_1, T_1, T_2). For calculations including point charges, we deleted all MM energy contributions, keeping only the electronic energy of the molecule in the presence of the MM charges (term E_{QM}(QM; MMpc) in eq 14). All energies are relative to the gas-phase equilibrium energy of BP86 or LVC, respectively.

In Figure 6, we compare these four data sets by plotting various energy differences. In panel (a), we start with the difference between the BP86 energies including MM charges and those without MM charges. Thus, these energy differences represent the energetic stabilization of the respective states by the Coulomb interaction with the solvent charges. As can be seen, different electronic states are affected in different ways. The S_0 state (black) is strongly stabilized by the interaction with the solvent because the considered snapshots were sampled from the trajectory in the S_0; hence, the snapshots

87

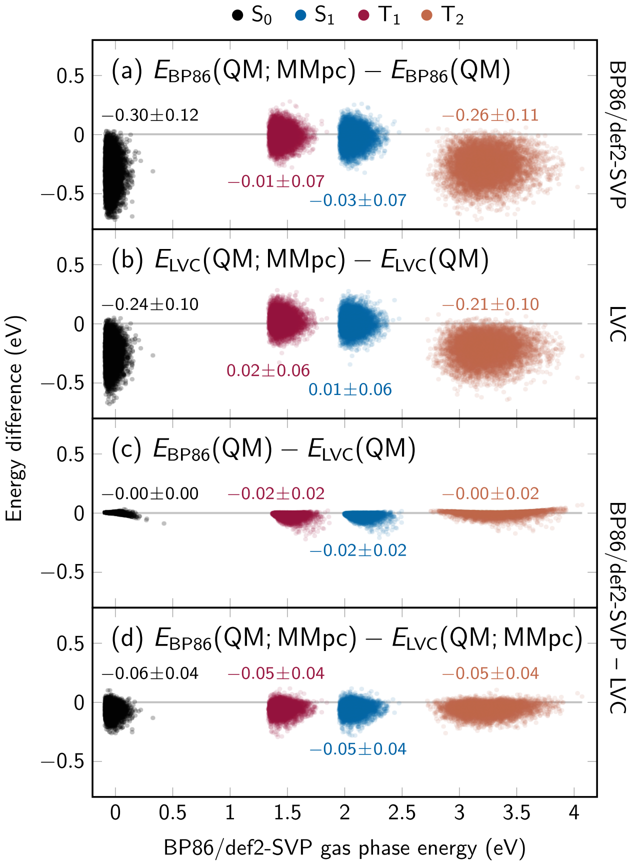

Figure 6. Scatter plots of energy differences computed at 9502 geometries. (a) Energy difference between BP86 calculation including point charges and BP86 without MM charges, i.e., electronic solvent stabilization energy. (b) Analogous energy difference using LVC-DME2/MM. (c) Energy difference between BP86 and LVC without MM charges, i.e., gas-phase agreement between the methods. (d) Energy difference between BP86/MM and LVC-DME2/MM, i.e., solution-phase agreement. The states are color-coded as S_0 (black), S_1 (blue), T_1 (red), and T_2 (orange). The mean values with standard deviations are included for each distribution (all in eV).

contain many solvent arrangements that are favorable for the S_0 state. A similar picture is seen for the T_2 state, which exhibits electrostatics very similar to those of the S_0 state, as discussed above. On the contrary, the T_1 and S_1 states are not stabilized by the interaction with the solvent.

In panel (b), we show the same energy differences as in panel (a) but for the LVC/MM single-point calculations. It can be seen that the general trends of solvent stabilization (and the distribution of energies) are very well reproduced, with strong stabilization for S_0 and T_2, and little effect on T_1 and S_1. However, slight differences can be observed, especially in that the stabilization of S_0 and T_2 is systematically too small, by about 0.05 eV. This is consistent with the observations above that our DME charges predict slightly too weak hydrogen bonds and a slightly too shallow ESP.

In panels (c and d), we compare the two electronic structure methods directly, as it is not possible to compare the scatter plots in panels (a and b) point by point. Panel (c) shows the deviations between the gas-phase BP86 and LVC energies. Here, the agreement is excellent, with systematic and random errors on the order of 0.02 eV (0.5 kcal/mol), or even less for the S_0 state. This shows that thioformaldehyde in the ground state can be accurately described by a harmonic oscillator potential, at least for geometries that are in the vicinity of the S_0 minimum. This can be attributed to the rigidity of the molecule, i.e., the absence of low-frequency, strongly anharmonic, or curvilinear vibrational modes and the presence of only one ground-state minimum. This rigidity is a general prerequisite for the applicability of the LVC approach to any molecule.

In panel (d), we show the energetic deviations between the BP86/MM and LVC/MM calculations. The deviations are slightly larger than those in the gas phase, where the additional deviations are due to the imperfections of the DME in describing the true electrostatic interaction with the solvent. As mentioned above, the most relevant sources of errors here are the use of point multipoles and the neglect of the geometry dependence and polarizability of the electron density. However, we want to stress that the shown differences of around 0.05 ± 0.04 eV are equivalent to an error of 1−2 kcal/mol. If the systematic shift of about −0.05 eV across all states is ignored—as it will not affect dynamics, then the errors are about 1 kcal/mol. This is typically considered to be a desirable degree of accuracy in computing electronic energies. Hence, it appears that our LVC/MM approach using a DME can reproduce solvation energetics to a satisfactory degree, which is confirmed by the obtained solvent distributions shown above. Slight improvements might be possible by using different restraint parameters during the RESP fit, where the current restraints were chosen to be somewhat conservative to guard against overfitting.

4.5. Additional Remarks.

As with many other model potential energy surface approaches,[21−24] the accuracy of LVC/MM is bounded by the accuracy of the reference electronic structure method. Hence, a careful selection of the single- or multireference level of theory[79,80] is of high importance. A particularly relevant aspect is whether the parametrization should be carried out with vacuum quantum chemistry or using implicit solvation treatment, where both approaches have their merits.

Parametrization in vacuum has been used extensively for various force fields,[81,82] so LVC models used together with such force fields might be parametrized in vacuum, too, for consistency. Furthermore, LVC models with several diabatic states include some polarizability effects (from solvent-induced mixing of diabatic states)—in such models, parametrization should be done in vacuum to avoid double-counting of solvent-induced changes to charge distribution and geometry.[83] A model parametrized in vacuum might also be transferable to different solvents if some polarizability is included. On the contrary, if the LVC model cannot be expected to provide sufficient polarizability (e.g., due to a too small diabatic basis), then it might make sense to parametrize using implicit solvation. This will provide multipole charges and geometries that are closer to the true condensed-phase ones.[83]

In the present case, parametrization was carried out in vacuum, but nearly identical parameters are obtained in implicit solvation. Repeating the parametrization using IEFPCM in water,[84] the reference coordinates change by 0.001 Å, the frequencies by 14 cm^{-1}, and the multipole parameters by at most 0.03 au (see Table S7). Thus, for thioformaldehyde, the solvation treatment during parametrization seems to make little difference, and already the vacuum parameters reproduce the solvation energies to 1 kcal/mol (Figure 6).

Significant improvements over the presented accuracy of the electrostatics (to further improve the agreement of LVC with its reference) would require additional implementations. The simplest addition would be to go beyond quadrupoles, including octupoles and potentially hexadecapoles. However, this would increase the number of parameters and thus the risk of overfitting significantly. Furthermore, it can be argued[85] that multipoles higher than quadrupoles are not needed as long as all occupied or transition orbitals are predominantly composed of *s* and *p* functions. In order to improve the description of charge penetration, point multipoles could be replaced by Gaussian multipoles.[86,87] The geometry dependence of the multipole charges (i.e., charge redistribution) could be further modeled by different charge flux models[34,88] or more simply using linear dependence of multipole charges on normal modes. Further, polarizabilities could be treated (beyond solvent-induced mixing of diabatic states) using induced dipole models, Drude oscillators, etc.,[89−91] possibly on both LVC and MM atoms. Finally, in addition to improving the description of the electrostatics, the LVC Hamiltonian itself can be improved by including higher-order terms in the Taylor expansion of $\mathbf{W}$ (eq 4). For example, quadratic and bilinear terms $\gamma_{nn}^{(i)}$ and $\gamma_{nm}^{(i)}$ would provide frequency shifts and Duschinsky rotations for the diabatic states.

We note that all of these additions would greatly increase the number of parameters, especially considering that our LVC/MM model is primarily intended for running nonadiabatic dynamics simulations using (possibly) a large number of electronic states. It is not clear whether one can robustly and efficiently obtain all of the necessary parameters for all electronic states and transition densities. Furthermore, these additions would increase the computational cost significantly, which might not be worthwhile unless the overall accuracy is significantly improved.

4.6. Computational Cost. For reference, we also briefly discuss the computational performance of our LVC/MM implementation. The four 1 ns trajectories discussed above were each computed on a single core of an Intel Xeon Gold-6234 16-core processor at a clock speed of 3.30 GHz. The DFT/MM trajectory using ORCA 5 was finished in approximately 240 h, giving a time of 1.72 s per time step. In contrast, each of the LVC/MM trajectories took 18 h, for a time of 0.13 s per time step. In all cases, approximately 0.06 s per time step is consumed by the MM calculation using OpenMM. The difference between the DFT and LVC calculations thus represents a speedup of more than an order of magnitude. We note that part of this speedup is due to several code optimizations that we carried out in the %3 4 0 , implementation[28] of SHARC.

A speedup of an order of magnitude does not seem to be much considering that we compare a full-fledged electronic structure calculation including gradients with a simple harmonic oscillator and Coulomb scheme. However, we must note that thioformaldehyde in water is a very small test system (4 QM atoms and 3273 MM atoms), picked partially for its affordability to run a 1 ns ab initio QM/MM trajectory. For larger molecules or other electronic structure methods, the speedup of LVC/MM over QM/MM is expected to be vastly larger. We expect that the dominant cost in LVC/MM scales linearly in the number of LVC atoms and in the number of MM atoms as well as quadratically in the number of states. Only the numerical differentiation steps in the gradients (eqs 13 and 22) scale quadratically in the number of LVC atoms, but they are still very cheap. We confirmed the linear scaling with preliminary data from two other LVC/MM projects run in our group. There, another system with one state, 12 LVC atoms, and 8324 MM atoms took about 0.8 s per time step. A third system with one state, 61 LVC atoms, and 13500 MM atoms took roughly 4 s per time step. In contrast, the most efficient electronic structure methods scale at least cubically with the number of atoms (i.e., the number of basis functions). Many methods for excited states are even more expensive, whereas LVC/MM scales independently of the chosen reference method. Thus, it is easily conceivable that LVC/MM can be 3−5 orders of magnitude faster than QM/MM simulations, analogous to gas-phase LVC models.[14]

5. CONCLUSIONS

We have presented a complete framework for a hybrid linear vibronic coupling model electrostatically embedded into a molecular mechanics environment, termed LVC/MM. Within LVC/MM, multiple coupled potential energy surfaces of a solute molecule are described by using a reference harmonic oscillator and state-specific constant and linear coupling terms in a diabatic basis. We have shown how to extend LVC models to be rotationally and translationally invariant using the Kabsch algorithm to lift the restriction that the molecule must be aligned with its reference geometry. Subsequently, we introduced a Coulomb interaction matrix into LVC, whose matrix elements are computed from distributed multipole expansions for each diabatic electronic state/state pair. This allows for the computation of energies, gradients, and nonadiabatic coupling vectors for the entire LVC/MM system. Finally, we developed an extension of the restrained electrostatic potential fit technique to distributed multipoles.

The new LVC/MM method was implemented in the SHARC molecular dynamics package. The Kabsch algorithm and electrostatic embedding were incorporated into the SHARC-LVC interface, while the RESP fitting technique was implemented as a separate library that can be linked to any of the supported ab initio codes. We also implemented a general QM/MM interface and an OpenMM interface for SHARC. Finally, we added droplet and tether potentials to the SHARC dynamics driver and optimized the performance of the %3 4 0 , code and LVC interface.

The new method was applied to thioformaldehyde in water, which is a small test system that shows anisotropic solvation. By comparing to a 1 ns reference trajectory computed at the BP86/def2-SVP/MM level of theory, we show that LVC/MM can capture solvation effects that cannot be described with simple point charge models. Radial distribution functions were reproduced within a few % error and solvation energies within 1−2 kcal/mol. At the same time, LVC/MM provides a speedup of at least 1 order of magnitude over the reference DFT calculations and potentially much larger speedups for larger systems.

In summary, LVC/MM in SHARC provides a new approach to describe many picosecond nonadiabatic dynamics in solvated or embedded molecules at very low computational cost. The diabatic distributed multipole model is restricted to stiff and not too polarizable molecules in the same way that the underlying linear vibronic coupling model is restricted to stiff molecules. However, we believe that LVC/MM provides an unprecedented approach to describe the nonadiabatic dynamics of solvent molecules around an excited solute and offers unique opportunities for describing multichromophoric systems.

A. DERIVATION OF MULTIPOLAR RESP

RESP charges are fitted using a least-squares error function. The total error in the ESP $F_{\text{error}}^{(ij)}$ over all grid points $\mathbf{r}_g$, for a state pair ij and including only monopoles, is calculated as

$$F_{\text{error}}^{(ij)} = \sum_g^G \left[V_{\text{esp}}^{(ij)}(\mathbf{r}_g) - \sum_a^A \frac{P_a^{(ij)}}{|\mathbf{r}_a - \mathbf{r}_g|} \right]^2 \tag{31}$$

The electrostatic potential $V_{\text{esp}}^{(ij)}$ at $\mathbf{r}_g$ is calculated with eq 17. The optimal charges $P_a^{(ij)}$ can be found by differentiating eq 31 with respect to the monopole charges and setting the result to zero

$$\frac{\mathrm{d}F_{\text{error}}^{(ij)}}{\mathrm{d}P_{a'}^{(ij)}} = -\sum_g^G \frac{2}{|\mathbf{r}_{a'} - \mathbf{r}_g|} \cdot \left[V_{\text{esp}}^{(ij)}(\mathbf{r}_g) - \sum_a^A \frac{P_a^{(ij)}}{|\mathbf{r}_a - \mathbf{r}_g|} \right] = 0 \tag{32}$$

In the RESP model, eq 31 is modified with a hyperbolic penalty function

$$F_{\text{error}}^{(ij)} = \sum_g^G \left[V_{\text{esp}}^{(ij)}(\mathbf{r}_g) - \sum_a^A \frac{P_a^{(ij)}}{|\mathbf{r}_a - \mathbf{r}_g|} \right]^2 + c_1 \sum_a^A \left(\sqrt{(P_a^{(ij)} - P_{a,\text{ref}}^{(ij)})^2 - c_2^2} - c_2 \right) \tag{33}$$

The charges $P_{a,\text{ref}}^{(ij)}$ are reference charges toward which the charges are restrained; in the entire manuscript, we generally assume all $P_{a,\text{ref}}^{(ij)} = 0$ and omit them from all equations below.

The equation to find the optimal charges $P_a^{(ij)}$ can then be written as

$$\frac{\mathrm{d}F_{\text{error}}^{(ij)}}{\mathrm{d}P_{a'}^{(ij)}} = -\sum_g^G \frac{2}{|\mathbf{r}_{a'} - \mathbf{r}_g|} \left[V_{\text{esp}}^{(ij)}(\mathbf{r}_g) - \sum_a^A \frac{P_a^{(ij)}}{|\mathbf{r}_a - \mathbf{r}_g|} \right] - \frac{c_1 P_{a'}^{(ij)}}{\sqrt{(P_{a'}^{(ij)})^2 - c_2^2}} = 0 \tag{34}$$

After defining the restraining function C as

$$C(P_{a'}^{(ij)}) = \frac{c_1}{\sqrt{(P_{a'}^{(ij)})^2 - c_2^2}} \tag{35}$$

Equation 34 can be rearranged to

$$\frac{\mathrm{d}F_{\text{error}}^{(ij)}}{\mathrm{d}P_{a'}^{(ij)}} = -\sum_g^G \frac{2V_{\text{esp}}^{(ij)}(\mathbf{r}_g)}{|\mathbf{r}_{a'} - \mathbf{r}_g|} + \sum_g^G \frac{2}{|\mathbf{r}_{a'} - \mathbf{r}_g|} \sum_a^A \frac{P_a^{(ij)}}{|\mathbf{r}_a - \mathbf{r}_g|} - C(P_{a'}^{(ij)}) P_{a'}^{(ij)} = 0 \tag{36}$$

By further rearrangement, we can obtain

$$\sum_a^A \left(-C(P_{a'}^{(ij)}) \delta_{a'a} + \sum_g^G \frac{2}{|\mathbf{r}_{a'} - \mathbf{r}_g|} \frac{1}{|\mathbf{r}_a - \mathbf{r}_g|} \right) P_a^{(ij)} = \sum_g^G \frac{2V_{\text{esp}}^{(ij)}(\mathbf{r}_g)}{|\mathbf{r}_{a'} - \mathbf{r}_g|} \tag{37}$$

where we introduced the Kronecker delta to pull the constraint into the sum over a. We can now define

$$Y_{a'}^{(ij)} = \sum_g^G \frac{2V_{\text{esp}}^{(ij)}(\mathbf{r}_g)}{|\mathbf{r}_{a'} - \mathbf{r}_g|} \tag{38}$$

and

$$L_{a'a} = \sum_g^G \frac{2}{|\mathbf{r}_{a'} - \mathbf{r}_g|} \frac{1}{|\mathbf{r}_a - \mathbf{r}_g|} \tag{39}$$

to write eq 37 in matrix notation

$$(\mathbf{L} - \mathbf{1C}(\mathbf{P}^{(ij)}))\mathbf{P}^{(ij)} = \mathbf{Y}^{(ij)} \tag{40}$$

where $\mathbf{1}$ is a unit matrix and $\mathbf{C}$ is the vector collecting the restraint elements $C(P_a^{(ij)})$.

The extension of the described RESP procedure to arbitrary multipole moments is rather straightforward by inserting eq 19 into eq 31. For clarity, we introduce the index p that enumerates the different multipole components (monopole, x, y, z, xx, yy, $\cdots$) and extend the total error by the multipole potentials

$$F_{\text{error}}^{(ij)} = \sum_g^G \left[V_{\text{esp}}^{(ij)}(\mathbf{r}_g) - \sum_a^A \sum_p^{10} (P_{ap}^{(ij)} \cdot T_{apg}) \right]^2 + c_1 \sum_a^A \sum_p^{10} \left(\sqrt{(P_{ap}^{(ij)})^2 - c_2^2} - c_2 \right) \tag{41}$$

From this equation, one can derive the multipolar analogue of eq 37

$$\sum_a^A \sum_p^{10} \left(-C(P_{a'p'}^{(ij)}) \delta_{a'a} \delta_{p'p} + \sum_g^G 2T_{a'p'g} T_{apg} \right) P_{ap}^{(ij)} = 2 \sum_g^G V_{\text{esp}}^{(ij)} T_{a'p'g} \tag{42}$$

By defining

$$Y_{a'p'}^{(ij)} = 2 \sum_g^G V_{\text{esp}}^{(ij)}(\mathbf{r}_g) T_{a'p'g} \tag{43}$$

and

$$L_{a'p',ap} = \sum_g^G 2T_{a'p'g} T_{apg} \tag{44}$$

and considering $a'p'$ and ap as composite indices, we end up at the same form of the matrix equation in eq 40.

■ ASSOCIATED CONTENT

Supporting Information

The Supporting Information is available free of charge at https://pubs.acs.org/doi/10.1021/acs.jctc.3c00805.

> Linear vibronic coupling parameters, raw parameter file contents, correlation plots for the RESP fit of transition densities, 3D difference solvent distribution plots, hydrogen bond lifetimes, vibrational frequencies from trajectories, and DME fits using implicit solvation (PDF)

■ AUTHOR INFORMATION

Corresponding Author

Sebastian Mai – *Institute of Theoretical Chemistry, Faculty of Chemistry, University of Vienna, 1090 Vienna, Austria;* orcid.org/0000-0001-5327-8880; Email: sebastian.mai@univie.ac.at

Authors

Severin Polonius – *Institute of Theoretical Chemistry, Faculty of Chemistry, University of Vienna, 1090 Vienna, Austria; Vienna Doctoral School in Chemistry (DoSChem), University of Vienna, 1090 Vienna, Austria;* orcid.org/0000-0003-0445-4694

Oleksandra Zhuravel – *Institute of Theoretical Chemistry, Faculty of Chemistry, University of Vienna, 1090 Vienna, Austria*

Brigitta Bachmair – *Vienna Doctoral School in Chemistry (DoSChem), University of Vienna, 1090 Vienna, Austria; Research Platform on Accelerating Photoreaction Discovery (ViRAPID), University of Vienna, 1090 Vienna, Austria;* orcid.org/0000-0002-2346-7995

Complete contact information is available at: https://pubs.acs.org/10.1021/acs.jctc.3c00805

Notes

The authors declare no competing financial interest.

■ ACKNOWLEDGMENTS

The authors thank Leticia González and Felix Plasser for initial guidance on the topic and the test system, and the University of Vienna for continuous support, in particular in the framework of the ViRAPID research platform. The computational results presented have been achieved (in part) using the Vienna Scientific Cluster (VSC).

■ REFERENCES

(1) Yonehara, T.; Hanasaki, K.; Takatsuka, K. Fundamental Approaches to Nonadiabaticity: Toward a Chemical Theory beyond the Born–Oppenheimer Paradigm. *Chem. Rev.* **2012**, *112*, 499–542.

(2) Tavernelli, I. Nonadiabatic Molecular Dynamics Simulations: Synergies between Theory and Experiments. *Acc. Chem. Res.* **2015**, *48*, 792–800.

(3) Crespo-Otero, R.; Barbatti, M. Recent Advances and Perspectives on Nonadiabatic Mixed Quantum–Classical Dynamics. *Chem. Rev.* **2018**, *118*, 7026–7068.

(4) Curchod, B. F. E.; Martínez, T. J. Ab Initio Nonadiabatic Quantum Molecular Dynamics. *Chem. Rev.* **2018**, *118*, 3305–3336.

(5) Agostini, F.; Curchod, B. F. E. Different Flavors of Nonadiabatic Molecular Dynamics. *Wiley Interdiscip. Rev.: Comput. Mol. Sci.* **2019**, *9*, No. e1417.

(6) Barbatti, M. Nonadiabatic Dynamics with Trajectory Surface Hopping Method. *Wiley Interdiscip. Rev.: Comput. Mol. Sci.* **2011**, *1*, 620–633.

(7) Wang, L.; Akimov, A.; Prezhdo, O. V. Recent Progress in Surface Hopping: 2011–2015. *J. Phys. Chem. Lett.* **2016**, *7*, 2100–2112.

(8) Mai, S.; Marquetand, P.; González, L. *Quantum Chemistry and Dynamics of Excited States*; John Wiley & Sons, Ltd, 2020; Chapter 16, pp 499–530.

(9) Tully, J. C. Molecular Dynamics with Electronic Transitions. *J. Chem. Phys.* **1990**, *93*, 1061–1071.

(10) Granucci, G.; Persico, M.; Spighi, G. Surface Hopping Trajectory Simulations with Spin-Orbit and Dynamical Couplings. *J. Chem. Phys.* **2012**, *137*, No. 22A501.

(11) Cui, G.; Thiel, W. Generalized Trajectory Surface-Hopping Method for Internal Conversion and Intersystem Crossing. *J. Chem. Phys.* **2014**, *141*, No. 124101.

(12) Mai, S.; Marquetand, P.; González, L. A General Method to Describe Intersystem Crossing Dynamics in Trajectory Surface Hopping. *Int. J. Quantum Chem.* **2015**, *115*, 1215–1231.

(13) Toldo, J. M.; do Casal, M. T.; Ventura, E.; do Monte, S. A.; Barbatti, M. Surface Hopping Modeling of Charge and Energy Transfer in Complex Environments. *Phys. Chem. Chem. Phys.* **2023**, 8293–8316, DOI: 10.1039/D3CP00247K.

(14) Zobel, J. P.; Heindl, M.; Plasser, F.; Mai, S.; González, L. Surface Hopping Dynamics on Vibronic Coupling Models. *Acc. Chem. Res.* **2021**, *54*, 3760–3771.

(15) Senn, H. M.; Thiel, W. QM/MM Methods for Biomolecular Systems. *Angew. Chem., Int. Ed.* **2009**, *48*, 1198–1229.

(16) Brunk, E.; Rothlisberger, U. Mixed Quantum Mechanical/Molecular Mechanical Molecular Dynamics Simulations of Biological Systems in Ground and Electronically Excited States. *Chem. Rev.* **2015**, *115*, 6217–6263.

(17) Nelson, T. R.; White, A. J.; Bjorgaard, J. A.; Sifain, A. E.; Zhang, Y.; Nebgen, B.; Fernandez-Alberti, S.; Mozyrsky, D.; Roitberg, A. E.; Tretiak, S. Non-Adiabatic Excited-State Molecular Dynamics: Theory and Applications for Modeling Photophysics in Extended Molecular Materials. *Chem. Rev.* **2020**, *120*, 2215–2287.

(18) Granucci, G.; Persico, M.; Toniolo, A. Direct Semiclassical Simulation of Photochemical Processes with Semiempirical Wave Functions. *J. Chem. Phys.* **2001**, *114*, 10608–10615.

(19) Fabiano, E.; Keal, T. W.; Thiel, W. Implementation of Surface Hopping Molecular Dynamics Using Semiempirical Methods. *Chem. Phys.* **2008**, *349*, 334–347.

(20) Humeniuk, A.; Mitrić, R. DFTBaby: A Software Package for Non-Adiabatic Molecular Dynamics Simulations Based on Long-Range Corrected Tight-Binding TD-DFT(B). *Comput. Phys. Commun.* **2017**, *221*, 174–202.

(21) Frankcombe, T. J.; Collins, M. A.; Worth, G. A. Converged quantum dynamics with modified Shepard interpolation and Gaussian wave packets. *Chem. Phys. Lett.* **2010**, *489*, 242–247.

(22) Park, J. W.; Rhee, Y. M. Towards the Realization of Ab Initio Dynamics at the Speed of Molecular Mechanics: Simulations with Interpolated Diabatic Hamiltonian. *ChemPhysChem* **2014**, *15*, 3183–3193.

(23) Dral, P. O.; Barbatti, M. Molecular Excited States through a Machine Learning Lens. *Nat. Rev. Chem.* **2021**, *5*, 388–405.

(24) Westermayr, J.; Dral, P. O.; Marquetand, P. *Quantum Chemistry in the Age of Machine Learning*; Dral, P. O., Ed.; Elsevier, 2023; pp 467–488.

(25) Nottoli, M.; Mazzeo, P.; Lipparini, F.; Cupellini, L.; Mennucci, B. A ΔSCF Model for Excited States within a Polarisable Embedding. *Mol. Phys.* **2022**, *121*, No. e2089605.

(26) Mališ, M.; Luber, S. Trajectory Surface Hopping Nonadiabatic Molecular Dynamics with Kohn–Sham ΔSCF for Condensed-Phase Systems. *J. Chem. Theory Comput.* **2020**, *16*, 4071–4086.

(27) Köppel, H.; Domcke, W.; Cederbaum, L. S. Theory of Vibronic Coupling in Linear Molecules. *J. Chem. Phys.* **1981**, *74*, 2945–2968.

(28) Plasser, F.; Gómez, S.; Menger, M. F. S. J.; Mai, S.; González, L. Highly Efficient Surface Hopping Dynamics Using a Linear Vibronic Coupling Model. *Phys. Chem. Chem. Phys.* **2019**, *21*, 57–69.

(29) Mai, S.; Marquetand, P.; González, L. Nonadiabatic Dynamics: The SHARC Approach. *Wiley Interdiscip. Rev.: Comput. Mol. Sci.* **2018**, *8*, No. e1370.

(30) Mai, S.; Richter, M.; Heindl, M.; Menger, M. F. S. J.; Atkins, A.; Ruckenbauer, M.; Plasser, F.; Ibele, L. M.; Kropf, S.; Oppel, M.; Marquetand, P.; González, L. SHARC2.1: Surface Hopping Including Arbitrary Couplings — Program Package for Non-Adiabatic Dynamics, 2019.

(31) Kramer, C.; Gedeck, P.; Meuwly, M. Atomic Multipoles: Electrostatic Potential Fit, Local Reference Axis Systems, and Conformational Dependence. *J. Comput. Chem.* **2012**, *33*, 1673−1688.

(32) Stone, A. J. Distributed Multipole Analysis, or How to Describe a Molecular Charge Distribution. *Chem. Phys. Lett.* **1981**, *83*, 233−239.

(33) Ponder, J. W.; Wu, C.; Ren, P.; Pande, V. S.; Chodera, J. D.; Schnieders, M. J.; Haque, I.; Mobley, D. L.; Lambrecht, D. S.; DiStasio, R. A. J.; Head-Gordon, M.; Clark, G. N. I.; Johnson, M. E.; Head-Gordon, T. Current Status of the AMOEBA Polarizable Force Field. *J. Phys. Chem. B* **2010**, *114*, 2549−2564.

(34) Park, J. W.; Rhee, Y. M. Diabatic Population Matrix Formalism for Performing Molecular Mechanics Style Simulations with Multiple Electronic States. *J. Chem. Theory Comput.* **2014**, *10*, 5238−5253.

(35) Bayly, C. I.; Cieplak, P.; Cornell, W.; Kollman, P. A. A Well-Behaved Electrostatic Potential Based Method Using Charge Restraints for Deriving Atomic Charges: The RESP Model. *J. Phys. Chem. A* **1993**, *97*, 10269−10280.

(36) Abedi, M.; Levi, G.; Zederkof, D. B.; Henriksen, N. E.; Pápai, M.; Møller, K. B. Excited-State Solvation Structure of Transition Metal Complexes from Molecular Dynamics Simulations and Assessment of Partial Atomic Charge Methods. *Phys. Chem. Chem. Phys.* **2019**, *21*, 4082−4095.

(37) Stone, A. *The Theory of Intermolecular Forces*; OUP Oxford, 2013.

(38) Mulliken, R. S. Electronic Population Analysis on LCAO−MO Molecular Wave Functions. I. *J. Chem. Phys.* **1955**, *23*, 1833−1840.

(39) Hirshfeld, F. L. Bonded-Atom Fragments for Describing Molecular Charge Densities. *Theor. Chim. Acta* **1977**, *44*, 129−138.

(40) Reed, A. E.; Weinstock, R. B.; Weinhold, F. Natural Population Analysis. *J. Chem. Phys.* **1985**, *83*, 735−746.

(41) Bader, R. F. W. A Quantum Theory of Molecular Structure and Its Applications. *Chem. Rev.* **1991**, *91*, 893−928.

(42) Breneman, C. M.; Wiberg, K. B. Determining Atom-Centered Monopoles from Molecular Electrostatic Potentials. The Need for High Sampling Density in Formamide Conformational Analysis. *J. Comput. Chem.* **1990**, *11*, 361−373.

(43) Mai, S.; Atkins, A. J.; Plasser, F.; González, L. The Influence of the Electronic Structure Method on Intersystem Crossing Dynamics. The Case of Thioformaldehyde. *J. Chem. Theory Comput.* **2019**, *15*, 3470−3480.

(44) Zhang, L.; Shu, Y.; Sun, S.; Truhlar, D. G. Direct Coherent Switching with Decay of Mixing for Intersystem Crossing Dynamics of Thioformaldehyde: The Effect of Decoherence. *J. Chem. Phys.* **2021**, *154*, No. 094310.

(45) Fumanal, M.; Plasser, F.; Mai, S.; Daniel, C.; Gindensperger, E. Interstate Vibronic Coupling Constants between Electronic Excited States for Complex Molecules. *J. Chem. Phys.* **2018**, *148*, No. 124119.

(46) Kabsch, W. A Solution for the Best Rotation to Relate Two Sets of Vectors. *Acta Cryst. A* **1976**, *32*, 922−923.

(47) Warshel, A.; Levitt, M. Theoretical Studies of Enzymic Reactions: Dielectric, Electrostatic and Steric Stabilization of the Carbonium Ion in the Reaction of Lysozyme. *J. Mol. Biol.* **1976**, *103*, 227−249.

(48) Joergensen, P.; Simons, J. *Second Quantization-Based Methods in Quantum Chemistry*, 1st ed.; Academic Press: New York, 1981.

(49) Case, D.; Aktulga, H.; Belfon, K.; Ben-Shalom, I.; Berryman, J.; Brozell, S.; Cerutti, D.; Cheatham, T.; Cisneros, G.; Cruzeiro, V.; Darden, T.; Forouzesh, N.; Giambaşu, G.; Giese, T.; Gilson, M.; Gohlke, H.; Goetz, A.; Harris, J.; Izadi, S.; Izmailov, S.; Kasavajhala, K.; Kaymak, M.; King, E.; Kovalenko, A.; Kurtzman, T.; Lee, T.; Li, P.; Lin, C.; Liu, J.; Luchko, T.; Luo, R.; Machado, M.; Man, V.; Manathunga, M.; Merz, K.; Miao, Y.; Mikhailovskii, O.; Monard, G.; Nguyen, H.; O'Hearn, K.; Onufriev, A.; Pan, F.; Pantano, S.; Qi, R.; Rahnamoun, A.; Roe, D.; Roitberg, A.; Sagui, C.; Schott-Verdugo, S.; Shajan, A.; Shen, J.; Simmerling, C.; Skrynnikov, N.; Smith, J.; Swails, J.; Walker, R.; Wang, J.; Wang, J.; Wei, H.; Wu, X.; Wu, Y.; Xiong, Y.; Xue, Y.; York, D.; Zhao, S.; Zhu, Q.; Kollman, P. *Amber 2023*, 2023.

(50) Singh, U. C.; Kollman, P. A. An Approach to Computing Electrostatic Charges for Molecules. *J. Comput. Chem.* **1984**, *5*, 129−145.

(51) Cox, S. R.; Williams, D. E. Representation of the molecular electrostatic potential by a net atomic charge model. *J. Comput. Chem.* **1981**, *2*, 304−323.

(52) Besler, B. H.; Merz, K. M., Jr; Kollman, P. A. Atomic Charges Derived from Semiempirical Methods. *J. Comput. Chem.* **1990**, *11*, 431−439.

(53) Frisch, M. J.; Trucks, G. W.; Schlegel, H. B.; Scuseria, G. E.; Robb, M. A.; Cheeseman, J. R.; Scalmani, G.; Barone, V.; Petersson, G. A.; Nakatsuji, H.; Li, X.; Caricato, M.; Marenich, A. V.; Bloino, J.; Janesko, B. G.; Gomperts, R.; Mennucci, B.; Hratchian, H. P.; Ortiz, J. V.; Izmaylov, A. F.; Sonnenberg, J. L.; Williams-Young, D.; Ding, F.; Lipparini, F.; Egidi, F.; Goings, J.; Peng, B.; Petrone, A.; Henderson, T.; Ranasinghe, D.; Zakrzewski, V. G.; Gao, J.; Rega, N.; Zheng, G.; Liang, W.; Hada, M.; Ehara, M.; Toyota, K.; Fukuda, R.; Hasegawa, J.; Ishida, M.; Nakajima, T.; Honda, Y.; Kitao, O.; Nakai, H.; Vreven, T.; Throssell, K.; Montgomery, J. A., Jr.; Peralta, J. E.; Ogliaro, F.; Bearpark, M. J.; Heyd, J. J.; Brothers, E. N.; Kudin, K. N.; Staroverov, V. N.; Keith, T. A.; Kobayashi, R.; Normand, J.; Raghavachari, K.; Rendell, A. P.; Burant, J. C.; Iyengar, S. S.; Tomasi, J.; Cossi, M.; Millam, J. M.; Klene, M.; Adamo, C.; Cammi, R.; Ochterski, J. W.; Martin, R. L.; Morokuma, K.; Farkas, O.; Foresman, J. B.; Fox, D. J. *Gaussian 16*, revision C.01, 2016.

(54) Lebedev, V. I. Quadratures on a Sphere. *USSR Comput. Math. Math. Phys.* **1976**, *16*, 10−24.

(55) Sun, Q.; Berkelbach, T. C.; Blunt, N. S.; Booth, G. H.; Guo, S.; Li, Z.; Liu, J.; McClain, J. D.; Sayfutyarova, E. R.; Sharma, S.; Wouters, S.; Chan, G. K.-L. PySCF: The Python-based Simulations of Chemistry Framework. *Wiley Interdiscip. Rev.: Comput. Mol. Sci.* **2018**, *8*, No. e1340.

(56) Sun, Q.; Zhang, X.; Banerjee, S.; Bao, P.; Barbry, M.; Blunt, N. S.; Bogdanov, N. A.; Booth, G. H.; Chen, J.; Cui, Z.-H.; Eriksen, J. J.; Gao, Y.; Guo, S.; Hermann, J.; Hermes, M. R.; Koh, K.; Koval, P.; Lehtola, S.; Li, Z.; Liu, J.; Mardirossian, N.; McClain, J. D.; Motta, M.; Mussard, B.; Pham, H. Q.; Pulkin, A.; Purwanto, W.; Robinson, P. J.; Ronca, E.; Sayfutyarova, E. R.; Scheurer, M.; Schurkus, H. F.; Smith, J. E. T.; Sun, C.; Sun, S.-N.; Upadhyay, S.; Wagner, L. K.; Wang, X.; White, A.; Whitfield, J. D.; Williamson, M. J.; Wouters, S.; Yang, J.; Yu, J. M.; Zhu, T.; Berkelbach, T. C.; Sharma, S.; Sokolov, A. Y.; Chan, G. K.-L. Recent Developments in the PySCF Program Package. *J. Chem. Phys.* **2020**, *153*, No. 024109.

(57) Furche, F.; Ahlrichs, R. Adiabatic Time-Dependent Density Functional Methods for Excited State Properties. *J. Chem. Phys.* **2002**, *117*, 7433−7447.

(58) Casida, M. E. *Recent Advances in Density Functional Methods*; World Scientific: Singapore, 1995; pp 155−192.

(59) Alenaizan, A.; Burns, L. A.; Sherrill, C. D. Python Implementation of the Restrained Electrostatic Potential Charge Model. *Int. J. Quantum Chem.* **2020**, *120*, No. e26035.

(60) Mai, S.; Avagliano, D.; Heindl, M.; Marquetand, P.; Menger, M. F. S. J.; Oppel, M.; Plasser, F.; Polonius, S.; Ruckenbauer, M.; Shu, Y.; Truhlar, D. G.; Zhang, L.; Zobel, P.; González, L. *SHARC3.0: Surface Hopping Including Arbitrary Couplings — Program Package for Non-Adiabatic Dynamics*, 2023. DOI: 10.5281/zenodo.7828641

(61) Becke, A. D. Density-Functional Exchange-Energy Approximation with Correct Asymptotic Behavior. *Phys. Rev. A* **1988**, *38*, 3098−3100.

(62) Perdew, J. P. Density-Functional Approximation for the Correlation Energy of the Inhomogeneous Electron Gas. *Phys. Rev. B* **1986**, *33*, 8822−8824.

(63) Weigend, F.; Ahlrichs, R. Balanced Basis Sets of Split Valence, Triple Zeta Valence and Quadruple Zeta Valence Quality for H to Rn: Design and Assessment of Accuracy. *Phys. Chem. Chem. Phys.* **2005**, *7*, 3297−3305.

(64) Neese, F. Software Update: The ORCA Program System—Version 5.0. *Wiley Interdiscip. Rev.: Comput. Mol. Sci.* **2022**, *12*, No. e1606.

(65) Vosko, S. H.; Wilk, L.; Nusair, M. Accurate Spin-Dependent Electron Liquid Correlation Energies for Local Spin Density Calculations: A Critical Analysis. *Can. J. Phys.* **1980**, *58*, 1200−1211.

(66) Jorgensen, W. L.; Chandrasekhar, J.; Madura, J. D.; Impey, R. W.; Klein, M. L. Comparison of Simple Potential Functions for Simulating Liquid Water. *J. Chem. Phys.* **1983**, *79*, 926−935.

(67) He, X.; Man, V. H.; Yang, W.; Lee, T.-S.; Wang, J. A Fast and High-Quality Charge Model for the next Generation General AMBER Force Field. *J. Chem. Phys.* **2020**, *153*, No. 114502.

(68) Mai, S.; Gattuso, H.; Monari, A.; González, L. Novel Molecular-Dynamics-Based Protocols for Phase Space Sampling in Complex Systems. *Front. Chem.* **2018**, *6*, No. 495.

(69) Andersen, H. C. Rattle: A "Velocity" Version of the Shake Algorithm for Molecular Dynamics Calculations. *J. Comput. Phys.* **1983**, *52*, 24−34.

(70) Avagliano, D.; Bonfanti, M.; Garavelli, M.; González, L. QM/MM Nonadiabatic Dynamics: The SHARC/COBRAMM Approach. *J. Chem. Theory Comput.* **2021**, *17*, 4639−4647.

(71) Grønbech-Jensen, N.; Farago, O. A Simple and Effective Verlet-type Algorithm for Simulating Langevin Dynamics. *Mol. Phys.* **2013**, *111*, 983−991.

(72) Reiner, M. M.; Bachmair, B.; Tiefenbacher, M. X.; Mai, S.; González, L.; Marquetand, P.; Dellago, C. Nonadiabatic Forward Flux Sampling for Excited-State Rare Events. *J. Chem. Theory Comput.* **2023**, *19*, 1657−1671.

(73) Sankararamakrishnan, R.; Konvicka, K.; Mehler, E. L.; Weinstein, H. Solvation in Simulated Annealing and High-Temperature Molecular Dynamics of Proteins: A Restrained Water Droplet Model. *Int. J. Quantum Chem.* **2000**, *77*, 174−186.

(74) Eastman, P.; Swails, J.; Chodera, J. D.; McGibbon, R. T.; Zhao, Y.; Beauchamp, K. A.; Wang, L.-P.; Simmonett, A. C.; Harrigan, M. P.; Stern, C. D.; Wiewiora, R. P.; Brooks, B. R.; Pande, V. S. OpenMM 7: Rapid Development of High Performance Algorithms for Molecular Dynamics. *PLoS Comput. Biol.* **2017**, *13*, No. e1005659.

(75) Ponder, J. W.; Case, D. A. *Advances in Protein Chemistry*; Protein Simulations; Academic Press, 2003; Vol. *66*, pp 27−85.

(76) Legon, A. C.; Millen, D. J. Angular Geometries and Other Properties of Hydrogen-Bonded Dimers: A Simple Electrostatic Interpretation of the Success of the Electron-Pair Model. *Chem. Soc. Rev.* **1987**, *16*, 467−498.

(77) Del Bene, J. E. Molecular Orbital Theory of the Hydrogen Bond. IV. The Dimers ROH···OCH2. *J. Chem. Phys.* **1973**, *58*, 3139−3145.

(78) García, A. E.; Stiller, L. Computation of the mean residence time of water in the hydration shells of biomolecules. *J. Comput. Chem.* **1993**, *14*, 1396−1406.

(79) Dreuw, A.; Head-Gordon, M. Single-Reference Ab Initio Methods for the Calculation of Excited States of Large Molecules. *Chem. Rev.* **2005**, *105*, 4009−4037.

(80) Lischka, H.; Nachtigallová, D.; Aquino, A. J. A.; Szalay, P. G.; Plasser, F.; Machado, F. B. C.; Barbatti, M. Multireference Approaches for Excited States of Molecules. *Chem. Rev.* **2018**, *118*, 7293−7361.

(81) MacKerell, A. D.; Bashford, D.; Bellott, M.; Dunbrack, R. L.; Evanseck, J. D.; Field, M. J.; Fischer, S.; Gao, J.; Guo, H.; Ha, S.; Joseph-McCarthy, D.; Kuchnir, L.; Kuczera, K.; Lau, F. T. K.; Mattos, C.; Michnick, S.; Ngo, T.; Nguyen, D. T.; Prodhom, B.; Reiher, W. E.; Roux, B.; Schlenkrich, M.; Smith, J. C.; Stote, R.; Straub, J.; Watanabe, M.; Wiórkiewicz-Kuczera, J.; Yin, D.; Karplus, M. All-Atom Empirical Potential for Molecular Modeling and Dynamics Studies of Proteins. *J. Phys. Chem. B* **1998**, *102*, 3586−3616.

(82) Hornak, V.; Abel, R.; Okur, A.; Strockbine, B.; Roitberg, A.; Simmerling, C. Comparison of multiple Amber force fields and development of improved protein backbone parameters. *Proteins* **2006**, *65*, 712−725.

(83) Duan, Y.; Wu, C.; Chowdhury, S.; Lee, M. C.; Xiong, G.; Zhang, W.; Yang, R.; Cieplak, P.; Luo, R.; Lee, T.; Caldwell, J.; Wang, J.; Kollman, P. A point-charge force field for molecular mechanics simulations of proteins based on condensed-phase quantum mechanical calculations. *J. Comput. Chem.* **2003**, *24*, 1999−2012.

(84) Tomasi, J.; Mennucci, B.; Cammi, R. Quantum Mechanical Continuum Solvation Models. *Chem. Rev.* **2005**, *105*, 2999−3094.

(85) Stone, A.; Alderton, M. Distributed Multipole Analysis. *Mol. Phys.* **1985**, *56*, 1047−1064.

(86) Wheatley, R. J. Gaussian Multipole Functions for Describing Molecular Charge Distributions. *Mol. Phys.* **1993**, *79*, 597−610.

(87) Cisneros, G. A. Application of Gaussian Electrostatic Model (GEM) Distributed Multipoles in the AMOEBA Force Field. *J. Chem. Theory Comput.* **2012**, *8*, 5072−5080.

(88) Liu, C.; Piquemal, J.-P.; Ren, P. Implementation of Geometry-Dependent Charge Flux into the Polarizable AMOEBA+ Potential. *J. Phys. Chem. Lett.* **2020**, *11*, 419−426.

(89) Jing, Z.; Liu, C.; Cheng, S. Y.; Qi, R.; Walker, B. D.; Piquemal, J.-P.; Ren, P. Polarizable Force Fields for Biomolecular Simulations: Recent Advances and Applications. *Annu. Rev. Biophys.* **2019**, *48*, 371−394.

(90) Hagras, M. A.; Glover, W. J. Polarizable Embedding for Excited-State Reactions: Dynamically Weighted Polarizable QM/MM. *J. Chem. Theory Comput.* **2018**, *14*, 2137−2144.

(91) Bondanza, M.; Nottoli, M.; Cupellini, L.; Lipparini, F.; Mennucci, B. Polarizable Embedding QM/MM: The Future Gold Standard for Complex (Bio)Systems? *Phys. Chem. Chem. Phys.* **2020**, *22*, 14433−14448.

Recommended by ACS

PMC-IZ: A Simple Algorithm for the Electrostatics Calculation in Slab Geometric Molecular Dynamics Simulations

Yu-Peng Huang, Yi Qin Gao, et al.

JANUARY 09, 2024

JOURNAL OF CHEMICAL THEORY AND COMPUTATION READ

A Fast, Convenient, Polarizable Electrostatic Model for Molecular Dynamics

Liangyue Wang, Michael K. Gilson, et al.

JANUARY 19, 2024

JOURNAL OF CHEMICAL THEORY AND COMPUTATION READ

Polarizable Embedding without Artificial Boundary Polarization

Sonata Kvedaravičiūtė, Jógvan Magnus Haug

JULY 17, 2023

JOURNAL OF CHEMICAL THEORY AND COMPUTATION READ

Assessment of Electrostatic Energy-Based Charge Model for Modeling the Electrostatic Interaction in Water Solvent

Xianwei Wang, John Z. H. Zhang, et al.

SEPTEMBER 01, 2023

JOURNAL OF CHEMICAL THEORY AND COMPUTATION READ

Get More Suggestions >

APPENDIX A.1.2

Resolving Photoinduced Femtosecond Three-Dimensional Solute–Solvent Dynamics through Surface Hopping Simulations

SEVERIN POLONIUS, DAVID LEHRNER, LETICIA GONZÁLEZ, SEBASTIAN MAI

J. Chem. Theory Comput., **20**, 4738-–4750 (2024).
`https://doi.org/10.1021/acs.jctc.4c00169`

Contributions:

SEVERIN POLONIUS ...performed all simulations and analyses, wrote the initial draft, and finalized the manuscript.

DAVID LEHRNER ...contributed implementations to the SHARC MOLCAS interface.

LETICIA GONZÁLEZ ...conceived the scope of the manuscript and contributed to the final manuscript.

SEBASTIAN MAI ...planned the manuscript with the authors, supervised all developments, analyses and writing, and contributed to the final manuscript.

Article reprinted under the terms of the Creative Commons CC BY license.

JCTC Journal of Chemical Theory and Computation

pubs.acs.org/JCTC

Article

Open Access

This article is licensed under CC-BY 4.0

Resolving Photoinduced Femtosecond Three-Dimensional Solute–Solvent Dynamics through Surface Hopping Simulations

Severin Polonius, David Lehrner, Leticia González, and Sebastian Mai*

Cite This: https://doi.org/10.1021/acs.jctc.4c00169

Read Online

Downloaded via UNIV OF VIENNA on June 3, 2024 at 11:15:19 (UTC).
See https://pubs.acs.org/sharingguidelines for options on how to legitimately share published articles.

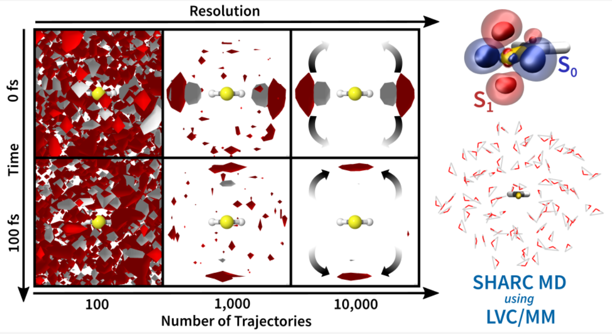

ABSTRACT: Photoinduced dynamics in solution is governed by mutual solute–solvent interactions, which give rise to phenomena like solvatochromism, the Stokes shift, dual fluorescence, or charge transfer. Understanding these phenomena requires simulating the solute's photoinduced dynamics and simultaneously resolving the three-dimensional solvent distribution dynamics. If using trajectory surface hopping (TSH) to this aim, thousands of trajectories are required to adequately sample the time-dependent three-dimensional solvent distribution functions, and thus resolve the solvent dynamics with sub-Ångstrom and femtosecond accuracy and sufficiently low noise levels. Unfortunately, simulating thousands of trajectories with TSH in the framework of hybrid quantum mechanical/molecular mechanical (QM/MM) can be prohibitively expensive when employing ab initio electronic structure methods. To tackle this challenge, we recently introduced a computationally efficient approach that combines efficient linear vibronic coupling models with molecular mechanics (LVC/MM) via electrostatic embedding [Polonius et al., JCTC **2023,** *19,* 7171–7186]. This method provides solvent-embedded, nonadiabatically coupled potential energy surfaces while scaling similarly to MM force fields. Here, we employ TSH with LVC/MM to unravel the photoinduced dynamics of two small thiocarbonyl compounds solvated in water. We describe how to estimate the number of trajectories required to produce nearly noise-free three-dimensional solvent distribution functions and present an analysis based on approximately 10,000 trajectories propagated for 3 ps. In the electronic ground state, both molecules exhibit in-plane hydrogen bonds to the sulfur atom. Shortly after excitation, these bonds are broken and reform perpendicular to the molecular plane on timescales that differ by an order of magnitude due to steric effects. We also show that the solvent relaxation dynamics is coupled to the electronic dynamics, including intersystem crossing. These findings are relevant to advance the understanding of the coupled solute–solvent dynamics of solvated photoexcited molecules, e.g., biologically relevant thio-nucleobases.

1. INTRODUCTION

The intricate interplay between solute and solvent molecules is key to understand solubility, structure, (catalytic) reactivity, as well as molecular dynamics and the nature of electronic states.[1−5] Importantly, solvent molecules do not only exert electrostatic influence on a solute molecule and its electronic states but are also reciprocally influenced by the electronic structure of the solute. This is particularly true for photoinduced processes where excited electronic states can exhibit drastically different electrostatics compared to the ground state and to each other.[6] These differences in electrostatics are at the origin of phenomena like solvatochromism, the Stokes shift,[7,8] solvent-dependent dual fluorescence,[9,10] or solvent-dependent charge transfer dynamics.[11,12] All of these phenomena involve complex entangled dynamics of solute and solvent involving all of their nuclear and electronic degrees of freedom.

The experimental observation of ultrafast coupled solute–solvent dynamics is very challenging and often requires the combination of multiple techniques such as time-resolved X-ray solution scattering,[12−15] transient absorption spectroscopy,[16,17] or X-ray fluorescence spectroscopy.[18−20] These challenges make computational simulations essential in the analysis and interpretation of such experiments. These simulations should ideally be able to describe (i) the nonadiabatic dynamics of a solute molecule, (ii) the mutual interaction of solute and solvent molecules with (iii) femtosecond time resolution but simultaneously on (iv) sufficiently long timescales, and with (v) sufficiently low noise levels of the (three-dimensional) solvent distribution functions at an adequate spatial resolution. The requirements (i)−(iii) can be met by nonadiabatic molecular dynamics simulations,[21−25] for instance with trajectory surface hopping

Received: February 9, 2024
Revised: April 22, 2024
Accepted: May 7, 2024

© XXXX The Authors. Published by American Chemical Society

(TSH)[26−28] in a quantum mechanical/molecular mechanics (QM/MM) framework, i.e., employing a quantum-mechanical description of the solute coupled with a classical solvent.[29−31] In contrast, the requirements (iv) and (v) pose a significant challenge due to the high computational cost associated with ab initio TSH simulations. While current state-of-the-art (solute-focused) TSH simulations are typically limited to a few hundred trajectories[23] and propagation times of a few picoseconds, a detailed description of solute−solvent dynamics would require thousands of trajectories (vide infra) and propagation up to tens or even hundreds of picoseconds.[32,33]

Recently, we have presented a novel approach to perform solvation-focused TSH simulations through the combination of a linear vibronic coupling (LVC) model[34] with a classically described solvent in a QM/MM fashion, using electrostatic embedding based on distributed multipoles for the solute.[35] This approach, called LVC/MM, is an extension of the LVC model approach that has previously been shown to enable highly efficient TSH simulations within the surface hopping including arbitrary coupling (SHARC)[36−39] program package.

The goal of this work is to demonstrate how the LVC/MM method facilitates the simulation of the coupled evolution of the solute's nuclei and electrons—including intersystem crossing (ISC)—and the three-dimensional solvent distribution, with a simultaneous sub-Å and femtosecond accuracy. The method is applied to unravel the solute−solvent relaxation dynamics of thioformaldehyde (CH_2S) and thioacetone (CMe_2S) in water (Figure 1a,b). Although these compounds are highly reactive and short-lived in solution and in the gas phase, where they oligomerize within seconds,[40] they still constitute useful test systems for three reasons: (i) CH_2S is the smallest thiocarbonyl and has been previously used to benchmark the performance of different electronic structure methods and decoherence schemes in TSH,[41,42] as well as to demonstrate the capabilities of the LVC/MM method in the ground state.[35] The present study adds thioacetone (CMe_2S) as a heavier analogue to investigate the effect of steric hindrance. (ii) The nonadiabatic dynamics of both molecules is governed by the $^1n\pi^*$−$^3\pi\pi^*$ (S_1−T_2) energy gap,[43−45] which is too large to allow fast ISC[41] in the gas phase but is dynamically modulated in aqueous solution by hydrogen bonds[35] (Figures 1c and S1). (iii) Both molecules can serve as prototypes to understand solute−solvent dynamics of larger molecules containing thiocarbonyl groups, e.g., biologically relevant thionated nucleobase analogues.[46−50]

In the following, we outline the core equations of the LVC/MM method (Section 2) and describe the computations in terms of the LVC model parametrization, system preparation with MM, and nonadiabatic dynamics using SHARC (Section 3). Importantly, in Section 4, we discuss novel aspects of the analysis of temporally and spatially resolved solvent distributions and provide guidelines for choosing the number of trajectories depending on the investigated processes. Finally, in Section 5, we analyze the results obtained for both thiocarbonyls.

2. THEORY

Here, we only provide the essential equations of electrostatic embedding LVC/MM—the method is fully documented in ref 35. The solute is described by the LVC Hamiltonian matrix $\mathbf{H}_{\mathrm{LVC}}(\mathbf{R}_{\mathrm{QM}})$, which is constructed from coupled harmonic oscillators in normal-mode coordinates for all diabatic states.

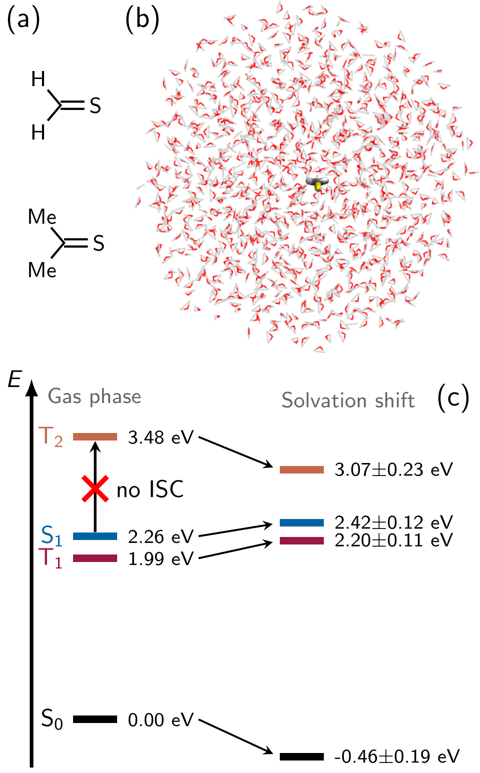

Figure 1. (a) Structures of CH_2S and CMe_2S, (b) simulated water droplet with CH_2S, and (c) equilibrium energies for the gas phase and respective solvation shift for CH_2S. The gas-phase energies are taken from the LVC parameters (obtained at the MS-CASPT2 level of theory). The solvation shifts are calculated from averages and standard deviations from an equilibrated LVC/MM trajectory in the S_0 state in solution and include the electrostatic embedding term. The state characters are discussed in Section 5.1.

In LVC/MM, these diabatic states are electrostatically coupled to a set of point charges via the interaction matrix **X**

$$\mathbf{H}_{\mathrm{LVC/MM}}(\mathbf{R}_{\mathrm{QM}}, \mathbf{R}_{\mathrm{MM}}) = \mathbf{H}_{\mathrm{LVC}}(\mathbf{R}_{\mathrm{QM}}) + \mathbf{X}(\mathbf{R}_{\mathrm{QM}}, \mathbf{R}_{\mathrm{MM}}) \tag{1}$$

The interaction term X_{ij} of two states i and j is given by

$$X_{ij} = \sum_{b}^{B} q_b \left(\delta_{ij} \sum_{a}^{A} \frac{Z_a}{|\mathbf{r}_a - \mathbf{r}_b|} - \int \mathrm{d}\mathbf{r} \frac{\rho^{(ij)}}{|\mathbf{r} - \mathbf{r}_b|} \right) \tag{2}$$

where q_b and $\mathbf{r}_b$ are charges and positions of the solvent atoms, Z_a and $\mathbf{r}_a$ are charges and positions of the solute atoms, and $\rho^{(ij)}$ is an electron density ($i = j$) or transition density ($i \neq j$). The term X_{ij} describes solvent-induced shifts in energy ($i = j$) and solvent-induced state mixing ($i \neq j$).

LVC models typically do not carry explicit information about the electronic wave functions (or densities). Thus, each $\rho^{(ij)}$ in eq 2 is represented through a distributed multipole expansion (DME)[51] fitted for each ij, consisting of a partial charge, dipole moment, and quadrupole moment for each solute atom, which reproduce the electrostatic potential of the reference density. The interaction term X_{ij} can then be rewritten as

$$X_{ij} = \sum_{b}^{B} q_b \left(\delta_{ij} \sum_{a}^{A} \frac{Z_a}{|\mathbf{r}_a - \mathbf{r}_b|} - \sum_{a}^{A} \mathbf{Q}_a^{(ij)} \cdot \mathbf{T}_{ab} \right) \tag{3}$$

where $\mathbf{Q}_a^{(ij)}$ is the vector collecting the monopole, dipole, and quadrupole charges for atom a and state pair ij and $\mathbf{T}_{ab}$ is the corresponding geometric tensor of the multipole expansion.[51] As discussed previously,[35] the DME parameters $\mathbf{Q}_a^{(ij)}$ depend on molecular orientation, so we use the Kabsch algorithm[52] to transform the coordinates at each time step into the reference coordinate system. This allows computing rotationally invariant gradients and nonadiabatic couplings in LVC/MM.

3. COMPUTATIONAL DETAILS

The investigation of the coupled solute−solvent excited-state dynamics of CH_2S and CMe_2S consists of several steps that will be described in detail in the subsections below. In short: First, a set of LVC parameters (reference harmonic oscillator, vertical shifts, linear intrastate and interstate couplings, spin−orbit couplings, and DME parameters) was generated for each molecule. Second, we set up and pre-equilibrated both molecular systems (CH_2S and CMe_2S in water) using classical molecular dynamics in AMBER.[53] Third, we performed LVC/MM simulations with SHARC[38,39] in the electronic ground state to finalize the equilibration and produce initial conditions. Fourth, we carried out nonadiabatic LVC/MM TSH simulations after excitation to the S_1 state. Afterward, the results of the simulations were analyzed. The analysis of the solvent distribution dynamics and the required number of trajectories—one of the main foci of this work—are described separately in Section 4.

3.1. LVC Setup. For both molecules, the S_0 was optimized and frequencies were calculated with RIJCOSX-MP2[54] and the cc-pVTZ basis set[55,56] using the ORCA program package.[57] These calculations provided the reference harmonic oscillators used in the LVC models (usually called V_0 in the LVC literature[35]). The vibronic coupling parameters were evaluated using finite differences[37,58] with multistate complete active space second-order perturbation theory (MS-CASPT2), using OpenMolcas v22.06.[59]

The CASPT2 calculations used the cc-pVTZ basis set,[55,56] an IPEA shift of 0.25 au,[60] an imaginary level shift of 0.1 au,[61] and the Cholesky decomposition. For CH_2S, we used an active space of 10 electrons in 9 orbitals, covering the sulfur lone pair, the π/π^* pair, and the σ/σ^* pairs of the three bonds (see Figure S2). The state-average complete active space self-consistent field (CASSCF) and MS-CASPT2[62] computations included the first 9 singlet and first 9 triplet excited states, to stabilize the active space. For CMe_2S, we used a smaller active space of 6 electrons in 5 orbitals (lone pair, π/π^*, σ/σ^* of the C═S bond, see Figure S3) as we encountered convergence issues with the (10,9) active space. This smaller active space was found to be stable when using the first 5 singlet and 4 triplet states. Based on previous work,[41] different active spaces can be expected to only affect overall excitation energies but not excited-state energy gaps or geometries. For both molecules, the LVC models were constructed for the first four states (S_0, S_1, T_1, and T_2).

The DME parameters[63] needed for electrostatic embedding were obtained by applying the restrained electrostatic potential (RESP) fit method[64] (extended to treat multipoles[35]) to the relaxed electronic and transition densities. The extraction of these densities from OpenMolcas calculations for the subsequent RESP fits was newly implemented in the SHARC−OpenMolcas interface as part of the present work. In the RESP fits, we used the same settings as in our previous work,[35] i.e., the original Merz−Singh−Kollman scheme and vdW radii, and a Lebedev quadrature with a density of 10 points/Å^2. The used restraint parameter c_2 (see eq 33 in ref 35) was 0.0005, 0.0015, and 0.003 (in units of elementary charge) for monopoles, dipoles, and quadrupoles, respectively.

The LVC model parameter files for both molecules are provided in the Supporting Information, whose contents are summarized in Figure S4.

3.2. System Preparation. Both solute−solvent systems were prepared using tools from the AMBER package.[53] The molecules were solvated in a 15 Å truncated octahedron box of TIP3P[65] water (1091 and 1155 water molecules, respectively), as in our previous work.[35] Using a 2 fs time step, periodic boundary conditions, SHAKE[66] for bonds involving H, and GAFF2 parameters[67] for the solutes, the systems were then relaxed for 1000 steps to remove bad contacts and cavities from the initially generated box, heated for 50 ps to 300 K (*NVT* ensemble), and equilibrated for 50 ns at 300 K and 1 bar (*NpT* ensemble). The final coordinates and velocities were reimaged into the original box (with the solute centered) and converted to the SHARC initial condition format.[68]

AMBER input files are given in the Supporting Information, whose contents are summarized in Figure S4.

3.3. SHARC Dynamics. As we showed previously,[35] the first solvation shell of CH_2S cannot be correctly simulated without including quadrupole charges on the S atom. Hence, the final snapshot of each AMBER trajectory was re-equilibrated using LVC/MM in the S_0 to sample the initial conditions needed for TSH. The S_0 simulations for both molecules were run with S_0-only LVC-parameter files using a 2 fs time step. All solute and solvent distances involving H atoms were constrained to their equilibrium distances using the RATTLE algorithm implemented in SHARC 3.0.[69,70] We simulated 1 ns employing a Langevin thermostat[71] set to 293.15 K with a friction constant of 0.02 fs^{-1}, a droplet potential,[72] and a tether potential for the solute[35] (for further details, see the input files provided in the Supporting Information). The first 50 ps serve as a re-equilibration step (to adapt the system from the force-field-based ensemble to the ensemble corresponding to LVC/MM) and were discarded. Snapshots were taken every 100 fs for the remaining 0.95 ns, producing 9500 and 9499 initial conditions for CH_2S and CMe_2S, respectively.[73] This very large number of initial conditions is rationalized below in Section 4.2.

Using these sets of initial conditions for the two molecules, we performed TSH simulations including the entire water droplet. For comparison, we also performed TSH simulations in the gas phase by deleting all water molecules from the initial conditions. All initial conditions were propagated with a 0.5 fs time step for 3 ps after excitation to the S_1. The TSH electronic wave function was propagated with a 0.02 fs time step using the local diabatization method.[74,75] An energy-based decoherence correction scheme[76] was applied to the electronic wave function, taking only the kinetic energy of the solute atoms into account. Likewise, the velocity vector rescaling after a hop was only applied to the solute atoms.

To reduce the produced TSH data to a manageable amount, data were stored every 5 fs during the first 100 fs and every 50 fs thereafter, for 79 data points per trajectory. For a subset of 500 trajectories, all time steps were retained for the analysis of the evolution of electronic populations. For reference purposes, we furthermore simulated trajectories in the S_0 for 1 ps, starting from the same initial conditions but with their initial velocity vectors multiplied by −1.

SHARC input files and setup/analysis scripts are given in the Supporting Information, whose contents are summarized in Figure S4.

4. DETAILS ON SOLVENT DYNAMICS ANALYSIS

In this section, we discuss the novel aspects of analyzing the three-dimensional solvent distribution and its dynamics around a photoexcited solute. We first discuss how the distribution functions should be computed and then discuss the number of trajectories required to achieve a certain spatial resolution at an acceptable noise level.

4.1. Trajectory Analysis. One of our primary goals is understanding the structure and dynamics of the solvation shell around the molecule. Hence, the nuclear coordinates from all the trajectories (totaling coordinates of about 4 billion atoms per system) were analyzed using two different kinds of distribution functions.

First, we compute radial distribution functions (RDFs) between the solute S atom and the water O atoms. The bin width was chosen as 0.05 Å and the RDFs were normalized by dividing with $4\pi R^2\,\mathrm{d}R n_{\mathrm{traj}}\rho_{\mathrm{water}}$. The RDFs extracted from the S_0 trajectories served as reference to calculate difference RDFs. The temporal evolution was then extracted using singular value decomposition (SVD) of the difference RDFs, $\Delta\mathrm{RDF}(R, t) = \sum_i V_i(R)\cdot s_i\cdot U_i(t)$.

Second, as the RDFs cannot capture the complete solvent shell dynamics around the molecule, we also compute three-dimensional histograms of water O and H atom occurrences around the solute. We call these three-dimensional histograms "3D spatial distribution functions" (3D-SDFs) below. One important difference between the RDF and 3D-SDF analyses is that the RDFs are invariant under rotation of the solute (because they depend only on interatomic distances), whereas the 3D-SDFs do depend on the solute's orientation. Thus, for the 3D-SDF analysis, the trajectory coordinates need to be aligned before aggregating the histograms. In the present work, this was performed with two different protocols. Both protocols can be defined in terms of a transformation operator $\hat{T}_k(t)$ for every trajectory k, which is obtained as a function $\hat{T}_k(t) = f(\mathbf{R}_k^{(\mathrm{solute})}(t), \mathbf{R}_{\mathrm{ref}}^{(\mathrm{solute})})$. This operator superimposes the nuclear coordinates of the solute $\mathbf{R}_k^{(\mathrm{solute})}(t)$ in trajectory k at time t onto the solute reference coordinates $\mathbf{R}_{\mathrm{ref}}^{(\mathrm{solute})}$. The operator is obtained through the Kabsch algorithm[52] and applies a series of translation, rotation, and translation to a set of solute and/or solvent coordinates (details are given in Section 2.2 of ref 35).

In the first of the two protocols, for each trajectory the solute coordinates $\mathbf{R}_k(t)$ of all time steps are superimposed onto a common reference structure

$$\mathbf{R}'_k(t) = \hat{T}_k(t)\mathbf{R}_k(t) \tag{4}$$

In this way, the solute serves as a fixed reference, allowing to aggregate the solvent distribution relative to the solute. Thus, we call the so-obtained 3D-SDFs to be from the "molecule's perspective". Because this perspective describes where the solvent is relative to the molecule (and its functional groups), it allows the direct interpretation of the solvent−solute interactions (e.g., solvation shifts of different electronic states). However, in this perspective, one can only observe the apparent motion of the solvent relative to the solute, whereas it is not possible to observe the actual solvent motion in an outside, fixed laboratory frame. Thus, intrinsic solvent relaxation timescales, diffusion coefficients, and similar quantities will be inaccessible.

In the second protocol, each trajectory is superimposed onto the reference using the transformation operator for $t = 0$ fs

$$\mathbf{R}'_k(t) = \hat{T}_k(0)\mathbf{R}_k(t) \tag{5}$$

In this way, the solute trajectories will diverge from the reference orientation, so it is not possible to investigate the solvent dynamics relative to the solute. However, this perspective features a fixed, inertial frame of reference, meaning one can observe the intrinsic solvent fluctuations in three-dimensional space, giving access to solvent relaxation timescales. Thus, this is the "solvent's perspective".

The 3D-SDFs were collected using the cpptraj program from AmberTools23.[53] We employed three-dimensional grid cells with an edge length of 0.5 Å (i.e., with volume of 0.125 Å^3). This value is approximately equivalent to the highest resolutions in experimental X-ray crystallography achieved to date[77,78] and is also approximately equal to the radius of a H atom and hence corresponds roughly to the smallest features of atomic positions that are desirable to be resolved in the solvent distribution. All depictions of the solute molecules and the 3D-SDFs were composed using the Jmol program.[79] The 3D-SDF temporal evolution was also analyzed using SVD, $\Delta\mathrm{SDF}(x,y,z,t) = \sum_i V_i(x,y,z)\cdot s_i\cdot U_i(t)$.

4.2. Number of Trajectories. The last point to discuss here is the estimation of the number of trajectories required to resolve the solvent dynamics via the 3D-SDFs with a desired grid spacing. The expectation value of the number of O atoms (and thus water molecules) in a grid cell is given by

$$\langle N_{\mathrm{O\ per\ cell}}\rangle = \frac{\rho_{\mathrm{water}} N_{\mathrm{A}} V_{\mathrm{cell}}}{M_{\mathrm{water}}} \tag{6}$$

where ρ_{water} is the density of water, N_{A} is Avogadro's constant, V_{cell} is the volume of a grid cell, and M_{water} is the molar mass of water. At room temperature, this corresponds to about 0.0042 water molecules per grid cell (with V_{cell} = 0.125 Å^3), showing that the grid cells are significantly smaller than the solvent molecules.

The standard deviation of $\langle N_{\mathrm{O\ per\ cell}}\rangle$ due to density fluctuations[80,81] can be computed from

$$\sigma_{\mathrm{O\ per\ cell}} = \sqrt{\frac{k_{\mathrm{B}}T\chi}{V_{\mathrm{cell}}}}\langle N_{\mathrm{O\ per\ cell}}\rangle = \sqrt{k_{\mathrm{B}}T\chi V_{\mathrm{cell}}}\frac{\rho_{\mathrm{water}}N_{\mathrm{A}}}{M_{\mathrm{water}}} \tag{7}$$

where k_{B} is Boltzmann's constant, T is the temperature, and χ is the isothermal compressibility (about 0.45 GPa^{-1} for water at standard conditions[82]). Comparison of eqs 6 and 7 shows that the number of water molecules per cell grows linearly with V_{cell} while the standard deviation grows with $\sqrt{V_{\mathrm{cell}}}$. Hence, larger grid cells will provide less noisy 3D-SDFs, although at the cost of reducing the spatial resolution of the investigated solvent dynamics. Thus, a more expedient way to reduce the noise of the 3D-SDFs is to employ several trajectories. This is equivalent to replacing V_{cell} by $n_{\mathrm{traj}}V_{\mathrm{cell}}$ in eqs 6 and 7, so that the final relative standard deviation is

$$\frac{\sigma_{\mathrm{O\ per\ cell}}}{\langle N_{\mathrm{O\ per\ cell}}\rangle} = \sqrt{\frac{k_{\mathrm{B}}T\chi}{V_{\mathrm{cell}}n_{\mathrm{traj}}}} \tag{8}$$

To adequately estimate the noise level of the 3D-SDFs, we also need to consider that for very small grid cells, as the ones used here, the effective isothermal compressibility is much higher than in the macroscopic limit.[81] In Figure S5, we estimate the effective isothermal compressibility of TIP3P water to be 7.32 GPa^{-1} for a grid spacing of 0.5 Å. With this value, eq 8 becomes approximately $\sqrt{\frac{241}{n_{\text{traj}}}}$.

The relation in eq 8 is shown in the contour plot in Figure 2a, providing the relative standard deviation as a function of the grid spacing and n_{traj} with χ = 7.32 GPa^{-1}. A trajectory number of 100 (typical for many TSH studies) thus would produce a relative standard deviation of 155% in the 3D-SDF, making the identification of significant solvent dynamics very difficult. Instead, 1000 trajectories correspond to a 50% deviation and 10,000 trajectories to 16% deviation. Figure 2b provides examples that showcase how well the features of the solvent distribution can be discerned in the 3D-SDFs for different numbers of trajectories at t = 0 fs. Figure S6 provides additional examples for 100 trajectories and for later times along the trajectories.

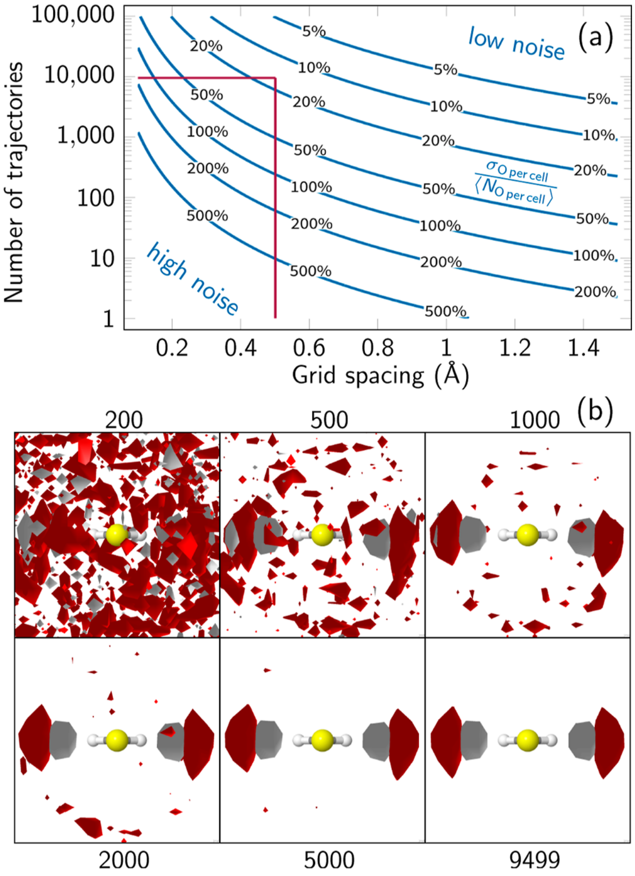

Figure 2. (a) Contour plot of $\frac{\sigma_{\text{O per cell}}}{\langle N_{\text{O per cell}}\rangle}$ as a function of V_{cell} and n_{traj} for TIP3P at standard conditions and χ = 7.32 GPa^{-1} (eq 8) and (b) comparison of 3D-SDFs around CH_2S (molecule's perspective) for different numbers of trajectories. The red lines in (a) indicate the values for V_{cell} and n_{traj} chosen for the analysis in this paper. The 3D-SDFs in (b) were plotted at the same relative isovalue of $3n_{\text{traj}}\langle N_{\text{O per cell}}\rangle$ with red and gray indicating occurrences of oxygen and hydrogen atoms, respectively.

We note that the trajectory number estimation also in principle requires to know how strongly anisotropic the solvent distribution is around the solute and how much the distribution changes during the dynamics. Here, strongly increased local solvent density (e.g., from ground-state hydrogen bonds) will be easier to observe than weak features (e.g., the second solvation shell). Observing weaker features requires to lower the isovalue in the 3D-SDF plots, but this also will produce more noisy plots. To obtain sufficiently noise-free plots, the isovalue should be larger than the average number of atoms per cell, plus three standard deviations. This aspect is exemplified in Figures S7 and S8, which show the 3D-SDFs for CH_2 at t = 0 fs and t = 100 fs for different number of trajectories and different isovalues. In Figure S7, the first column uses a relative isovalue of 5 (i.e., isovalue of $5N_{\text{traj}}\langle N_{\text{O per cell}}\rangle$). Thus, only the strongest features, the very strong ground-state hydrogen bond, are visible, and only 500 trajectories are needed to suppress the noise in the plot. Unfortunately, as Figure S7 (first column) shows, at a relative isovalue of 5 also the evolving solvent distribution at t = 100 fs is completely suppressed. A lower relative isovalue of 3 (Figures S7 and S8, second column) allows observing the photoinduced solvent dynamics, but full noise suppression requires at least 2000 trajectories. At relative isovalues of 1.66 and 2.0, the entire first solvation shell can be observed with ≥5000 trajectories. At an isovalue of 1.33, one can even observe a very shallow second solvation shell, although a huge number of trajectories (≥10,000 trajectories) is needed to resolve the solvation shell over the random fluctuations around the average density (Figures S7 and S8, last column) that takes place throughout the box and that is quantified by eq 8. However, we note that for the remainder of the discussion, we focus on the hydrogen bond regions, which are the most interesting aspect due to their interaction with the solute's excited-state dynamics.

Overall, Figure 2 indicates that to observe the dynamics of rather strong hydrogen bonds, a trajectory number between 1000 and 10,000 seems to be sufficient. We assume that similar numbers are required for other solvents but would recommend that approximate effective isothermal compressibilities should be computed at the beginning of 3D-SDF analyses as described above.

5. RESULTS AND DISCUSSION

In the following subsections, we first briefly recapitulate the excited-state electronic structure of CH_2S and CMe_2S. We then discuss the observed solvent relaxation dynamics by means of the RDFs, then by the 3D-SDFs, and finally the electronic dynamics, which is strongly coupled to the solvent dynamics.

5.1. Electronic Structure in the Gas Phase.

The electronic structure of CH_2S[41] has four low-lying (<3.5 eV) electronic states, which are the closed-shell ground state (S_0), the singlet $^1n\pi^*$ state (S_1), the triplet $^3n\pi^*$ state (T_1), and the triplet $^3\pi\pi^*$ state (T_2). The gas-phase vertical excitation energies are 2.26, 1.99, and 3.48 eV for the S_1, T_1, and T_2 states, respectively (see Figure 1). Higher-lying excited states are experimentally measured and theoretically predicted to occur well above 5 eV.[43] The electronic structure of CMe_2S is analogous, with vertical excitation energies of 2.47, 2.30, and 3.35 eV for S_1, T_1, and T_2, respectively (see Figure S1). It should be noted that the S_0 and T_2 states both have a high electron density in the molecular plane due to the doubly occupied S lone pair; in contrast, the S_1 and T_1 states ($n\pi^*$) have an increased electron density above and below the molecules. This results in differences in the electrostatic

https://doi.org/10.1021/acs.jctc.4c00169
J. Chem. Theory Comput. XXXX, XXX, XXX−XXX

potential generated by the different states, where S_0 and T_2 have minima in the molecular plane and S_1 and T_1 perpendicular to it. These differences between the states can be recognized from Figures S9 and S10, which show the electronic state and transition densities and their exerted electrostatic potential.

The differences in electron densities are expected to drive the solvent relaxation dynamics. In the S_0 and T_2, hydrogen bonds to S are formed in the molecular plane.[35] These hydrogen bonds stabilize S_0 and T_2, reducing the S_1−T_2 gap (compared to gas phase) and enhancing the possibility of ISC (see Figures 1 and S1). However, excitation to S_1 is expected to lead to a redistribution of hydrogen bonds to out-of-plane positions, which will stabilize S_1 and T_1, widening the S_1−T_2 gap over time and shutting down ISC.

5.2. Time-Resolved Solvent Dynamics: RDFs. Figure 3a shows the average RDF between the S and water O atoms for both systems at t = 0 fs (green) and at t = 3000 fs (orange). The initial RDFs differ rather strongly between the molecules: CH_2S exhibits a small maximum at 3.0 Å and a slightly stronger maximum at 3.5 Å. In contrast, CMe_2S has a shoulder at 3.8 Å and a much higher maximum at 4.8 Å. After 3000 fs, the RDFs have changed slightly. In CH_2S, the small 3.0 Å maximum vanishes and the main peak increases and slightly shifts to 3.4 Å, whereas in CMe_2S the shoulder weakens and shifts to 3.1 Å but the maximum remains unchanged. We note that the RDFs show an extended flat region between 8 and 13 Å, which shows that the droplet is large enough to contain the structured solvation shell around the molecule and an additional 5 Å buffer region to the droplet surface. We assume that this is large enough to avoid significant perturbations of the solute−solvent dynamics by boundary effects, even though no periodic boundary conditions are used.

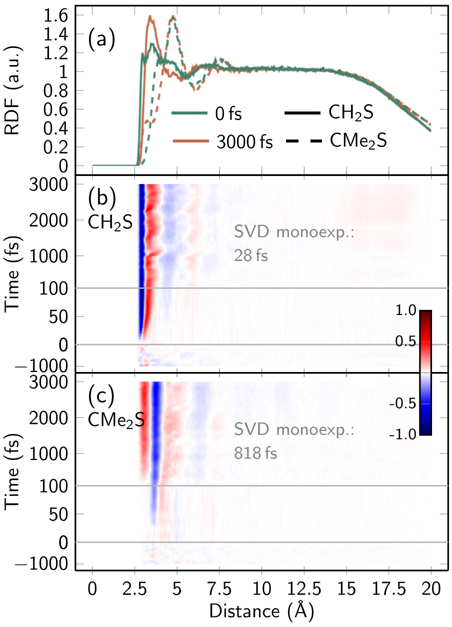

Figure 3. (a) RDFs for both molecules at times 0 and 3000 fs and (b,c) time-resolved difference RDFs between the S atom and water O atoms. For the difference RDFs, the reference is the average RDF between −1000 and 0 fs. Note the three-range split of the time axis in (b,c).

Figure 3b,c shows the temporal evolution of the difference RDFs, where the average RDF between −1000 and 0 fs serves as a reference. Note that we use difference RDFs instead of absolute RDFs for clarity, as is common in the X-ray scattering community.[83] The difference RDFs for negative times show random fluctuations in the equilibrated ground state, exhibiting very low noise levels. Significant changes in the RDFs can be observed at positive times, after excitation of the solute. In the case of CH_2S, the RDF around 2.9 Å decreases already after 20 fs and increases at 3.1 Å; for later times, this pattern simply grows further. This suggests that the water O atoms withdraw from the S atom as a result of the change in solvent distribution. An exponential fit to the first SVD component of the difference RDF yields a time constant of approximately 30 fs. This is consistent with the reported inertial response times for solvent relaxation dynamics in water,[8] although the 3D-SDF analysis below will provide further insights into this solvent dynamics.

Interestingly, the increase−decrease pattern is different for CH_2S than for CMe_2S. For the latter, water actually approaches the solute after excitation, which can be recognized from the shift of the first shoulder toward a lower distance in Figure 3a. Figure 3c shows much slower dynamics for CMe_2S. Here, after about 50 fs a small decrease around 3.7 Å appears, and after several 100 fs an increase of around 3.0 Å arises. The fit of the first SVD component gives a time constant of about 800 fs, more than 1 magnitude slower than for CH_2S.

5.3. Time-Resolved Solvent Dynamics: 3D-SDFs. The RDFs provide only a limited picture of the actual solvent reorganization dynamics around the molecule because they do not include any angular or spatial information. Therefore, in Figure 4 we show the obtained time-dependent 3D-SDFs of water around the solute molecules. Due to the very large number of trajectories (9500), the 3D-SDFs are almost free of distracting noise, even though we employ a resolution of 0.5 Å and do not employ any temporal averaging for maximum time resolution. As discussed in Section 4.1, we produced two sets of 3D-SDFs per molecule, from the "molecule's perspective" and "solvent's perspective", which will be discussed step-by-step in the following.

At t = 0 fs, all four panels show very similar pictures of two strong in-plane hydrogen bonds of water to the solute S atom. The pictures agree with each other because by definition the two perspectives are identical at t = 0 and because the S_0 electron density around the S atom is very similar for both molecules.

Figure 4a employs the molecule's perspective, where the 9500 geometries at each time step are aligned with the reference structure. Hence, in this perspective, the CH_2 molecule stays fixed at the center of the images, and the solvent evolves around it. It can be seen that already 25 fs after excitation, the hydrogen bonds are broken and the water molecules start "flowing" around the molecule toward the out-of-plane positions. It is also visible that the H atom density drops faster (less visible gray-colored region) than the O atom density, due to the higher mobility of the water H atoms. Two (weaker) out-of-plane hydrogen bonds to the C atom form within about 100 fs. For longer times, these hydrogen bonds seem to be rather stable and appear unchanged after 3000 fs. This can also be observed nicely in the Supporting Information Movie. We performed an SVD of the time-dependent 3D-SDF; a monoexponential fit of the first temporal component provides a time constant of approximately 20 fs, as given in

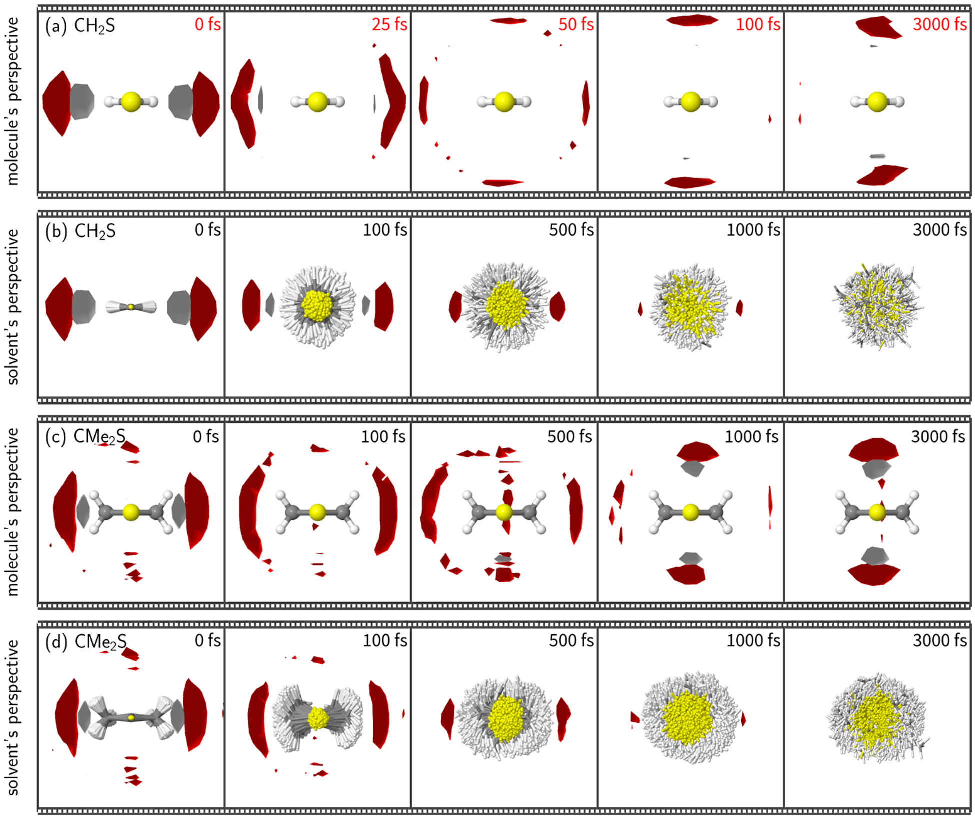

Figure 4. Time-resolved 3D-SDFs of water H and O atom occurrences around (a,b) CH_2S and (c,d) CMe_2S. The solvent dynamics is displayed in two different ways, from the (a,c) molecule's perspective and (b,d) from the solvent's perspective (see Section 4.1). In (a,c), all snapshots are aligned to the ground-state equilibrium of the respective solute molecule which is depicted. The gray and red regions indicate H and O occurrences with an isovalue of $3N_{\text{traj}}\langle N_{\text{O per cell}}\rangle$. Note that in (a) different points in time are shown than in the other panels because the solvent dynamics around CH_2S in the molecule's perspective has a much shorter timescale than the ones in the other panels, as discussed in the text.

Figure 5. We note that for the 3D-SDFs, the first SVD component can only capture part of the solvent relaxation because in the 3D-SDFs time and position are correlated. Thus, the obtained time constant should only be regarded as a rough characterization of the solvent relaxation time. This is an astonishingly small time constant for the breaking and reforming of hydrogen bonds after photoexcitation of a solute. Experimental studies typically report values of 1 to 2 magnitudes slower for such processes.[8,11,84,85]

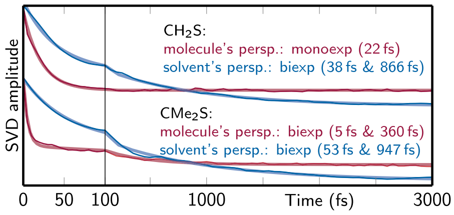

Figure 5. First temporal components $U_1(t)$ of SVDs of the 3D-SDFs shown in Figure 4a−d. The given time constants are obtained by mono- or biexponential fits of $U_1(t)$. Note that the first SVD component only captures part of the solvent dynamics and thus provides only a qualitative time constant to compare the two molecules.

In order to understand how the solvent relaxation dynamics around CH_2S can be orders of magnitude faster than in other systems, we turn to Figure 4b, showing the 3D-SDF from the solvent's perspective. Unlike the molecule's perspective, the solvent's perspective exhibits a fixed frame of reference, allowing us to discern the intrinsic flux of the solvent distribution through three-dimensional space. In Figure 4b (note the different time points plotted compared to panel a), we can observe that the water molecules that formed the two in-plane hydrogen bonds to the S atom are still approximately in the same position after 100 fs. This shows that the solvent distribution requires time to break the existing hydrogen bonding networks and form new hydrogen bonds in response to the excitation of the solute. The broad distribution of the CH_2S molecule, which is rotated around its C−S bond, suggests that the molecular orientation changed drastically. At later times, one can see that the regions of high water occupancy gradually decay, being slightly visible at 1000 fs but vanished before 3000 fs. At the same time, the CH_2S molecules continue to randomize their orientation due to diffusion processes.

In total, we find that CH_2S simply rotates around the C−S bond to reform the hydrogen bonds and accommodate the new electronic state within the solvation shell in the fastest possible way, much faster than the intrinsic solvent rearrangement alone would allow. The timescale, extent, and final distribution of this rotation is shown in Figure S11a. In particular, the distribution shows a fast divergence within the first 100 fs and a slight peak after 100 fs at about 90°, which is the ideal angle to facilitate the excited-state out-of-plane hydrogen bonds. Figure S11a also shows large differences between negative times (in S_0) and positive times (after excitation), showing that solute rotation in the excited state is not diffusion-driven. We characterized the solvent dynamics in the solvent's perspective through an SVD of the 3D-SDF and fitted time constants of about 40 and 900 fs with a biexponential function (Figure 5a) Here, the first time constant corresponds to inertial/librational motion (i.e., hydrogen bond breaking), while the second one is in line with previous experimental measurements of water relaxation timescales.[8,11,84,85] We note that in the solvent's perspective, the fitted time constants only correspond to the decay of the initial solvent structure but do not describe the reformation of hydrogen bonds that was visible in the molecule's perspective.

Compared to CH_2S, the solvent relaxation dynamics of CMe_2S shows some interesting differences. First, in Figure 4c it can be seen that, from the molecule's perspective, the solvent shows the dissolution of the two in-plane hydrogen bonds to the S atom and the creation of two out-of-plane hydrogen bonds to the C atom, similar to CH_2S. However, this process takes significantly longer in CMe_2S than in CH_2S, as visible by comparing panels a and c, e.g., panel a at 25 fs presents a similar solvent distribution as panel c at 100 fs, and panel a at 100 fs is comparable to panel c at 1000 fs. The much slower solvent dynamics in CMe_2S can be explained in the solvent's perspective in panel d. Here, it can be discerned that this molecule is strongly hindered in its rotation around the C−S bond due to the steric bulk (i.e., the drag) of the methyl groups. Hence, in CMe_2S the reformation of the hydrogen bond network is limited by the timescale of the solvent rearrangement, unlike in CH_2S where molecular rotation contributes to the reformation. The rotational dynamics of CMe_2S is presented in Figure S11b, which shows that the rotation is effectively suppressed by the solvent cage. Interestingly, the time constants for the solvent relaxation in the solvent's perspective (Figure 5) of CMe_2S are about 50 and 900 fs, which agree very well with the ones of CH_2S. This is in strong contrast to the time constants obtained from the molecule's perspective (CH_2S: 22 fs, CMe_2S: 5 and 360 fs).

The time-dependent 3D-SDFs (Figure 4) clearly show more details of the solvent dynamics than the RDFs (Figure 3). Using the 3D-SDFs, it is even possible to explain why the difference RDFs show the withdrawal of water from excited CH_2S but an approaching of water to excited CMe_2S. The reasons are steric hindrance and how the excited-state hydrogen bonds are formed. In CH_2S, the hydrogen bonds in the ground state are not sterically hindered and thus are very close to the S atom. In the excited state, the hydrogen bonds are more strongly attracted to the C atom, so they move further away from the S atom. An analysis of the hydrogen bond count over time (see Figure S12a) and a corresponding fit shows that the hydrogen bonds break within about 20 fs and reform within 200 fs in CH_2S. Contrarily, in CMe_2S, the hydrogen bonds in the ground state are slightly hindered by the methyl groups and thus are longer than in CH_2S. In excited CMe_2S, the out-of-plane hydrogen bonds are less obstructed, so they can approach the molecule more closely than in the ground state, leading to a shift of the RDF maximum to shorter values. Here, the hydrogen bonds break within 40 fs and reform after about 900 fs (see Figure S12b), significantly slower than in CH_2S. We note that these time constants of hydrogen bond breaking/formation depend on the criteria for counting the hydrogen bonds and thus are only qualitative.

Although the RDFs and 3D-SDFs in principle describe the same dynamics, we note that the obtained time constants are not fully consistent. The time constants derived from the SVD of the difference RDFs (CH_2S: 28 fs, CMe_2S: 818 fs) are neither consistent with the time constants from the molecule's perspective nor with the ones from the solvent's perspective. This is remarkable, as both the RDFs and the solvent's perspective 3D-SDFs describe the local solvent dynamics relative to the solute. However, the highly anisotropic dynamics visible in the 3D-SDFs around the thiocarbonyl groups simply cannot be represented in full detail in the difference RDFs.

5.4. Electronic Dynamics. In addition to information about the solute's and solvent's nuclear degrees of freedom, the LVC/MM-TSH trajectories provide information about the electronic wave functions, analogous to ab initio TSH trajectories. Figure 6 shows the average eigenenergies of the coupled LVC Hamiltonian (eq 1) of the whole trajectory swarms; the shaded areas indicate one standard deviation. The figure shows that, for both molecules, the eigenenergies are approximately constant at negative times, indicating proper equilibration in the ground state. After excitation to the S_1 state at $t = 0$ fs, one can observe strong oscillations in the S_0 and T_2 energies within the first 100 fs. These oscillations have periods of about 30 fs for CH_2S and 25 fs for CMe_2S, which correspond to about 1111 and 1333 cm^{-1}, respectively. Both frequencies match the C−S stretching modes (frequencies of 1106 and 1336 cm^{-1}, respectively), which are strongly excited in the S_1 state (Figure S13).[41]

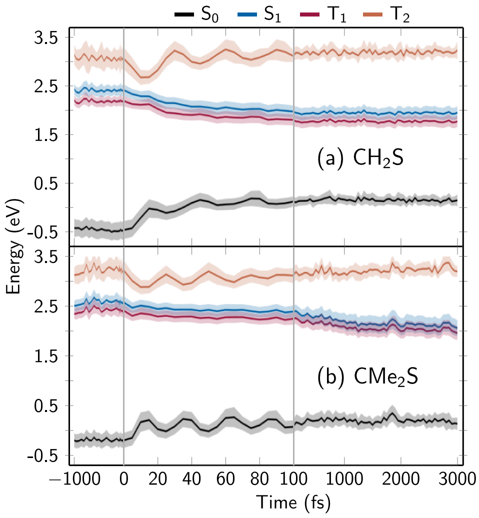

Figure 6. Eigenenergies of the electrostatically embedded LVC Hamiltonian matrix (excluding MM contributions) of the (a) CH_2S and (b) CMe_2S systems. The energies of S_0, S_1, T_1, and T_2 are shown in black, blue, red, and orange, respectively. Lines show the average over all trajectories and the shaded area indicates one standard deviation.

The C−S stretch mode strongly modulates the S_1−T_2 energy gap and thus mediates ISC. ISC is not possible in the gas phase because the S_1−T_2 energy gap never gets sufficiently small (Figures 1c and S1), as discussed in ref 41. In aqueous solution, the T_2 state is stabilized by the hydrogen bonds formed in the S_0. Thus, after 12 fs the average S_1−T_2 energy gap reaches a minimum. However, as shown in Figures 6 and S14, after excitation to S_1 the S_1 and T_1 states eventually become stabilized by the solvent relaxation dynamics. In CH_2S, the S_1 is shifted by −0.4 eV within 100 fs, while in CMe_2S, the

S_1 is shifted by a similar amount within approximately 1500 fs (see Table S1 for numerical values). These solvent-induced shifts widen the S_1−T_2 energy gap so much that ISC shuts down very quickly.

The population dynamics presented in Figure 7 is fully consistent with the dynamic singlet−triplet energy gap (see Figure S14) and with a time-dependent, very subtle mixing of the two triplet states (Figure S15). First, there is a rapid but small increase in the triplet population within the first 30 fs for both systems due to the closing of the S_1−T_2 energy gap (Figure 6). Here, ISC is more pronounced for CH_2S because its singlet−triplet energy gap is slightly smaller. However, further transfer of population to the T_2 is inhibited at later times because the solvent dynamics stabilizes the S_1 and thus widens the S_1−T_2 energy gap. Trajectories in the T_2 eventually return to the S_1, as the T_2 electron density favors small S_1−T_2 energy gaps, just like the S_0 density. Figure S14b,c nicely shows the small amount of trajectories for which the S_1−T_2 energy gaps remain close to zero for about 100 fs.

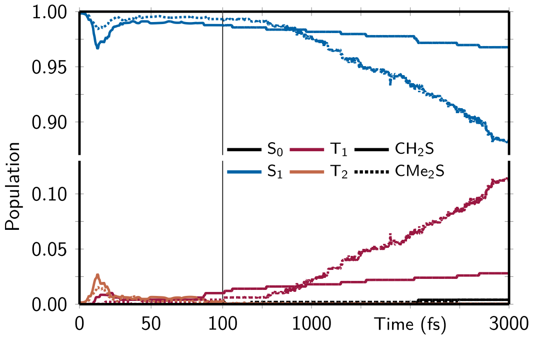

Figure 7. Evolution of electronic populations (spin-free states summed over triplet M_S components) for S_0, S_1, T_1, and T_2 in black, blue, red, and orange, respectively, of CH_2S (solid) and CMe_2S (dotted).

At later times, instead one can observe direct and slow population transfer from S_1 to T_1. Based on the electronic characters of these states at the Franck−Condon point (both are $n\pi^*$ states) and the El-Sayed rule,[86] this is surprising; the spin−orbit couplings between the S_1 and T_1 are exactly zero in the diabatic basis of the LVC model. Figure S14 shows that the S_1 → T_1 ISC is enabled by nuclear motion that breaks the molecular symmetry so that the T_1 and T_2 states mix (Figure S15), giving rise to nonzero spin−orbit couplings between S_1 and T_1. For CH_2S, this mixing can only occur by interaction of the solvent with the T_1−T_2 (or S_0−S_1) transition density, as all interstate coupling constants (λ parameters[37,58]) are zero by symmetry. On the contrary, for CMe_2S there are four normal modes that have the correct symmetry to couple T_1 with T_2 (or S_0 with S_1), in addition to solvent interaction with the transition densities. The presence of intramolecular degrees of freedom that couple S_1 and T_1 by mixing is the reason why S_1 → T_1 ISC occurs significantly faster in CMe_2S than in CH_2, as visible in Figure 7. A second driving factor for faster ISC in CMe_2S is the smaller S_1−T_1 energy gaps (Figure S14). A simple linear fit of the T_1 population between 100 and 3000 fs yields a time constant of 26 ± 3 ps for CMe_2S and 130 ± 40 ps for CH_2S.

Overall, these results evidence the complex relationship between the solute's electronic and the solvent's nuclear degrees of freedom. The electron density of the ground state determines the initial solvent distribution, which in turn governs the solute's excited-state energy gaps. The solute's intramolecular motion drives ISC after excitation to S_1, but ISC is influenced by the solvent in two ways. On the one hand, the solvent distribution adapts quickly to the S_1 electron density—which shuts down sub-ps ISC to T_2—while on the other hand, random solvent fluctuations perturb the solute's symmetry and thus enable slow ISC to T_1. Due to the similar electronic character, electrostatic potential, and potential energy surface, the ISC from S_1 to T_1 does not further affect the solute's or solvent's nuclear motion.

6. COMPUTATIONAL COST

We have already discussed the computational cost and scaling of the LVC/MM method in our previous work,[35] although focusing on CH_2S and the ground state. We found that LVC/MM is about 1 order of magnitude faster, compared to a QM/MM reference trajectory at the BP86/def2-SVP level of theory. The present work gives us the opportunity to further highlight the computational efficiency of LVC/MM in the context of excited-state simulations. All timings are given as averages and using a single core of an Intel Xeon E5-2650 v3 processor (2.30 GHz clock speed), unless otherwise stated.

As written above, both trajectory swarms (each with about 9500 trajectories and 6000 time steps) required a combined 114 million single-point calculations. For CH_2S (1091 waters), each LVC/MM time step took 120 ms, each trajectory took 12.5 min, and the entire trajectory swarm thus cost about 2000 CPU h. For the slightly larger CMe_2S (1155 waters), a time step took 400 ms, each trajectory took 40 min, and the entire swarm cost 7000 CPU h. This very modest computational cost can be compared to the cost of equivalent ab initio QM/MM trajectories. We computed one QM/MM trajectory for each system using the TDA-BP86/def2-SVP level of theory, as in our previous work.[35] The single-core computational cost was found to be 25 h per trajectory (15 s/step) for CH_2S and 102 h per trajectory (60 s/step) for CMe_2S. For the entire trajectory swarms, the cost would therefore amount to about 240,000 CPU h and nearly 1,000,000 CPU h, respectively, for CH_2S and CMe_2S, which is feasible but requires significant resources. Thus, even compared to a very affordable excited-state electronic structure method like TDA-BP86, LVC/MM provides a speed-up of about 2 orders of magnitude.

However, the LVC models used in the simulations above were not parametrized from TDA-BP86 but rather from MS-CASPT2. Here, we simply estimated the expected cost from a gas-phase single-point calculation including gradients,[87] without including the MM point charges or their gradients. Thus, the following estimates are lower bounds. For CH_2S, an MS-CASPT2 single-point calculation took 6 min, which can be extrapolated to 600 h per trajectory and about 6 million CPU h for the swarm. For CMe_2S, the cost is approximately ten times as large (i.e., 6000 h per trajectory, nearly as much as the entire LVC/MM swarm), yielding a staggering overall cost of about 57 million CPU h. This is clearly beyond the capabilities of many, if not most, current research groups. In contrast, LVC/MM is clearly affordable and exhibits a speed-up of 3 to 4 orders of magnitude over MS-CASPT2.

We also want to comment briefly on the amount of data produced. At every time step, SHARC[39] stores information on the electronic states and wave function as well as coordinates and velocities of all nuclei. For systems with MM solvent, the latter data grow very quickly for long simulation time and large trajectory swarms. For either of the two systems (3277 atoms for CH_2S, 3495 atoms for CMe_2S), each time step produces about 160 kB of nuclear data. Thus, a trajectory with 6000 time steps corresponds to about 1 GB of data, and one trajectory swarm to about 9 TB. In order to reduce the amount of data, we have saved coordinate data only every 5 fs during the first 100 fs and every 50 fs thereafter, which requires about 120 GB per trajectory swarm. A higher time resolution in the 3D-SDFs without excessive memory usage can be achieved by dividing the trajectory swarm into batches, aggregating partial 3D-SDFs and then deleting the raw coordinate data of the current batch before continuing to the next batch.

7. CONCLUSIONS

In the present work, we have demonstrated the capabilities of the recently published LVC/MM method,[35] which implements electrostatic embedding of linear vibronic coupling models in MM environments, for use in TSH. This extremely efficient method allows simulating tens of thousands of TSH trajectories for many picoseconds and including thousands of MM solvent molecules. In particular, we were able to simulate 9500 trajectories of 3 ps length in about 2000 CPUh for the smallest employed system. Therefore, the method makes it possible to sample the time-dependent 3D-SDFs around an excited solute. Such 3D-SDFs provide much more insights into solvent relaxation than the typically employed RDFs. However, reaching acceptable noise levels in the 3D-SDFs requires extensive sampling—several thousand trajectories for few-femtosecond and sub-Ångstrom resolution in water. We show that 3D-SDFs are affected by the solute's orientation and rotation and therefore can be analyzed in different ways. To that end, we discuss the "molecule's perspective" and the "solvent's perspective". The former employs a corotating coordinate system to map the time-dependent distribution of the solvent relative to the solute—this perspective is beneficial to interpret solute-focused spectroscopic observations governed by solute–solvent interactions. Conversely, the solvent's perspective uses a fixed coordinate system to analyze the timescales of the intrinsic solvent reorganization in three-dimensional space.

The LVC/MM TSH method has been applied to two model thiocarbonyl compounds, thioformaldehyde (CH_2S) and thioacetone (CMe_2S). These molecules exhibit two in-plane hydrogen bonds to the S atom in the ground state. After excitation to the S_1 state, the solvent-induced small singlet–triplet gap enables nonzero ISC yield, in contrast to the gas phase, where no ISC is observed. However, quickly after excitation, the solvent responds to the change in solute electron density, breaking the in-plane hydrogen bonds and forming two new out-of-plane hydrogen bonds to the C atom. This process widens the singlet–triplet gap, shutting down ISC. The relaxation timescales of the solvent depend strongly on the investigated solute. In CH_2S, hydrogen bonds are broken and reformed via a fast and directed rotation around the C–S bond within only 100 fs. In CMe_2S, rotation is sterically hindered by the methyl groups, so that hydrogen bond reformation takes approximately 1 ps. We expect that similar hydrogen bond dynamics is at play in larger (thio-)carbonyl compounds in aqueous solution, for example in the ultrafast ISC of thionated nucleobases.

■ ASSOCIATED CONTENT

Supporting Information

The Supporting Information is available free of charge at https://pubs.acs.org/doi/10.1021/acs.jctc.4c00169.

Gas-phase and solvated energies for CMe_2S, active space orbitals for both thiocarbonyls, explanations for supplementary input files, computed mean and standard deviation of 3D-SDF of TIP3P water box, noise level of 3D-SDFs using different numbers of trajectories and isovalues, electronic densities and electrostatic potentials around sulfur atoms of both molecules, time evolution of molecular rotation angle, hydrogen bond count analysis, shifted eigenenergies over time, convolutions of coherently excited normal modes over time, time-dependent spin–orbit couplings and energy gaps, and time-dependent overlap between the triplet states (PDF)

LVC/MM parameter files for both molecules, SHARC inputs for all solvated trajectories, scripts for system preparation, and scripts used for solvation analysis (ZIP)

Movie of the time evolution of the 3D-SDF in the molecule's and solvent's perspective for CH_2S and CMe_2S (MP4)

■ AUTHOR INFORMATION

Corresponding Author

Sebastian Mai – *Institute of Theoretical Chemistry, Faculty of Chemistry, University of Vienna, 1090 Vienna, Austria;* orcid.org/0000-0001-5327-8880;
Email: sebastian.mai@univie.ac.at

Authors

Severin Polonius – *Institute of Theoretical Chemistry, Faculty of Chemistry, University of Vienna, 1090 Vienna, Austria; Vienna Doctoral School in Chemistry (DoSChem), University of Vienna, 1090 Vienna, Austria;* orcid.org/0000-0003-0445-4694
David Lehrner – *Institute of Theoretical Chemistry, Faculty of Chemistry, University of Vienna, 1090 Vienna, Austria*
Leticia González – *Institute of Theoretical Chemistry, Faculty of Chemistry, University of Vienna, 1090 Vienna, Austria; Vienna Research Platform on Accelerating Photoreaction Discovery, University of Vienna, 1090 Vienna, Austria;* orcid.org/0000-0001-5112-794X

Complete contact information is available at:
https://pubs.acs.org/10.1021/acs.jctc.4c00169

Notes

The authors declare no competing financial interest.

■ ACKNOWLEDGMENTS

This research was funded in whole or in part by the Austrian Science Fund FWF (grant DOI 10.55776/I6116) and the Deutsche Forschungsgemeinschaft DFG (TRR234 "CataLight", Project ID no. 364549901, subproject C3). For open access purposes, the authors have applied a CC-BY public copyright license to any author accepted manuscript version arising from this submission. The computational results have been achieved in part using the Vienna Scientific Cluster (VSC5). The authors thank Oleksandra Zhuravel for preliminary calculations on CH_2S and the University of Vienna for continuous support, in particular within the framework of the Doctoral School of Chemistry (DoSChem).

REFERENCES

(1) Burgess, J. Solvent Effects on Visible Absorption Spectra of Bis-(2,2'-Bipyridyl) Biscyanoiron(II), Bis-(1,10-Phenanthroline)-Biscyanoiron(II), and Related Compounds. *Spectrochim. Acta, Part A* **1970**, *26*, 1369−1374.

(2) Linert, W.; Gutmann, V. Structural and Electronic Responses of Coordination Compounds to Changes in the Molecule and Molecular Environment. *Coord. Chem. Rev.* **1992**, *117*, 159−183.

(3) Taft, R. W.; Pienta, N. J.; Kamlet, M. J.; Arnett, E. M. Linear solvation energy relationships. 7. Correlations between the solvent-donicity and acceptor-number scales and the solvatochromic parameters .pi.*, alpha., and .beta. *J. Org. Chem.* **1981**, *46*, 661−667.

(4) Sadkowski, P. J.; Fleming, G. R. The Influence of Solvent—Solute Interaction on Radiationless Processes: Excited State Dynamics of 1,8-Anilinonaphthalene Sulphonate and Related Molecules. *Chem. Phys.* **1980**, *54*, 79−89.

(5) Pápai, M.; Abedi, M.; Levi, G.; Biasin, E.; Nielsen, M. M.; Møller, K. B. Theoretical Evidence of Solvent-Mediated Excited-State Dynamics in a Functionalized Iron Sensitizer. *J. Phys. Chem. C* **2019**, *123*, 2056−2065.

(6) Abedi, M.; Levi, G.; Zederkof, D. B.; Henriksen, N. E.; Pápai, M.; Møller, K. B. Excited-State Solvation Structure of Transition Metal Complexes from Molecular Dynamics Simulations and Assessment of Partial Atomic Charge Methods. *Phys. Chem. Chem. Phys.* **2019**, *21*, 4082−4095.

(7) Bagchi, B.; Oxtoby, D. W.; Fleming, G. R. Theory of the Time Development of the Stokes Shift in Polar Media. *Chem. Phys.* **1984**, *86*, 257−267.

(8) Jimenez, R.; Fleming, G. R.; Kumar, P. V.; Maroncelli, M. Femtosecond Solvation Dynamics of Water. *Nature* **1994**, *369*, 471−473.

(9) Nottoli, M.; Mennucci, B.; Lipparini, F. Excited State Born−Oppenheimer Molecular Dynamics through Coupling between Time Dependent DFT and AMOEBA. *Phys. Chem. Chem. Phys.* **2020**, *22*, 19532−19541.

(10) Larsen, M. A. B.; Stephansen, A. B.; Alarousu, E.; Pittelkow, M.; Mohammed, O. F.; Sølling, T. I. Solvent-Dependent Dual Fluorescence of the Push−Pull System 2-Diethylamino-7-Nitrofluorene. *Phys. Chem. Chem. Phys.* **2018**, *20*, 5942−5951.

(11) Biasin, E.; Fox, Z. W.; Andersen, A.; Ledbetter, K.; Kjær, K. S.; Alonso-Mori, R.; Carlstad, J. M.; Chollet, M.; Gaynor, J. D.; Glownia, J. M.; Hong, K.; Kroll, T.; Lee, J. H.; Liekhus-Schmaltz, C.; Reinhard, M.; Sokaras, D.; Zhang, Y.; Doumy, G.; March, A. M.; Southworth, S. H.; Mukamel, S.; Gaffney, K. J.; Schoenlein, R. W.; Govind, N.; Cordones, A. A.; Khalil, M. Direct Observation of Coherent Femtosecond Solvent Reorganization Coupled to Intramolecular Electron Transfer. *Nat. Chem.* **2021**, *13*, 343−349.

(12) Zederkof, D. B.; Møller, K. B.; Nielsen, M. M.; Haldrup, K.; González, L.; Mai, S. Resolving Femtosecond Solvent Reorganization Dynamics in an Iron Complex by Nonadiabatic Dynamics Simulations. *J. Am. Chem. Soc.* **2022**, *144*, 12861−12873.

(13) Kim, K. H.; Kim, J. G.; Oang, K. Y.; Kim, T. W.; Ki, H.; Jo, J.; Kim, J.; Sato, T.; Nozawa, S.; Adachi, S.-i.; Ihee, H. Femtosecond X-ray Solution Scattering Reveals That Bond Formation Mechanism of a Gold Trimer Complex Is Independent of Excitation Wavelength. *Struct. Dyn.* **2016**, *3*, 043209.

(14) Kim, T. K.; Lee, J. H.; Wulff, M.; Kong, Q.; Ihee, H. Spatiotemporal Kinetics in Solution Studied by Time-Resolved X-Ray Liquidography (Solution Scattering). *ChemPhysChem* **2009**, *10*, 1958−1980.

(15) Katayama, T.; Choi, T.-K.; Khakhulin, D.; Dohn, A. O.; Milne, C. J.; Vankó, G.; Németh, Z.; Lima, F. A.; Szlachetko, J.; Sato, T.; Nozawa, S.; Adachi, S.-i.; Yabashi, M.; Penfold, T. J.; Gawelda, W.; Levi, G. Atomic-Scale Observation of Solvent Reorganization Influencing Photoinduced Structural Dynamics in a Copper Complex Photosensitizer. *Chem. Sci.* **2023**, *14*, 2572−2584.

(16) Chen, L. X. Taking Snapshots of Photoexcited Molecules in Disordered Media by Using Pulsed Synchrotron X-rays. *Angew. Chem., Int. Ed.* **2004**, *43*, 2886−2905.

(17) Chen, L. X.; Shelby, M. L.; Lestrange, P. J.; Jackson, N. E.; Haldrup, K.; Mara, M. W.; Stickrath, A. B.; Zhu, D.; Lemke, H.; Chollet, M.; Hoffman, B. M.; Li, X. Imaging Ultrafast Excited State Pathways in Transition Metal Complexes by X-ray Transient Absorption and Scattering Using X-ray Free Electron Laser Source. *Faraday Discuss.* **2016**, *194*, 639−658.

(18) Gaffney, K. J. Capturing Photochemical and Photophysical Transformations in Iron Complexes with Ultrafast X-ray Spectroscopy and Scattering. *Chem. Sci.* **2021**, *12*, 8010−8025.

(19) Kunnus, K.; Vacher, M.; Harlang, T. C. B.; Kjær, K. S.; Haldrup, K.; Biasin, E.; van Driel, T. B.; Pápai, M.; Chabera, P.; Liu, Y.; Tatsuno, H.; Timm, C.; Källman, E.; Delcey, M.; Hartsock, R. W.; Reinhard, M. E.; Koroidov, S.; Laursen, M. G.; Hansen, F. B.; Vester, P.; Christensen, M.; Sandberg, L.; Németh, Z.; Szemes, D. S.; Bajnóczi, É.; Alonso-Mori, R.; Glownia, J. M.; Nelson, S.; Sikorski, M.; Sokaras, D.; Lemke, H. T.; Canton, S. E.; Møller, K. B.; Nielsen, M. M.; Vankó, G.; Wärnmark, K.; Sundström, V.; Persson, P.; Lundberg, M.; Uhlig, J.; Gaffney, K. J. Vibrational Wavepacket Dynamics in Fe Carbene Photosensitizer Determined with Femtosecond X-ray Emission and Scattering. *Nat. Commun.* **2020**, *11*, 634.

(20) Vester, P.; Kubicek, K.; Alonso-Mori, R.; Assefa, T.; Biasin, E.; Christensen, M.; Dohn, A. O.; van Driel, T. B.; Galler, A.; Gawelda, W.; Harlang, T. C. B.; Henriksen, N. E.; Kjær, K. S.; Kuhlman, T. S.; Németh, Z.; Nurekeyev, Z.; Pápai, M.; Rittman, J.; Vankó, G.; Yavas, H.; Zederkof, D. B.; Bergmann, U.; Nielsen, M. M.; Møller, K. B.; Haldrup, K.; Bressler, C. Tracking Structural Solvent Reorganization and Recombination Dynamics Following E- Photoabstraction from Aqueous I- with Femtosecond X-Ray Spectroscopy and Scattering. *J. Chem. Phys.* **2022**, *157*, 224201.

(21) Yonehara, T.; Hanasaki, K.; Takatsuka, K. Fundamental Approaches to Nonadiabaticity: Toward a Chemical Theory beyond the Born−Oppenheimer Paradigm. *Chem. Rev.* **2012**, *112*, 499−542.

(22) Tavernelli, I. Nonadiabatic Molecular Dynamics Simulations: Synergies between Theory and Experiments. *Acc. Chem. Res.* **2015**, *48*, 792−800.

(23) Crespo-Otero, R.; Barbatti, M. Recent Advances and Perspectives on Nonadiabatic Mixed Quantum−Classical Dynamics. *Chem. Rev.* **2018**, *118*, 7026−7068.

(24) Curchod, B. F. E.; Martínez, T. J. Ab Initio Nonadiabatic Quantum Molecular Dynamics. *Chem. Rev.* **2018**, *118*, 3305−3336.

(25) Agostini, F.; Curchod, B. F. E. Different Flavors of Nonadiabatic Molecular Dynamics. *Wiley Interdiscip. Rev.: Comput. Mol. Sci.* **2019**, *9*, No. e1417.

(26) Barbatti, M. Nonadiabatic Dynamics with Trajectory Surface Hopping Method. *Wiley Interdiscip. Rev.: Comput. Mol. Sci.* **2011**, *1*, 620−633.

(27) Wang, L.; Akimov, A.; Prezhdo, O. V. Recent Progress in Surface Hopping: 2011−2015. *J. Phys. Chem. Lett.* **2016**, *7*, 2100−2112.

(28) Mai, S.; Marquetand, P.; González, L. *Quantum Chemistry and Dynamics of Excited States*; John Wiley & Sons, Ltd, 2020; Chapter 16, pp 499−530, .

(29) Senn, H. M.; Thiel, W. QM/MM Methods for Biomolecular Systems. *Angew. Chem., Int. Ed.* **2009**, *48*, 1198−1229.

(30) Brunk, E.; Rothlisberger, U. Mixed Quantum Mechanical/Molecular Mechanical Molecular Dynamics Simulations of Biological Systems in Ground and Electronically Excited States. *Chem. Rev.* **2015**, *115*, 6217−6263.

(31) Nelson, T. R.; White, A. J.; Bjorgaard, J. A.; Sifain, A. E.; Zhang, Y.; Nebgen, B.; Fernandez-Alberti, S.; Mozyrsky, D.; Roitberg, A. E.; Tretiak, S. Non-Adiabatic Excited-State Molecular Dynamics: Theory and Applications for Modeling Photophysics in Extended Molecular Materials. *Chem. Rev.* **2020**, *120*, 2215−2287.

(32) Venkatraman, R. K.; Orr-Ewing, A. J. Solvent Effects on Ultrafast Photochemical Pathways. *Acc. Chem. Res.* **2021**, *54*, 4383−4394.

(33) Rosspeintner, A.; Lang, B.; Vauthey, E. Ultrafast Photochemistry in Liquids. *Annu. Rev. Phys. Chem.* **2013**, *64*, 247−271.

(34) Köppel, H.; Domcke, W.; Cederbaum, L. S. Theory of Vibronic Coupling in Linear Molecules. *J. Chem. Phys.* **1981**, *74*, 2945−2968.

(35) Polonius, S.; Zhuravel, O.; Bachmair, B.; Mai, S. LVC/MM: A Hybrid Linear Vibronic Coupling/Molecular Mechanics Model with Distributed Multipole-Based Electrostatic Embedding for Highly Efficient Surface Hopping Dynamics in Solution. *J. Chem. Theory Comput.* **2023**, *19*, 7171−7186.

(36) Zobel, J. P.; Heindl, M.; Plasser, F.; Mai, S.; González, L. Surface Hopping Dynamics on Vibronic Coupling Models. *Acc. Chem. Res.* **2021**, *54*, 3760−3771.

(37) Plasser, F.; Gómez, S.; Menger, M. F. S. J.; Mai, S.; González, L. Highly Efficient Surface Hopping Dynamics Using a Linear Vibronic Coupling Model. *Phys. Chem. Chem. Phys.* **2019**, *21*, 57−69.

(38) Mai, S.; Marquetand, P.; González, L. Nonadiabatic Dynamics: The SHARC Approach. *Wiley Interdiscip. Rev.: Comput. Mol. Sci.* **2018**, *8*, No. e1370.

(39) Mai, S.; Avagliano, D.; Heindl, M.; Marquetand, P.; Menger, M. F. S. J.; Oppel, M.; Plasser, F.; Polonius, S.; Ruckenbauer, M.; Shu, Y.; Truhlar, D. G.; Zhang, L.; Zobel, P.; González, L. *SHARC3.0: Surface Hopping Including Arbitrary Couplings — Program Package for Non-adiabatic Dynamics*, 2023. https://sharc-md.org/.

(40) Lipscomb, R. D.; Sharkey, W. H. Characterization and Polymerization of Thioacetone. *J. Polym. Sci., Part A-1: Polym. Chem.* **1970**, *8*, 2187−2196.

(41) Mai, S.; Atkins, A. J.; Plasser, F.; González, L. The Influence of the Electronic Structure Method on Intersystem Crossing Dynamics. The Case of Thioformaldehyde. *J. Chem. Theory Comput.* **2019**, *15*, 3470−3480.

(42) Zhang, L.; Shu, Y.; Sun, S.; Truhlar, D. G. Direct Coherent Switching with Decay of Mixing for Intersystem Crossing Dynamics of Thioformaldehyde: The Effect of Decoherence. *J. Chem. Phys.* **2021**, *154*, 094310.

(43) Clouthier, D. J.; Ramsay, D. A. The Spectroscopy of Formaldehyde and Thioformaldehyde. *Annu. Rev. Phys. Chem.* **1983**, *34*, 31−58.

(44) Judge, R. H.; Moule, D. C.; Bruno, A. E.; Steer, R. P. Thioketone Spectroscopy: An Analysis of the Lower Electronic Transitions in Thioacetone and Thioacetaldehyde. *Chem. Phys. Lett.* **1983**, *102*, 385−389.

(45) Kawasaki, M.; Kasatani, K.; Ogawa, Y.; Sato, H. Spectra and Emission Lifetimes of H2CS($\tilde{A}$ $^1A_2$). *Chem. Phys.* **1983**, *74*, 83−88.

(46) Borrego-Varillas, R.; Teles-Ferreira, D. C.; Nenov, A.; Conti, I.; Ganzer, L.; Manzoni, C.; Garavelli, M.; Maria de Paula, A.; Cerullo, G. Observation of the Sub-100 Femtosecond Population of a Dark State in a Thiobase Mediating Intersystem Crossing. *J. Am. Chem. Soc.* **2018**, *140*, 16087−16093.

(47) Sánchez-Rodríguez, J. A.; Mohamadzade, A.; Mai, S.; Ashwood, B.; Pollum, M.; Marquetand, P.; González, L.; Crespo-Hernández, C. E.; Ullrich, S. 2-Thiouracil Intersystem Crossing Photodynamics Studied by Wavelength-Dependent Photoelectron and Transient Absorption Spectroscopies. *Phys. Chem. Chem. Phys.* **2017**, *19*, 19756−19766.

(48) Mai, S.; Pollum, M.; Martínez-Fernández, L.; Dunn, N.; Marquetand, P.; Corral, I.; Crespo-Hernández, C. E.; González, L. The Origin of Efficient Triplet State Population in Sulfur-Substituted Nucleobases. *Nat. Commun.* **2016**, *7*, 13077.

(49) Pollum, M.; Martínez-Fernández, L.; Crespo-Hernández, C. E. *Photoinduced Phenomena in Nucleic Acids I: Nucleobases in the Gas Phase and in Solvents*; Barbatti, M., Borin, A. C., Ullrich, S., Eds.; *Topics in Current Chemistry*; Springer International Publishing: Cham, 2015; pp 245−327..

(50) Pollum, M.; Jockusch, S.; Crespo-Hernández, C. E. 2,4-Dithiothymine as a Potent UVA Chemotherapeutic Agent. *J. Am. Chem. Soc.* **2014**, *136*, 17930−17933.

(51) Stone, A. *The Theory of Intermolecular Forces*; OUP Oxford, 2013; .

(52) Kabsch, W. A. A solution for the best rotation to relate two sets of vectors. *Acta Crystallogr., Sect. A: Found. Crystallogr.* **1976**, *32*, 922−923.

(53) Case, D.; Aktulga, H.; Belfon, K.; Ben-Shalom, I.; Berryman, J.; Brozell, S.; Cerutti, D.; Cheatham III, T.; Cisneros, G.; Cruzeiro, V.; Darden, T.; Forouzesh, N.; Giambaşu, G.; Giese, T.; Gilson, M.; Gohlke, H.; Goetz, A.; Harris, J.; Izadi, S.; Izmailov, S.; Kasavajhala, K.; Kaymak, M.; King, E.; Kovalenko, A.; Kurtzman, T.; Lee, T.; Li, P.; Lin, C.; Liu, J.; Luchko, T.; Luo, R.; Machado, M.; Man, V.; Manathunga, M.; Merz, K.; Miao, Y.; Mikhailovskii, O.; Monard, G.; Nguyen, H.; O'Hearn, K.; Onufriev, A.; Pan, F.; Pantano, S.; Qi, R.; Rahnamoun, A.; Roe, D.; Roitberg, A.; Sagui, C.; Schott-Verdugo, S.; Shajan, A.; Shen, J.; Simmerling, C.; Skrynnikov, N.; Smith, J.; Swails, J.; Walker, R.; Wang, J.; Wang, J.; Wei, H.; Wu, X.; Wu, Y.; Xiong, Y.; Xue, Y.; York, D.; Zhao, S.; Zhu, Q.; Kollman, P. *Amber 2023*, 2023. https://ambermd.org/index.php.

(54) Kossmann, S.; Neese, F. Efficient Structure Optimization with Second-Order Many-Body Perturbation Theory: The RIJCOSX-MP2 Method. *J. Chem. Theory Comput.* **2010**, *6*, 2325−2338.

(55) Dunning, T. H. Gaussian Basis Sets for Use in Correlated Molecular Calculations. I. The Atoms Boron through Neon and Hydrogen. *J. Chem. Phys.* **1989**, *90*, 1007−1023.

(56) Woon, D. E.; Dunning, T. H. Gaussian Basis Sets for Use in Correlated Molecular Calculations. III. The Atoms Aluminum through Argon. *J. Chem. Phys.* **1993**, *98*, 1358−1371.

(57) Neese, F. Software Update: The ORCA Program System—Version 5.0. *Wiley Interdiscip. Rev.: Comput. Mol. Sci.* **2022**, *12*, No. e1606.

(58) Fumanal, M.; Plasser, F.; Mai, S.; Daniel, C.; Gindensperger, E. Interstate Vibronic Coupling Constants between Electronic Excited States for Complex Molecules. *J. Chem. Phys.* **2018**, *148*, 124119.

(59) Fdez Galván, I.; Vacher, M.; Alavi, A.; Angeli, C.; Aquilante, F.; Autschbach, J.; Bao, J. J.; Bokarev, S. I.; Bogdanov, N. A.; Carlson, R. K.; Chibotaru, L. F.; Creutzberg, J.; Dattani, N.; Delcey, M. G.; Dong, S. S.; Dreuw, A.; Freitag, L.; Frutos, L. M.; Gagliardi, L.; Gendron, F.; Giussani, A.; González, L.; Grell, G.; Guo, M.; Hoyer, C. E.; Johansson, M.; Keller, S.; Knecht, S.; Kovačević, G.; Källman, E.; Li Manni, G.; Lundberg, M.; Ma, Y.; Mai, S.; Malhado, J. P.; Malmqvist, P. Å.; Marquetand, P.; Mewes, S. A.; Norell, J.; Olivucci, M.; Oppel, M.; Phung, Q. M.; Pierloot, K.; Plasser, F.; Reiher, M.; Sand, A. M.; Schapiro, I.; Sharma, P.; Stein, C. J.; Sørensen, L. K.; Truhlar, D. G.; Ugandi, M.; Ungur, L.; Valentini, A.; Vancoillie, S.; Veryazov, V.; Weser, O.; Wesołowski, T. A.; Widmark, P.-O.; Wouters, S.; Zech, A.; Zobel, J. P.; Lindh, R. OpenMolcas: From Source Code to Insight. *J. Chem. Theory Comput.* **2019**, *15*, 5925−5964.

(60) Zobel, J. P.; Nogueira, J. J.; González, L. The IPEA Dilemma in CASPT2. *Chem. Sci.* **2017**, *8*, 1482−1499.

(61) Forsberg, N.; Malmqvist, P.-Å. Multiconfiguration Perturbation Theory with Imaginary Level Shift. *Chem. Phys. Lett.* **1997**, *274*, 196−204.

(62) Finley, J.; Malmqvist, P.-Å.; Roos, B. O.; Serrano-Andrés, L. The Multi-State CASPT2 Method. *Chem. Phys. Lett.* **1998**, *288*, 299−306.

(63) Stone, A. J. Distributed Multipole Analysis, or How to Describe a Molecular Charge Distribution. *Chem. Phys. Lett.* **1981**, *83*, 233−239.

(64) Bayly, C. I.; Cieplak, P.; Cornell, W.; Kollman, P. A. A Well-Behaved Electrostatic Potential Based Method Using Charge Restraints for Deriving Atomic Charges: The RESP Model. *J. Phys. Chem.* **1993**, *97*, 10269−10280.

(65) Jorgensen, W. L.; Chandrasekhar, J.; Madura, J. D.; Impey, R. W.; Klein, M. L. Comparison of Simple Potential Functions for Simulating Liquid Water. *J. Chem. Phys.* **1983**, *79*, 926−935.

(66) Ryckaert, J.-P.; Ciccotti, G.; Berendsen, H. J. C. Numerical Integration of the Cartesian Equations of Motion of a System with Constraints: Molecular Dynamics of *n*-Alkanes. *J. Comput. Phys.* **1977**, *23*, 327−341.

(67) He, X.; Man, V. H.; Yang, W.; Lee, T.-S.; Wang, J. A Fast and High-Quality Charge Model for the next Generation General AMBER Force Field. *J. Chem. Phys.* **2020**, *153*, 114502.

(68) Mai, S.; Gattuso, H.; Monari, A.; González, L. Novel Molecular-Dynamics-Based Protocols for Phase Space Sampling in Complex Systems. *Front. Chem.* **2018**, *6*, 495.
(69) Andersen, H. C. Rattle: A "Velocity" Version of the Shake Algorithm for Molecular Dynamics Calculations. *J. Comput. Phys.* **1983**, *52*, 24−34.
(70) Avagliano, D.; Bonfanti, M.; Garavelli, M.; González, L. QM/MM Nonadiabatic Dynamics: The SHARC/COBRAMM Approach. *J. Chem. Theory Comput.* **2021**, *17*, 4639−4647.
(71) Reiner, M. M.; Bachmair, B.; Tiefenbacher, M. X.; Mai, S.; González, L.; Marquetand, P.; Dellago, C. Nonadiabatic Forward Flux Sampling for Excited-State Rare Events. *J. Chem. Theory Comput.* **2023**, *19*, 1657−1671.
(72) Sankararamakrishnan, R.; Konvicka, K.; Mehler, E. L.; Weinstein, H. Solvation in Simulated Annealing and High-Temperature Molecular Dynamics of Proteins: A Restrained Water Droplet Model. *Int. J. Quantum Chem.* **2000**, *77*, 174−186.
(73) Balucani, U.; Brodholt, J. P.; Vallauri, R. Analysis of the Velocity Autocorrelation Function of Water. *J. Phys.: Condens. Matter* **1996**, *8*, 6139−6144.
(74) Granucci, G.; Persico, M.; Toniolo, A. Direct Semiclassical Simulation of Photochemical Processes with Semiempirical Wave Functions. *J. Chem. Phys.* **2001**, *114*, 10608−10615.
(75) Mai, S.; Marquetand, P.; González, L. A General Method to Describe Intersystem Crossing Dynamics in Trajectory Surface Hopping. *Int. J. Quantum Chem.* **2015**, *115*, 1215−1231.
(76) Zhu, C.; Nangia, S.; Jasper, A. W.; Truhlar, D. G. Coherent Switching with Decay of Mixing: An Improved Treatment of Electronic Coherence for Non-Born−Oppenheimer Trajectories. *J. Chem. Phys.* **2004**, *121*, 7658−7670.
(77) Blakeley, M. P.; Hasnain, S. S.; Antonyuk, S. V. Sub-Atomic Resolution X-ray Crystallography and Neutron Crystallography: Promise, Challenges and Potential. *Int. Union Crystallogr.* **2015**, *2*, 464−474.
(78) Dubach, V. R. A.; Guskov, A. The Resolution in X-ray Crystallography and Single-Particle Cryogenic Electron Microscopy. *Crystals* **2020**, *10*, 580.
(79) Jmol development team. *Jmol: An Open-Source Java Viewer for Chemical Structures in 3D*, 2016.
(80) English, N. J.; Tse, J. S. Density Fluctuations in Liquid Water. *Phys. Rev. Lett.* **2011**, *106*, 037801.
(81) Strøm, B. A.; Simon, J.-M.; Schnell, S. K.; Kjelstrup, S.; He, J.; Bedeaux, D. Size and Shape Effects on the Thermodynamic Properties of Nanoscale Volumes of Water. *Phys. Chem. Chem. Phys.* **2017**, *19*, 9016−9027.
(82) Fine, R. A.; Millero, F. J. Compressibility of Water as a Function of Temperature and Pressure. *J. Chem. Phys.* **1973**, *59*, 5529−5536.
(83) Dohn, A. O.; Biasin, E.; Haldrup, K.; Nielsen, M. M.; Henriksen, N. E.; Møller, K. B. On the Calculation of X-Ray Scattering Signals from Pairwise Radial Distribution Functions. *J. Phys. B: At., Mol. Opt. Phys.* **2015**, *48*, 244010.
(84) Nimmrich, A.; Panman, M. R.; Berntsson, O.; Biasin, E.; Niebling, S.; Petersson, J.; Hoernke, M.; Björling, A.; Gustavsson, E.; van Driel, T. B.; Dohn, A. O.; Laursen, M.; Zederkof, D. B.; Tono, K.; Katayama, T.; Owada, S.; Nielsen, M. M.; Davidsson, J.; Uhlig, J.; Hub, J. S.; Haldrup, K.; Westenhoff, S. Solvent-Dependent Structural Dynamics in the Ultrafast Photodissociation Reaction of Triiodide Observed with Time-Resolved X-ray Solution Scattering. *J. Am. Chem. Soc.* **2023**, *145*, 15754−15765.
(85) Haldrup, K.; Gawelda, W.; Abela, R.; Alonso-Mori, R.; Bergmann, U.; Bordage, A.; Cammarata, M.; Canton, S. E.; Dohn, A. O.; van Driel, T. B.; Fritz, D. M.; Galler, A.; Glatzel, P.; Harlang, T.; Kjær, K. S.; Lemke, H. T.; Møller, K. B.; Németh, Z.; Pápai, M.; Sas, N.; Uhlig, J.; Zhu, D.; Vankó, G.; Sundström, V.; Nielsen, M. M.; Bressler, C. Observing Solvation Dynamics with Simultaneous Femtosecond X-ray Emission Spectroscopy and X-ray Scattering. *J. Phys. Chem. B* **2016**, *120*, 1158−1168.
(86) El-Sayed, M. A. Spin—Orbit Coupling and the Radiationless Processes in Nitrogen Heterocyclics. *J. Chem. Phys.* **1963**, *38*, 2834−2838.
(87) Nishimoto, Y.; Battaglia, S.; Lindh, R. Analytic First-Order Derivatives of (X)MS, XDW, and RMS Variants of the CASPT2 and RASPT2 Methods. *J. Chem. Theory Comput.* **2022**, *18*, 4269−4281.

APPENDIX A.2 APPLICATION TO AN IRON COMPLEX IN WATER

APPENDIX A.2.1

Three-Dimensional Nonadiabatic Solvent Reorganization Dynamics of an Iron Complex

SEVERIN POLONIUS, LETICIA GONZÁLEZ, SEBASTIAN MAI

unpublished manuscript

Contributions:

SEVERIN POLONIUS ...made all necessary implementations in SHARC, performed all analyses, constructed the figures, and wrote and adapted the initial draft.

LETICIA GONZÁLEZ ...conceived the scope of the manuscript.

SEBASTIAN MAI ...planned the manuscript, closely supervised the developments and analyses, and revised the initial draft.

Three-Dimensional Nonadiabatic Solvent Reorganization Dynamics of an Iron Complex

Severin Polonius,[†,‡] Leticia González,[*,†] and Sebastian Mai[*,†]

[†]*Institute of Theoretical Chemistry, Faculty of Chemistry, University of Vienna, Währinger Str. 17, 1090 Vienna, Austria.*
[‡]*University of Vienna, Vienna Doctoral School in Chemistry (DoSChem), Währinger Str. 42, 1090 Vienna, Austria.*

E-mail: leticia.gonzalez@univie.ac.at; sebastian.mai@univie.ac.at

Abstract

Not only ligand field splitting plays a major role in the lifetimes of different excited state populations in transition metal complexes but also the solvent exerts a considerable influence. For the disentanglement of the solvated excited-state dynamics of the electronic wave function as well as solute and solvent structure, excited-state simulations are needed in addition to experimental investigations. However, the necessary nonadiabatic molecular dynamics simulations of the solvated systems over long time scales remain computationally demanding and are scarce. On such study performed by members of our group investigates the excited-state dynamics of the $[\mathrm{Fe(CN)_4(bipy)}]^{2-}$complex in water over 700 fs [Zederkof et al. JACS **2022**, *144*, 28, 12861–12873]. The study shows the electronic dynamics, as well as the time-dependent solute and solvent structure. The investigations also indicate that additional information both on longer time-scales as well as larger sample sizes for the solvent dynamics are beneficial to the understanding of this system. Therefore, we aim to perform large-scale trajectory surface hopping simulations on $[\mathrm{Fe(CN)_4(bipy)}]^{2-}$ that allow not only investigations on the electronic dynamics but also noise-free three-dimensionally resolved solvent dynamics over long time scales. Such simulations are possible with a novel approach combining efficient linear vibronic coupling models with molecular mechanics (LVC/MM) via electrostatic embedding [Polonius et al., JCTC **2023**, *19*, 7171–7186]. In comparison to the previous study, we show that LVC/MM is able produce accurate results in terms the overall intersystem crossing time scale, as well as dynamical bond length distributions and time-dependent radial distribution functions at a fraction of computational cost. Additionally, we are able to resolve a oscillatory behavior in the time-dependent RDF and changes in three-dimensional solvent structure over time. We find that the initial solvation shell concentrated at the cyanide ligands decreases in less than 100 fs after excitation. Thereafter, hydrogen bonds are established at the bipyridyl ligand within 1000 fs stabilizing the metal-to-ligand-charge-transfer states additionally.

1 Introduction

The photoactivated dynamics of a solute molecule in an environment of solvent molecules is a frequently encountered situation encountered in chemistry.[1–3] These dynamics and underlying processes can be investigated with various experimental techniques. The system of interest can be observed with femtosecond resolution in terms of its electronic wave function via, e.g., transient absorption spectroscopy,[4–6] X-ray fluorescence spectroscopy,[7–9] or photoelectron spectroscopy.[10,11] The nuclear dynamics initiated by the photoexcitation is usually measured using X-ray scattering experiments.[6,7,12–16] This spectroscopy reveals temporal evolution of the atomic nuclei during the dynamics and hence gives insight into the solute's vibrational response and relaxation,[17] and measures the solvents response through phenomena such as libration and diffusion.[3,18]

Transition metal clusters, prominently 4d and 5d metals, are well-studied systems, and 3d metal clusters have recently gained interest for economic and sustainability reasons.[19,20] Compared to the the 4d/5d metals, 3d metal clusters have the shortened lifetime of metal-to-ligand-charge-transfer (MLCT) states, which are important for their function as sensitizers or catalysts.[21] The MLCT states have nano- to microsecond lifetimes in ruthenium(II)-polypyridyl complexes[22,23] but in comparable iron(II) complexes the MLCT state is quenched via metal-centered (MC) states within femtoseconds.[16,24,25] In order to achieve longer MLCT lifetimes, the MC states of these iron complexes may be destabilized with respect to the MLCT states by increasing the ligand field strength through, e.g., π-accepting cyanide, carbene, or carbonyl ligands.[21,26–28]

$[\mathrm{Fe(CN)_4(bipy)}]^{2-}$ has a particularly strong ligand field introduced by the cyanide and bipyridyl ligand and is polar which destabilizes the MC states against the MLCT states.[29] The complex is an interesting system (i) to investigate the influence of combining σ-donating and π-accepting ligands to increase the lifetime of MLCT states,[26–28] (ii) to observe a potentially meta-stable MC state in experiments,[29] and (iii) to additionally gauge the influence of the solvent on the lifetimes of both MC and MLCT states.[8,29,30] The solvent has a considerable effect on the dynamics of $[\mathrm{Fe(CN)_4(bipy)}]^{2-}$ as the MLCT states is quenched in less than 200 fs[8,29] but much slower in di-methyl-sulfoxide with lifetimes of multiple picosends.[31,32]

In a previous collaboration of our group, experimental results on $[\mathrm{Fe(CN)_4(bipy)}]^{2-}$ in water were supplied with mixed quantum mechanical/molecular mechanical (QM/MM) surface hopping including arbitrary couplings (SHARC)[33,34] simulations that disentangled the dynamics in terms of electronic wave function and nuclear degrees of freedom from solute and solvent within the first 700 fs after excitation.[30] The authors find MLCT and MC lifetimes in the picosecond range and investigate the coupled solute–solvent response via time-dependent radial distribution functions (RDFs). Their results indicate that SHARC simulations on longer time scales and with more trajectories can be beneficial to resolve the long term dynamics and the different contributions of the coupled solute–solvent response.

In this study, we use the novel of LVC/MM method[35] to facilitate large trajectory swarms in SHARC simulations over long time scales that allow the not only the generation of time-resolved RDFs but also three dimensional spatial distribution functions (3D-SDFs).[36] We report similar findings in terms of electronic populations, intersystem crossing (ISC) rate, time-dependent solute bond lengths and RDFs as the previous work at a fraction of the computational cost.[30] Additionally, we are able to observe oscillatory behavior in the time-dependent RDFs and changes in three-dimensional solvent structure over time, and perform a analysis of a subset of trajectories that reveals stark differences in the solvation structure between MLCT and MC dominated populations.

2 Computational Details

2.1 Ab-Initio Setup and Geometry Optimization

For continuity with previous work,[30] we used a comparable level of theory to generate the reference data for the parametrization of the linear vibronic coupling (LVC) model for $[\mathrm{Fe(CN)_4(bipy)}]^{2-}$. This includes a geometry optimization, frequency calculation and all single-point calculations. We used the B3LYP* functional,[37] and the def2-TZVP basis set for the iron center and the def2-SVP basis set for the other atoms. For all calculations, we also used high convergence criteria with the SCF convergence set to $1 \cdot 10^{-10}$ au and the "superfine" grid option in GAUSSIAN.[38] We additionally used the empirical dispersion correction GD3BJ as defined in ORCA5.[39,40]

Before we were able to compute the reference calculations for the model, we needed to address some issues regarding the inclusion of implicit solvation via CPCM: (i) the first excited states of the iron complex in the gas phase are close in energy to the ground state (excitation energies below 0.5 eV) which leads to instabilities in the single-point calculations of the parametrization later (see Fig. S1) (ii) parametrizing the LVC model with a dielectric constant of 80.2 for water accounts for the solvent effect twice in LVC/MM calculations which we confirmed by calculating a spectrum (see Fig. S2) The polarizability of the electronic density of the solvent molecules is not accounted for by the force field for LVC/MM, and its inclusion into the LVC model should therefore not lead to double counting. For this reason, we decided to use the dielectric constant of water in the high-frequency limit $\varepsilon_r = 1.7689$ in the implicit solvation for all computations. This lead to large enough excitation energy of the first excited states to alleviate problem (i) as can be seen in Fig. S1.

We set the geometry optimization to be constraint to a C_{2v} symmetry for the molecular structure. At the obtained nuclear coordinates, we calculated the frequencies of $[Fe(CN)_4(bipy)]^{2-}$ with the settings described above.

2.2 Parametrization of the LVC Model

With the computed geometry and normal modes of $[Fe(CN)_4(bipy)]^{2-}$, we set up the calculation for the LVC model according to Ref. 41. We decided to include the first 21 singlet and 20 triplet states in the model. This choice originated from overlap calculations including 31 singlets and 30 triplets with CPCM using an epsilon of 80.2 to gauge the behavior of the states in the solvated system. Analysis of the overlap and character of the states with the TheoDORE program[42] revealed that the important six lowest MC triplet states can be represented within the first 20 triplet states with our CPCM settings. For the numerical evaluation of the λ parameters, we performed single-point calculations at displaced geometries along each mass–frequency-weighted normal model scaled by 0.05 and 0.1. In this study, we extended the set of parameters of standard LVC models to account for some state-specific shifts in frequency of selected normal modes. These parameters will be briefly explained here. In a general vibronic coupling model,[41,43,44] the elements of the diabatic vibronic coupling matrix W_{ij} are constructed as a Taylor series expansion around the mass–frequency weighted normal coordinates $\mathbf{Q} = 0$

$$\begin{aligned} W_{ij} = \delta_{ij} \Bigg(& V_0(\mathbf{Q}) + \varepsilon_i + \sum_k \kappa_k^{(i)} Q_k \\ & + \sum_{kl} \gamma_{kl}^{(ii)} Q_k Q_l + \cdots \Bigg) \\ & + (1 - \delta_{ij}) \Bigg(\eta_{ij} + \sum_k \lambda_k^{(ij)} Q_k \\ & + \sum_{kl} \gamma_{kl}^{(ij)} Q_k Q_l \cdots \Bigg), \end{aligned} \tag{1}$$

where

$$\kappa_k^{(i)} = \left(\frac{\partial W_{ii}}{\partial Q_k} \right)_{\mathbf{Q}=0} \tag{2}$$

$$\lambda_k^{(ij)} = \left(\frac{\partial W_{ij}}{\partial Q_k} \right)_{\mathbf{Q}=0} \tag{3}$$

$$\gamma_{kl}^{(ij)} = \left(\frac{\partial^2 W_{ij}}{\partial Q_k \partial Q_l} - \omega_k \delta_{kl} \right)_{\mathbf{Q}=0}. \tag{4}$$

Here, the $V_0(\mathbf{Q}) = \frac{1}{2} \sum_k \omega_k Q_k^2$ is the ground state potential energy function with the frequency ω_k of the k-th normal mode, ε_i is the vertical excitation energy of the electronic state i at $\mathbf{Q} = 0$, η^{ij} are constant couplings parameters, $\kappa_n^{(i)}$ and $\lambda_n^{(ij)}$ are the first-order intrastate and interstate vibronic coupling constants, and $\gamma_{kl}^{(ij)}$ are the second-order coupling constants. Specifically, $\gamma_{kk}^{(ii)}$ are the state-specific frequency shifts that modify the curvature of the ground-state oscillator of the corresponding mode. We decided to extend the LVC model in the SHARC code[34] with the $\gamma_{kk}^{(ii)}$ to account for pronounced changes in oscillator strengths between modes in the electronic ground-state and excited states. For the numerical evaluation of the γ parameters, we additionally calculated single points at displacements 0.2 and 0.4 along all symmetric modes (13 modes) that elongate the Fe-N$_{\text{bpy}}$ and Fe-C$_{\text{eq.}}$ bonds. This choice is motivated by Fig. S3, which shows that the inclusion of these parameters specifically increases the accuracy of the ^{3}MC states in the LVC model. The γ values are then calculated from these further displacements via as the mean as

$$\begin{aligned}\gamma_k^{(ij)} &= \frac{2}{N}\sum_n^N \omega_{k,n} \\ &= \frac{2}{N}\sum_n^N \frac{\left[E^{(ij)}(h_{k,n}) - E^{(ij)}(0)\right]}{h_{k,n}^2}.\end{aligned} \tag{5}$$

Here, $\omega_{k,n}$ is the evaluated frequency of normal mode k at displacement n and $E^{(ij)}(h_{k,n})$ is the diabatized energy at $h_{k,n}$ in normal mode coordinates. We only included $\gamma_k^{(ii)}$ in the LVC parameters for all states with major MC character at the equilibrium geometry and normal modes that affect the bond lengths between the metal center and equatorial ligands.

The distributed multipole expansions (DMEs) in the LVC model are evaluated using the procedure outlined in Ref. 35 and restraint parameters of 0.001, 0.003 and 0.006 for the multipole orders with target charges for the monopolar terms set to 0 and van-der-Waals radii as recommended in Ref. 45. We additionally computed all state and transition dipole moments from the electronic densities obtained from the calculations.[35] For the simulations, we fitted DMEs for each diabatic the electronic states and included them in the LVC model. The spin–orbit coupling parameters included in the LVC model are calculated using ORCA5,[40] with settings equivalent to the GAUSSIAN calculations; the RMSD of the adiabatic energies is 0.0010 au.

2.3 Generation of Initial Conditions

The initial conditions for the excited state dynamics are generated using both MD and LVC/MM calculations. The procedure is adapted from both Ref. 46 and Ref. 30. For the MD simulations using AMBER22,[47] we use the parameter file containing the generated force field for [Fe(CN)$_4$(bipy)]$^{2-}$ from Ref. 30; in which we changed the charges to our fitted monopoles of the ground state. As a water model, we used SPC-Fw.[48] The iron complex is solvated in a truncated-octahedron water box containing 5412 water molecules and two Na$^+$ ions with 25 Å between the complex and the closest face of the box. Using a time step of 0.5 fs, we relaxed the generated solvation box, then heated to 300 K over 20 ps (NVT ensemble), equilibrated to 1 bar over 500 ps (NPT ensemble), and then propagated for 45 ns. From these 45 ns, we took snapshots every 1.5 ps to obtain 30,000 initial conditions with which we proceeded further.

In order to approximately account for the zero-point energy of the complex that cannot be described with nuclear dynamics, we increased the kinetic energy of [Fe(CN)$_4$(bipy)]$^{2-}$ through a local reheating step with 600 K as proposed in Refs. 46 For the local reheating step, the atomic positions of the solvent nuclei are not propagated using the 'ibelly' option of the `AMBER` program[47] and are thus effectively frozen. Subsequently, the solute complex was reheated to 600 K over 40 ps. We deviated in the duration of the local reheating step to ensure that the kinetic energy of the solute had stabilized. Afterward, the velocities of the solvent molecules were reset to the values before freezing. This generates a system in which the solute molecule has kinetic energy approximately equivalent to 600 K and solvent at 300 K.

At this point, we deviate from the original procedure to some degree, as the efficiency of the LVC/MM method allows for a longer re-equilibration. All 30,000 initial conditions with the solvent at 300 K and the solute at approximately 600 K are re-imaged to center iron complex and re-equilibrated between 500 and 550 fs at random using SHARC[34] and LVC/MM. We therefore combined the switch to non-periodic boundary conditions and the QM/MM relaxation of the original procedure while also extending the duration by 250 fs; this ensured a complete relaxation of the system. During the reequilibration period, we save the nuclear coordinates of the last 100 fs every 5 fs for later analysis.

2.4 Excited State Dynamics

The initial conditions are excited at the first absorption band in a window between 482 nm to 502 nm (2.52 ± 0.1 eV) according to the calculated spectrum (Fig 1a) below. This resulted in the excitation of 4473 initial conditions into the lowest 5 singlet excited states with a majority (97.6%) in the S_3 state. The trajectory swarm is set up using all 4473 excited initial conditions. The trajectories are propagated with the surface hopping including arbitrary couplings (SHARC) method[33] and corresponding program.[34] In the simulations, we used the local diabatization approach,[49,50] the energy-based decoherence correction,[51] rescaling of the solute atom velocities after a hop parallel to their velocity vector, and no frustrated hops. In the SHARC simulation, the lowest six singlet and seven triplet states are used for the dynamics; the LVC model still included 21 singlet and 20 triplet states. The propagation timestep is set to 0.02 fs for the electronic wave function and to 0.5 fs for the nuclear positions and velocities. All trajectories are propagated for 5000 fs. Each trajectory is computed on a single Intel Xeon E5-2650 v3 CPU and had an average wall time of 13 h; this corresponds to about 4.7 seconds per step compared to about 16×15 minutes per step with TDDFT.[30]

Data on the electronic wave function (Hamiltonian, overlap and transformation matrices) are stored every 1 fs for times up to 700 fs and then every 5 fs (1560 data points); the nuclear coordinates are save every 5 fs for times up to 700 fs and then every 25 fs (312 data points). The complete dataset on electronic and nuclear data for the whole trajectory swarm amounted to 1.1 TiB.

2.5 Trajectory analysis

With the computed trajectories, we analyze the motion of the solute, $[Fe(CN)_4(bipy)]^{2-}$, the solvent water molecules and the coupling between them.

The electronic dynamics are analyzed with respect to the electronic populations and the characters of the excited states. The characterization of the electronic states is performed in the diabatic basis at the reference geometry using the TheoDORE program.[42] The electronic populations in the diagonal basis are then transformed back into the diabatic basis so that the electronic state characters can be assigned. The diabatic populations were fitted using the SHARC program[34] with either a monoexponential ansatz or a specified model. Errors for the obtained time-constants are computed via bootstrapping.[52]

The dynamical response of the chosen bond lengths is analyzed by calculating the respective average of symmetry-equivalent bond lengths for each trajectory and time step. Subsequently, the data is aggregated in terms on average and a Gaussian convolution over all trajectories. For time steps before excitation at $t = 0$,fs, no distinction is made in terms of electronic character of the diabatic state. For time steps after excitation, averages and Gaussian convolutions are calculated from subsets of trajectories based on the character of the electronic wave function being either MLCT or ^{3}MC; the character is determined from the square norm of corresponding diabatic coefficients being larger than 0.9.

Radial distribution functions (RDFs) are calculated between different pairs of atom collections. All RDFs are evaluated with bin widths of 0.05 Å and normalized with the factor $\frac{4\pi}{3}\left[(R+dR)^3 - R^3\right]$ using the `cpptraj` program of the AmberTools program package.[47] The average RDFs from 100 to 0 fs before excitation serve as a reference to compute difference RDFs (ΔRDFs) over time. The temporal behavior of the ΔRDFs is then analyzed by calculating singular value decompositions (SVDs) as $\Delta\text{RDF}(R,t) = \sum_i V_i(R) \cdot s_i \cdot U_i(t)$.

The three-dimensional spatial distribution functions (3D-SDFs), which we introduced in our previous work,[35] are evaluated in the molecule's perspective, where the solute coordinates are aligned to a reference structure at every time step. In this work, we deviate from the construction of 3D-SDFs as simple three-dimensional histograms and evaluated them using a kernel density estimation procedure (KDE).[53,54] Although computationally more demanding in its construction, a KDE requires fewer data points to achieve smooth distribution functions. We used a Gaussian distribution function as kernel for the KDE, which was computed as

$$\mathrm{KDE}(\mathbf{R}_g) = \sum_{i}^{N_{\mathrm{traj}}} \sum_{a}^{N_a} \frac{\exp\left(\frac{|\mathbf{R}_g - \mathbf{R}_{ia}|^2}{2\sigma^2}\right)}{\sqrt{2\pi\sigma^2}}. \qquad (6)$$

Here, the KDE at the Cartesian grid point $\mathbf{R}_g$ is the sum of three-dimensional Gaussian distribution function for all trajectories N_{traj} and all atoms of chosen type in the system N_a with coordinates $\mathbf{R}_{ia}$. The variance of the Gaussian function σ is set to 0.5 Å corresponding to the bin width chosen in our previous work[36] The KDEs were evaluated on a grid of 40 points in each Cartesian direction and a grid spacing of 0.5 Å. The three-dimensional solvent distributions adhere to the C_{2v} symmetry that is imposed by the molecular framework of the solute. Hence, we applied the corresponding symmetry operations to the constructed KDEs by summing up all symmetry-equivalent data points. This effectively quadrupled our sampling size and lead to less noise and more pronounced features in the plotted 3D-SDFs.

3 Results and Discussion

3.1 Absorption Spectrum

Fig. 1 shows the absorption spectra calculated from the initial conditions prepare with the LVC/MM method in this work and the initial conditions used in Ref 30 with the TDDFT/MM reference method. Both spectra do not show absorption bands originating from the lowest two singlet states; albeit these states are not completely dark in the LVC/MM spectrum. The first absorption band in both spectra stems from the S_3 state. This band has a peak at 492 nm in panel (a) and 526 nm in panel (b) which corresponds to a difference of 0.16 eV. The absorption band has a comparable shape and relative intensity. The second and third band at 357 nm and 269 nm with LVC/MM compared to 369 nm 281 nm for the reference are shifted by 0.11 eV and 0.19 eV, respectively. The shape and relative intensity of the second band differ between the methods, as it is more symmetric and intense in panel (a) and less intense and tailing toward lower energies in panel (b). The second band differs mainly in intensity and composition. The S_{13} state appears in this band instead of the second for LVC/MM instead of the reference.

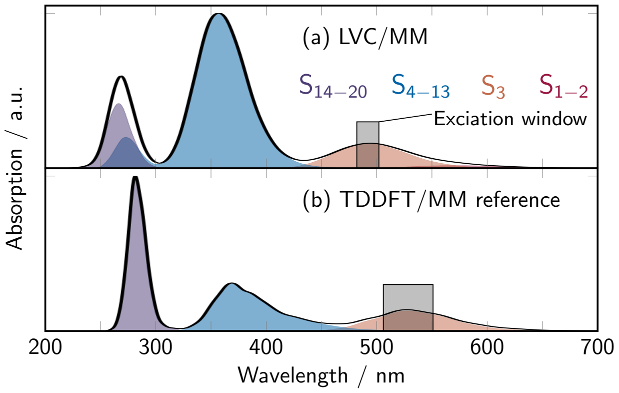

Figure 1: Absorption spectra of $[\mathrm{Fe(CN)_4(bipy)}]^{2-}$ in water computed with (a) the LVC/MM model from 30,000 initial conditions and (b) the TDDFT/MM reference method from 500 initial conditions provided by the authors of Ref 30. The different absorption bands are highlighted by collecting the singlet states as they appear in the reference spectrum: S_1 and S_2 in red, S_3 in orange, S_4 to S_{13} in blue and S_{14} to S_{20} in purple. Both spectra are convoluted with Gaussian distribution functions (full-width-half-maximum of 0.1 eV) and normalized to 1. The gray shaded area indicates the used excitation window.

The shifts in the spectra could have multiple origins. The difference in the equilibration period can be excluded as a source, a spectrum on the reference initial conditions with LVC/MM leads to a spectrum with similar shifts. Therefore, the differences in the spectra should only be attributed to the differences in the methods, especially the approximations made in the LVC/MM model. The shifts are rather due to the limitations of the distributed multipole expansion used instead of a polarizable and diffuse electronic density which have led to similar shifts in energy in previous work.[35] The differences especially for the higher states might stem from a increasing error in the description of the adiabatic states in the limited basis of diabatic states. Despite these differences, the low-lying singlet states, especially the important S_3 absorption band, are well described within our model. Most likely coincidentally, the absorption peak of the S_3 state at 492 nm is close to the experimentally reported peak position at 500 nm.[29]

3.2 Electronic Dynamics

Fig. 2 shows the dynamics of the electronic populations in different aggregations. The adiabatic populations in panel (a) show that the fast ISC rate within the first 1000 fs, after which about 90% of the population is in the triplet manifold. The first three triplet states are populated in decreasing amount from lowest to highest triplet. The singlet population is initially dominated by the S_3 state. While the overall singlet population decreases, the proportions of first the S_2 and then S_1 state increase. The remaining singlet population of about 6% can be attributed to the S_1 state. The total population transfer between singlet and triplet states is shown in Fig. 2b together with a monoexponential fit. It can be recognized that the transfer occurs within the first 1000 fs. The fitted time constant of the general ISC is with 211 ± 4 fs almost identical to the TDDFT reference of 210 fs.[30] Panel (c) of Fig. 2 displays the population dynamics in the diabatic basis for which characters of the electronic wave function are determined. The initial singlet population is mostly of MLCT character and no ^{1}MC population is observed during the dynamics. The ground-state singlet is populated very slowly. The population transfer via ISC into the triplet states is split into the ^{3}MC states and the other triplet states with dominantly MLCT character. The ^{3}MC reach a final population of about 31% with a trend to increase; the other triplet states reach a final population of 62% with a decreasing trend. The schematic of the kinetic model used to fit the population dynamics features a separate ^{1}Cold population which represents the stable population of the adiabatic S_1 state (see Fig. 2a). This state accounts for about 6% of the ^{1}MLCT population. The model predicts fast population transfers from the initial singlet population to the ^{3}MC states and ^{3}MLCT states with time constants of 687 ± 20 fs and 311 ± 6 fs. These constants have low uncertainties, and their ratio reflects the ratio of the final populations of both triplet manifolds. This is because the internal conversion between the two triplet populations from MLCT to MC is very slow with 100^{+47}_{-32} ps; the error is large shows that the simulation time of 5 ps is not long enough to properly fit this constant. Similarly, the population of the ^{3}MC state is slowly transferred into the ground state with a time constant of 90 ± 15 ps.

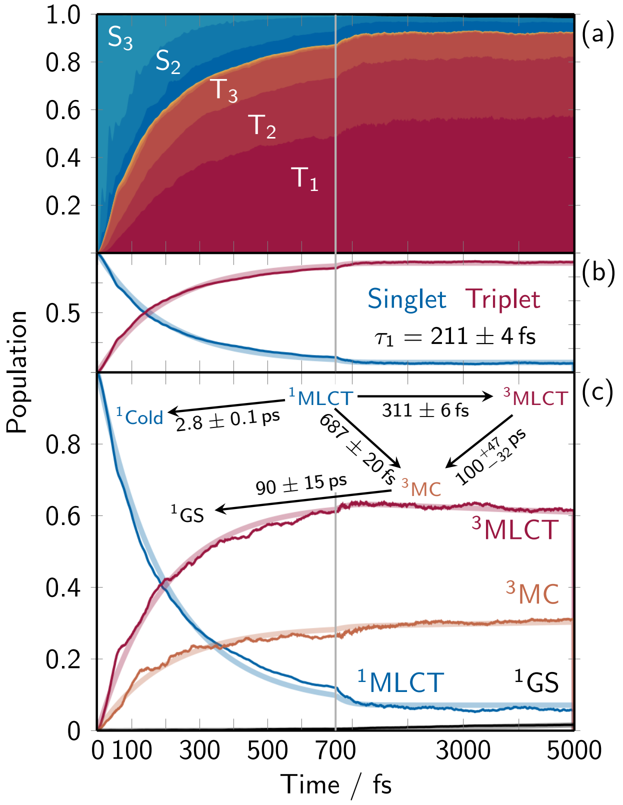

Figure 2: Dynamics of the electronic populations during the simulation. (a) Stacked-area plot showing the contributions from each adiabatic excited state with a black ground state singlet, excited singlet states from dark blue to light blue, and excited triplet states from dark red to light orange. (b) Total singlet and triplet populations (thin lines) and corresponding mono-exponential fits (thick lines). (c) Time-dependent diabatic populations (thin lines) for the ground state (GS) in black, the ^{1}MLCT states that was excited into in blue, the ^{3}MC states in orange, and the ^{3}MLCT states comprising all other triplet states (majorly MLCT character) in red. The thick lines indicate the global fitting results from the shown kinetic model.

The fast ISC rate from singlet to triplet manifolds shows both that the triplet states are energetically more favorable than the singlet states and that there are large spin–orbit couplings. The dynamics in general are comparable to the TDDFT reference in Ref. 30. The major difference inferred from the kinetic models is the internal conversion rate between the MC and MLCT triplet manifolds. Although its uncertainty is large, the rate of 100 ps on average is more than a magnitude slower than the reported TDDFT results of 2.2 ps. The slow internal conversion rate can be attributed to the comparable excitation energies of the diabatic MC and MLCT triplet manifolds over the course of the whole dynamics (see Fig. S4). Experimental results show that the conversion rate is directly influenced by the stabilization of the ^{3}MC states.[29] Both the t_{2g} and e_g orbitals of the metal center are influenced by the environment and, in turn, influence the stabilization of the MC triplet states. Hence, it can be reasoned that the ^{3}MC states are not stabilized enough in the LVC/MM model compared to the other triplet states, by either restrictions in the harmonic oscillators or the solvent interaction. The included γ_{kk}^{ii} parameters increased the accuracy of the ^{3}MC states (see Tab. S1). Therefore, either more second-order parameters need to be included, or this represents a limitation of the DME within the LVC/MM model. The slower population transfer into the ground state from the ^{3}MC states might also be influenced by the respective excitation energy. The excitation energy of the MC states is expected to be less influenced by the solvation shell than the MLCT states as the electronic ground state and the MC states exhibit similar electrostatic potentials.

Even with the pronounced difference in the final population ratio between the triplet manifolds of about $2/3$, the bifurcation into these states which is expected from experimental data is described by the model.[8,29,30] The corresponding dynamics in the solvation shell need to be interpreted in light of this difference but can be deemed useful in the disentanglement of the different contributions to the overall nuclear dynamics of the system.

3.3 Dynamical Response of the Solute Structure

Fig. 3 shows the time-dependent bond length distributions of collections of trajectories based on their electronic state. It should be noted that the lines that indicate the average of trajectories in the MC states do not start at $t = 0$ fs but only as soon as there are trajectories with MC active states. Panel (a) shows the Fe–N$_{\text{bpy}}$ bond length which is about 2.0 Å in the ground state before excitation. After excitation at $t = 0$ fs the bond length increased for both MLCT and MC states with oscillations that are multi-frequent. The bond length for trajectories in MC states increases to about 2.2 Å within the first 100 fs and remains a this value. The trajectories in the MLCT states also increase but to a smaller degree to about 2.1 Å. The shade of the color indicates that most trajectories have a bond length between the MC and MLCT averages; consistent with the electronic populations in Fig 2c most there are more trajectories in the MLCT states. The average Fe–CN$_{\text{ax}}$ bond length (panel (b)) does show coherent motion throughout the whole simulation before and after the simulation but does not deviate from its average bond length of about 1.9 Å with a deviation of less than 0.1 Å. Fig. 3c shows that the average length for the Fe–CN$_{\text{eq}}$ bond does not deviate from the ground-state average of 1.9 Å for the MLCT states throughout the simulation; the distribution is slightly higher. However, the trajectories in the MC states reach a increased bond length of about 2.0 Å in less than 100 fs.

The results of the characterized bond length analysis suggest that the stabilization of the MC states correlates with an increase in bond distance of the equatorial ligands.[55] The bonds are weakened upon population of the MC states. The population of the MLCT states only influences the bond length with the bipyridyl ligand. The Fe–N$_{\text{bpy}}$ appears to be influenced by multiple normal modes that are vibrationally excited after $t = 0$ fs. The changes in bond length are consistent with the findings of the reference.[30] All bond length distributions deviate from the mean symmetrically after the excitation (see Tab. S2). The width of the distributions of the Fe–N$_{\text{bpy}}$ and Fe–CN$_{\text{eq}}$ in Ref. 30 are larger for the MC states than MLCT states and the MC distribution also appear to be skewed towards larger deviations for the MC states. These findings cannot be reproduced by the LVC model even though the averages are reproduced. If the MC states are stabilized through anharmonicity in the corresponding normal modes, the LVC model cannot reproduce these effects well enough. This can explain insufficient stabilization of the MC states leading to slower population transfer. Either stronger frequency shifts or anharmonicity in the normal modes stabilizing the MC states lead to a faster vibrational relaxation into the ground state, which in the LVC/MM dynamics is significantly slower than experimental

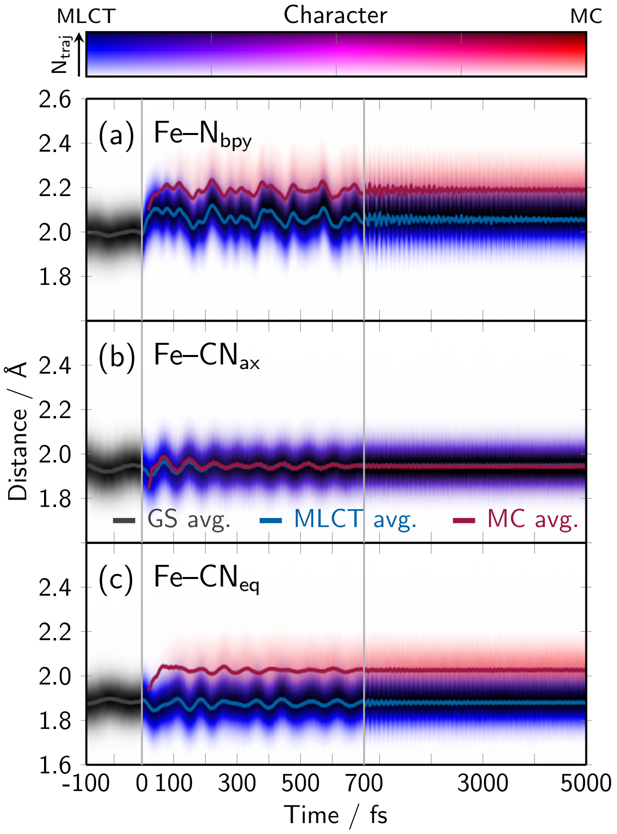

Figure 3: Distributions of different bond lengths over time decomposed into the contribution of electronic states with different character. Both the averages (lines) and distributions (shaded areas) are shown for the iron to bipyridyl nitrogen bond length (Fe–N_{bpy}) in panel a, the iron to axial cyanide carbon bond length (Fe–CN_{ax}) in panel b, and the iron to equatorial cyanide carbon bond length (Fe–CN_{eq}) in panel c. The ground state is indicated by black and gray colors. The contributions to the bond lengths of the excited states with different character are indicated by red for MC states to over purple for a mixture to blue for MLCT states. The luminance of each color decreases with the number of corresponding trajectories with active MC or MLCT state.

findings.[29]

3.4 Dynamical Response of the Solvent Structure

Fig. 4 shows the RDFs of C_{bpy}–H_{sol}, C_{CN}–H_{sol}, and N–H_{sol} in panels (a-c) respectively. It can be seen that C_{bpy}–H_{sol} does have comparably weak first solvation shell. However, the RDF at $t = 700$ fs shows an increase in water hydrogen atoms at distances between 2 and 3 Å. The other two atom pairings show strong first solvation shells at about 2.5Å for C_{CN}–H_{sol} and about 1.9 Å for N–H_{sol}. Both signals decrease at $t = 700$,fs and remain at approximately the same level until the end of the simulation.

Fig. 4d shows a consistent increase in the difference RDFs over time for C_{bpy}–H_{sol}. The increase is rapid at the beginning ($\tau = 277$ fs) and also features an oscillation visible at distances between 3 and 4 Å; the period of this oscillation is evaluated using a Fourier transform to beat $378\,\mathrm{cm}^{-}1$ which corresponds to a period of 88 fs. This oscillation coincides with the frequency of a bipyridyl ring-ring stretch mode that stretches both rings outward parallel to their connecting bond; the oscillation in this signal matches with experimental findings.[30] An analysis of the average distance between symmetry-equivalent bipyridyl carbon atoms results that move during the ring-ring stretch mode, results in a period of 87 fs. This confirms the result and indicates that the beating visible in Fig. 4d is a result of solute vibration. Both C_{CN}–H_{sol}, and N–H_{sol} difference RDFS show a stark initial decrease of the first solvation shell ($\tau = 73$ fs and $\tau = 47$ fs). The C_{CN}–H_{sol} increases most drastically between 5 and 6 Å. The first solvation shell of N–H_{sol} initially shifts towards slightly larger values; the positive signal mostly vanishes within the first 700 fs. The time constants for the initial changes of the difference RDFs are evaluated through a monoexponential fit of the first SVD component.

The RDFs indicate a rapid decrease in the strong first solvation shell around the cyanide ligands after excitation. The time constants of this decrease are consistent with inertial effects/libration motion in water.[3,56] This initial response is then followed by a further decrease in the first solvation shell visible in Fig. 4f. The slow increase in the C_{bpy}–H_{sol} RDF is the reaction of the solvent molecules to the increased electron density in the bipyridyl ligand through MLCT processes. After 1000 fs, the C_{bpy}–H_{sol} and C_{CN}–H_{sol} TD-RDFs gradually increase their established features. The N–H_{sol} shows that the initial increase around 2 Å dissipates again after 1000 fs.

Fig. 5 shows the three-dimensional spatial distribution functions (3D-SDFs) of the water oxygen

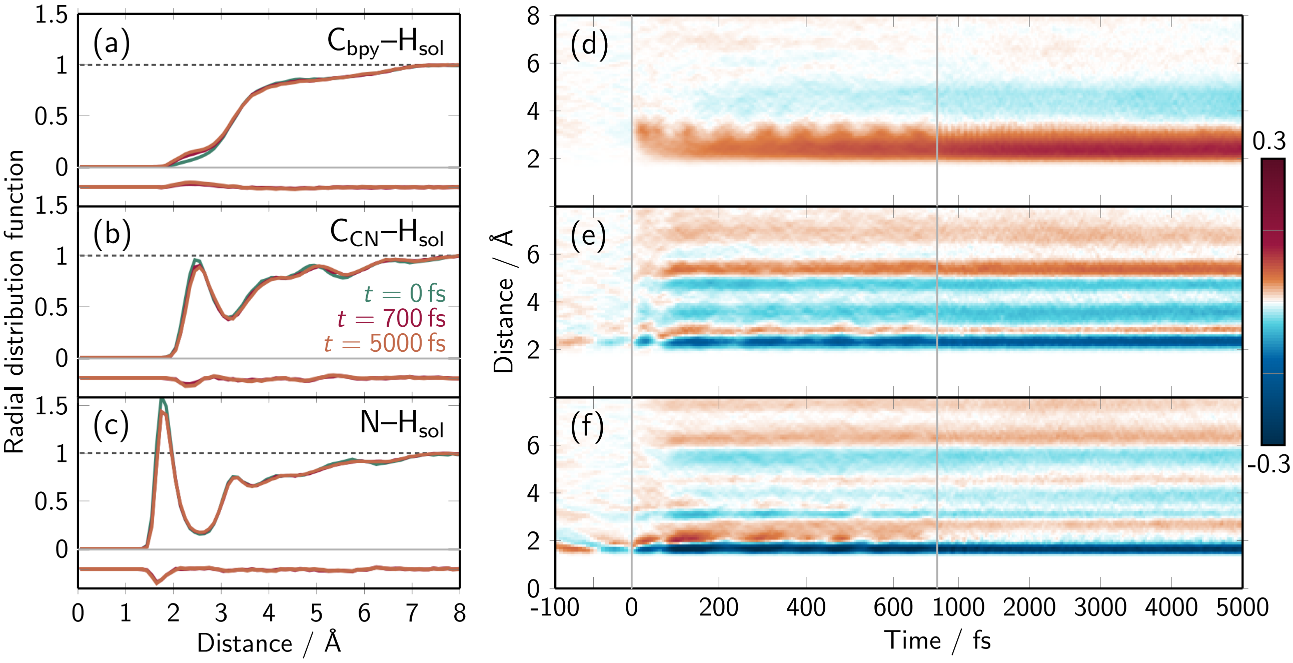

Figure 4: Radial distribution functions (RDF) at different times after excitation (a-c) and corresponding time-dependent difference RDFs (d-f). (a-c) Show the bipyridyl carbon–water hydrogen (C_{bpy}–H_{sol}), cyanide carbon–water hydrogen (C_{CN}–H_{sol}) and nitrogen–water hydrogen (N–H_{sol}) RDFs at $t = 0$ fs in green, $t = 700$ fs in red and $t = 5000$ fs in orange (the respective differences are shown below 0). Panels (d-f) show the respective time-dependent difference RDFS corresponding to (a-c) with positive deviations in red colors and negative deviations in blue colors.

and hydrogen atoms at $t = 0$ and the difference from these 3D-SDFs at times thereafter. At $t = 0$, the strong first solvation shell around the cyanide ligands is clearly visible with more extensive features around the axial cyanide ligends towards the nitrogen atoms on the bipyridyl ligand. However, the 3D-SDF does not show a strong first solvation shell at the bipyridyl carbon atoms, which is in line with the corresponding RDF (see Fig. 4a) 100 fs after the excitation, the solvation shell is weakened around all nitrogen atoms, especially close to the bipyridyl ligand; at the equatorial cyanide ligands the decrease is only observable on the outward facing side. Additionally, an increase in oxygen atom occurrence is visible above the center of the bipyridyl ligand (green isosurface in panel c at 100 fs), which is aligns with the increase visible in the TD-RDF of N–H_{sol} (Fig. 4f). The short time frame after excitation of this shift indicates inertial response/libration motion; a monoexponential fit on the first SVD component of the Δ3D-SDFs results in a time constant of 75 fs which is consistent with time scales from literature.[3,18] After 500 and 1000 fs, the solvation shell at the equatorial cyanide ligands decreases further in a similar fashion. The increase in oxygen atom occurrence above the center of the bipyridyl ligand vanishes after 500 fs. At this point, the oxygen occurrence is visibly increased above and below the *para*-carbon atom atoms. At the end of the simulation, all the features described above are increased. Additional analysis of slices along lines of in the 3D-SDF at the bipyridyl and axial cyanide features over time (see Fig. S6 and Fig. S7), do not indicate any oscillations in these features. The 3D-SDFs are constructed in a way that only couples them to the center-of-mass motion of the solute and not its vibrational degrees of freedom. Therefore, the absence of oscillations, especially in the bipyridyl feature (Fig. S6), strengthen the argument that the oscillations visible the corresponding TD-RDF (see Fig. 4a) originate solely from solute vibrations.

The results show a fast initial response leading to a decrease in hydrogen bonding at the cyanide groups followed by an slow increase in hydrogen bonding at the by-pyridyl ligand. An analysis

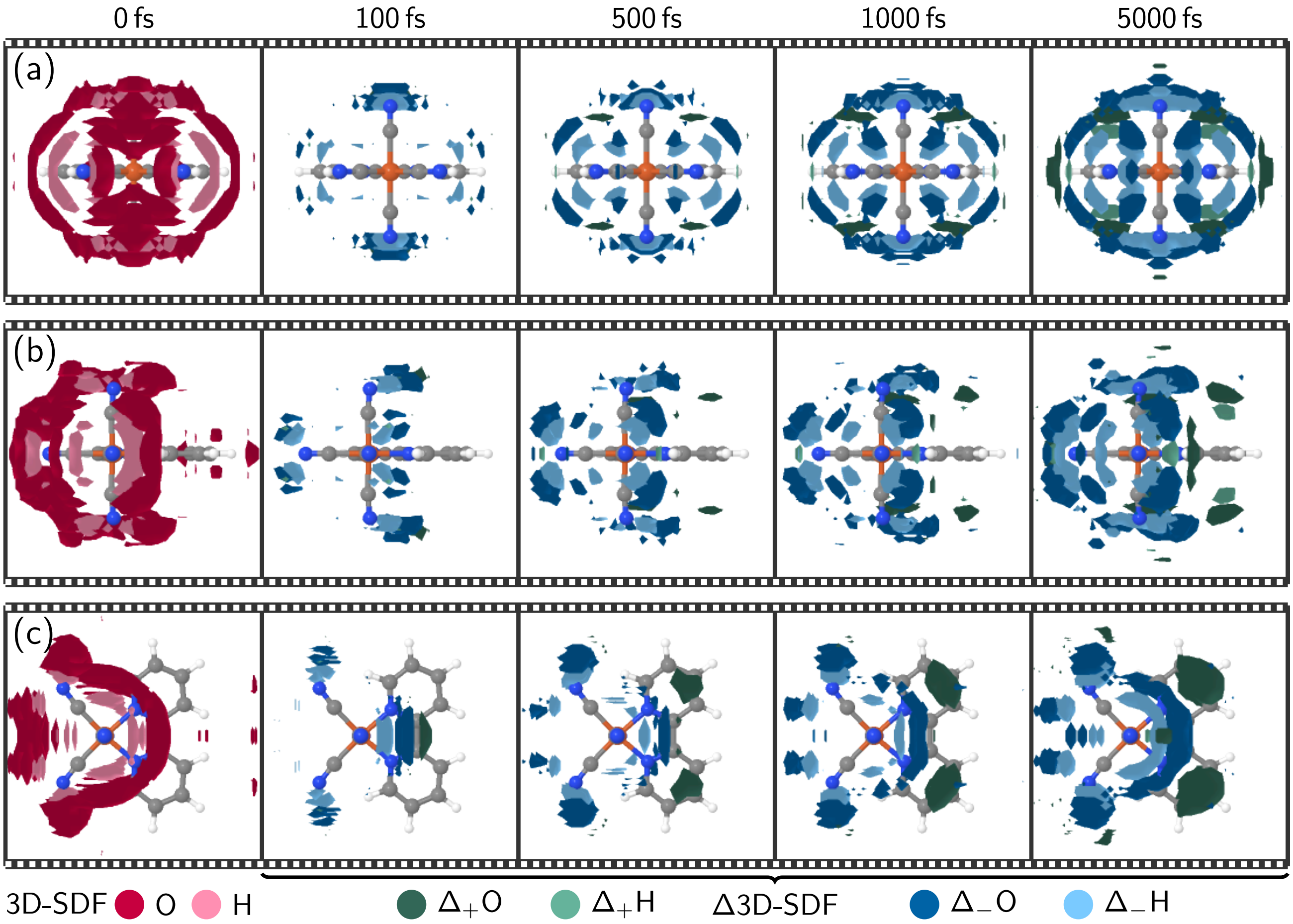

Figure 5: Symmetry adapted three-dimensional spatial distribution functions (3D-SDFs) of water oxygen and hydrogen atoms at $t = 0$ fs and difference 3D-SDFs thereafter. In all panels at $t = 0$ fs spatial regions with an occurrence higher than 2.5 times the average are colored red for oxygen atoms and pink for hydrogen atoms. For the Δ3D-SDFs ($t > 0$ fs), the iso value is set to 0.5 times the average; positive deviations are colored with green colors and negative deviations with blue colors with oxygens in the darker and hydrogens in the lighter shade. Panels (a-c) show different different orientations of the system.

of the time-dependent hydrogen bond counts for N_{CN} and C_{bpy} give respective time constants of $\tau_1 = 14$ fs and $\tau_1 = 32$ fs for the initial response and $\tau_1 = 240$ fs and $\tau_1 = 495$ fs for the secondary response (see Fig. S5). The C_{bpy} hydrogen bonds form because of the long-lived MLCT states and stabilize them further.

An analysis of the solvation shell at the end of the simulation for which only trajectories in the ^{3}MC are used, can be seen in Fig. 6. Because a smaller set of trajectories is used in the analysis, the Δ3D-SDF shown is subject to some degree of noise, which is mostly visible on the edges. We interpret this figure under the assumption that the majority of the trajectories that are in the ^{3}MC state at $t = 5000$ f were in the ^{3}MC states for a long enough time for a stable solvation shell. Analyzing the characters of the respective trajectories shows, that 84% of the trajectories are in the ^{3}MC states for more than 90% of the last 1000 fs, and 88% of them are more than 90% of the last 500 fs. Therefore the presented 3D-SDF depicts the solvation shell for a consistent population of at least 76% ^{3}MC for the last 1000 fs. There are large differences in comparison the solvation shells of the full set of trajectories (see Fig. 5(a-c) at $t = 5000$ fs). The strength of the first solvation shell above and below the bipyridyl ligand is unaffected. At the the equatorial cyanide groups, the solvation shell is decreased in the proximity and increased further away. To a smaller extent, this can also be seen in the Δ3D-SDF at the axial cyanide ligands.

The change in distance of the first solvation shell correlates well with the change is bond length of the cyanide ligands in the ^{3}MC states (see Fig. 3). Overall, the features in the solvation shell of this ^{3}MC dominated subset of trajectories concentrate at the cyanide ligands (Fig. 5). This behavior can be expected, since the solvation shell adapts to the electrostatic potential exerted by the states and is able to stabilize the corresponding states. Additionally, this further highlights differences in the electrostatic potential of the MLCT and MC triplet manifolds. Since the ^{3}MC solvation shell does not show changes around the bipyridyl ligand, it can be expected that this solvation shell does not stabilize the MLCT state and does not lead to a increase in its lifetime.

4 Summary and Conclusions

In this manuscript, we applied the LVC/MM model to simulate the photoactivated dynamical solute–solvent response of $[\mathrm{Fe(CN)_4(bipy)}]^{2-}$ in water. We performed a SHARC[34] simulation with 4473 trajectories on a system comprising more than 16000 atoms for 5 ps for 6 singlet and 7 triplet states. The electronic wave function responds quickly via ISC from the S_3 state to the first three triplet states within 211 fs which matches experimental and other computational results.[30] The time scales of the bifurcation into MC and MLCT triplet states are qualitatively in agreement. The difference in final ratio between the species, as well as the slower time constants for the IC from MLCT to MC triplet and vibrational relaxation from the MC state into the ground state, can be explained. Bond length distributions of the iron center to the ligands reveal accurate average bond lengths for both triplet manifolds but also the absence of anharmonicity and widely spread bond lengths for the equatorial ligands. The latter stabilize the ^{3}MC states and govern the population transfer into and from these states which has been shown experimentally.[29] Time-dependent RDFs do not only show a fast inertial response between 40 and 70 fs but also resolve coherent oscillation in the bipyridyl ligand interaction with the solvent atoms, which has been calculated as well in Ref. 30. We could show that this oscillation solely stems from solute vibration, since these oscillations are consistent with coherent solute motion but cannot be seen in the time-dependent 3D-SDFs. In addition to this, the temporally resolved Δ3D-SDFs show the initial withdrawal of the solvation shell at the cyanide ligands with as fast response time, as well as a slow build up of hydrogen bonds at the bipyridyl ligand. The build-up solvation shell is projected to stabilize the MLCT state. An analysis of a subset of trajectories, showed that a major ^{3}MC population leads to a drastically different solvation shell that does not affect the solvation shell at the bipyridyl ligand. The respective solvation shell can be expected to increase the lifetime of the MC states and while not affecting the MLCT lifetimes.

Overall, the obtained nonadiabatic dynamics of the electronic wave function, solute atoms, solvent atoms, and solute–solvent interactions reflect former experimental and theoretical findings, and extend them. A surface hopping simulation of this scale has not been done before and opens up many possibilities for the investigation of large solvated systems. As demonstrated in this study, the LVC/MM method, if used with an appropriate domain, can help to resolve the intricate interplay of the solute and solvent during photo-activated nonadiabatic dynamics of large molecular systems with many excited states.

Conflicts of interest

The authors declare no conflicts of interest.

Acknowledgements

This research was funded in whole or in part by the Austrian Science Fund FWF (grant DOI 10.55776/I6116) and the Deutsche Forschungsgemeinschaft DFG (TRR234 “CataLight”, Project ID No. 364549901, subproject C3). For open access purposes, the authors have applied a CC-BY public copyright license to any author-accepted manuscript version arising from this submission. The computational results have been achieved in part using the Vienna Scientific Cluster (VSC5). The authors thank the University of Vienna for continuous support, in particular within the framework of the Doctoral School of Chemistry (DoSChem).

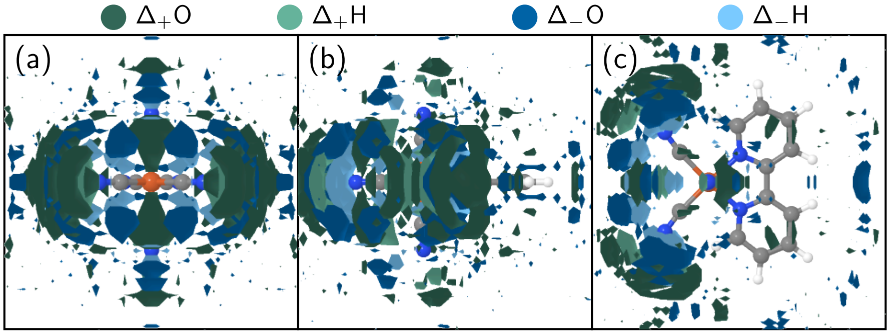

Figure 6: Deviations of in the three-dimensional spatial distribution function for a subset of trajectories with dominant ^{3}MC at $t = 5000$ fs in comparison with the ground-state equilibrium from three different perspectives. The used subset of trajectories had a stable population in the ^{3}MC states of at least 76% for the last 1000 fs. In all panels spatial regions with an occurrence deviating more than 0.5 times the average are colored shown for oxygen atoms and pink for hydrogen atoms; positive deviations are colored with green colors and negative deviations with blue colors with oxygens in the darker and hydrogens in the lighter shade.

References

(1) Venkatraman, R. K.; Orr-Ewing, A. J. Solvent Effects on Ultrafast Photochemical Pathways. *Acc. Chem. Res.* **2021**, *54*, 4383–4394, DOI: `10.1021/acs.accounts.1c00549`.

(2) Kumpulainen, T.; Lang, B.; Rosspeintner, A.; Vauthey, E. Ultrafast Elementary Photochemical Processes of Organic Molecules in Liquid Solution. *Chem. Rev.* **2017**, *117*, 10826–10939, DOI: `10.1021/acs.chemrev.6b00491`.

(3) Jimenez, R.; Fleming, G. R.; Kumar, P. V.; Maroncelli, M. Femtosecond Solvation Dynamics of Water. *Nature* **1994**, *369*, 471–473, DOI: `10.1038/369471a0`.

(4) Dobryakov, A. L.; Kovalenko, S. A.; Weigel, A.; Pérez-Lustres, J. L.; Lange, J.; Müller, A.; Ernsting, N. P. Femtosecond Pump/Supercontinuum-Probe Spectroscopy: Optimized Setup and Signal Analysis for Single-Shot Spectral Referencing. *Rev. Sci. Instrum* **2010**, *81*, 113106, DOI: `10.1063/1.3492897`.

(5) Kovalenko, S. A.; Schanz, R.; Hennig, H.; Ernsting, N. P. Cooling Dynamics of an Optically Excited Molecular Probe in Solution from Femtosecond Broadband Transient Absorption Spectroscopy. *J. Chem. Phys.* **2001**, *115*, 3256–3273, DOI: `10.1063/1.1380696`.

(6) Chen, L. X.; Shelby, M. L.; Lestrange, P. J.; Jackson, N. E.; Haldrup, K.; Mara, M. W.; Stickrath, A. B.; Zhu, D.; Lemke, H.; Chollet, M.; Hoffman, B. M.; Li, X. Imaging Ultrafast Excited State Pathways in Transition Metal Complexes by X-ray Transient Absorption and Scattering Using X-ray Free Electron Laser Source. *Faraday Discuss.* **2016**, *194*, 639–658, DOI: `10.1039/C6FD00083E`.

(7) Gaffney, K. J. Capturing Photochemical and Photophysical Transformations in Iron Complexes with Ultrafast X-ray Spectroscopy and Scattering. *Chem. Sci.* **2021**, *12*, 8010–8025, DOI: `10.1039/D1SC01864G`.

(8) Kunnus, K.; Vacher, M.; Harlang, T. C. B.; Kjær, K. S.; Haldrup, K.; Biasin, E.; van Driel, T. B.; Pápai, M.; Chabera, P.; Liu, Y.; Tatsuno, H.; Timm, C.; Källman, E.; Delcey, M.; Hartsock, R. W.; Reinhard, M. E.; Koroidov, S.; Laursen, M. G.; Hansen, F. B.; Vester, P.; Christensen, M.; Sandberg, L.; Németh, Z.; Szemes, D. S.; Bajnóczi, É.; Alonso-Mori, R.; Glownia, J. M.; Nelson, S.; Sikorski, M.; Sokaras, D.; Lemke, H. T.; Canton, S. E.; Møller, K. B.; Nielsen, M. M.; Vankó, G.; Wärnmark, K.; Sundström, V.; Persson, P.; Lundberg, M.; Uh-

lig, J.; Gaffney, K. J. Vibrational Wavepacket Dynamics in Fe Carbene Photosensitizer Determined with Femtosecond X-ray Emission and Scattering. *Nat. Commun.* **2020**, *11*, 634, DOI: `10.1038/s41467-020-14468-w`.

(9) Vester, P.; Kubicek, K.; Alonso-Mori, R.; Assefa, T.; Biasin, E.; Christensen, M.; Dohn, A. O.; van Driel, T. B.; Galler, A.; Gawelda, W.; Harlang, T. C. B.; Henriksen, N. E.; Kjær, K. S.; Kuhlman, T. S.; Németh, Z.; Nurekeyev, Z.; Pápai, M.; Rittman, J.; Vankó, G.; Yavas, H.; Zederkof, D. B.; Bergmann, U.; Nielsen, M. M.; Møller, K. B.; Haldrup, K.; Bressler, C. Tracking Structural Solvent Reorganization and Recombination Dynamics Following E- Photoabstraction from Aqueous I- with Femtosecond X-Ray Spectroscopy and Scattering. *J. Chem. Phys.* **2022**, *157*, 224201, DOI: `10.1063/5.0107224`.

(10) Wang, C.; Waters, M. D. J.; Zhang, P.; Suchan, J.; Svoboda, V.; Luu, T. T.; Perry, C.; Yin, Z.; Slavíček, P.; Wörner, H. J. Different Timescales during Ultrafast Stilbene Isomerization in the Gas and Liquid Phases Revealed Using Time-Resolved Photoelectron Spectroscopy. *Nat. Chem.* **2022**, *14*, 1126–1132, DOI: `10.1038/s41557-022-01012-0`.

(11) Riley, J. W.; Wang, B.; Woodhouse, J. L.; Assmann, M.; Worth, G. A.; Fielding, H. H. Unravelling the Role of an Aqueous Environment on the Electronic Structure and Ionization of Phenol Using Photoelectron Spectroscopy. *J. Phys. Chem. Lett.* **2018**, *9*, 678–682, DOI: `10.1021/acs.jpclett.7b03310`.

(12) Kjær, K. S.; van Driel, T. B.; Kehres, J.; Haldrup, K.; Khakhulin, D.; Bechgaard, K.; Cammarata, M.; Wulff, M.; Sørensen, T. J.; Nielsen, M. M. Introducing a Standard Method for Experimental Determination of the Solvent Response in Laser Pump, X-ray Probe Time-Resolved Wide-Angle X-ray Scattering Experiments on Systems in Solution. *Phys. Chem. Chem. Phys.* **2013**, *15*, 15003–15016, DOI: `10.1039/C3CP50751C`.

(13) Nimmrich, A.; Panman, M. R.; Berntsson, O.; Biasin, E.; Niebling, S.; Petersson, J.; Hoernke, M.; Björling, A.; Gustavsson, E.; van Driel, T. B.; Dohn, A. O.; Laursen, M.; Zederkof, D. B.; Tono, K.; Katayama, T.; Owada, S.; Nielsen, M. M.; Davidsson, J.; Uhlig, J.; Hub, J. S.; Haldrup, K.; Westenhoff, S. Solvent-Dependent Structural Dynamics in the Ultrafast Photodissociation Reaction of Triiodide Observed with Time-Resolved X-ray Solution Scattering. *J. Am. Chem. Soc.* **2023**, *145*, 15754–15765, DOI: `10.1021/jacs.3c00484`.

(14) Kim, K. H.; Kim, J. G.; Oang, K. Y.; Kim, T. W.; Ki, H.; Jo, J.; Kim, J.; Sato, T.; Nozawa, S.; Adachi, S.-i.; Ihee, H. Femtosecond X-ray Solution Scattering Reveals That Bond Formation Mechanism of a Gold Trimer Complex Is Independent of Excitation Wavelength. *Struct. Dyn.* **2016**, *3*, 043209, DOI: `10.1063/1.4948516`.

(15) Katayama, T.; Choi, T.-K.; Khakhulin, D.; Dohn, A. O.; Milne, C. J.; Vankó, G.; Németh, Z.; Lima, F. A.; Szlachetko, J.; Sato, T.; Nozawa, S.; Adachi, S.-i.; Yabashi, M.; Penfold, T. J.; Gawelda, W.; Levi, G. Atomic-Scale Observation of Solvent Reorganization Influencing Photoinduced Structural Dynamics in a Copper Complex Photosensitizer. *Chem. Sci.* **2023**, *14*, 2572–2584, DOI: `10.1039/D2SC06600A`.

(16) Haldrup, K.; Gawelda, W.; Abela, R.; Alonso-Mori, R.; Bergmann, U.; Bordage, A.; Cammarata, M.; Canton, S. E.; Dohn, A. O.; van Driel, T. B.; Fritz, D. M.; Galler, A.; Glatzel, P.; Harlang, T.; Kjær, K. S.; Lemke, H. T.; Møller, K. B.; Németh, Z.; Pápai, M.; Sas, N.; Uhlig, J.; Zhu, D.; Vankó, G.; Sundström, V.; Nielsen, M. M.; Bressler, C. Observing Solvation Dynamics with Simultaneous Femtosecond X-ray Emission Spectroscopy and X-ray Scattering. *J. Phys. Chem. B* **2016**, *120*, 1158–1168, DOI: `10.1021/acs.jpcb.5b12471`.

(17) Pigliucci, A.; Duvanel, G.; Daku, L. M. L.; Vauthey, E. Investigation of the Influence

of Solute-Solvent Interactions on the Vibrational Energy Relaxation Dynamics of Large Molecules in Liquids. *J. Phys. Chem. A* **2007**, *111*, 6135–6145, DOI: `10.1021/jp069010y`.

(18) Linert, W.; Gutmann, V. Structural and Electronic Responses of Coordination Compounds to Changes in the Molecule and Molecular Environment. *Coord. Chem. Rev.* **1992**, *117*, 159–183, DOI: `10.1016/0010-8545(92)80023-K`.

(19) Zobel, J. P.; González, L. The Quest to Simulate Excited-State Dynamics of Transition Metal Complexes. *JACS Au* **2021**, *1*, 1116–1140, DOI: `10.1021/jacsau.1c00252`.

(20) Chergui, M. Ultrafast Photophysics of Transition Metal Complexes. *Acc. Chem. Res.* **2015**, *48*, 801–808, DOI: `10.1021/ar500358q`.

(21) Wenger, O. S. Is Iron the New Ruthenium? *Chem. – Eur. J.* **2019**, *25*, 6043–6052, DOI: `10.1002/chem.201806148`.

(22) Damrauer, N. H.; Cerullo, G.; Yeh, A.; Boussie, T. R.; Shank, C. V.; McCusker, J. K. Femtosecond Dynamics of Excited-State Evolution in [Ru(Bpy)3]2+. *Science* **1997**, *275*, 54–57, DOI: `10.1126/science.275.5296.54`.

(23) Brown, D. G.; Sanguantrakun, N.; Schulze, B.; Schubert, U. S.; Berlinguette, C. P. Bis(Tridentate) Ruthenium–Terpyridine Complexes Featuring Microsecond Excited-State Lifetimes. *J. Am. Chem. Soc.* **2012**, *134*, 12354–12357, DOI: `10.1021/ja3039536`.

(24) Monat, J. E.; McCusker, J. K. Femtosecond Excited-State Dynamics of an Iron(II) Polypyridyl Solar Cell Sensitizer Model. *J. Am. Chem. Soc.* **2000**, *122*, 4092–4097, DOI: `10.1021/ja992436o`.

(25) Nozawa, S.; Sato, T.; Chollet, M.; Ichiyanagi, K.; Tomita, A.; Fujii, H.; Adachi, S.-i.; Koshihara, S.-y. Direct Probing of Spin State Dynamics Coupled with Electronic and Structural Modifications by Picosecond Time-Resolved XAFS. *J. Am. Chem. Soc.* **2010**, *132*, 61–63, DOI: `10.1021/ja907460b`.

(26) Liu, Y.; Harlang, T.; Canton, S. E.; Chábera, P.; Suárez-Alcántara, K.; Fleckhaus, A.; Vithanage, D. A.; Göransson, E.; Corani, A.; Lomoth, R.; Sundström, V.; Wärnmark, K. Towards Longer-Lived Metal-to-Ligand Charge Transfer States of Iron(II) Complexes: An N-heterocyclic Carbene Approach. *Chem. Commun.* **2013**, *49*, 6412–6414, DOI: `10.1039/C3CC43833C`.

(27) Harlang, T. C. B.; Liu, Y.; Gordivska, O.; Fredin, L. A.; Ponseca, C. S.; Huang, P.; Chábera, P.; Kjaer, K. S.; Mateos, H.; Uhlig, J.; Lomoth, R.; Wallenberg, R.; Styring, S.; Persson, P.; Sundström, V.; Wärnmark, K. Iron Sensitizer Converts Light to Electrons with 92% Yield. *Nature Chem* **2015**, *7*, 883–889, DOI: `10.1038/nchem.2365`.

(28) Duchanois, T.; Etienne, T.; Cebrián, C.; Liu, L.; Monari, A.; Beley, M.; Assfeld, X.; Haacke, S.; Gros, P. C. An Iron-Based Photosensitizer with Extended Excited-State Lifetime: Photophysical and Photovoltaic Properties. *Eur. J. Inorg. Chem.* **2015**, *2015*, 2469–2477, DOI: `10.1002/ejic.201500142`.

(29) Kjær, K. S.; Kunnus, K.; Harlang, T. C. B.; Driel, T. B. V.; Ledbetter, K.; Hartsock, R. W.; Reinhard, M. E.; Koroidov, S.; Li, L.; Laursen, M. G.; Biasin, E.; Hansen, F. B.; Vester, P.; Christensen, M.; Haldrup, K.; Nielsen, M. M.; Chabera, P.; Liu, Y.; Tatsuno, H.; Timm, C.; Uhlig, J.; Sundstöm, V.; Németh, Z.; Szemes, D. S.; Bajnóczi, É.; Vankó, G.; Alonso-Mori, R.; Glownia, J. M.; Nelson, S.; Sikorski, M.; Sokaras, D.; Lemke, H. T.; Canton, S. E.; Wärnmark, K.; Persson, P.; Cordones, A. A.; Gaffney, K. J. Solvent Control of Charge Transfer Excited State Relaxation Pathways in [Fe(2,2′-Bipyridine)(CN)4]2-. *Phys. Chem. Chem. Phys.* **2018**, *20*, 4238–4249, DOI: `10.1039/C7CP07838B`.

(30) Zederkof, D. B.; Møller, K. B.; Nielsen, M. M.; Haldrup, K.; González, L.; Mai, S. Resolving Femtosecond Solvent

Reorganization Dynamics in an Iron Complex by Nonadiabatic Dynamics Simulations. *J. Am. Chem. Soc.* **2022**, *144*, 12861–12873, DOI: `10.1021/jacs.2c04505`.

(31) Zhang, W.; S. Kjær, K.; Alonso-Mori, R.; Bergmann, U.; Chollet, M.; A. Fredin, L.; G. Hadt, R.; W. Hartsock, R.; Harlang, T.; Kroll, T.; Kubiček, K.; T. Lemke, H.; W. Liang, H.; Liu, Y.; M. Nielsen, M.; Persson, P.; S. Robinson, J.; I. Solomon, E.; Sun, Z.; Sokaras, D.; van Driel, T. B.; Weng, T.-C.; Zhu, D.; Wärnmark, K.; Sundström, V.; J. Gaffney, K. Manipulating Charge Transfer Excited State Relaxation and Spin Crossover in Iron Coordination Complexes with Ligand Substitution. *Chem. Sci.* **2017**, *8*, 515–523, DOI: `10.1039/C6SC03070J`.

(32) Kunnus, K.; Li, L.; J. Titus, C.; Jun Lee, S.; E. Reinhard, M.; Koroidov, S.; S. Kjær, K.; Hong, K.; Ledbetter, K.; B. Doriese, W.; C. O'Neil, G.; S. Swetz, D.; N. Ullom, J.; Li, D.; Irwin, K.; Nordlund, D.; A. Cordones, A.; J. Gaffney, K. Chemical Control of Competing Electron Transfer Pathways in Iron Tetracyano-Polypyridyl Photosensitizers. *Chem. Sci.* **2020**, *11*, 4360–4373, DOI: `10.1039/C9SC06272F`.

(33) Mai, S.; Marquetand, P.; González, L. Nonadiabatic Dynamics: The SHARC Approach. *WIREs Comput. Mol. Sci.* **2018**, *8*, e1370, DOI: `10.1002/wcms.1370`.

(34) Mai, S.; Avagliano, D.; Heindl, M.; Marquetand, P.; Menger, M. F. S. J.; Oppel, M.; Plasser, F.; Polonius, S.; Ruckenbauer, M.; Shu, Y.; Truhlar, D. G.; Zhang, L.; Zobel, P.; González, L. SHARC3.0: Surface Hopping Including Arbitrary Couplings — Program Package for Non-Adiabatic Dynamics. `https://sharc-md.org/`, 2023.

(35) Polonius, S.; Zhuravel, O.; Bachmair, B.; Mai, S. LVC/MM: A Hybrid Linear Vibronic Coupling/Molecular Mechanics Model with Distributed Multipole-Based Electrostatic Embedding for Highly Efficient Surface Hopping Dynamics in Solution. *J. Chem. Theory Comput.* **2023**, *19*, 7171–7186, DOI: `10.1021/acs.jctc.3c00805`.

(36) Polonius, S.; Lehrner, D.; González, L.; Mai, S. Resolving Photoinduced Femtosecond Three-Dimensional Solute–Solvent Dynamics through Surface Hopping Simulations. *J. Chem. Theory Comput.* **2024**, *20*, 4738–4750, DOI: `10.1021/acs.jctc.4c00169`.

(37) Salomon, O.; Reiher, M.; Hess, B. A. Assertion and Validation of the Performance of the B3LYP⋆ Functional for the First Transition Metal Row and the G2 Test Set. *J. Chem. Phys.* **2002**, *117*, 4729–4737, DOI: `10.1063/1.1493179`.

(38) Frisch, M. J.; Trucks, G. W.; Schlegel, H. B.; Scuseria, G. E.; Robb, M. A.; Cheeseman, J. R.; Scalmani, G.; Barone, V.; Petersson, G. A.; Nakatsuji, H.; Li, X.; Caricato, M.; Marenich, A. V.; Bloino, J.; Janesko, B. G.; Gomperts, R.; Mennucci, B.; Hratchian, H. P.; Ortiz, J. V.; Izmaylov, A. F.; Sonnenberg, J. L.; Williams-Young, D.; Ding, F.; Lipparini, F.; Egidi, F.; Goings, J.; Peng, B.; Petrone, A.; Henderson, T.; Ranasinghe, D.; Zakrzewski, V. G.; Gao, J.; Rega, N.; Zheng, G.; Liang, W.; Hada, M.; Ehara, M.; Toyota, K.; Fukuda, R.; Hasegawa, J.; Ishida, M.; Nakajima, T.; Honda, Y.; Kitao, O.; Nakai, H.; Vreven, T.; Throssell, K.; Montgomery, J. A., Jr.; Peralta, J. E.; Ogliaro, F.; Bearpark, M. J.; Heyd, J. J.; Brothers, E. N.; Kudin, K. N.; Staroverov, V. N.; Keith, T. A.; Kobayashi, R.; Normand, J.; Raghavachari, K.; Rendell, A. P.; Burant, J. C.; Iyengar, S. S.; Tomasi, J.; Cossi, M.; Millam, J. M.; Klene, M.; Adamo, C.; Cammi, R.; Ochterski, J. W.; Martin, R. L.; Morokuma, K.; Farkas, O.; Foresman, J. B.; Fox, D. J. Gaussian 16 Revision C.01. 2016.

(39) Proppe, J.; Gugler, S.; Reiher, M. Gaussian Process-Based Refinement of Dispersion Corrections. *J. Chem. Theory Comput.* **2019**, *15*, 6046–6060, DOI: `10.1021/acs.jctc.9b00627`.

(40) Neese, F. Software Update: The ORCA Program System—Version 5.0. *WIREs Comput. Mol. Sci.* **2022**, *12*, e1606, DOI: `10.1002/wcms.1606`.

(41) Fumanal, M.; Plasser, F.; Mai, S.; Daniel, C.; Gindensperger, E. Interstate Vibronic Coupling Constants between Electronic Excited States for Complex Molecules. *J. Chem. Phys.* **2018**, *148*, 124119, DOI: `10.1063/1.5022760`.

(42) Plasser, F. TheoDORE: A Toolbox for a Detailed and Automated Analysis of Electronic Excited State Computations. *J. Chem. Phys.* **2020**, *152*, 084108, DOI: `10.1063/1.5143076`.

(43) Köppel, H.; Domcke, W.; Cederbaum, L. S. Theory of Vibronic Coupling in Linear Molecules. *J. Chem. Phys.* **1981**, *74*, 2945–2968, DOI: `10.1063/1.441417`.

(44) Zobel, J. P.; Heindl, M.; Plasser, F.; Mai, S.; González, L. Surface Hopping Dynamics on Vibronic Coupling Models. *Acc. Chem. Res.* **2021**, *54*, 3760–3771, DOI: `10.1021/acs.accounts.1c00485`.

(45) Abedi, M.; Levi, G.; Zederkof, D. B.; Henriksen, N. E.; Pápai, M.; Møller, K. B. Excited-State Solvation Structure of Transition Metal Complexes from Molecular Dynamics Simulations and Assessment of Partial Atomic Charge Methods. *Phys. Chem. Chem. Phys.* **2019**, *21*, 4082–4095, DOI: `10.1039/c8cp06567e`.

(46) Mai, S.; Gattuso, H.; Monari, A.; González, L. Novel Molecular-Dynamics-Based Protocols for Phase Space Sampling in Complex Systems. *Front. Chem.* **2018**, *6*, DOI: `10.3389/fchem.2018.00495`.

(47) Case, D.; Aktulga, H.; Belfon, K.; Ben-Shalom, I.; Berryman, J.; Brozell, S.; Cerutti, D.; Cheatham III, T.; Cisneros, G.; Cruzeiro, V.; Darden, T.; Forouzesh, N.; Giambaşu, G.; Giese, T.; Gilson, M.; Gohlke, H.; Goetz, A.; Harris, J.; Izadi, S.; Izmailov, S.; Kasavajhala, K.; Kaymak, M.; King, E.; Kovalenko, A.; Kurtzman, T.; Lee, T.; Li, P.; Lin, C.; Liu, J.; Luchko, T.; Luo, R.; Machado, M.; Man, V.; Manathunga, M.; Merz, K.; Miao, Y.; Mikhailovskii, O.; Monard, G.; Nguyen, H.; O'Hearn, K.; Onufriev, A.; Pan, F.; Pantano, S.; Qi, R.; Rahnamoun, A.; Roe, D.; Roitberg, A.; Sagui, C.; Schott-Verdugo, S.; Shajan, A.; Shen, J.; Simmerling, C.; Skrynnikov, N.; Smith, J.; Swails, J.; Walker, R.; Wang, J.; Wang, J.; Wei, H.; Wu, X.; Wu, Y.; Xiong, Y.; Xue, Y.; York, D.; Zhao, S.; Zhu, Q.; Kollman, P. Amber 2023. `https://ambermd.org/index.php`, 2023.

(48) Wu, Y.; Tepper, H. L.; Voth, G. A. Flexible Simple Point-Charge Water Model with Improved Liquid-State Properties. *J. Chem. Phys.* **2006**, *124*, 024503, DOI: `10.1063/1.2136877`.

(49) Granucci, G.; Persico, M.; Toniolo, A. Direct Semiclassical Simulation of Photochemical Processes with Semiempirical Wave Functions. *J. Chem. Phys.* **2001**, *114*, 10608–10615, DOI: `10.1063/1.1376633`.

(50) Plasser, F.; Granucci, G.; Pittner, J.; Barbatti, M.; Persico, M.; Lischka, H. Surface Hopping Dynamics Using a Locally Diabatic Formalism: Charge Transfer in the Ethylene Dimer Cation and Excited State Dynamics in the 2-Pyridone Dimer. *J. Chem. Phys.* **2012**, *137*, 22A514, DOI: `10.1063/1.4738960`.

(51) Granucci, G.; Persico, M.; Zoccante, A. Including Quantum Decoherence in Surface Hopping. *J. Chem. Phys.* **2010**, *133*, 134111, DOI: `10.1063/1.3489004`.

(52) Nangia, S.; Jasper, A. W.; Miller, T. F., III; Truhlar, D. G. Army Ants Algorithm for Rare Event Sampling of Delocalized Nonadiabatic Transitions by Trajectory Surface Hopping and the Estimation of Sampling Errors by the Bootstrap Method. *J. Chem. Phys.* **2004**, *120*, 3586–3597, DOI: `10.1063/1.1641019`.

(53) Scott, D. W. *Multivariate Density Estimation:*

Theory, Practice, and Visualization; John Wiley & Sons, 2015.

(54) Narsky, I.; Porter, F. C. *Statistical Analysis Techniques in Particle Physics: Fits, Density Estimation and Supervised Learning*; John Wiley & Sons, 2013.

(55) Gawelda, W.; Pham, V.-T.; Benfatto, M.; Zaushitsyn, Y.; Kaiser, M.; Grolimund, D.; Johnson, S. L.; Abela, R.; Hauser, A.; Bressler, C.; Chergui, M. Structural Determination of a Short-Lived Excited Iron(II) Complex by Picosecond X-Ray Absorption Spectroscopy. *Phys. Rev. Lett.* **2007**, *98*, 057401, DOI: `10.1103/PhysRevLett.98.057401`.

(56) Biasin, E.; Fox, Z. W.; Andersen, A.; Ledbetter, K.; Kjær, K. S.; Alonso-Mori, R.; Carlstad, J. M.; Chollet, M.; Gaynor, J. D.; Glownia, J. M.; Hong, K.; Kroll, T.; Lee, J. H.; Liekhus-Schmaltz, C.; Reinhard, M.; Sokaras, D.; Zhang, Y.; Doumy, G.; March, A. M.; Southworth, S. H.; Mukamel, S.; Gaffney, K. J.; Schoenlein, R. W.; Govind, N.; Cordones, A. A.; Khalil, M. Direct Observation of Coherent Femtosecond Solvent Reorganization Coupled to Intramolecular Electron Transfer. *Nat. Chem.* **2021**, *13*, 343–349, DOI: `10.1038/s41557-020-00629-3`.

Supporting Information: Three-Dimensional Nonadiabatic Solvent Reorganization Dynamics of an Iron Complex

Severin Polonius,[†,‡] Leticia González,[*,†] and Sebastian Mai[*,†]

†*Institute of Theoretical Chemistry, Faculty of Chemistry, University of Vienna, Währinger Str. 17, 1090 Vienna, Austria.*
‡*University of Vienna, Vienna Doctoral School in Chemistry (DoSChem), Währinger Str. 42, 1090 Vienna, Austria.*

E-mail: leticia.gonzalez@univie.ac.at; sebastian.mai@univie.ac.at

Contents

S1 Shifts in Excitation Energy from Solvent Effects S-2

S2 Double Counting of Solvent Interaction S-3

S3 Improvement of LVC Model with State-Specific Frequency Shifts S-4

S4 Time-Dependent Excitation Energies S-5

S5 Bond length Distributions after Excitation S-6

S6 Hydrogen Bond Analysis S-7

S7 Time-Dependent 3D-SDF Slices S-8

References S-10

S1 Shifts in Excitation Energy from Solvent Effects

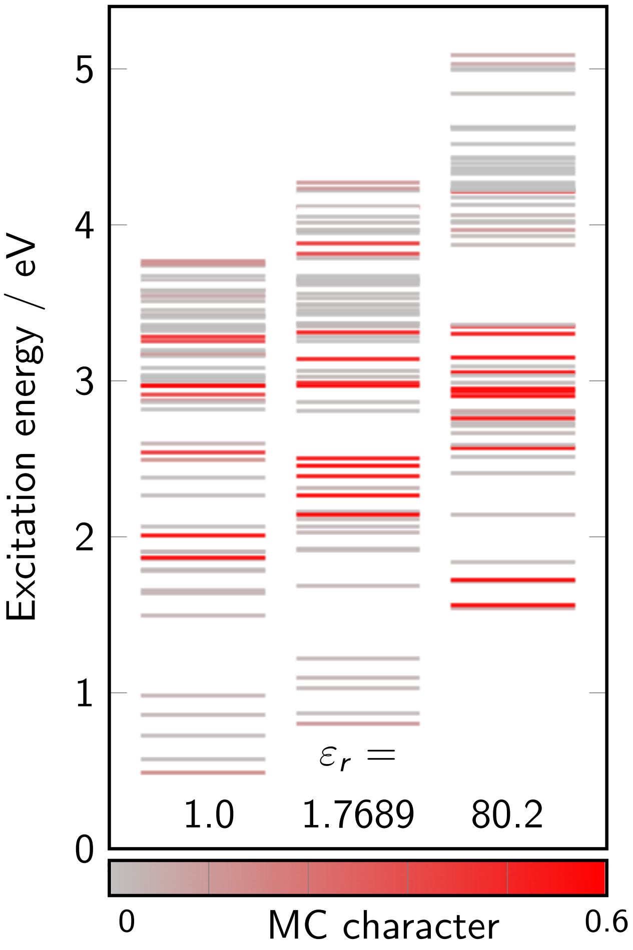

Figure S1: Excitation energies of $[\mathrm{FeCN_4bpy}]^{2+}$ including implicit solvation with different dielectric constants ε_r. The shade indicated the metal-centered character of the respective excited state.

S2 Double Counting of Solvent Interaction

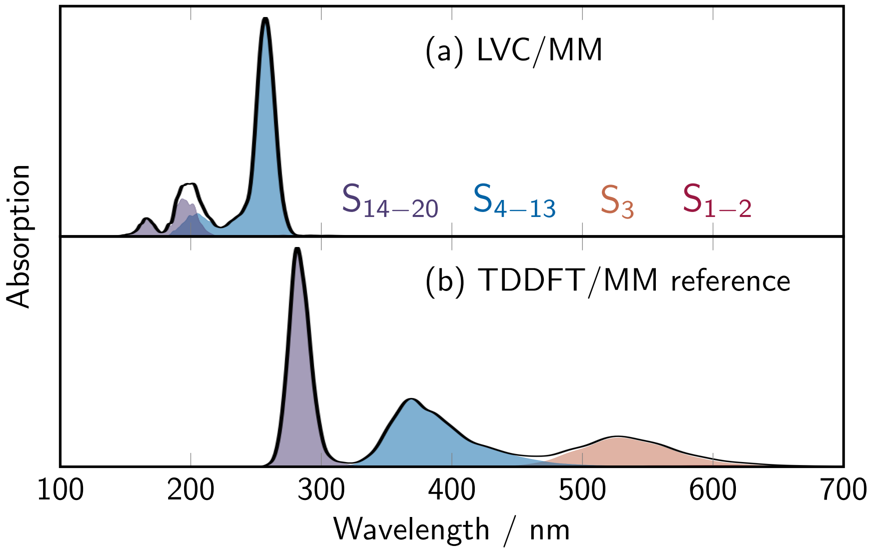

Figure S2: Spectrum of explicitely solvated [FeCN$_4$bpy]$^{2+}$ on 500 initial conditions. Panel (a) shows the results for a LVC/MM model that was parametrized with implicit solvation ($\varepsilon_r = 80.2$). Panel (b) shows the corresponding TDDFT/MM reference spectrum on the same initial conditions. The different absorption bands are highlighted by collecting the singlet states as they appear in the reference spectrum: S_1 and S_2 in red, S_3 in orange, S_4 to S_{13} in blue and S_{14} to S_{20} in purple. The initial conditions are provided by the authors of S1.

S3 Improvement of LVC Model with State-Specific Frequency Shifts

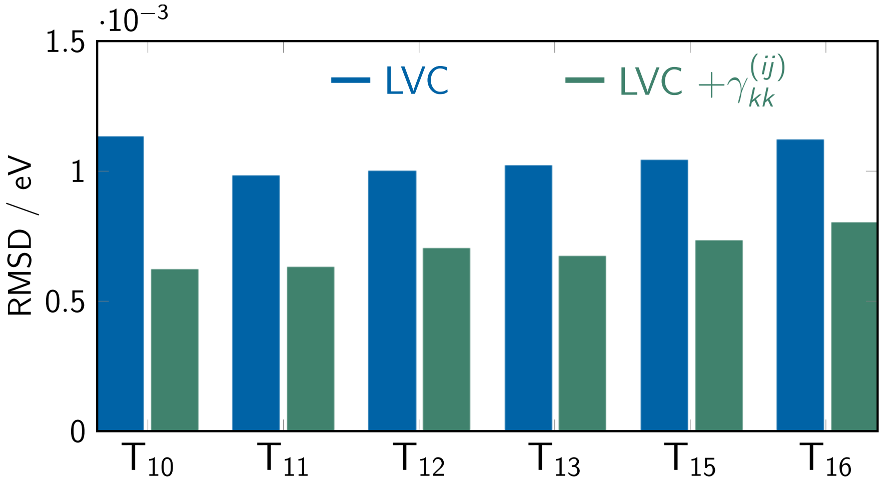

Figure S3: Root-mean-square deviations (RMSDs) of the excitation energies of triplet states with major metal-centered character computed with LVC models against the TDDFT reference. The RMSDs are compared for the LVC model with state-specific frequency shifts ($\gamma_{kk}^{(ii)}$) in green and without them in blue. The RMSDs are calculated from scans ($Q_k \in [-0.5, 0.5]$) of selected normal modes (11, 15, 19, 20, 31, 32, 47, and 71) that affect bond length between the iron center and equatorial ligands of $[\mathrm{FeCN_4bpy}]^{2+}$.

S4 Time-Dependent Excitation Energies

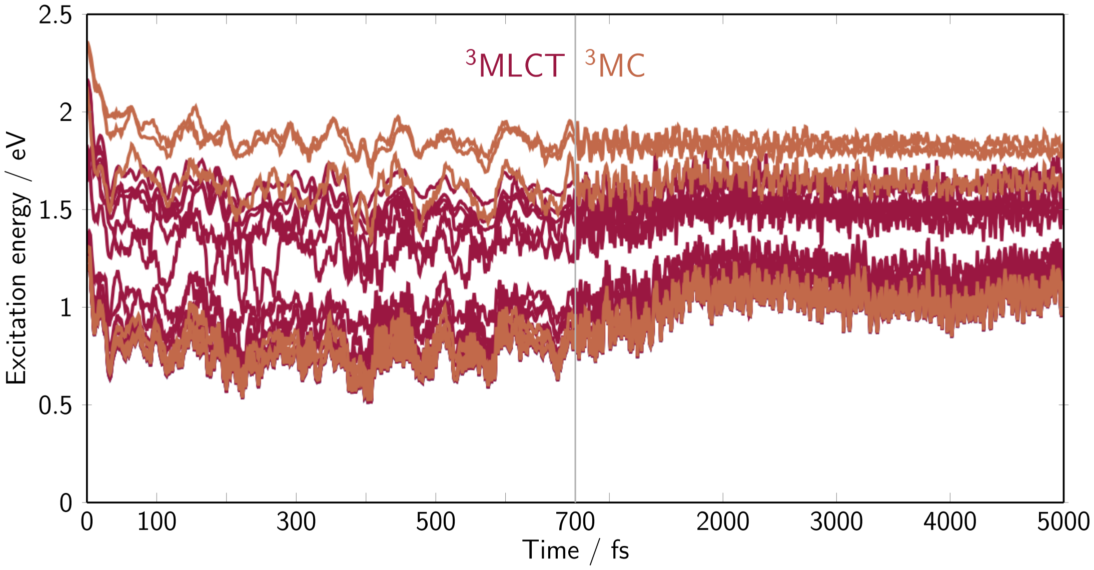

Figure S4: Average diabatic excitation energies of metal-centered (MC) and metal-to-ligand-charge-transfer (MLCT) triplet states in orange and red over time.

S5 Bond length Distributions after Excitation

Table S1: Root-mean-square values of positive deviations (RMSD_+) and negative deviations (RMSD_-) from the mean bond length value after excitation shown in Fig. 3.

	MLCT		MC	
	RMSD_+	RMSD_-	RMSD_+	RMSD_-
Fe–$\mathrm{N_{bipy}}$	0.069	0.070	0.080	0.082
Fe–$\mathrm{CN_{ax}}$	0.066	0.064	0.065	0.063
Fe–$\mathrm{CN_{eq}}$	0.063	0.062	0.070	0.073

S6 Hydrogen Bond Analysis

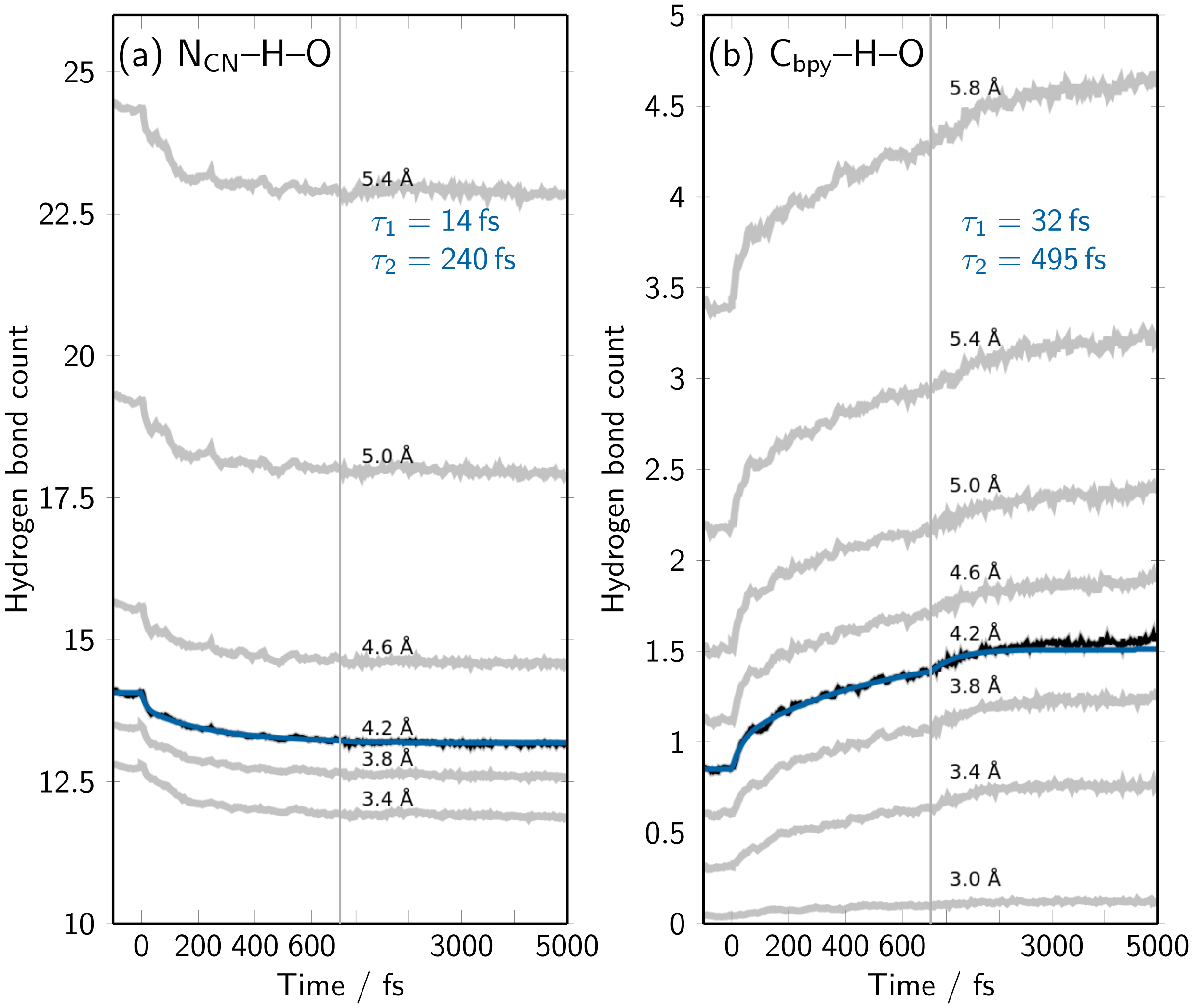

Figure S5: Time-dependent hydrogen bond counts at with different distance thresholds. Panel (a) shows the hydrogen bond counts for the cyanide nitrogen atoms and panel (b) the counts for the bi-pyridyl carbon atoms. A bi-exponential fit for the black curve (blue line) results in the two time constants given in the plot.

S7 Time-Dependent 3D-SDF Slices

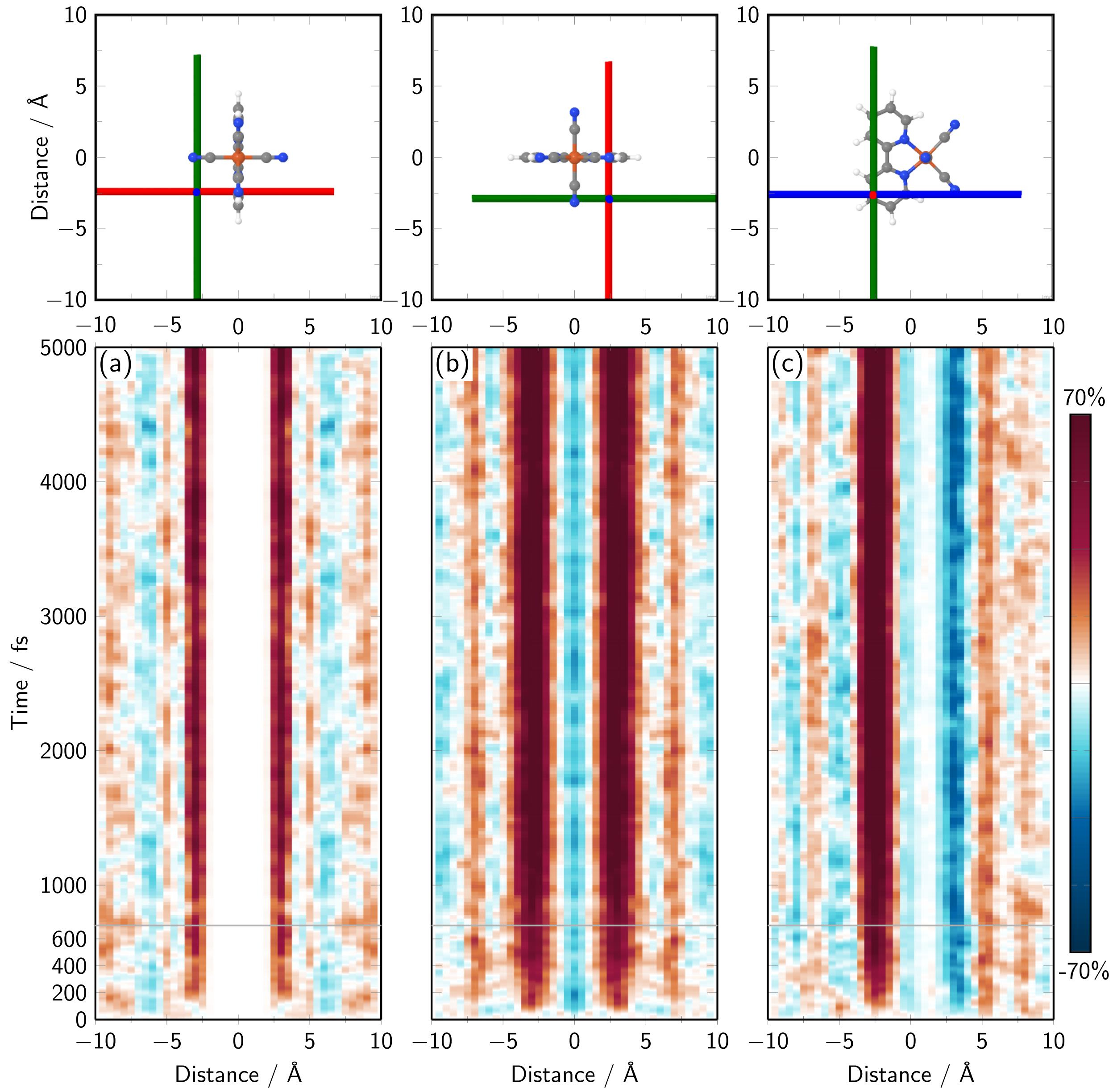

Figure S6: Time-dependent 3D-SDF values on line slices in different Cartesian directions with origin close to the bi-pyridyl ligand. Panels (a-c) show the different directions as depicted in the respective graphics above.

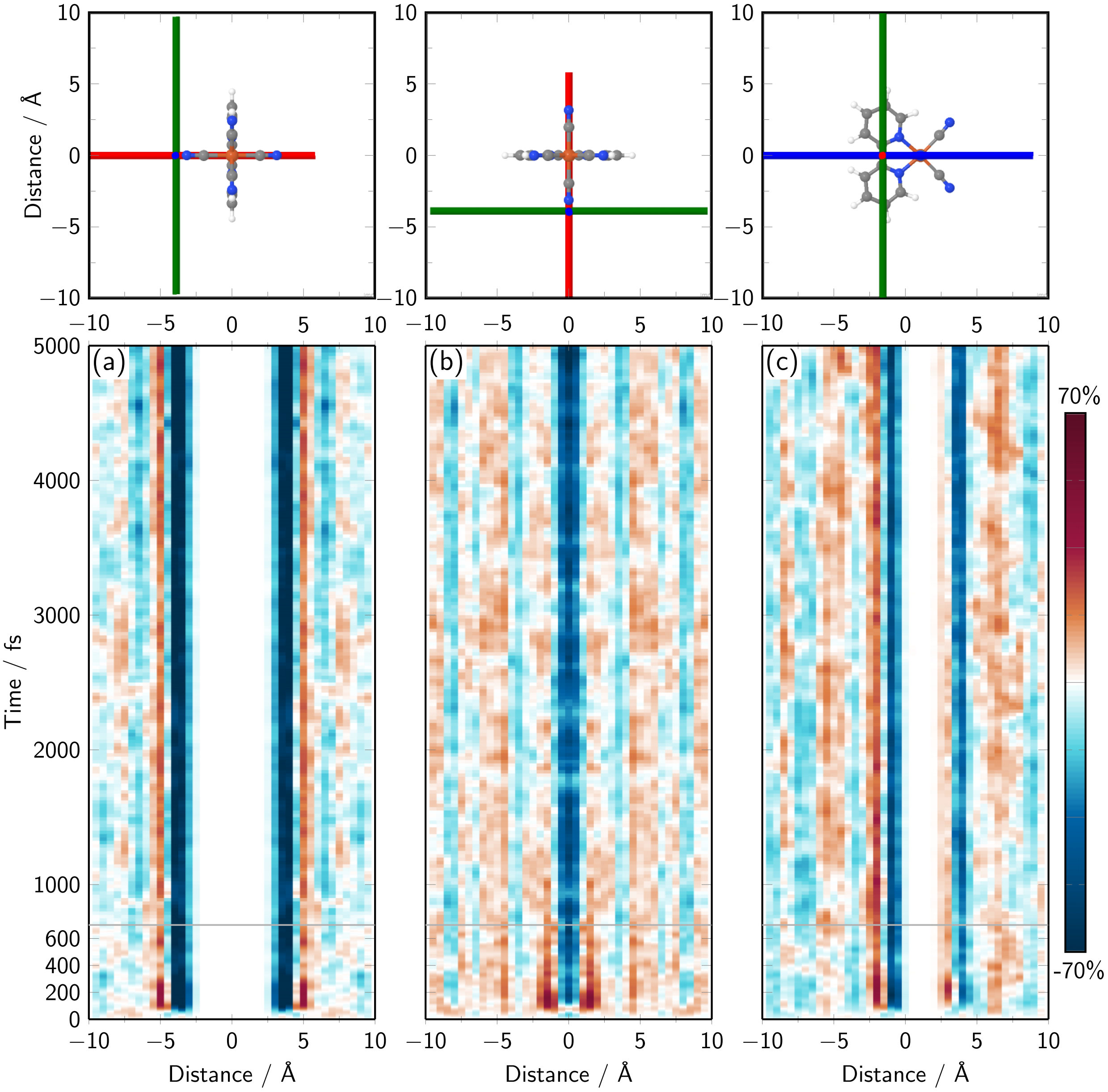

Figure S7: Time-dependent 3D-SDF values on line slices in different Cartesian directions with origin close to one axial cyanide ligand. Panels (a-c) show the different directions as depicted in the respective graphics above.

References

(S1) Zederkof, D. B.; Møller, K. B.; Nielsen, M. M.; Haldrup, K.; González, L.; Mai, S. Resolving Femtosecond Solvent Reorganization Dynamics in an Iron Complex by Nonadiabatic Dynamics Simulations. *J. Am. Chem. Soc.* **2022**, *144*, 12861–12873.

ACKNOWLEDGMENTS

I want to express my gratitude Prof. Leticia González for giving me the opportunity to grow as a scientist, software developer, and person under her supervision. I am especially grateful for the freedom, trust, reassurance, her availability for all kinds of questions, and the support she gave me, especially as my project took off in a direction all of us did not anticipate.

Before starting my PhD, I wanted and knew that I would thrive under close supervision, and I got everything I wished for and more from Dr. Sebastian Mai. He is not only knowledgeable in everything that is quantum chemistry but also deeply cares about his students. I will always admire his unyielding patience in explaining things over and over whilst fighting with my premature stubbornness. With this quality alone, I am convinced that he will be a great father, and I wish him and his wife all the best. Speaking of Katrin Mai, she is not only fun to be around, but I also want to thank her for making Mondays sweeter with her amazing cake creations.

Another person without my work—in fact no ones work—would have been possible is Dr. Markus Oppel. I want to thank him for maintaining and extending the best file-system and compute-cluster, which I know of, and for deepening my interest in high-performance computing and software development. I shared a lot of funny moments with Denis Hoxha, especially when I made him install yet another special program that I "really desperately" needed. He is a great guy and was always there, when I needed help. Monika Schett did not only guide me through the bureaucratic madhouse the university can often be, but also was a source of support in all situations. I am very thankful for her and to know that she is on our side. In the chaotic times in which I started the PhD, Sophie Gröber helped me with all non-scientific problems of starting in a new group, university and city—starting from alleviating the remnants of former member in my office to sharing advice that influences me until this day.

From the unofficial "SHARC" office, I want to thank my first office-mate, Dr. Moritz Heindl, who introduced me to amazing board games, showed me how to give engaging and educational presentations, and demonstrated a way to keep ones sanity while writing the thesis. Lorenz Grünewald has been my next and longest office-mate, and I will always have fond memories of our time together which were full of song, memes, Austrian "Grant", politics, and his scientific advice as a physicist. With him, there never was a boring day in the office. While not being there for the same amount of time as Lorenz, Rahul Jingar did not take long to win me over with the power of anime, music, and memes. It is always good to have people that share your odd obsessions, meet for One Piece binge-watching sessions, and eat spicy food with.

When Tomislav 'the Glorious' Piteša joined the office, not only did I get a partner in crime for the development of SHARC but also another mentor—especially for handling density matrices from our favorite program. Thank you for all your help, motivation, and the many laughs we shared in the office.

Of the other group members, I want to thank former member Dr. Leon Freitag for recommending this group and taking the time to answer all my questions about a possible PhD position. From the other postdocs in the group, I want to thank

Dr. Štěpán Sršeň and Dr. Johannes Dietschreit for their help and scientific advice especially in the latter stages of the thesis.

I also want to extend my gratitude towards all other members of the group for all the interesting chats at lunch, camaraderie, boardgame evenings and breaks, collaborative teaching and talks, coffee breaks, academic weekends, helpful scripts and advice, and so much more. There is no better feeling than knowing that I was never alone in my struggles.

Further, I want to thank my supervised bachelor students Oleksandra Zhuravel and David Lehrner for their curiosity and help in the early stages of LVC/MM. My officially and unofficially supervised master students Cheng Luo and Laurens van Dam also deserve my thanks for not only being great students—at times struggling with my inventions—but also being great companions and additions to the whole group.

Of the many friends that I made along the way, I especially mention and thank a few of them distinctly. Starting with Dr. David Xu, I immediately had the best lab partner and friend to survive the Bachelors degree with. You pushed me towards greater heights and showed me what is possible, while always having great advice. Without the initial guidance and constant mentorship of Dr. Robin Feldmann during the Masters degree, I would have discovered my love for software development much to late and would have not joined the quantum chemical community. He and Hendrik Schmitt have been a substantial influence in all aspects of my life: musically, culinarily, politically, and personally. I will never forget the time in our shared flat and I am happy to still have you as friends. I also want to thank Dr. Francesco Bosia for taking me on as a student, when I just started getting into programming and software development. Your close, instructional, trusting and light-hearted supervision style has laid the foundation for my journey onwards in the field of theoretical chemistry and as a software developer.

I am also very grateful for the dear friends I made in the group: Richard Jacobi, Dóra Vörös, Julia Franz, and Nadja Singer. You really made my last four years in Vienna and thank you for your support in the months of writing this thesis. I also want to thank Lena, Maria, Leonie, and Amanda for their friendship and a cozy place that I—way too often—came home late to from work. I am also grateful for some of my longest standing friends Patrick Gierl and Raphi Meier for their emotional support, advice and fun times spent together.

My scientific journey would have never been possible without my parents. Thank you for always having my back and supporting me in every decision along the way.

Lastly, for something that is not done often enough in these times, I leave the following quote:

"I wanna thank me. I wanna thank me for believing in me. I wanna thank me for doing all this hard work. I wanna thank me for having no days off. I wanna thank me for never quittin'..."

– Snoop Dogg (2018)

CURRICULUM VITAE

Severin Carl Claudio Polonius

Education

– present April 2021	Dr. rer. nat. in Chemistry **University of Vienna**, Austria Supervisors: Prof. Leticia González Co-supervisor: Dr. Sebastian Mai
– July 2020 September 2018	M. Sc. in Chemistry | Grade: 5.57[a] **Federal Institute of Technology Zurich**, Switzerland Thesis: “Parametrization of semiempirical models for excited states” Supervisor: Prof. Markus Reiher
– August 2018 October 2015	B. Sc. in Chemistry | Grade: 1.7[b] **Technical University of Munich**, Germany Thesis: “Thermal- and Photoreactions of Diethyl Ether, Phenol and *tert*-Butanol on TiO_2(110)” Supervisors: Prof. Ulrich Kaspar Heiz
– July 2015 September 2007	Abitur | Grade: 1.2[c] **St.-Michaels-Gymnasium Metten**, Germany

Publications

2. S. Polonius, D. Lehrner, L. González, S. Mai: Resolving Photoinduced Femtosecond Three-Dimensional Solute–Solvent Dynamics through Surface Hopping Simulations, *J. Chem. Theory Comput.*, **20**, 4738 (2024).

1. S. Polonius, O. Zhuravel, B. Bachmair, S. Mai: LVC/MM: A Hybrid Linear Vibronic Coupling/Molecular Mechanics Model with Distributed Multipole-Based Electrostatic Embedding for Highly Efficient Surface Hopping Dynamics in Solution, *J. Chem. Theory Comput.*, **19**, 7171 (2023).

Conference Talks

2. S. Polonius: Nonadiabatic dynamics in solution using linear vibronic coupling models, 3rd DoSChem International Symposium, 06.07.2023–07.07.2023, Vienna, Austria.

1. S. Polonius: Methodological Development for Non-Adiabatic Dynamics in Multi-chromophoric Systems, Panel A DoSChem 2022 Retreat, 30.05.2022–02.06.2022, Styria, Austria.

---

[a] 6 is the highest, 1 is the lowest grade; passmark is 4.

[b] 1 is the highest, 5 is the lowest grade; passmark is 4.

[c] 1 is the highest, 6 is the lowest grade; passmark is 4.

Conference Posters

6. S. Polonius, L. González, S. Mai: Elucidating Time-dependent Nonadiabatic Three-dimensional Solute–Solvent Dynamics via Surface Hopping Simulations, 1st ViRaPID Workshop, 26.02.2024–29.02.2024, Vienna, Austria.
5. S. Polonius, L. González, S. Mai: A Matter of Perspective: Resolving the Three-dimensional Femto-second Solvent Relaxation in Thiocarbonyls through Nonadiabatic Dynamics Simulations, DoSChem Panel A Retreat, 19.02.2024–21.02.2024, Szidónia castle, Hungary.
4. S. Polonius, L. González, S. Mai: LVC/MM: Combining Linear Vibronic Coupling Models with Molecular Mechanics using Distributed Multipole-based Electrostatic Embedding, 59th Symposium on Theoretical Chemistry, 04.09.2023–11.09.2023, Zurich, Switzerland.
3. S. Polonius, L. González, S. Mai: Nonadiabatic Dynamics in Solution using Linear Vibronic Coupling Models, European Computational and Theoretical Conference (CompChem 2023), 27.08.2023–31.08.2023, Thessaloniki, Greece.
2. S. Polonius, L. González, S. Mai: When Monopoles are not enough: Taking the Restrained Electrostatic Potential Fit to the Multipolar Level, DoSChem Panel A Retreat, 20.03.2023–22.03.2023, Zeillern, Austria.
1. S. Polonius, L. González, S. Mai: Highly Efficient Non-adiabatic Dynamics in Solution Using Linear Vibronic Coupling Models with Electrostatic Embedding, 58th Symposium on Theoretical Chemistry, 18.09.2022–22.09.2022, Heidelberg, Germany.

Teaching Experience

8. Tutorial “Modern Quantum Chemistry Exercises” (Master course), March 2024–June 2024, University of Vienna, Austria.
7. Tutorial “Quantum Dynamics” (Master course), October 2021 – February 2022/October 2023–February 2024, University of Vienna, Austria.
6. Tutorial “Quantum Mechanical Exercises” (Bachelor course), June 2022/February 2023/June 2023/February 2024, University of Vienna, Austria.
5. Co-supervision of a Master Student (Cheng Luo), 2023, University of Vienna, Austria.
4. Co-supervision of a Bachelor Student (David Lehrner), 2022, University of Vienna, Austria.
3. Co-supervision of a Bachelor Student (Oleksandra Zhuravel), 2021, University of Vienna, Austria.
2. Tutorial “Informatics I for Chemists” (Bachelor course), September 2019–December 2019, Federal Institute of Technology Zurich, Switzerland.
1. Tutorial “Quantum Mechanics I” (Bachelor course), October 2017–February 2018, Technical University of Munich, Germany.

Experience in Software Development

4. SHARC, 2021–2024 refactoring and extensions within the scope of the PhD thesis, Prof. Leticia González and Dr. Sebastian Mai, University of Vienna, Austria.
3. Corporate PaaS software, 2020, Full-stack web development intern, Exnaton AG, Zurich, Switzerland.
2. Scine Sparrow, 2019-2020 “Semiempirical electronic spectroscopy: beyond ortho-gonalization-corrected methods”, Prof. Markus Reiher and Dr. Francesco Bosia, ETH Zurich, Switzerland.
1. GROMOS software package, 2019, “Introducing quantum mechanical calculations into the RE-EDS scheme”, Prof. Sereina Riniker, ETH Zurich, Switzerland.

Languages

German: mother tongue
English: fluent

Computer Skills

Systems & Platforms: Linux, Cuda, OpenMP, MPI, LaTeX
Programming Languages: Python, Bash, C++, Javascript, Rust, Fortran